University of Glasgow

Williams, Morag Jean (2021) Evaluation of fine-pitch hybrid silicon pixel detector prototypes for the CLIC vertex detector in laboratory and test-beam measurements. PhD thesis.

https://theses.gla.ac.uk/82196/

Copyright and moral rights for this work are retained by the author

A copy can be downloaded for personal non-commercial research or study, without prior permission or charge

This work cannot be reproduced or quoted extensively from without first obtaining permission in writing from the author

The content must not be changed in any way or sold commercially in any format or medium without the formal permission of the author

When referring to this work, full bibliographic details including the author, title, awarding institution and date of the thesis must be given

Enlighten: Theses
https://theses.gla.ac.uk/
research-enlighten@glasgow.ac.uk

Evaluation of Fine-Pitch Hybrid Silicon Pixel Detector Prototypes for the CLIC Vertex Detector in Laboratory and Test-Beam Measurements

DOCTORAL THESIS

Author:
Ms. Morag Jean WILLIAMS

Supervisors:
Dr. Dominik DANNHEIM
Prof. Aidan ROBSON
Dr. Richard BATES

A thesis submitted in fulfilment of the requirements for the Degree of Doctor of Philosophy

in the

School of Physics and Astronomy
College of Science and Engineering

UNIVERSITY OF GLASGOW

November 2020

Abstract

The Compact Linear Collider (CLIC) is a concept for a high-energy, high-luminosity $e^+ e^-$ linear collider for precision measurements of Standard Model processes and to search for new phenomena, proposed to be built after the lifetime of the upgraded Large Hadron Collider. The beam conditions expected at CLIC impose strict requirements on the CLIC detector design in order for the physics programme to be achieved. In the vertex detector subsystem, the pixelated detectors are required to achieve a spatial resolution of approximately 3 µm, a hit detection efficiency $\geq$99.7%, a timing resolution of $\leq$5 ns, and a material budget per layer of 0.2% of a radiation length. Currently, no pixel detector technology can achieve these requirements simultaneously, therefore prototype pixel detectors with novel designs are being developed and tested within the CLIC detector and physics collaboration.

The CLICpix2 hybrid readout ASIC aims to fulfil the CLIC vertex detector requirements. It has been designed using a 65 nm CMOS process with a fine pixel pitch of $25\times25\,\mu m^2$, simultaneous per-pixel charge and time measurements, and power-pulsing capabilities.

Within this thesis, the performance of CLICpix2 ASICs bump-bonded to active-edge planar silicon sensors is evaluated using laboratory and test-beam measurements. The detectors were hybridised using a novel single-chip bonding process, and the interconnect quality is quantified using a data-driven pixel categorisation scheme. High interconnect qualities are achieved for a small number of assemblies, with yields up to 99.6%. The formulated categorisation method successfully identifies unexpected behaviour of the devices, which were used as feedback to the manufacturer to optimise the solder bump-bonding process. Calibration measurements are also performed to convert the threshold and charge measurements of the assemblies into physical units.

The performance of the two highest quality assemblies is evaluated and compared to the CLIC vertex detector requirements. Test-beam data recorded at the CERN and DESY test-beam facilities with CLICpix2 planar sensor assemblies is reconstructed using the Corryvreckan software framework, significantly contributed to as part of this study. Similar results are recorded for both assemblies, despite the large differences in test-beam telescope set-ups and data reconstruction processes used for each. The intrinsic spatial resolution of CLICpix2 assemblies with 130 µm planar sensors is determined to be $<$3 µm. CLICpix2 planar sensor assemblies are calculated to have hit detection efficiencies of above 99.95% at the optimal operating conditions, and an intrinsic timing resolution of $\leq$5 ns is achieved after a time-walk correction is applied to the pixel data. The CLICpix2 detectors meet the hit detection efficiency, spatial resolution, and timing resolution requirements of the CLIC vertex detector with planar silicon sensors of thickness 130 µm. To achieve these requirements with the target sensor thickness of 50 µm, a silicon sensor with enhanced charge sharing or a smaller pixel pitch would be required.

Contents

Introduction 1

I R&D of pixel detectors for particle physics experiments 3

1 Semiconductor pixel detectors for HEP 5
1.1 Basic semiconductor concepts of pixel detectors . . . 6
1.1.1 Semiconductors and the PN junction . . . 6
1.1.2 Charge generation from incident particles . . . 8
1.1.2.1 Multiple coulomb scattering . . . 8
1.1.2.2 Energy loss of heavy charged particles . . . 9
1.1.2.3 Charge generation . . . 9
1.1.3 Charge transport and sharing . . . 10
1.2 Front-end electronics of pixelated detectors . . . 11
1.2.1 Signal generation and detection . . . 11
1.2.2 Readout ASIC . . . 12
1.3 Pixel detector performance . . . 13
1.3.1 Design and operation aspects of sensors . . . 14
1.3.1.1 Reverse bias voltage . . . 14
1.3.1.2 Pixel capacitance . . . 14
1.3.2 Design and operation aspects of pixel electronics . . . 15
1.3.2.1 Noise and threshold adjustment . . . 15
1.3.2.2 Temperature . . . 15
1.3.3 Pixel detector figures of merit . . . 15
1.4 Bump-bonding of hybrid pixel detectors . . . 17
1.4.1 The bump-bonding process . . . 17
1.4.2 Challenges of bump-bonding . . . 18

2 R&D for the CLIC detector 21
2.1 High energy physics at particle colliders . . . 21
2.2 The Compact Linear Collider . . . 23
2.2.1 Physics potential of CLIC . . . 23
2.2.2 The CLIC accelerator . . . 24
2.2.3 Beam-induced backgrounds . . . 25
2.3 The CLIC detector . . . 26
2.3.1 CLICdet outer detectors . . . 26
2.3.2 Inner detectors . . . 27
2.3.2.1 Inner detector requirements . . . 27
2.3.2.2 CLIC tracking detector layout and technologies . . . 28
2.3.2.3 CLIC vertex detector layout and technologies . . . 29

II Characterisation of CLICpix2 planar sensor assemblies 31

3 CLICpix2 hybrid assemblies with planar sensors 33
3.1 CLICpix2 readout ASIC . . . 33
3.1.1 ASIC design . . . 33
3.1.2 Notable features of the ASIC . . . 37
3.2 Active-edge planar silicon sensors . . . 37
3.2.1 Advacam production . . . 37
3.2.2 FBK-CMM production . . . 39
3.3 CLICpix2 bump-bonding at IZM . . . 39
3.4 Material budget calculation of CLICpix2 planar assemblies . . . 40

4 Laboratory characterisation of CLICpix2 planar sensor assemblies 45
4.1 Caribou DAQ system and Peary DAQ software . . . 45
4.1.1 Caribou DAQ system . . . 45
4.1.2 Peary DAQ software . . . 46
4.2 Initial testing . . . 47
4.2.1 X-ray imaging . . . 48
4.2.2 I-V characteristics . . . 48
4.2.3 Pixel equalisation . . . 50
4.2.4 Summary of initial laboratory testing results . . . 52
4.3 Pixel categorisation . . . 53
4.3.1 Radioactive source exposure . . . 53
4.3.2 Test-pulse injection . . . 56
4.3.3 Categorisation of pixels . . . 57
4.3.3.1 Assemblies 16 and 20 . . . 57
4.3.3.2 Assemblies 19 and 14 . . . 60
4.3.3.3 Assemblies 9, 15 and 21 . . . 61
4.4 Temperature stability studies . . . 63
4.4.1 Voltage DAC temperature dependence . . . 63
4.4.2 Mitigation measures during CLICpix2 data taking . . . 65
4.5 Charge and threshold calibration . . . 66
4.5.1 Threshold calibration . . . 66
4.5.2 Time-over-threshold calibration . . . 69
4.5.2.1 Calibration of test-pulse injection . . . 71
4.5.2.2 Surrogate function calibration curves . . . 73
4.6 Summary of laboratory testing of CLICpix2 planar sensor assemblies . . . 78

III Performance evaluation of CLICpix2 planar sensor assemblies 79

5 Test-beam facilities and telescopes 81
5.1 Test-beam and telescope concepts . . . 81
5.2 CERN, SPS test-beam facilities . . . 82
5.2.1 CLICdp Timepix3 telescope . . . 82
5.2.1.1 The Timepix3 readout ASIC . . . 83
5.2.1.2 Telescope set-up . . . 84
5.2.1.3 CLICpix2 device integration . . . 85
5.2.1.4 Test-beam DAQ system . . . 85
5.3 DESY II test-beam facilities . . . 86

5.3.1 EUDET Mimosa26 telescope . . . 86
5.3.1.1 The Mimosa26 monolithic detector . . . 87
5.3.1.2 Telescope set-up . . . 87
5.3.1.3 CLICpix2 device integration . . . 87
5.3.1.4 Test-beam DAQ system . . . 87

6 The Corryvreckan reconstruction framework 91
6.1 Architecture of the software . . . 92
6.1.1 Object data storage . . . 92
6.1.2 Configuration files . . . 92
6.2 The modular reconstruction chain . . . 93
6.2.1 Data input . . . 93
6.2.2 Usage of timing information in reconstruction . . . 95
6.2.3 Telescope and DUT alignment . . . 96
6.2.4 η correction . . . 96
6.2.5 Data and analysis output . . . 96
6.3 Documentation and code repository . . . 97

7 Test-beam data reconstruction 99
7.1 Reconstruction of CLICdp Timepix3 telescope test-beam data . . . 99
7.1.1 Temperature analysis of test-beam data . . . 100
7.1.2 Corryvreckan configuration . . . 100
7.1.3 Telescope performance . . . 104
7.2 Reconstruction of EUDET Mimosa26 telescope test-beam data . . . 104
7.2.1 Temperature analysis of test-beam data . . . 105
7.2.1.1 Temperature variation within single runs . . . 105
7.2.1.2 Temperature variation over multiple runs . . . 107
7.2.2 Corryvreckan configuration . . . 109
7.2.3 Telescope performance . . . 114

8 CLICpix2 performance 117
8.1 Analysis of track-associated clusters . . . 117
8.1.1 Cluster size . . . 117
8.1.1.1 Cluster size as a function of bias voltage . . . 117
8.1.1.2 In-pixel cluster size . . . 119
8.1.1.3 Cluster size as a function of threshold . . . 120
8.1.2 Pixel and cluster charge . . . 120
8.2 Efficiency . . . 124
8.2.1 Total efficiency . . . 124
8.2.2 Efficiency over the matrix and in-pixel efficiency . . . 125
8.3 Spatial resolution . . . 127
8.3.1 Spatial residual and positional resolution along the X axis . . . 127
8.3.2 Spatial residual and positional resolution along the Y axis . . . 128
8.3.3 Spatial residual as a function of bias voltage and threshold . . . 130
8.3.4 Spatial residual for different cluster widths . . . 131
8.4 Timing resolution . . . 133

Conclusion **137**

A Additional figures from Chapter 4 **139**

B Corryvreckan test-beam reconstruction configuration files **143**

C Additional figures from Chapter 8 **149**

List of Tables

3.1 Summary of the main design parameters of the CLICpix2 ASIC design [51] [7]. . . . 34
3.2 Summary of periphery DACs of the CLICpix2 ASIC important to the study [7]. . . . 35
3.3 Summary of all CLICpix2 assemblies with N-in-P, active-edge planar sensors produced. 41
3.4 Summary of the CLICpix2+planar assemblies material budget calculation. 43

4.1 Summary of initial testing results of CLICpix2 planar sensor assemblies. The threshold equalisation results of assemblies 16 and 20 can be found in units of e^- in Table 4.3. 55
4.2 Summary of pixel categorisation results for CLICpix2 planar sensor assemblies. The CLICpix2 ASIC has a total of 16384 pixels. 58
4.3 Threshold equalisation of CLICpix2 planar sensor assemblies 16 and 20 in units of e^-. 69

7.1 Temperature measurements of four Timepix3 planes within the CLICdp Timepix3 telescope at the SPS test-beam facility. The data spans the period 6.30pm 09/11/2018 to 8.04am 12/11/2018. 100
7.2 Input parameters for spatial resolution simulation of the CLICdp Timepix3 telescope at SPS North Area, CERN. The Z positions were measured for the data taking period of November 2018. 105
7.3 Input parameters for spatial resolution simulation of the EUDET Mimosa26 telescope at the DESY II test-beam facility. The Z positions were measured for the data taking period of July 2019. 115

List of Figures

1.1 Diagram of one pixel cell of a hybrid pixel detector. The charged particle traverses the sensor, generating charge carriers in the depletion zone. Charges move in the electric field created by the bias voltage at the sensor backside. This induces a current on the pixel pad, detected by the readout electronics. Image from [8]. 6
1.2 Diagram of the electron energy band structure of, insulating, conducting, and semiconducting materials, including intrinsic, extrinsic N-type, and extrinsic P-type semiconductors. E_D denotes shallow donor levels and E_A denotes shallow acceptor levels inserted by dopant atoms. 7
1.3 Diagram of the electron energy band structure of semiconductor materials, including a PN-junction. E_D denotes shallow donor levels and E_A denotes shallow acceptor levels inserted by dopant atoms. 8
1.4 Average energy loss of particles in different media as a function of $\beta\gamma$, calculated using by the Bethe-Bloch equation. Image from [14]. 10
1.5 Simulation of charge transport and collection at three neighbouring electrodes of the sensor over time for a MIP traversing the central region, using the Allpix^2 framework. The visualisation only shows electrons that have reached a sensor implant within the depicted integration time [16]. 11
1.6 Schematic of a generic PUC. Image based on [8]. 12
1.7 Diagram showing the time-walk that occurs between signals of different magnitude. . 17
1.8 Diagram of UBM deposition using the lift-off technique. Image from [18]. 18

2.1 Summary of the fundamental particles of the SM of particle physics. Image from [23]. 22
2.2 SM cross sections for key $e^+ e^-$ processes as a function of the CM energy. Image from [5]. 23
2.3 CLIC accelerator complex at the 3 TeV energy stage, showing the novel two-beam accelerating concept. Image from [31]. 25
2.4 Diagram of the CLIC main linear accelerator as it would be implemented at CERN near Geneva in Switzerland, showing the accelerator length for each energy stage. Image from [32]. 25
2.5 Histogram of the integrated luminosity per year in the proposed CLIC staging scenario. The total luminosity is shown in blue and the luminosity at CM energies above 99% of the nominal are shown in in red. Image from [30]. 25
2.6 A 3D diagram of the CLIC detector design. It has pixelated low-mass inner detectors, fine-grained calorimeters optimised for particle flow analysis, 4 T superconducting solenoid magnet, and a muon identification system within the iron yoke. Image from [38]. 26
2.7 A 2D cross-sectional diagram of one quadrant of the CLIC detector design. Image from [38]. 27
2.8 Diagram of the CLIC detector design, as would be placed in the detector cavern of CLIC. Image from [38]. 27

2.9 Schematic of the CLIC tracking detector, depicted in yellow. The cylindrical support tube of the tracker, shown in light grey, separates the inner and outer regions of the tracker. Image modified from [38]. . . . 29
2.10 Schematic of the CLIC vertex detector and beam pipe. The barrel section of the vertex detector has three double layers, and the end-caps have a spiralled design. The first barrel layer of the detector is at a radius of 31 mm from the interaction point. Image from [38]. . . . 30

3.1 Image of a CLICpix2 ASIC glued and wire-bonded to to a readout PCB. Image credit CLICdp. . . . 34
3.2 Layout design of the top-metal layers of the CLICpix2 ASIC in a grid of 5x4 pixels, showing the mirrored column design. . . . 34
3.3 Schematic of the CLICpix2 analogue front-end. . . . 35
3.4 Diagram of the ToT and ToA pixel measurements of the CLICpix2 ASIC. Figure is not to scale and based on a similar image from [54]. . . . 36
3.5 Illustration of the effect of ikrum and clock divider settings on the ToT measurement of CLICpix2. Diagram is not to scale. . . . 36
3.6 Illustration of the process flow of producing active-edge N-in-P sensors by the manufacturer. Image based on [59]. . . . 38
3.7 Image of two active-edge planar sensors from FBK-CMM, showing the design of the staggered active-edge implant trenches. The sensor on the left has no guard ring while it is present for the sensor on the right, as indicated by the larger distance between the implant trenches and the pixel matrix. . . . 39
3.8 Image of a CLICpix2 ASIC with deposited solder bumps, showing the full pixel matrix. Image credit Fraunhofer IZM [62]. . . . 40
3.9 Image of a CLICpix2 ASIC with deposited solder bumps, showing a corner of the pixel matrix in more detail [6]. . . . 40
3.10 Image of a CLICpix2 assembly with a 130 µm thick active-edge sensor. The sensor (on-top) is bump-bonded to the ASIC (underneath), which is itself wire-bonded to a readout PCB [6]. . . . 41
3.11 Pictorial representation of the vertical layers considered to calculate the material budget of CLICpix2+planar assemblies. This figure is not to scale and covers two pixel pads in the horizontal axis. . . . 42
3.12 Diagram of the PCB layer stack used for CLICpix2+planar assemblies. . . . 42
3.13 Cross-sectional image of a bonded CLICpix2+planar assembly. Image credit Fraunhofer IZM [62]. . . . 42

4.1 An example Caribou set-up for laboratory measurements. Image from [6]. . . . 46
4.2 Voltage of the `threshold_LSB`/`MSB` measured by the CLICpix2 ASIC output multiplexer, showing the non-monotonic behaviour of the DAC between MSB values. Image from [7]. . . . 47
4.3 Graph of the measured linearised `threshold` voltage output of CLICpix2 planar sensor assembly 16. . . . 47
4.4 X-ray image of CLICpix2 assembly 16, provided by the manufacturer [62]. . . . 48
4.5 X-ray image of CLICpix2 assembly 19, provided by the manufacturer [62]. . . . 48
4.6 X-ray image of CLICpix2 assembly 20, provided by the manufacturer [62]. . . . 49
4.7 X-ray image of CLICpix2 assembly 21, provided by the manufacturer [62]. . . . 49
4.8 IV curve for CLICpix2 planar sensor assemblies 14 and 19, where the current limit of 100 µA was reached at a bias voltage of −78 V and −66 V respectively. . . . 49

4.9 IV curve for CLICpix2 planar sensor assembly 14 and 19, zoomed into the low current range. . . . 49
4.10 Equalisation measurement of CLICpix2 planar sensor assembly 16 with an applied bias voltage of -60 V. . . . 50
4.11 Equalisation measurement of CLICpix2 planar sensor assembly 20 with an applied bias voltage of -60 V. . . . 50
4.12 2D map of turn-on threshold for CLICpix2 planar sensor assembly 16 with an applied bias voltage of -60 V, using equalised matrix settings. . . . 51
4.13 2D map of turn-on threshold for CLICpix2 planar sensor assembly 20 with an applied bias voltage of -60 V, using equalised matrix settings. . . . 51
4.14 2D map of the noise RMS width for CLICpix2 planar sensor assembly 16 with an applied bias voltage of -60 V, using equalised matrix settings. . . . 51
4.15 2D map of the noise RMS width for CLICpix2 planar sensor assembly 20 with an applied bias voltage of -60 V, using equalised matrix settings. . . . 51
4.16 Microscope image of the damaged region of the ASIC of CLICpix2 planar sensor assembly 18. . . . 52
4.17 IV curve for CLICpix2 planar sensor assembly 22. . . . 52
4.18 Histogram of the hit rate observed for a radioactive source measurement using CLICpix2 planar sensor assembly 20 with nominal operational threshold and bias voltage applied. The dashed lines indicate a region of $\pm 3\sigma$ around the mean of the Gaussian fit. . . . 54
4.19 Histogram of the hit rate observed for a radioactive source measurement using CLICpix2 planar sensor assembly 15 with nominal operational threshold and bias voltage applied. The dashed lines indicate a region of $\pm 3\sigma$ around the mean of the Gaussian fit. . . . 54
4.20 Diagram of test pulse generation using the test capacitor of CLICpix2, drawn not to scale. Charge pulses of equal magnitude are generated in both polarities. If the pulse height is large, significant secondary overshoot peaks are generated from charge conservation. . . . 56
4.21 Pixel categorisation results for CLICpix2 planar sensor assembly 16 for nominal threshold and bias voltage. . . . 59
4.22 Pixel categorisation results for CLICpix2 planar sensor assembly 20 for nominal threshold and bias voltage. . . . 59
4.23 2D histogram of pixel counts for CLICpix2 planar sensor assembly 20 when exposed to a source of fluorescence X-rays created using an electron beam incident on a copper target. . . . 60
4.24 2D histogram of pixel counts for CLICpix2 planar sensor assembly 16 when exposed to a particle beam from the CERN SPS facility [66]. . . . 60
4.25 Pixel categorisation results for CLICpix2 planar sensor assembly 19 for nominal threshold and bias voltage. . . . 61
4.26 Pixel categorisation results for CLICpix2 planar sensor assembly 14 for nominal threshold and bias voltage. . . . 61
4.27 2D histogram of pixel counts for CLICpix2 planar sensor assembly 14 when exposed to a particle beam from the CERN SPS facility [66]. . . . 62
4.28 2D histogram of pixel counts for CLICpix2 planar sensor assembly 19 when exposed to a particle beam from the DESY II facility [67]. . . . 62
4.29 Pixel categorisation results for CLICpix2 planar sensor assembly 21 for nominal threshold and bias voltage. . . . 62

4.30 Solder bump cross-section of CLICpix2 planar sensor assembly 9 showing three unconnected bumps, provided by the manufacturer [62]. 62
4.31 2D hit map of pixel counts from a Sr-90 source exposure measurement of CLICpix2 planar sensor assembly 9 for nominal threshold and bias voltage. 63
4.32 2D hit map of pixel counts from a Sr-90 source exposure measurement of CLICpix2 planar sensor assembly 15 for nominal threshold and bias voltage. 63
4.33 Graph showing the voltage of `test_cap_1` vs. time for CLICpix2 assembly 16 with nominal threshold and bias voltage applied. 64
4.34 Graph showing the voltage of (`test_cap_1-test_cap_2`) vs. time for CLICpix2 assembly 16 with nominal threshold and bias voltage applied. 64
4.35 Graph showing the on-chip measured temperature vs. time for CLICpix2 assembly 16 with nominal threshold and bias voltage applied. 65
4.36 Graph showing the voltage of `test_cap_1` vs. temperature for CLICpix2 assembly 16 with a linear fit with nominal threshold and bias voltage applied. 66
4.37 Graph showing the voltage of `threshold` vs. temperature for CLICpix2 assembly 16 with a linear fit with nominal threshold and bias voltage applied. 66
4.38 Schematic of the set-up used for X-ray fluorescence measurements, where the DUT is a CLICpix2 planar sensor assembly. Image from [70]. 67
4.39 Histogram of the normalised average number of counts in even columns as a function of `threshold` value for CLICpix2 planar sensor assembly 20 at a bias voltage of -60 V. Three data sets are shown: X-ray fluorescence spectrum of a Cu target, X-ray fluorescence spectrum of a Fe target, and when no X-ray source present. 68
4.40 Histogram of the normalised average number of counts in odd columns as a function of `threshold` value for CLICpix2 planar sensor assembly 20 at a bias voltage of -60 V. Three data sets are shown: X-ray fluorescence spectrum of a Cu target, X-ray fluorescence spectrum of a Fe target, and when no X-ray source present. 68
4.41 Histogram of the normalised average number of counts in even columns as a function of `threshold` value for CLICpix2 planar sensor assembly 16 at a bias voltage of -60 V. Three data sets are shown: X-ray fluorescence spectrum of a Cu target, X-ray fluorescence spectrum of a Fe target, and when no X-ray source present. 69
4.42 Histogram of the normalised average number of counts in odd columns as a function of `threshold` value for CLICpix2 planar sensor assembly 16 at a bias voltage of -60 V. Three data sets are shown: X-ray fluorescence spectrum of a Cu target, X-ray fluorescence spectrum of a Fe target, and when no X-ray source present. 69
4.43 Graph of `threshold` value as a function of energy for the even columns of CLICpix2 planar sensor assembly 20 at a bias voltage of -60 V. 70
4.44 Graph of `threshold` value as a function of energy for the odd columns of CLICpix2 planar sensor assembly 20 at a bias voltage of -60 V. 70
4.45 Graph of `threshold` value as a function of energy for the even columns of CLICpix2 planar sensor assembly 16 at a bias voltage of -60 V. 70
4.46 Graph of `threshold` value as a function of energy for the odd columns of CLICpix2 planar sensor assembly 16 at a bias voltage of -60 V. 70
4.47 Profile histograms of the fraction of hit pixels recorded in the matrix during test pulse injection as a function of `threshold` for CLICpix2 planar sensor assembly 20 at a bias voltage of -60 V. Distributions are shown for when all pixels are analysed, and when odd or even columns are considered separately. 71

4.48 Profile histograms of the fraction of hit pixels recorded in the matrix during test pulse injection as a function of `threshold` for CLICpix2 planar sensor assembly 16 at a bias voltage of -60 V. Distributions are shown for when all pixels are analysed, and when odd or even columns are considered separately. 71
4.49 ToT calibration curve for pixel (0,4) of CLICpix2 planar sensor assembly 20 with nominal threshold and bias voltage applied. 73
4.50 ToT calibration curve for pixel (0,4) of CLICpix2 planar sensor assembly 20 with nominal threshold and bias voltage applied, zoomed into the low ToT region. 73
4.51 2D map of the A parameters obtained from the surrogate function fit to the ToT calibration curve of the pixel. For CLICpix2 planar sensor assembly 20 with nominal threshold and bias voltage applied. 75
4.52 1D histograms of the A parameters obtained from the surrogate function fit to the ToT calibration curve of the pixel, showing the difference between odd and even columns. For CLICpix2 planar sensor assembly 20 with nominal threshold and bias voltage applied. 75
4.53 2D map of the B parameters obtained from the surrogate function fit to the ToT calibration curve of the pixel. For CLICpix2 planar sensor assembly 20 with nominal threshold and bias voltage applied. 76
4.54 1D histograms of the B parameters obtained from the surrogate function fit to the ToT calibration curve of the pixel, showing the difference between odd and even columns. For CLICpix2 planar sensor assembly 20 with nominal threshold and bias voltage applied. 76
4.55 2D map of the C parameters obtained from the surrogate function fit to the ToT calibration curve of the pixel. For CLICpix2 planar sensor assembly 20 with nominal threshold and bias voltage applied. 76
4.56 1D histograms of the C parameters obtained from the surrogate function fit to the ToT calibration curve of the pixel, showing the difference between odd and even columns. For CLICpix2 planar sensor assembly 20 with nominal threshold and bias voltage applied. 76
4.57 2D map of the T parameters obtained from the surrogate function fit to the ToT calibration curve of the pixel. For CLICpix2 planar sensor assembly 20 with nominal threshold and bias voltage applied. 77
4.58 1D histograms of the T parameters obtained from the surrogate function fit to the ToT calibration curve of the pixel, showing the difference between odd and even columns. For CLICpix2 planar sensor assembly 20 with nominal threshold and bias voltage applied. 77
4.59 2D map of the χ^2 per NDOF values obtained from the surrogate function fit to the ToT calibration curve of the pixel. For CLICpix2 planar sensor assembly 20 with nominal threshold and bias voltage applied. 77
4.60 1D histograms of the χ^2 per NDOF values obtained from the surrogate function fit to the ToT calibration curve of the pixel, showing the difference between odd and even columns. For CLICpix2 planar sensor assembly 20 with nominal threshold and bias voltage applied. 77

5.1 Illustration of a typical test-beam telescope set-up, consisting six reference planes and a central DUT. The coordinate system used in this study is indicated. 81
5.2 Image of the North Area experimental hall of CERN, showing the H6B beam-line area when facing downstream. 83

5.3 Image of the CLICdp Timepix3 telescope in the H6B beam-line of the CERN SPS North Area hall, showing its light-tight enclosure and mechanical systems. The particle beam from the SPS propagates along the positive Z axis from the right of the image to the left [77]. . . . 83
5.4 Image of the CLICdp Timepix3 telescope in the H6B beam-line of the CERN SPS North Area hall, showing seven reference planes and a CLICpix2 planar sensor assembly as a DUT [77]. . . . 83
5.5 A schematic of the front-end logic of single pixels and superpixels. Diagram from [54]. 84
5.6 Schematic of the DAQ system for the CLIC Timepix3 telescope at the SPS test-beam facility. . . . 85
5.7 Image of the DATURA telescope in beam-line 21 of the DESY Test-Beam Facility. The telescope set-up, TLU unit, voltage sources, and DAQ system can all be seen. The particle beam propagates parallel to the telescope system, from right to left in the image. . . . 86
5.8 Image of the DATURA telescope at the DESY Test-Beam Facility, with the Z axis from right to left. Six Mimosa26 telescope planes are seen. The additional Timepix3 time-reference plane is the last plane of the telescope in Z. A CLICpix2 planar sensor DUT is present between telescope planes 2 and 3. . . . 86
5.9 Image of the CLICpix2 aluminium holder made for the EUDET telescope at DESY. A CLICpix2 planar assembly, Caribou CaR board, and FMC cable are attached to the holder using screws and plastic sections. . . . 88
5.10 Image of a CLICpix2 planar sensor mounted between telescope planes 2 and 3 of the DATURA EUDET telescope at DESY. The Z axis of the telescope system goes from right to left in this picture. The DUT holder is mounted along the X axis using a supporting translation stage. . . . 88
5.11 Schematic of the DAQ system for the DATURA Mimosa26 telescope at the DESY II test-beam facility. . . . 88

6.1 An example section of a Corryvreckan main configuration file, showing configuration parameters of the framework and of a module. . . . 93
6.2 An example section of a Corryvreckan detector configuration file, specifying the properties of one device. . . . 93
6.3 Diagram of a typical Corryvreckan module chain for reconstruction of a telescope set-up containing a DUT, using an aligned geometry set-up. . . . 93
6.4 Schematic of the Corryvreckan event definition by the `[Metronome]` module. . . . 94
6.5 Schematic of the Corryvreckan event definition by a detector using a frame-based readout. The event building is configured to only add data from the data-driven detector if it is fully contained within the event time-window. . . . 94
6.6 Schematic of the Corryvreckan event definition by a TLU, combining trigger ID and timing information. The event is defined in time by the trigger timestamp and an optional time window indicated by $\pm\Delta$T. . . . 95

7.1 Diagram of the Corryvreckan modules used to reconstruct test-beam data taken using the CLICdp Timepix3 test-beam telescope with a CLICpix2 planar sensor assembly DUT. . . . 100
7.2 Cluster size distribution of telescope plane 2 of the CLICdp Timepix3 test-beam telescope. . . . 101
7.3 Cluster size distribution of CLICpix2 planar sensor assembly 16, before DUT-track association. . . . 101

7.4 η distribution for in-pixel cluster position correction for CLICpix2 planar sensor assembly 16 operated at a threshold of 626 e^- and an applied bias voltage of -25 V within the CLICdp Timepix3 test-beam telescope. . . . 102
7.5 χ^2 per NDOF of reconstructed tracks using a GBL track model for data taken with the CLICdp Timepix3 test-beam telescope. . . . 102
7.6 Hit detection efficiency as a function of spatial association criterion between DUT clusters and track incidence position, for CLICpix2 planar sensor assembly 16. . . . 103
7.7 Hit detection efficiency as a function of spatial association criterion between DUT clusters and track incidence position for CLICpix2 planar sensor assembly 16, zoomed into the high efficiency region. . . . 103
7.8 Biased track residual along the X axis of telescope plane 2 from the CLICdp Timepix3 test-beam telescope. . . . 104
7.9 Biased track residual along the Y axis of telescope plane 2 from the CLICdp Timepix3 test-beam telescope. . . . 104
7.10 Histogram of recorded temperature CLICpix2 assembly 19. Each temperature is measured with respect to the initially recorded value. . . . 106
7.11 Histogram of recorded temperature CLICpix2 assembly 19, zoomed in to show the initial temperature increase. Each temperature is measured with respect to the initially recorded value. . . . 106
7.12 Variation of cluster charge MPV as a function of temperature difference with respect to the initial temperature value of the data run, where a fan was applied to the CLICpix2 DUT. . . . 107
7.13 Variation of cluster charge MPV as a function of temperature difference with respect to the initial temperature value of the data run, where no fan was applied to the CLICpix2 DUT. . . . 107
7.14 Graph of the on-chip temperature change of CLICpix2 planar sensor assemblies over a 30 h period, where each bar represents temperature data from one run. The black bar is the temperature change from the initial value to the plateau temperature, the red star indicates the mean temperature of the run, and the grey bars show the $\pm 0.5\,^{\circ}$C measurement uncertainty. . . . 108
7.15 Diagram of the Corryvreckan modules used to reconstruct test-beam data taken using the EUDET Mimosa26 test-beam telescope with a CLICpix2 planar sensor assembly DUT. . . . 109
7.16 Diagram illustrating the event building scheme used in Corryvreckan to reconstruct the test-beam data taken using an EUDET Mimosa26 telescope with a CLICpix2 planar sensor DUT. . . . 110
7.17 Cluster size distribution of telescope plane 3, a Mimosa26 detector, of the EUDET Mimosa26 test-beam telescope. . . . 111
7.18 Cluster size distribution of CLICpix2 planar sensor assembly 20, before DUT-track association. . . . 111
7.19 Cluster size distribution of telescope plane 6, a Timepix3 detector, of the EUDET Mimosa26 test-beam telescope. . . . 111
7.20 η distribution for in-pixel cluster position correction for CLICpix2 planar sensor assembly 20 operated at a threshold of 665 e^- and an applied bias voltage of -25 V within the EUDET Mimosa26 test-beam telescope. . . . 111
7.21 χ^2 per NDOF of reconstructed tracks using a GBL track model for data taken with the EUDET Mimosa26 test-beam telescope. . . . 112
7.22 Hit detection efficiency as a function of DUT-track spatial association criterion, for CLICpix2 planar sensor assembly 20. . . . 113

7.23 Hit detection efficiency as a function of DUT-track spatial association criterion for CLICpix2 planar sensor assembly 20, focussing on the high efficiency region. 113
7.24 Hit detection efficiency as a function of DUT-track spatial association criterion, for CLICpix2 planar sensor assembly 20 operated at a 16.6 ke^- threshold. 113
7.25 Hit detection efficiency as a function of DUT-track spatial association criterion for CLICpix2 planar sensor assembly 20 operated at a 16.6 ke^- threshold, with a 2^{nd} order polynomial function fitted to the high efficiency region. 113
7.26 Biased spatial residual along the X axis of telescope plane 2, a Mimosa26 detector, from the EUDET Mimosa26 test-beam telescope. 114
7.27 Biased spatial residual along the Y axis of telescope plane 2, a Mimosa26 detector, from the EUDET Mimosa26 test-beam telescope. 114
7.28 Biased spatial residual along the X axis of telescope plane 6, a Timepix3 detector, from the EUDET Mimosa26 test-beam telescope. 115
7.29 Biased spatial residual along the Y axis of telescope plane 6, a Timepix3 detector, from the EUDET Mimosa26 test-beam telescope. 115

8.1 Cluster size distribution of assemblies 16 and 20, for the nominal threshold values and an applied bias voltage of -25 V. 118
8.2 Cluster size distribution of assemblies 16 and 20, for the nominal threshold values and an applied bias voltage of -60 V. 118
8.3 Mean cluster size of assemblies 16 and 20 as a function of the applied bias voltage, where the threshold of each detector is set to the nominal value. 119
8.4 In-pixel cluster size distribution of assembly 16 operated at a bias voltage of -25 V and nominal threshold. 119
8.5 In-pixel cluster size distribution of assembly 20 operated at a bias voltage of -25 V and nominal threshold. 119
8.6 In-pixel distribution of one-pixel sized clusters for assembly 16, operated at a bias voltage of -25 V and nominal threshold. 120
8.7 In-pixel distribution of one-pixel sized clusters for assembly 20, operated at a bias voltage of -25 V and nominal threshold. 120
8.8 Mean cluster size of assembly 20 as a function of threshold, for applied bias voltages of -25 V and -60 V. 121
8.9 In-pixel cluster size distribution of assembly 20 operated at a bias voltage of -25 V and a threshold of 9.2 ke^-. 121
8.10 Pixel charge distribution of assembly 16 for the nominal threshold value and an applied bias voltage of -25 V. 121
8.11 Pixel charge distribution of assembly 20 for the nominal threshold value and an applied bias voltage of -25 V. 121
8.12 In-pixel seed pixel charge distribution of assembly 16, operated at a bias voltage of -25 V and nominal threshold. 122
8.13 In-pixel seed pixel charge distribution of assembly 20, operated at a bias voltage of -25 V and nominal threshold. 122
8.14 Cluster charge distribution of assembly 16 for the nominal threshold value and an applied bias voltage of -25 V, fit with a Landau-Gaussian function. 123
8.15 Cluster charge distribution of assembly 20 for the nominal threshold value and an applied bias voltage of -25 V, fit with a Landau-Gaussian function. 123
8.16 MPV of cluster charge as a function of applied bias voltage, for assembly 16 operated at the nominal threshold. Two linear fit functions are applied to the data in the ranges indicated. 124

8.17 MPV of cluster charge as a function of applied bias voltage, for assembly 20 operated at the nominal threshold. Two linear fit functions are applied to the data in the ranges indicated. 124
8.18 Hit detection efficiency as a function of applied bias voltage for assemblies 16 and 20, both operated at the nominal threshold values. 125
8.19 Hit detection efficiency as a function of threshold for assembly 20 operated at an applied bias voltage of −25 V and −60 V. 126
8.20 Hit detection efficiency as a function of threshold for assembly 20 operated at an applied bias voltage of −25 Vand −60 V, focused in on the high efficiency plateau. . 126
8.21 2D map of hit detection efficiency across the matrix of assembly 16, operated at applied bias voltage of −25 V and nominal threshold, where the efficiency value is filled at the position of the associated DUT cluster. 126
8.22 2D map of hit detection efficiency across the matrix of assembly 20, operated at applied bias voltage of −25 V and nominal threshold, where the efficiency value is filled at the position of the associated DUT cluster. 126
8.23 In-pixel efficiency distribution of assembly 20, operated at a bias voltage of −25 V and nominal threshold. 127
8.24 In-pixel efficiency distribution of assembly 20, operated at a bias voltage of −25 V and a threshold of 9.2 ke^{-}. 127
8.25 Spatial residual along the X axis of assembly 16, operated at nominal threshold and an applied bias voltage of −25 V. 128
8.26 Spatial residual along the X axis of assembly 20, operated at nominal threshold and an applied bias voltage of −25 V. 128
8.27 Spatial residual along the Y axis of assembly 16, operated at nominal threshold and an applied bias voltage of −25 V. 129
8.28 Spatial residual along the Y axis of assembly 20, operated at nominal threshold and an applied bias voltage of −25 V. 129
8.29 Spatial residual along the X axis of assemblies 16 and 20 as a function of applied bias voltage, both operated at nominal threshold. 130
8.30 Spatial residual along the Y axis of assemblies 16 and 20 as a function of applied bias voltage, both operated at nominal threshold. 130
8.31 Spatial residual along the X axis of assembly 20 as a function of threshold, operated at applied bias voltages of −25 V and −60 V. 131
8.32 Spatial residual along the Y axis of assembly 20 as a function of threshold, operated at applied bias voltages of −25 V and −60 V. 131
8.33 Spatial residual along the X axis of assembly 16 for different projected cluster widths, operated at nominal threshold and an applied bias voltage of −25 V. 132
8.34 Spatial residual along the X axis of assembly 20 for different projected cluster widths, operated at nominal threshold and an applied bias voltage of −25 V. 132
8.35 Spatial residual along the Y axis of assembly 16 for different cluster widths, operated at nominal threshold and an applied bias voltage of −25 V. 132
8.36 Spatial residual along the Y axis of assembly 20 for different cluster widths, operated at nominal threshold and an applied bias voltage of −25 V. 132
8.37 2D distribution of pixel charge as a function of time residual for assembly 16, operated as an applied bias voltage of −60 V and nominal threshold. 134
8.38 Profile distribution of average time residual as a function of pixel charge for assembly 16, operated as an applied bias voltage of −60 V and nominal threshold. 134

8.39 2D distribution of pixel charge as a function of time residual for assembly 16 after time-walk correction, operated as an applied bias voltage of −60 V and nominal threshold. . . . 134
8.40 Profile distribution of average time residual as a function of pixel charge for assembly 16 after time-walk correction, operated as an applied bias voltage of −60 V and nominal threshold. . . . 134
8.41 Timing residual of assembly 16 before and after time-walk correction, operated at nominal threshold and an applied bias voltage of −60 V. . . . 135
8.42 Timing residual of assembly 16 after time-walk correction, operated at nominal threshold and an applied bias voltage of −60 V. . . . 135

A.1 X-ray image of CLICpix2 assembly 9, provided by IZM. . . . 139
A.2 X-ray image of CLICpix2 assembly 14, provided by IZM. . . . 139
A.3 X-ray image of CLICpix2 assembly 15, provided by IZM. . . . 139
A.4 X-ray image of CLICpix2 assembly 22, provided by IZM. . . . 139
A.5 2D map of the A parameters obtained from the surrogate function fit to the ToT calibration curve of the pixel with nominal threshold and bias voltage applied for CLICpix2+planar assembly 16. . . . 140
A.6 1D histograms of the A parameters obtained from the surrogate function fit to the ToT calibration curve of the pixel with nominal threshold and bias voltage applied for CLICpix2+planar assembly 16, showing the difference between odd and even columns. 140
A.7 2D map of the B parameters obtained from the surrogate function fit to the ToT calibration curve of the pixel with nominal threshold and bias voltage applied for CLICpix2+planar assembly 16. . . . 140
A.8 1D histograms of the B parameters obtained from the surrogate function fit to the ToT calibration curve of the pixel with nominal threshold and bias voltage applied for CLICpix2+planar assembly 16, showing the difference between odd and even columns. 140
A.9 2D map of the C parameters obtained from the surrogate function fit to the ToT calibration curve of the pixel with nominal threshold and bias voltage applied for CLICpix2+planar assembly 16. . . . 141
A.10 1D histograms of the C parameters obtained from the surrogate function fit to the ToT calibration curve of the pixel with nominal threshold and bias voltage applied for CLICpix2+planar assembly 16, showing the difference between odd and even columns. 141
A.11 2D map of the T parameters obtained from the surrogate function fit to the ToT calibration curve of the pixel with nominal threshold and bias voltage applied for CLICpix2+planar assembly 16. . . . 141
A.12 1D histograms of the T parameters obtained from the surrogate function fit to the ToT calibration curve of the pixel with nominal threshold and bias voltage applied for CLICpix2+planar assembly 16, showing the difference between odd and even columns. 141
A.13 2D map of the χ^2/ndof values obtained from the surrogate function fit to the ToT calibration curve of the pixel with nominal threshold and bias voltage applied for CLICpix2+planar assembly 16. . . . 142
A.14 1D histograms of the χ^2/ndof values obtained from the surrogate function fit to the ToT calibration curve of the pixel with nominal threshold and bias voltage applied for CLICpix2+planar assembly 16, showing the difference between odd and even columns. 142

B.1 Corryvreckan main configuration file for reconstruction of test-beam data taken with the CLICdp Timepix3 telescope, SPS, CERN, using a ToT+Cnt data taking mode. . . . 143

B.2 Example geometry configuration file for Corryvreckan for reconstruction of test-beam data taken with the CLICdp Timepix3 telescope, SPS, CERN, using a ToT+Cnt data taking mode. 144
B.3 Corryvreckan main configuration file for reconstruction of test-beam data taken with the CLICdp Timepix3 telescope, SPS, CERN, using a ToT+ToA data taking mode. . 145
B.4 Example geometry configuration file for Corryvreckan for reconstruction of test-beam data taken with the CLICdp Timepix3 telescope, SPS, CERN, using a ToT+ToA data taking mode. 146
B.5 Corryvreckan main configuration file for reconstruction of test-beam data taken with an EUDET Mimosa26 telescope, DESY-II, using a ToT+Cnt data taking mode. . . . 147
B.6 Example geometry configuration file for Corryvreckan for reconstruction of test-beam data taken with an EUDET Mimosa26 telescope, DESY-II, using a ToT+Cnt data taking mode. 148

C.1 Cluster size distribution of assemblies 16 and 20, for the nominal threshold values and an applied bias voltage of -25 V, with a logarithmic scale. 149
C.2 Cluster size distribution of assemblies 16 and 20, for the nominal threshold values and an applied bias voltage of -60 V, with a logarithmic scale. 149

For Grangig.

Acknowledgements

This text is the culmination of 3 years of research, and I benefited from the support I received from many directions.

I would like to thank all those involved in the maintenance and support of the CERN and DESY test-beam facilities used within this study. My thanks are given to Prof. Michael Campbell, Dr. Xavi Llopart, and Dr. Iraklis Kremastiotis for their many helpful discussions. Thank you to Mr. Thomas Fritzsch and Mr. Mario Rothermund from Fraunhofer IZM for their help in understanding the bump-bonding process used for the CLICpix2 assemblies and their feedback on my results.

Under the supervision of Dr. Dominik Dannheim I was able to learn, achieve, and progress as a physicist. He always has time for his students and made sure they had the best opportunities, something I was extremely thankful for. I thank Prof. Aidan Robson for the support he provided me with over the past eight years, both as a lecturer and supervisor. The continual effort he made to advise and guide me is greatly appreciated.

From day one, Dr. Simon Spannagel took me under his wing and gave me unending support and guidance, especially through tough times. Without him, this project would not have reached the level of quality it has and for that I am forever grateful.

During my time at CLICdp, I was grateful for the support and friendship I received from every colleague. Our group was very close, thanks to all the efforts made to organise social events and the leadership of Dr. Lucie Linssen. The extensive and uncomplicated help she provided, in aspects both within and outside of CERN, went above and beyond her remit and is a testament to her good leadership. A special thanks goes to Dr. Eva Sicking for being an amazing office mate, maintaining a great supply of motivation and chocolate in the office.

Every member of the CLICdp vertex and tracking team has helped this PhD project progress through discussions and encouragement. They made this experience the best it could be and I am thankful for the whole team. A special thank you goes to Dr. Magdalena Münker for her help reviewing this thesis.

My family have been there for me during all my studies, giving me the encouragement and means to achieve this PhD. To Dr. Dominik Arominski, thank you for the kindness and strength you have provided me with. The friends I made at university and during my PhD are some of the best people I know. Without them, I wouldn't have gotten to this point and wouldn't have had half as much fun along the way.

Despite the length of these acknowledgements, they cannot fully convey or cover every piece of support I received. To everyone I met along the way, thank you for your part in this PhD experience.

Declaration of Authorship

I, Ms. Morag Jean WILLIAMS, declare that this thesis titled, "Evaluation of Fine-Pitch Hybrid Silicon Pixel Detector Prototypes for the CLIC Vertex Detector in Laboratory and Test-Beam Measurements" and the work presented in it are my own. Where I have quoted the work of others, it is explicitly attributed and any published source given. This work has not been submitted for any other degree or other qualification at the University of Glasgow or any other institution.

Introduction

High energy physics (HEP) aims to explore the fundamental forces, processes, and constituent matter of the Universe. The Standard Model (SM) is the best theory of particle physics to date, successfully describing many of the observations made in HEP experiments. In its present form, however, it is an incomplete description of all particles and processes as many phenomena cannot be explained within the current SM framework. Advancements in theoretical particle physics beyond the SM (BSM) have provided testable predictions, the outcome of which can advance our understanding of the Universe.

Particle colliders are the modern-day tool to explore elementary particles and their interactions, enabling theoretical predictions to be tested at high energies. The Large Hadron Collider (LHC), based at the European Organisation for Nuclear Research (CERN), is the largest of these machines, reaching collision energies of 13 TeV [1]. The machine will be upgraded to increase the beam interaction rate by a factor of five, aiming to observe rare processes and indications of new physics. The High Luminosity LHC (HL-LHC) [2] is set to operate until approximately 2035.

After the lifetime of the HL-LHC, a new particle collider could address the unanswered questions relating to the SM. One such project is the Compact Linear Collider (CLIC), a concept for a future high-energy $e^+ e^-$ linear collider [3]. A three-staged construction of the accelerator complex is envisaged to optimise the physics potential of the machine, reaching particle collision energies from 350 GeV to 3 TeV [4]. Precision measurements of physics phenomena by the CLIC detector can identify any deviations of particle properties from the SM predictions, indicating areas of new physics. The direct discovery of new particles could validate theories such as supersymmetry [5].

The beam conditions expected at CLIC impose strict requirements on the CLIC detector design in order for the physics programme to be achieved [6]. The technologies to be used in the innermost detector subsystems, closest to the particle collision point, have a demanding set of requirements that currently no pixelated detector can achieve. To reach the performance goals, prototype pixel detectors with novel designs are being developed and tested. Each iteration of a prototype detector aims to improve on the previous designs in terms of performance figures of merit.

The design of the CLICpix2 readout application-specific integrated circuit (ASIC) for hybrid pixel detectors has been optimised for the CLIC detector application [7]. It aims to fulfil the requirements of the vertex detector subsystem with its small pixel pitch of $25 \times 25\,\mu m^2$, simultaneous per-pixel charge and time measurements, and power-pulsing capabilities to reduce the average power consumption during operation.

CLICpix2 ASICs have been bump-bonded to active-edge planar silicon sensors using a novel single-chip bonding process. This study evaluates the performance of these CLICpix2 planar sensor assemblies, using laboratory and test-beam measurements.

Part I of this thesis provides an overview of hybrid pixel detector technologies designed for future HEP experiments. The design and challenges of prototype hybrid pixel detectors are discussed in Chapter 1. An overview of the CLIC physics potential, the accelerator complex, and the detector design is given in Chapter 2.

Part II focusses on the characterisation of CLICpix2 planar sensor assemblies through detailed laboratory testing. Chapter 3 describes the CLICpix2 ASIC, the planar sensor design, and the solder bump-bonding hybridisation method used to manufacture the prototype assemblies. Laboratory measurements were performed to assess the functionality and interconnect quality of each CLICpix2

planar sensor assembly at the per-pixel level. These are described in Chapter 4, along with the calibration of threshold and pixel charge measurements into physical units.

In part III, the performance of the highest quality assemblies is evaluated using reconstructed test-beam data. Data was taken at the CERN Super Proton Synchrotron (SPS) and DESY-II test-beam facilities, with the reference telescope set-ups described in Chapter 5. The Corryvreckan software for flexible test-beam data reconstruction and analysis, described in Chapter 6, was significantly contributed to as part of this study. Chapter 7 describes the Corryvreckan reconstruction process performed on the recorded test-beam data sets. Finally, Chapter 8 contains the test-beam performance analysis of CLICpix2 planar sensor assemblies, and how they compare to the CLIC vertex detector requirements.

Part I

R&D of pixel detectors for particle physics experiments

Chapter 1

Semiconductor pixel detectors for HEP

Pixel detectors are segmented imaging devices that use semiconductor PN junctions to detect charged particles and photons. Many pixel detector designs exist with differing functionality and performance, each optimised for the intended application.

High Energy Physics (HEP) experiments often use pixel detector subsystems to detect high energy (GeV) charged particles travelling at velocities close to the speed of light, as discussed in Chapter 2. Their use is motivated by the high spatial and timing resolution that pixel detectors can achieve, allowing multiple particle trajectories to be distinguished with good resolution [8].

Different detector regions often use different pixel detector technologies, where the choice is driven by performance requirements and by restrictions such as time or cost. Two main groups of pixel detectors are distinguished: hybrid and monolithic technologies. In hybrid pixel detectors, the semiconductor sensor for charge generation is a separate element to the application-specific integrated circuit (ASIC) to detect the induced signal. A diagram of a generic hybrid detector pixel is shown in Figure 1.1. By separating these components the characteristics of the layers can be individually optimised, however the electrical and mechanical connection of the readout chip to the sensor can be a complex and expensive task. Monolithic pixel detectors avoid the problem of interconnection by integrating the necessary electronics into the sensor layer, but require design compromises to achieve this.

Independent of the technology chosen, most pixel detectors for HEP use doped crystalline silicon sensors. With this sensor material, signals in the order of 10 ke^- can be created from incident particles over thicknesses in the order of 100 µm [9]. Silicon also has a high charge carrier mobility, which reduces the charge readout time. In addition, it can be produced with the material budgets needed for the inner subsystems of particle detectors, where the radiation length of the materials should be minimised. Silicon wafer production is a well established industry, where manufacturing optimisations over time have allowed silicon to be grown with minimal impurities and inhomogeneities in the quantities necessary for large experiments.

To reach the performance goals of the next generation HEP experiments, new pixel detector technologies are needed. The prototyping process starts with the design of the pixel detector, normally developed using simulations of charged particle transport within the sensor and of the electronics response to induced signals. Prototype assemblies are then manufactured and tested, and the results inform the design of the next prototype. Ideally, with each iterating design of the readout electronics or semiconductor sensor the prototype performance is improved and any degrading effects are minimised. In addition, the hybridisation process itself can be a novel aspect of a prototype assembly, being either a challenging use case of an established technique or the development of a new hybridisation process. The prototyping process aims to fulfil all the desired performance requirements in the final pixel detector design.

This chapter focusses on hybrid pixel detectors for high energy charged particle detection. First, the basics of semiconductor materials and front-end electronics for pixel detectors are described. Then some important properties of sensors and electronics for the design and operation of pixel detectors

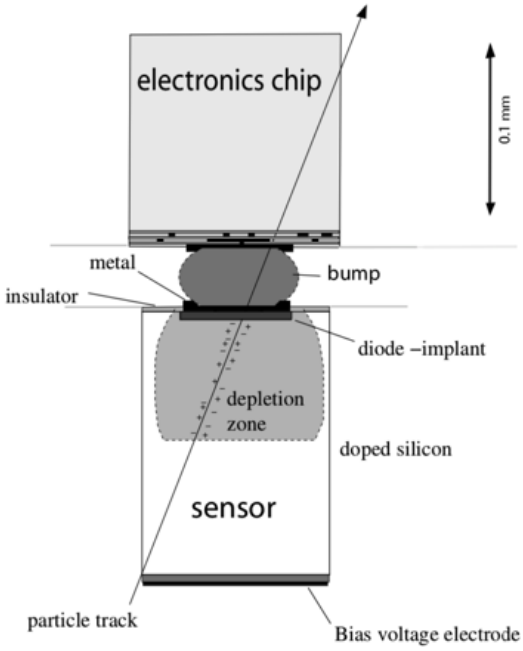

Figure 1.1: Diagram of one pixel cell of a hybrid pixel detector. The charged particle traverses the sensor, generating charge carriers in the depletion zone. Charges move in the electric field created by the bias voltage at the sensor backside. This induces a current on the pixel pad, detected by the readout electronics. Image from [8].

are discussed, along with the figures of merit used to determine pixel detector performance. Finally, the interconnection method of bump-bonding and its challenges are outlined.

1.1 Basic semiconductor concepts of pixel detectors

Pixel detectors exploit the properties of diodes for particle detection. An in-depth discussion of semiconductor materials and their properties is presented in [8] and [9]. In this section the aspects of the PN junction, charge generation, and charge transportation important to particle detection are discussed.

1.1.1 Semiconductors and the PN junction

The electrical properties of matter fall into three categories, based on the electron band structure of the material: conductor, semiconductor, and insulator.

The quantised energy levels of an atom are occupied with electrons with a distribution determined by Fermi-Dirac statistics, since electrons follow the Pauli exclusion principle, where the probability density at a given energy level is:

$$P(E) = \frac{1}{e^{\frac{(E-E_F)}{k_B T}} + 1} \tag{1.1}$$

where E is the energy of the electron state, k_B is the Boltzmann constant, and T is the absolute temperature. E_F is the Fermi energy: the energy value at which the occupancy probability is $\frac{1}{2}$. At a temperature of 0 K, all states up to an energy of E_F are filled with electrons, and all remaining energy levels are empty. At temperatures >0 K, electrons can be thermally excited or stimulated by incident photons to energy levels higher than E_F.

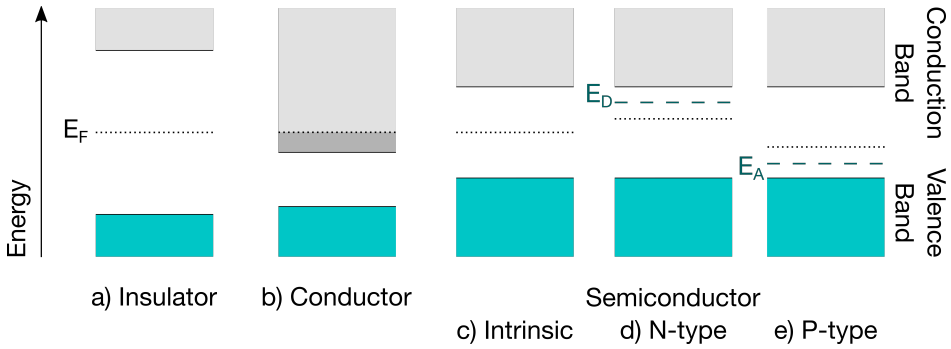

Figure 1.2: Diagram of the electron energy band structure of, insulating, conducting, and semiconducting materials, including intrinsic, extrinsic N-type, and extrinsic P-type semiconductors. E_D denotes shallow donor levels and E_A denotes shallow acceptor levels inserted by dopant atoms.

The relation between the Fermi energy and the electron band structure of a material determines its electrical properties, as shown in Figure 1.2. Electrons within higher energy levels of an atom have enough energy to move freely within the material. These states are collectively named the conduction band, and the remaining bound electron states are within the valence band. For most insulating materials, as shown in Figure 1.2.a, the difference in energy between the conduction and valence bands is large and E_F has a value within the bandgap. Due to this large bandgap, electrons cannot be easily excited into the conduction band even at high temperatures, therefore current does not typically flow through the material. A different behaviour occurs for metals as E_F has a value within the conduction band, as shown in Figure 1.2.b. In metals there are free electrons available to conduct current at all temperatures. For some metals, the valence and conduction bands overlap instead, with the same result in electrical conductivity. Semiconductors have a value of E_F within a small bandgap over which electrons can be thermally excited, as shown in Figure 1.2.c. At low temperatures, semiconductors act as insulators and their electrical conductivity increases with temperature.

The bandgap of crystalline silicon is 1.12 eV, making it an intrinsic semiconductor. The electrical properties of silicon can be modified by introducing impurity atoms into the lattice. In Figure 1.2.d and 1.2.e the resultant change in the Fermi energy from inserted dopant atoms is shown. Doped silicon with a concentration of N_A atoms from group-III of the periodic table introduces shallow acceptor energy levels and makes the material a P-type extrinsic silicon semiconductor. Each dopant atom has one fewer valence electron than the surrounding silicon atoms, effectively introducing the absence of a valence electron that can be viewed as a positive charge carrier called a hole. While some free electrons remain, holes are the majority charge carrier conducting current in the material. E_F in P-type semiconductors has a value closer to the valence band, altered by the inserted dopant atoms. The opposite case occurs when doping silicon with a concentration N_D of atoms from group-V of the periodic table. Additional valence electrons are introduced by the dopants within shallow donor states close to the conduction band. In an N-type extrinsic silicon semiconductor, electrons are the majority charge carriers and the value of E_F is closer to the conduction band.

Joining an N and P-type semiconductor results in the formation of a diode. Within the PN junction, the conduction and valence bands bend to form a common E_F between the two materials, caused by free charge carriers drifting with the carrier concentration gradient, as shown in Figure 1.3. The dopant ions remain fixed in the semiconductor lattice, therefore an electric field forms that opposes carrier movement and an equilibrium state is eventually reached. No free charge carriers remain within the PN-junction in equilibrium due to the electric field, therefore it is known as the depletion region. This results in an intrinsic built-in voltage V_{bi} across the depletion region, with a magnitude dependent on the difference between N_A and N_D.

By manufacturing a diode with metallic-semiconductor contacts on the parallel faces of the P and

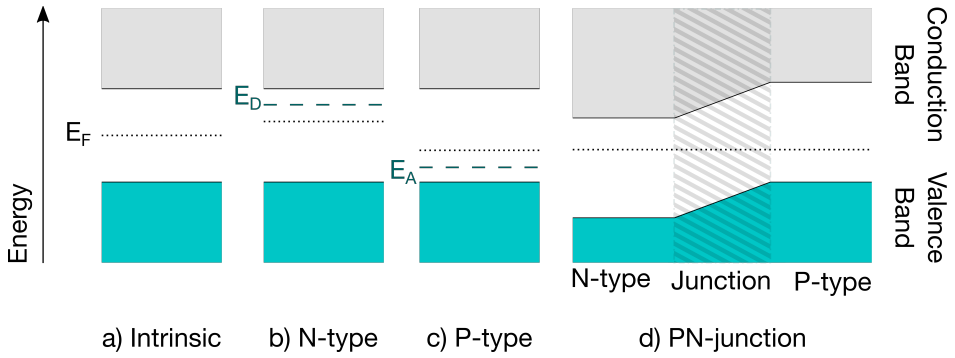

Figure 1.3: Diagram of the electron energy band structure of semiconductor materials, including a PN-junction. E_D denotes shallow donor levels and E_A denotes shallow acceptor levels inserted by dopant atoms.

N-type semiconductor, as indicated in Figure 1.1, an external bias voltage can be applied. An electric field is created across the PN-junction, where the applied voltage is either adds to or opposes the built-in voltage of the diode. The application of a forward bias, where the applied and built-in voltages are opposing, reduces the volume of the depletion region. A reverse bias voltage can be applied to the contacts in the direction of the built-in voltage, resulting in a larger depleted volume. The depth of the depletion region, W, at the PN junction under a reverse bias is given by:

$$W = \sqrt{\frac{2\varepsilon_0\varepsilon_{Si}}{e}\left(\frac{1}{N_A}+\frac{1}{N_D}\right)(V+V_{bi})} \tag{1.2}$$

where ε_0 is the dielectric permittivity of free space, ε_{Si} is the dielectric permittivity of silicon, e is the charge of an electron, and V is the external applied reverse bias voltage. An approximation to this equation can be made if $V_{bi} << V$ and there is a majority doping concentration, implying either $N_A >> N_D$ or $N_D >> N_A$. With these assumptions:

$$W \approx \sqrt{\frac{2\varepsilon_0\varepsilon_{Si}}{eN_M}V} \tag{1.3}$$

where N_M is the majority doping concentration.

Any charged particle or photon incident in the depleted region deposits a fraction of its energy, exciting electrons from the valence band to the conduction band. The created electrons and holes drift in opposite directions to the anode and cathode, inducing a detectable current signal in accordance with the Shockley-Ramo theorem [10] [11]. Either the anode or cathode contact is segmented into pixel contacts, therefore the position of the collected charge is known. After charge generation, the thermal equilibrium of the system is regained through increased electron-hole recombination. The recombination rate follows a characteristic exponential decay since it is proportional to the minority carrier concentration.

1.1.2 Charge generation from incident particles

1.1.2.1 Multiple coulomb scattering

As charged particles traverse a material, Coulomb interactions with nuclei cause multiple deflections in the particle trajectory [12]. The overall effect is a scattering angle distribution approximately equal

to a Gaussian with a mean value of zero and a Root Mean Square (RMS) of:

$$\theta_{RMS} = \frac{13.6\ \text{MeV}}{\beta\rho c}\sqrt{\frac{x}{X_0}}\left[1+0.038\ln\left(\frac{x}{X_0}\right)\right]z \tag{1.4}$$

where θ is the scattering angle, ρ is the particle momentum in MeV, β is the velocity of the particle in units of c, z is atomic number of the incident particle, and $\frac{x}{X_0}$ is the material thickness in radiation lengths.

1.1.2.2 Energy loss of heavy charged particles

An incident charged particle deposits a portion of its energy along its trajectory through the silicon layer. The process by which the energy loss occurs is dependent on the type and energy of the particle. The mean energy deposited, $-dE$, by a heavy charged particle per unit of distance, dx, is described by the Bethe-Bloch function [13] for particles with a mass larger than the electron rest mass:

$$-\frac{\mathrm{d}E}{\mathrm{d}x} = 2\pi L r_e^2 m_e c^2 \frac{Z}{A}\frac{z^2}{\beta^2}\left[\ln\left(\frac{2m_e c^2\gamma^2\beta^2 K_{max}}{I^2}\right) - 2\beta^2 + C_{corr}\right] \tag{1.5}$$

where $m_e c^2$ is the rest energy of an electron, r_e is the classical radius of the electron, L is Avogadro's number, A is the atomic number of the sensor material, Z is the atomic mass of the sensor material, I is the mean excitation energy, and γ is the Lorentz factor. K_{max} is the maximum energy transfer in a single collision for a particle of mass M:

$$K_{max} = \frac{2m_e c^2\beta^2\gamma^2}{1+\frac{2\gamma m_e}{M}+(\frac{m_e}{M})^2} \tag{1.6}$$

Finally, C_{corr} contains additional correction terms, such as density corrections for high energy particles or shell corrections for lower energy particles.

1.1.2.3 Charge generation

The number of electron-hole pairs, N_{pairs}, created by the particle traversing the depletion volume is given by:

$$N_{pairs} = \frac{E}{w} \tag{1.7}$$

where E is the total deposited energy and w is the mean ionisation energy of the semiconductor material. Crystalline silicon has an indirect bandgap, therefore phonon creation is required for electron excitation to the valence band. It has a bandgap energy of 1.12 eV and a w of approximately 3.65 eV.

The minimum of the Bethe-Bloch equation (1.5) occurs at approximately $\beta\gamma = 3$, as shown in Figure 1.4, defining a minimally ionising particle (MIP). The increase in average energy loss for particles with $\beta\gamma > 3$ is relatively low compared to the minimum, therefore any particle with a $\beta\gamma \geq 3$ can be approximately considered as minimally ionising. MIPs are usually the relevant particles when investigating the performance of HEP tracking detectors since they produce the lowest amount of signal, therefore the pixel detectors in these regions are optimised to detect MIPs.

Ionisation is subject to large statistical fluctuations, therefore Equation 1.5 only provides the average value of the energy loss distribution. These so-called Landau fluctuations [15] originate partially from δ-electrons that cause secondary ionisation, causing high energy tails such that the most probable value (MPV) occurs at a significantly lower energy than the mean. The MPV can be determined using a Landau-Gaussian fit function.

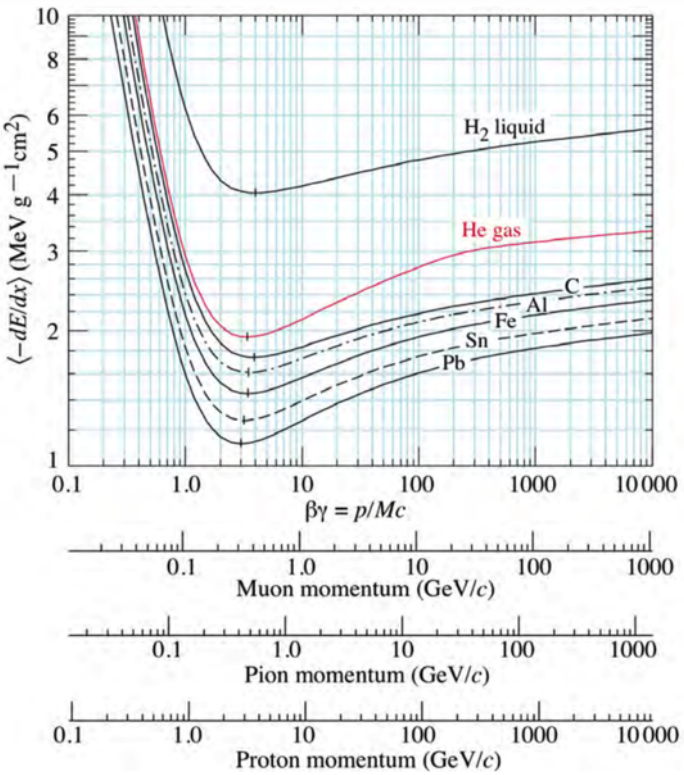

Figure 1.4: Average energy loss of particles in different media as a function of $\beta\gamma$, calculated using by the Bethe-Bloch equation. Image from [14].

1.1.3 Charge transport and sharing

Charge carriers within a semiconductor material are subject to random movements due to thermal energy. If no carrier density gradient is present, the result is an average travelled distance of zero. Charge carriers on average move from high to low density regions in the presence of a concentration gradient, with a spreading distribution over time. This overall movement of electrons and holes creates a diffusion current, with a current density, $J_{diffusion}$, described by:

$$\begin{aligned} J_{n,diffusion} &= -\frac{kT}{e}\mu_n \Delta n \\ J_{p,diffusion} &= -\frac{kT}{e}\mu_p \Delta p \end{aligned} \tag{1.8}$$

where $\mu_{n/p}$ is the carrier mobility of electrons/holes, T is the temperature, and $\Delta n/p$ is the concentration gradient of electrons/holes.

In addition to diffusion, charge carriers also travel towards the pixel contact or sensor backside following the electric field. The maximum velocity of this drift is proportional to the electric field strength via mobility, $\mu_{e/h}$, where increasing probability of impurity-charge carrier collisions causes the velocity saturation. $\mu_{e/h}$ is dependent on the impurity concentration, temperature, electric field, effective mass, doping concentration, and dopant type. The expression for the drift current density, J_{drift}, in an electric field, E, is:

$$\begin{aligned} J_{n,drift} &= -en\mu_n E \\ J_{p,drift} &= -ep\mu_p E \end{aligned} \tag{1.9}$$

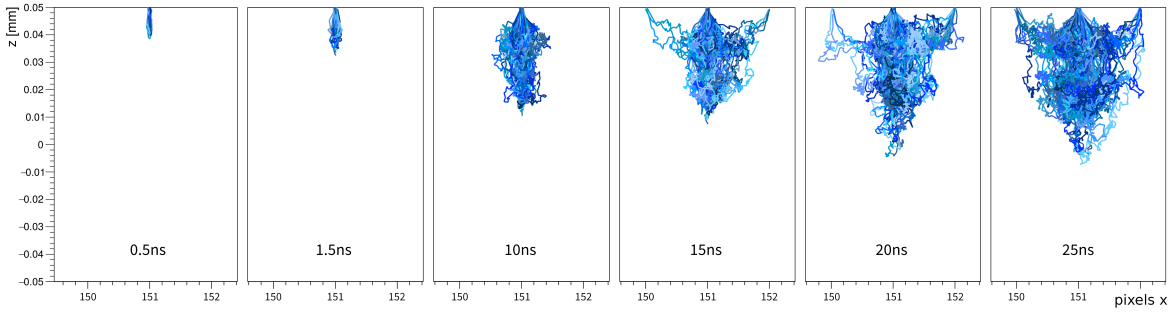

Figure 1.5: Simulation of charge transport and collection at three neighbouring electrodes of the sensor over time for a MIP traversing the central region, using the Allpix^2 framework. The visualisation only shows electrons that have reached a sensor implant within the depicted integration time [16].

The total current density is therefore given by:

$$J_{total} = J_{n,drift} + J_{p,drift} + J_{n,diffusion} + J_{p,diffusion} \tag{1.10}$$

In thermal equilibrium, J_{total} is zero as there is no carrier concentration gradient and the in-built voltage of the PN junction opposes drift. Figure 1.5 shows a simulation of a charged particle energy deposition in a semiconductor material as a function of time, where the combined effect of drift and diffusion can be seen. The created electrons drift toward a pixel contact, with an increasing lateral spread due to diffusion. Charges can diffuse sufficiently that an electrical signal is induced on a number of neighbouring pixels, as seen in this simulation. Detectable charge sharing can have a desirable effect on the pixel detector resolution, however any charge sharing below the detectable signal level degrades the charge measurement and the resolution of the device. It should be noted that the amount of diffusion that occurs reduces with increasing drift velocity, as this decreases the time charge carriers spend within the sensor.

Current generated without an external energy deposition is called leakage current. Thermally excited electron-hole pairs, sensor surface carrier generation, impurities from manufacturing or radiation damage, and electrical breakdown of the PN junction can all contribute to the creation of charge carriers that cause leakage current in the high electric field of the sensor.

1.2 Front-end electronics of pixelated detectors

Electrical signals induced by charges deposited in the sensor layer are detected by the readout chip. Pixel detector prototypes for HEP often have specialised design requirements that need custom electronic circuits to be designed. With the smaller features sizes available in recent years, these custom readout chips can include complex functionality within each pixel area.

1.2.1 Signal generation and detection

Signals detectable by the readout chip are induced by the movement of charge carriers within the sensor electric field to the pixel collection electrode in accordance with the Shockley-Ramo theorem [10] [11]. An instantaneous current, i, is generated according to the following formula:

$$i = q\vec{E}_w\vec{v} \tag{1.11}$$

where q is the charge magnitude, $\vec{v}$ is the velocity of the charge, and $\vec{E}_w$ is the weighting field. The latter is the field obtained by applying a unit potential to the pixel electrode and a ground potential

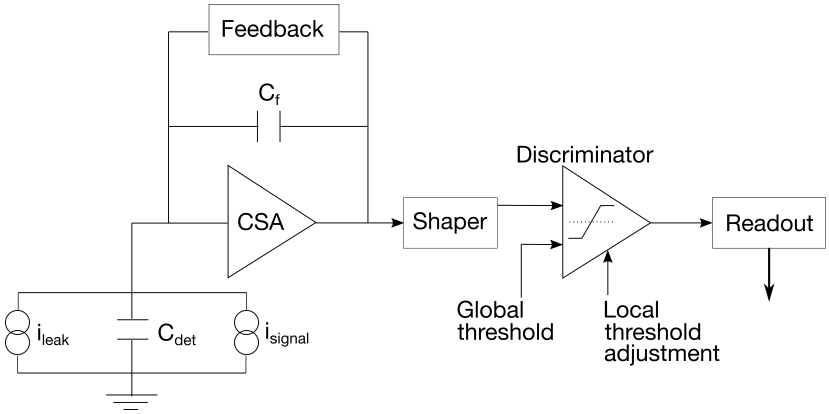

Figure 1.6: Schematic of a generic PUC. Image based on [8].

to all others. By integrating Equation 1.11 over a certain time period t_1 to $t_1 + \Delta T$, the total induced charge on the electrode, Q, can be obtained:

$$Q = \int_{t_1}^{t_1+\Delta T} i(t)dt = q[\phi_w(x_a) - \phi_w(x_b)] \tag{1.12}$$

where the charge has travelled from position x_a to x_b, and ϕ_w is the weighting potential. The integral of the induced signal is equal to the total collected charge, which can be less than the deposited charge if the charge collection efficiency of the device is less than 100%. If the pixel pitch is significantly smaller than the wafer thickness, the small pixel effect occurs: the majority of the signal is induced in the last section of the charge drift path and charges drifting to the back plane do not significantly contribute.

1.2.2 Readout ASIC

Several components are common to most readout ASICs despite possible difference in geometries, analogue circuits, or readout schemes [8].

The active area is a matrix of pixels, consisting of repeating pixel unit cells (PUCs). Each PUC has a similar area footprint as the pixel, and PUCs can be grouped into columns, sharing power bias and control signals. Meanwhile, the chip periphery controls the active area. Global control functions needed by each PUC are located on the periphery, setting parameters such as registers to indicate the readout mode and the hit detection threshold. An interface to the matrix columns distributes bias signals for the analogue and digital sections of the PUCs, and provides buffers for digital control signals and pixel data.

A PUC schematic is shown in Figure 1.6, consisting of the following parts: sensor, amplifier, feedback circuit, shaper, discriminator, and readout. The basic PUC model can be extended with additional functionality, for example the inclusion of a test-pulse injection circuit.

Sensor: The sensor wafer can be modelled by a total effective capacitance, C_{det}, with contributions coming from the capacitance to the backside, C_b, and the inter-pixel capacitance, C_{ip}. An induced current can therefore be defined as a parallel time-dependent current source, i_{signal}, while the leakage current from the sensor is represented as a parallel constant current source, i_{leak}.

Amplifier: The charge sensitive amplifier (CSA) is a crucial part of a PUC, as it converts the small input current into a measurable voltage step. The output voltage step, ΔV_{out}, from an input charge, q, is given by:

$$\Delta V_{out} = \frac{-q}{C_f}\left(1 + \frac{1}{G} + \frac{C_{in}}{GC_f}\right)^{-1} \tag{1.13}$$

where G is the inverting amplifier gain, and C_f is the feedback capacitance. C_{in} combines C_{det} with the amplifier capacitance and parasitic contributions. To achieve a high signal amplitude, the condition $G\,C_f >> C_{in}$ needs to be fulfilled. This also maintains a low voltage at the CSA input, reducing the inter-pixel capacitance. The choice of C_f is a balance between charge gain, gain uniformity across channels, input impedance, stability, and speed. The rise time of the amplifier to an instantaneous charge depends on the gain bandwidth and the closed loop gain. For a large detector capacitance or a small C_f, the rise time, τ, is slower following the following equation:

$$\tau = \frac{C_{in}}{G_0 w_0 C_f} \tag{1.14}$$

where $G_0\ w_0$ is the gain-bandwidth product.

Feedback circuit: The feedback loop removes signal charges from the CSA input, allowing the output voltage to return to its initial value. To avoid saturation or non-linearities of the CSA at high pixel hit rates, the discharge must fully occur before the next signal arrives. However, a high-rate discharge could reduce the pulse amplitude before it reaches its maximum value, an effect called shaping loss or ballistic deficit. Constant current or a resistive discharge schemes can be employed, where the choice balances high gain and large effective input capacitance.

Shaper: A band-pass filter limits the bandwidth of the output signal to reduce high and low frequency noise. In particular, the shaper reduces noise from the sensor leakage current. The fixed characteristics of the shaper give a predefined output signal shape. When the output of the CSA is a step function, the shaper provides a uni-polar output. As the amplifier must have a fast return to the baseline before the next signal, the shaper output includes an undershoot of the opposite polarity.

Discriminator: The discriminator, also known as the comparator, compares the shaper output to a configurable reference threshold voltage. The threshold sets the signal height required to generate a logic output signal, indicating a pixel hit. The applied threshold for each PUC is a combination of the global threshold voltage and any local threshold adjustment. The applied threshold must be set as low as possible to minimise hit detection efficiency losses, but high enough that noise contributions do not effect the measurement. Signal charge can be measured as the Time-over-Threshold (ToT) if a constant current feedback loop is used for the CSA, where there is a monotonous correspondence between signal charge and the width of the discriminator output signal at the applied threshold.

Readout: The digital hit signals of the discriminator are then processed by the digital pixel circuitry and the chip periphery before output. Both the rising and falling edges of the discriminator output are measured in clock cycles, therefore the measurement quality is dependent on the clock frequency as well as the uniformity of the CSA and discriminator outputs. Various readout schemes can be employed for pixel detectors, motivated by the intended application. An example is a binary readout scheme, where only the number of above-threshold signals is recorded per-pixel. An analogue readout scheme has pulse-height information available, as the signal is proportional to the collected charge. The readout processing time is known as dead-time, as signals above the threshold are not detected during this period.

1.3 Pixel detector performance

A number of performance aspects must be accounted for when designing and operating a pixel detector for it to function as desired. By optimising these sensor and ASIC properties and minimising degrading effects, the performance of the pixel detector will be improved when measuring figures of merit.

1.3.1 Design and operation aspects of sensors

1.3.1.1 Reverse bias voltage

The minimum reverse bias voltage, V_{dep}, required to deplete the full sensor thickness, d, of free charge carriers is described by:

$$V_{dep} \approx \frac{d^2 e N_{A/d}}{2\varepsilon_0 \varepsilon_{Si}} \tag{1.15}$$

using the assumptions used for Equation 1.3 [8]. Only charges produced within the depletion region can be detected. At reverse biases $\geq V_{dep}$ the depleted region is at its maximum size, therefore maximal charge is detected at these voltages. However, increasing the applied bias above V_{dep} will also increase the drift velocity and can reduce the amount of charge sharing. V_{dep} is therefore an important property to consider when operating a pixel detector. The value can be determined through laboratory measurements of capacitance as a function of bias voltage, since capacitance$\propto \frac{1}{\sqrt{W}}$, or through test-beam data analysis of cluster charge for different applied bias voltages.

Electrical breakdown of the semiconductor sensor can occur at the PN junction when a large reverse bias voltage is applied. Breakdown occurs through one of two mechanisms: avalanche multiplication due to impact ionisation of electron-hole pairs, or the quantum tunnelling of charge carriers through the bandgap known as Zener breakdown. The maximum reverse bias that can be safely applied is determined by measuring the leakage current as a function of applied bias voltage V_{bias}. At reverse biases below the depletion voltage, the current generated in the sensor volume increases proportionally to $\sqrt{V_{bias}}$. A plateau region of leakage current occurs after the sensor is fully depleted and before the breakdown voltage, which optimally would cover a wide voltage range. At the breakdown voltage, the current increases exponentially. Deviations from this behaviour can be used to identify issues with a pixel detector. Although the breakdown mechanisms themselves are not destructive to the sensor, the heat caused by the large breakdown current can cause damage. In addition, the front-end can be damaged by the high current. Pixel detectors are therefore operated in the plateau region of the current-voltage distribution.

Destructive electrical sparks can occur when a large potential difference exists between the sensor edge and the outermost pixels of the matrix. A guard ring is an equipotential conductor close to the matrix edge on all sides, ensuring a low-gradient voltage drop towards the physical sensor edge. The guard rings of a sensor can be designed as floating or connected to the ground potential.

1.3.1.2 Pixel capacitance

The sensor capacitance seen by the CSA in each pixel, C_{det}, originates from two main sources: capacitance to the sensor backside, and the inter-pixel capacitance. A low overall C_{det} value allows for fast signal shaping with low noise. The backside capacitance depends on the pixel area, backside implant size, and the sensor thickness. For a fully depleted planar silicon sensor, the backside capacitance, C_b, is equivalent to a parallel plate capacitor:

$$C_b = \varepsilon_0 \varepsilon_{Si} \frac{A}{d} \tag{1.16}$$

where ε_{Si} is the dielectric constant of silicon, A is the pixel area, and d is the sensor thickness. Inter-pixel capacitance coupling is generally higher than to the sensor backside. The capacitance between neighbouring pixels can cause cross-talk, an effect where the deposited charge in one pixel induces parasitic signals on one or more of the neighbouring pixels. Cross-talk increases the number of double and triple hits, introducing errors in the signal measurement, and therefore must be minimised. Inter-pixel capacitance can be reduced by increasing the distance between pixel centres, either by increasing

the inactive area between pixels or increasing the pixel pitch, however this also decreases the density of pixels [8].

1.3.2 Design and operation aspects of pixel electronics

1.3.2.1 Noise and threshold adjustment

A low noise level, equivalent to high signal to noise ratio (SNR), is required to measure small signals with a low detection threshold. A figure of merit for the noise level of a readout chip is the equivalent noise charge (ENC): the voltage variation RMS at the end of the analogue processing chain, divided by the signal output voltage for a single electron input charge [8]. Noise sources include pink noise, or $\frac{1}{f}$ noise, which is a frequency dependent noise caused by capture and release processes within the sensor. Dark current originates from the thermal generation of electron-hole pairs within the depletion region. The $\frac{1}{f}$ noise and thermal current of the shaper output are proportional to the detector capacitance. Shot noise is caused by leakage current, $I_{leakage}$, where ENC$\propto I_{leakage}$. ENC is mainly determined by the amplifier speed and the total input capacitance. For individual pixels with a high noise rate, the output of the CSA usually can be suppressed using a masking bit in the PUC configuration.

Variations are often observed between the threshold of pixels across the matrix. This can be caused by component mismatches due to production fluctuations, for example in the doping levels, oxide thickness, or physical size. Some systematic variations also occur, like voltage drops along columns or component mismatch due to a mirrored column layout. Local threshold fluctuations are also affected by differences in the CSA gain from pixel to pixel. Higher threshold pixels can be inefficient at hit detection, while lower threshold pixels can have high noise. A local threshold tuning is achieved using a trimming process to compensate for these differences, such as a digital trimming using correctional digital to analogue converter (DAC) values. Trimming moves significantly low or high thresholds closer to the baseline, decreasing the width of the baseline peak.

1.3.2.2 Temperature

Pixel detectors should be operated at low temperature to reduce the thermal current of the device, however full cooling systems can have a high material budget. For low material budget applications, the power consumption of the electronics should therefore be minimised. A dominant source of heating is the pixel frontend power consumption, which can be reduced by minimising the detector capacitance [8]. The power consumption of a pixel detector can be reduced using a power pulsing scheme, where the analogue or digital circuitry is put into a low-power state for intervals of time [17].

1.3.3 Pixel detector figures of merit

A number of figures of merit are used to measure the performance of a pixel detector prototype. Three common parameters are the hit detection efficiency, spatial resolution, and timing resolution. To determine these values experimentally, the trajectory of the incident particles must be known, requiring particle trajectory measurements from a reference system, as discussed further in Chapter 5.

Hit detection efficiency measures the fraction of incident particles that are detected by the detector, where an acceptable difference in space and time is defined between the true and the measured particle incidence point. A low threshold will artificially increase the efficiency as noise hits will be attributed to particle incidence detection, while at a high threshold hit detection inefficiencies are caused by signals remaining below threshold. With enough statistics, the efficiency within single pixel cells can be analysed and the effects of efficiency losses at the pixel edges and at the physical sensor edges from signals remaining below threshold can then be investigated.

Spatial resolution is highly dependent on the pixel pitch, charge sharing, and using a binary or an analogue readout. The intrinsic spatial resolution of the detector along the chosen axis, $\sigma_{intrinsic}$, can

be obtained from the following equation:

$$\sigma^2_{meas} = \sigma^2_{intrinsic} + \sigma^2_{track} \tag{1.17}$$

where σ_{track} is the pointing resolution of the particle tracks measured by the reference system, and σ_{meas} is the measured width of the unbiased spatial residual distribution. The spatial residual along an axis is the difference between the measured incidence point x_{meas} and the true incidence point of the particle x_{true}. A residual is unbiased if the data has not also been used to determine the particle trajectory, therefore x_{meas} and x_{true} are uncorrelated.

The binary spatial resolution of a pixel detector is calculated assuming a binary readout system, a uniform density, $D(x)$, of particles across the matrix, and a negligible amount of charge sharing between pixels. With no multi-pixel clusters, the x_{meas} is always defined as the centre of the single pixel. On average, the width of the spatial residual along an axis using the given assumptions is:

$$\begin{aligned}\sigma^2_{meas} &= \frac{\int_{\frac{-p}{2}}^{\frac{p}{2}} (x_{true} - x_{meas})^2 D(x_{true}) dx_{true}}{\int_{\frac{-p}{2}}^{\frac{p}{2}} D(x_{true}) dx_{true}} \\ &= \frac{p^2}{12}\end{aligned} \tag{1.18}$$

where the pixels have a pitch of p. This results in a 'top-hat' shaped residual of a well defined width.

Spatial resolution can be improved by reducing the pixel pitch, however the size is often limited due to the space required for the necessary components of the readout electronics and the size of the interconnects, as discussed in Section 1.4. σ_{meas} can be improved upon by using an analogue readout such that the signal is proportional to the induced charge, while also increasing charge sharing where an incident particle causes above threshold signals in a cluster of neighbouring pixels. With multi-pixel clusters, x_{meas} can be determined as the clusters charge weighted centre-of-gravity. In addition, non-linear charge sharing between pixels can be corrected for in the data analysis using an η function, discussed in Section 6.2.4. Using the information gained from the sharing of charge within a cluster and its overall shape, the particle incidence position can be measured with higher accuracy and gain a better resolution than $p/\sqrt{12}$. The amount of charge shared between pixels depends on the position and angle of the particle track with respect to the sensor layer, and the original charge of the particle. It should be noted that significant charge sharing can cause detection losses as the signal in the individual pixels falls below the threshold level.

With charge sharing, the shape of the residual becomes approximately a Gaussian and the width can be accurately defined as the σ of such a fit function to the distribution. However, effects such as δ-electrons cause non-Gaussian tails in the distribution, increasing the width measured by the Gaussian function. To reduce the effect of the non-Gaussian tails on the measured value, the width can be defined as a RMS. The total RMS can be significantly effected by single outliers far from the central distribution. Truncating the RMS measurement to the central 95% or 99.7% of the data provides a statistically stable value of any shaped distribution. A percentage of 95% corresponds to a two σ range, while the three σ range when using the central 99.7% includes a significant portion of the non-Gaussian tails. As multiple methods are used within the field, these three values are quoted for each residual width calculated in this thesis.

A precise measurement of the particle-detector incidence time is important for many pixel detector applications. The intrinsic timing resolution of a detector, $\sigma_{t,intrinsic}$, is calculated similarly to spatial resolution:

$$\sigma^2_{t,meas} = \sigma^2_{t,intrinsic} + \sigma^2_{t,track} \tag{1.19}$$

where $\sigma_{t,track}$ is the timing resolution of the particle tracks measured by the reference system, and

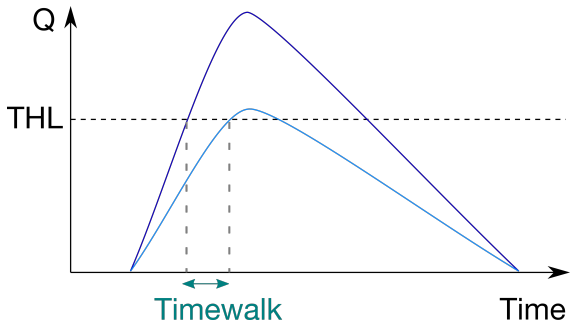

Figure 1.7: Diagram showing the time-walk that occurs between signals of different magnitude.

$\sigma_{t,meas}$ is the unbiased timing residual width of the detector. To quantify the timing residual width, the width of a Gaussian fit or the RMS of the central region of the distribution can be used. Systematic delays in the measured arrival time of each particle can be partially accounted for by applying a calibration during data reconstruction to account for them. The timing residual width can be reduced by ensuring the delay between charge deposition and the discriminator reaction is constant. The response time as a function of input charge can characterise this behaviour. Small signals just above the threshold cause a slow discriminator response compared to larger signals, as depicted in Figure 1.7. Amplitude noise causes a timing jitter dependent on the on the slope of the amplitude at the threshold-crossing point. The slope of the signal increases approximately linearly with the peak amplitude, for a given rise time. The timing jitter is inversely proportional to the amplitude of the signal divided by the rise time and proportional to the amplitude noise This difference in recorded arrival time for signals as a function of input charge is known as time-walk. Time-walk therefore will cause the timing residual distribution of the detector to be wider, negatively affecting the intrinsic time resolution. By fitting a function to the distribution of time residual as a function of pixel charge, the effect can be corrected for in data reconstruction [8].

1.4 Bump-bonding of hybrid pixel detectors

The sensor material and ASIC of a hybrid pixel detector need to be joined, providing both an electrical and physical connection between the sensor and chip at every pixel. It can be a complex task to achieve uniform, high-quality interconnections across the pixel matrix.

1.4.1 The bump-bonding process

Interconnections between the layers of a hybrid pixel detector can be achieved using different methods, the most common of which for HEP applications is solder bump-bonding. The method uses layers of metal on each pixel, and the electrical connection is made with the application of pressure and heat. Bump-bonding is useful for HEP pixel detectors since a high-density of interconnects can be made at small pixel pitches.

Multiple bump-bonding processes are available, commonly involving four stages: under bump metalisation (UBM) deposition, solder bump deposition, reflow, and flip-chip bonding [18].

UBM, also known as the plating base, is deposited on the pixel pads of the ASIC, sensor, or both. Typically composed of a refractory metal and a solderable metal, UBM ensures a long-term electrical connection between the readout chip and sensor material. It also functions as a diffusion barrier between the sensor and solder bump material, an adhesion layer for the solder bumps, and a protection from corrosion. UBM deposition can be performed through chemical reaction based methods, including electroless Ni-immersion gold (ENIG) and electrodeposition. 'Lift-off' deposition involves a photoresist mask and physical vapour deposition (PVD) as presented in Figure 1.8. Etching the

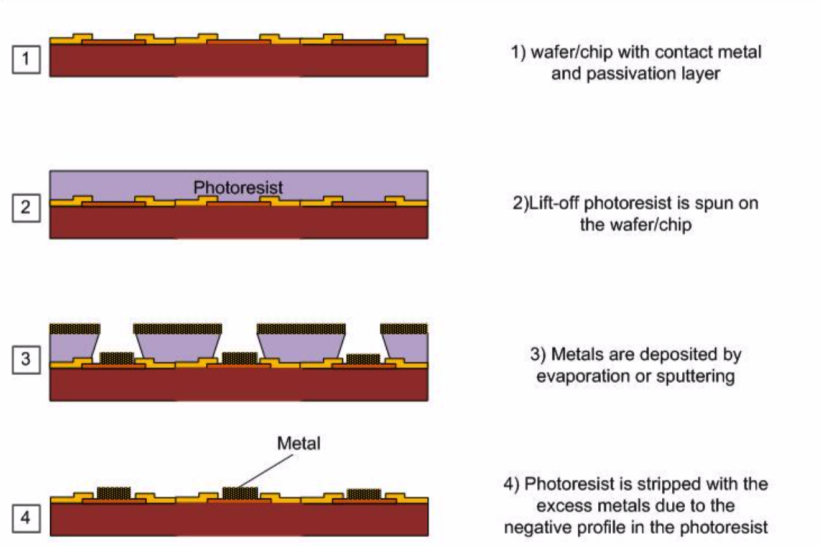

Figure 1.8: Diagram of UBM deposition using the lift-off technique. Image from [18].

photoresist layer only exposes the pixel pads due to the mask layer, and PVD is performed using either sputtering or evaporation techniques. When the photoresist is completely removed, the UBM only remains on the pixel pads as desired.

Solder bumps are small quantities of metal alloy placed onto the UBM, with a typical diameter equal to $\frac{1}{2}$ - $\frac{2}{3}$ times the pixel pitch. The required size of the solder bumps influences the bump-deposition method utilised. These include electroplating, stud-bumping, screen-printing, direct placement, ENIG, and evaporation/lift-off. Electroplating deposition, also known as electrochemical deposition, involves reducing the positive ions of a metal using a direct electric current and an electrolyte solution. This creates a metal film on the substrate, and a photoresist with etched openings ensures deposition only on the pixel areas. After bump deposition, the photoresist is removed.

The approximately cubic bumps are then reflowed using high temperatures, causing them to form a spherical-like shape due to the change in surface tension. The reflowed bumps are then ready to be used as an interconnection between the sensor and readout chip. Flip-chip bonding is a face-down bonding technique performed by placing the bumped layer, either the sensor or ASIC, onto the other using pressure and high temperatures to cause an electrical connection to form through the solder bumps. A perfect solder bump forms a cylinder-like shape after flip-chip connection. For ASICs with tens of thousands of pixels, high pressure needs to be applied to ensure connections across the matrix [18].

1.4.2 Challenges of bump-bonding

Bump-bonding is a useful interconnect technique for hybrid detectors with a high density of pixels [8]. It can produce assemblies with good electrical and thermal performance, as well as good reliability over time. However, this interconnection method consists of multiple steps that require the process parameters to be well-controlled.

There are many characteristics for an ideal bump-bond between the sensor and readout chip [18]. An increase in the distance between the two layers, known as the stand-off height, decreases the likelihood of electrical sparks across the gap when a high bias voltage is applied. It also reduces the capacitive coupling of the sensor and ASIC, and increases the mechanical stability of the device. The bump diameter after reflow should be $\frac{2}{3}$ times the pixel pitch or less to minimise the capacitive coupling between the solder and ASIC and to reduce the risk that the solder physically touches the readout chip. However, a small bump diameter may not bridge the gap between the sensor and ASIC,

causing no electrical or mechanical contact to be made. The minimum bump size can also be limited by the lithography precision. An ideal bump-bond would have UBM and bumps that are well aligned to the pixel pad, with no offset causing the solder to connect to the ASIC layer itself. The material used for the UBM and solder bumps need to be metallurgically compatible, but also suit the method used for deposition at the required pixel pitch. Ideally the UBM deposition process would be well controlled to ensure good adhesion and a long lifetime of the assembly, even when subject to thermal or mechanical stresses.

During the flip-chip process, a number of issues can arise that degrade the pixel detector performance or long-term reliability. If an uneven pressure is applied during bonding then unconnected regions occur where the gap between the layers is larger than the bump diameter. Thin sensors, often required in HEP for low material budget detectors, curve under changing temperature causing unconnected regions of pixels and in-built stress. Differences in the thermal expansion coefficient of the sensor and ASIC can also introduce shear stresses into the assembly. The alignment needs to be highly accurate during flip-chip bonding to centre the bumps on the opposing pixels, a process that becomes more difficult with decreasing pixel pitch. The solder bump-bonding of single chips is more challenging. UBM and bump solder deposition are usually wafer-level processes with masks. For bonding machinery optimised for wafers, single chip interconnection requires more manual input [18].

Chapter 2

R&D for the CLIC detector

Semiconductor pixel detectors are used in many radiation detection applications. Silicon pixel detectors are well suited for for particle tracking at high energy physics (HEP) experiments due to their characteristics of high spatial, timing and energy resolution of incident radiation; compact size; and low material budget.

At the time of writing, the Large Hadron Collider (LHC) [1] is the largest particle collider in the world and is situated at the European Organization for Nuclear Research (CERN) in Geneva, Switzerland. Each of the four main detectors situated around the 27 km circumference of this circular collider detect the proton-proton and heavy ion collisions with a centre of mass (CM) energy of 13 TeV. The aim is to observe fundamental particles and their interactions to test the predictions made by theoretical particle physics. An ongoing upgrade programme to become the High Luminosity LHC (HL-LHC) [2] will increase the beam luminosity by a factor of five, and the facility is set to operate until approximately 2035. Numerous future collider experiments are being investigated for after the HL-LHC lifetime, one of which is the Compact Linear Collider (CLIC) [3].

Within this chapter, the main concepts of collider experiments for particle physics will be briefly introduced. Then the CLIC concept for a future $e^+ e^-$ collider will be described in terms of its physics potential, accelerator system, and detector design, with a focus on the prototype technologies being investigated to achieve the challenging requirements of the CLIC vertex and tracking sub-detectors.

2.1 High energy physics at particle colliders

HEP aims to explore the fundamental forces, processes, and constituent matter of the Universe. The standard model (SM) is currently the best theoretical description of fundamental particles and their interactions. As shown in Figure 2.1, the SM consists of 17 fundamental particles separated into fermions and bosons [19].

Fermions, along with their anti-particle counterparts, are the fundamental constituent particles of matter. They have a spin of 1/2 and obey the Pauli exclusion principle, meaning that no two fermions can have the same quantum numbers. Fermions are further separated into six quarks, which are point-like particles which carry colour charge, and six leptons which interact via the weak force [20].

Gauge bosons mediate three of the four fundamental forces: strong, electromagnetic, and weak. The strong force binds colour-charged particles together through gluon exchange, as described by quantum chromodynamics (QCD). All charged particles interact through the electromagnetic force by exchanging photons, and particles with flavour have short-range weak interactions mediated by the W and Z bosons. These processes are described by the electroweak theory (EWT), which is a field theory incorporating quantum electrodynamics (QED) and the weak interactions

Discovered at the LHC in 2012 [21] [22], the Higgs particle is the only scalar boson and is an excitation of the Higgs-field. The Higgs field provides particles with mass, where the magnitude is proportional to their interaction strength with the field. All current LHC findings are consistent with the Higgs particle properties predicted by the SM [19].

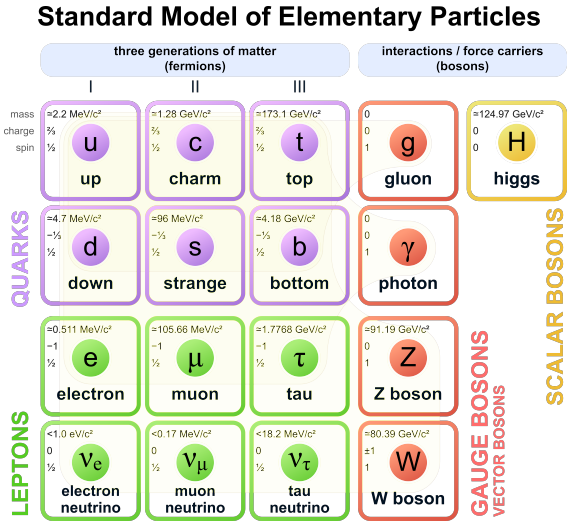

Figure 2.1: Summary of the fundamental particles of the SM of particle physics. Image from [23].

Although the SM successfully describes many observations in HEP experiments, in its current form it is an incomplete description of all particles and processes in HEP [24]. Gravity, the fourth force of nature, is excluded from the model as no quantum field theory of gravity has been formulated. General relativity instead describes it as a gravitational wave, detected in 2017 by the Advanced LIGO and Advanced Virgo experiments [25]. Another challenge for the SM is the large discrepancy between the weak force and gravity, for example in strength, also known as the hierarchy problem. The SM predicts neutrinos to be massless, however observations at the Super-Kamiokande [26] and Sudbury Neutrino Observatories [27] discovered that neutrinos can oscillate in lepton flavour, a phenomenon that can only occur if neutrinos have a non-zero mass. Other unsolved problems with the SM have an even broader scope: why do particles and coupling constants have the values they are measured to; why are there three generations of matter; how can the SM describe dark matter; why is there an asymmetry between matter and anti-matter in the Universe?

To resolve the issues mentioned and others, studies into Beyond SM (BSM) physics are ongoing. These developments in theoretical particle physics can provide testable predictions, either through direct observation or indirect measurements, the outcome of which can inform our understanding of particle physics.

Currently particle colliders are the preferred tool to explore elementary particles and their interactions, enabling theoretical predictions to be tested. Different designs of colliders are possible, dependent on the intended physics goals of the facility [28]. The design choices include the composition and energy of the particle beam, a linear or circular accelerator, and the detector design. However, a few common ideas remain. Within the accelerator complex, particles are accelerated to high energies within evacuated beam pipes. The particle beams are collided at an interaction point within a detector system with a high magnetic field. This detector has many layers, each with a specific measurement target and composition. The combined information from the detector layers can be used to identify the types of particles produced by the beam collision or secondary processes. Tracking layers measure the trajectory of the particle through the system, and from the track curvature in the magnetic field the momentum and charge of the particle can be calculated. Using dense calorimeter layers that induce and detect particle showers, the energy of particles can be measured. Not all particles interact with every layer of the detector, information that can also be used for particle identification. By analysing the information gained about each observed particle, BSM particles or phenomena resulting in characteristic production or decay signatures can be identified.

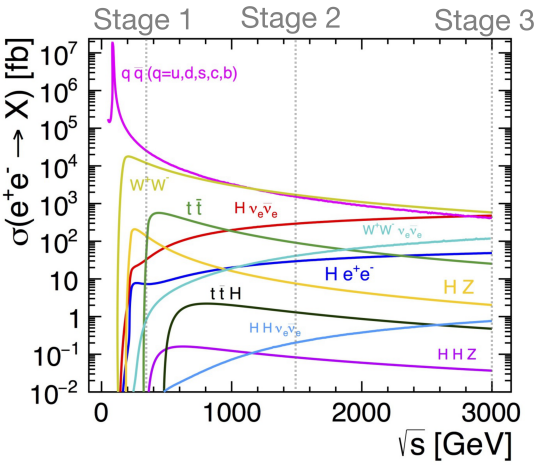

Figure 2.2: SM cross sections for key $e^+ e^-$ processes as a function of the CM energy. Image from [5].

2.2 The Compact Linear Collider

As particle collider experiments take a significant amount of time and resources to design and construct, groups around the world are working on the next generation of collider projects for the post-HL-LHC period.

CLIC is a concept for a future high-energy, high-luminosity $e^+ e^-$ linear collider [3]. It would be built at CERN and become operational towards the end of the HL-LHC programme. Using novel acceleration techniques, particles will be accelerated at a gradient of $100\,\mathrm{MV\,m^{-1}}$ and achieve CM energies of up to 3 TeV. A staged construction design is employed so that physics processes at different CM energies can be probed. The documents supplied in 2019-2020 by the CLIC collaboration to the European Strategy for Particle Physics (ESPP) update process can be obtained at [29].

2.2.1 Physics potential of CLIC

Lepton colliders are well suited for precision physics measurements as they collide fundamental particles. This means the collisions have a well-defined initial state and low levels of background processes compared to hadron colliders, where compound particles subject to QCD interactions are collided with unknown initial states of the subcomponents.

Many important physics measurements can be made at CLIC, in particular precision measurements of SM Higgs and Top quark physics. BSM physics can be discovered through the direct observation of new physics phenomena or the production of BSM particles. In addition, BSM can be indirectly detected through precision measurements of observables, such as coupling constants or particle mass. Significant deviations of particle properties from SM predictions would indirectly indicate BSM physics and using this method, energy scales higher than the CM of the collider can be probed. A detailed summary of the CLIC physics potential can be found in [5].

Three CM energies are planned for the CLIC accelerator, each chosen to probe physics phenomena of particular interest. An overview of the different SM processes available at different CM energies and their cross sections are shown in Figure 2.2.

The first energy stage of CLIC is designed to have a CM energy of 380 GeV, optimised through detailed simulation studies [4]. At this energy, the total decay width of the Higgs boson can be precisely measured using the Higgsstrahlung and WW-fusion production processes. This is a model independent method, as no assumptions on the Higgs decay process are necessary, that can only be carried out at lepton colliders. Multiple Higgs coupling constants to fermions and bosons can be measured with a precision of a few percent. A scan around the top mass pair-production threshold is

foreseen within this stage, from 350-380 GeV, to measure the top quark mass in a model independent manner in a clean experimental environment.

A CM energy of 1.5 TeV is planned for stage two of CLIC [4]. The top quark-Yukawa coupling can be determined by probing top quark pair production and additional Higgs production processes. In addition, the coupling of the top quark to the Z boson and photons through the electromagnetic and weak forces can be measured. Any deviations of these values from the predictions made by the SM would be an indicator of BSM physics. The SM also predicts that flavour-changing neutral currents of top quarks should not be observed by CLIC, therefore detection of this phenomenon would be an indirect observation of new physics.

At the final CM energy stage of 3 TeV, CLIC is sensitive to the Higgs self-coupling and rare Higgs decays. This energy scale can also be used to directly observe BSM physics, such as pair production of particles up to a mass of 1.5 TeV or single particle production up to 3 TeV. These BSM particles could be those proposed by the theory of supersymmetry, such as charginos or sleptons. As CLIC provides a clean interaction point with lower levels of backgrounds compared to hadron colliders, the properties of these potential new particles would be precisely measured. Examples of indirect measurements possible at the final energy stage are vector boson scattering to investigate the mechanism of electroweak symmetry breaking; determination of whether the Higgs is fundamental or composite from final state measurements; and deviations from SM predictions that indicate the presence of dark matter candidates.

By having a staged programme, CLIC can adapt to new insights from theory or from recent collider measurements. In particular, adaptations could be made to the CM energy of each stage if necessary to account for new theories or discoveries.

2.2.2 The CLIC accelerator

Linear lepton colliders avoid large synchrotron radiation energy losses by having straight beamlines, while at circular lepton colliders the bent particles lose energy proportional to $(energy/mass)^4$ due to synchrotron radiation [28]. One challenging aspect of linear colliders is that the beam must reach the collision energy after one pass through the accelerator system. CLIC therefore requires dense particle bunches accelerated with a large gradient of $100\,\mathrm{MV\,m^{-1}}$ to achieve the CM energies desired with a maximum collider length of 50.1 km [4] [30].

Detailed information on the implementation plan and technologies developed for the CLIC accelerator can be found in [30]. The CLIC accelerator complex is shown in Figure 2.3 for the 3 TeV energy stage. To achieve a high gradient using room temperature accelerating structures, a novel two-beam accelerating concept was developed. A high-intensity drive beam is accelerated to an energy of 2.4 GeV using 2.5 km of klystron accelerating cavities. Using power extraction structures, identified as decelerators in Figure 2.3, RF pulses are generated from the drive beam and transferred to the main electron or positron beam. The main beams are of a lower current than the drive beams, and therefore are accelerated to a higher energy through the RF transfer. The CLIC main beam structure consists at the 3 TeV stage of 312 bunches of particles, called a bunch train, with a 0.5 ns gap between bunches. As new main beams need to be created for each e^+ e^- collision, CLIC has a low duty cycle with 20 ms periods between bunch trains.

The CLIC accelerator will achieve three different CM energies due to its staged design: 380 GeV, 1.5 TeV, and 3 TeV. Each increase in energy is achieved by increasing the number of power extraction structures along the main beam-line. The length of the accelerator within the Geneva area can be seen in Figure 2.4 for each energy stage, increasing from 11.4 km to 50.1 km.

Unlike for circular e^+ e^- colliders, the luminosity at a linear e^+ e^- collider increases with CM energy [28], as shown by the histogram in Figure 2.5 of integrated luminosity as a function of CLIC run time. Each energy stage is foreseen to run for approximately eight years.

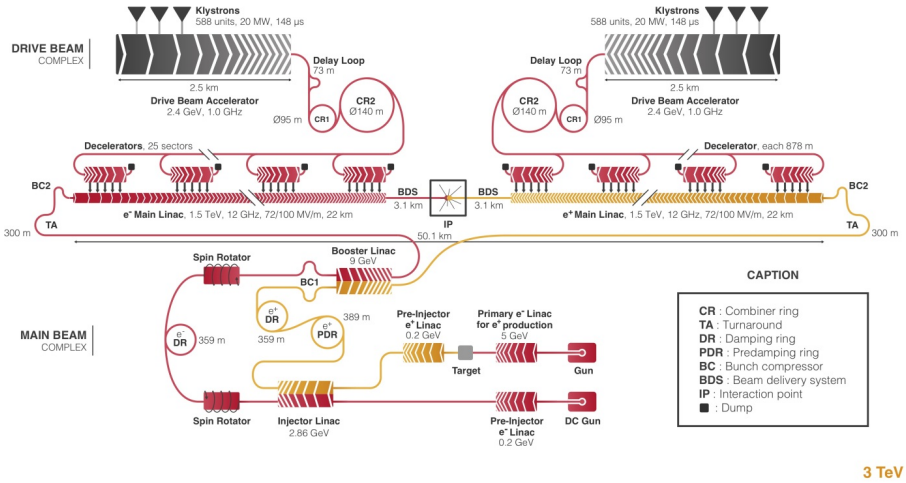

Figure 2.3: CLIC accelerator complex at the 3 TeV energy stage, showing the novel two-beam accelerating concept. Image from [31].

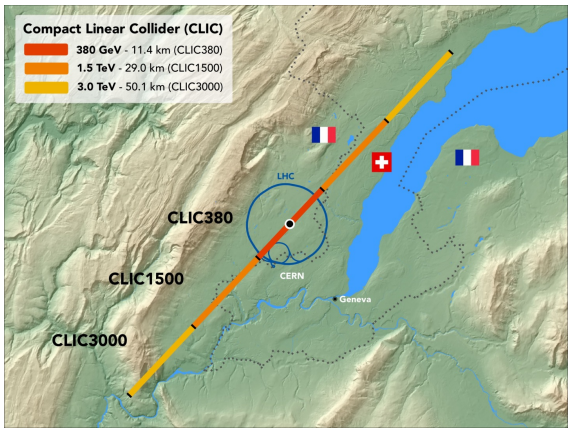

Figure 2.4: Diagram of the CLIC main linear accelerator as it would be implemented at CERN near Geneva in Switzerland, showing the accelerator length for each energy stage. Image from [32].

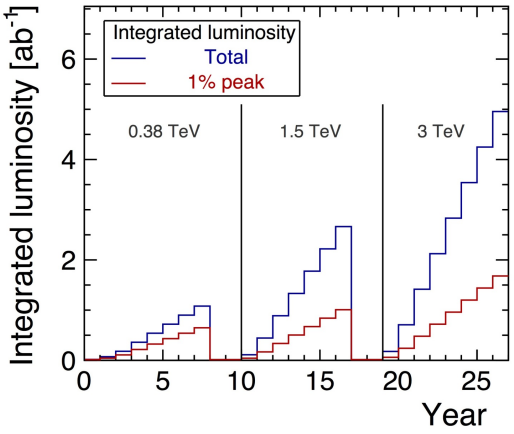

Figure 2.5: Histogram of the integrated luminosity per year in the proposed CLIC staging scenario. The total luminosity is shown in blue and the luminosity at CM energies above 99% of the nominal are shown in in red. Image from [30].

2.2.3 Beam-induced backgrounds

High energy e^+ e^- beams have a high probability of producing Beamstrahlung photons induced by the electromagnetic field of the opposing beam [33] [34]. While the desired high luminosity can only be achieved with nm scale beam sizes, this also increases the probability of the Beamstrahlung photons interacting to produce background particles.

Dedicated Geant-based full detector simulations have been used to study the beam-induced backgrounds at CLIC for the 380 GeV and 3 TeV stages [35] [36]. The main sources of backgrounds from the Beamstrahlung photon interactions are incoherent e^+ e^- pairs and hadrons. These background particles can interact with the detector material directly, or indirectly through backscattering from material at low angles since the background particles are boosted in the beam direction. In simulations, beam-induced backgrounds cause up to 8 hits per mm^2 per bunch train in the detector

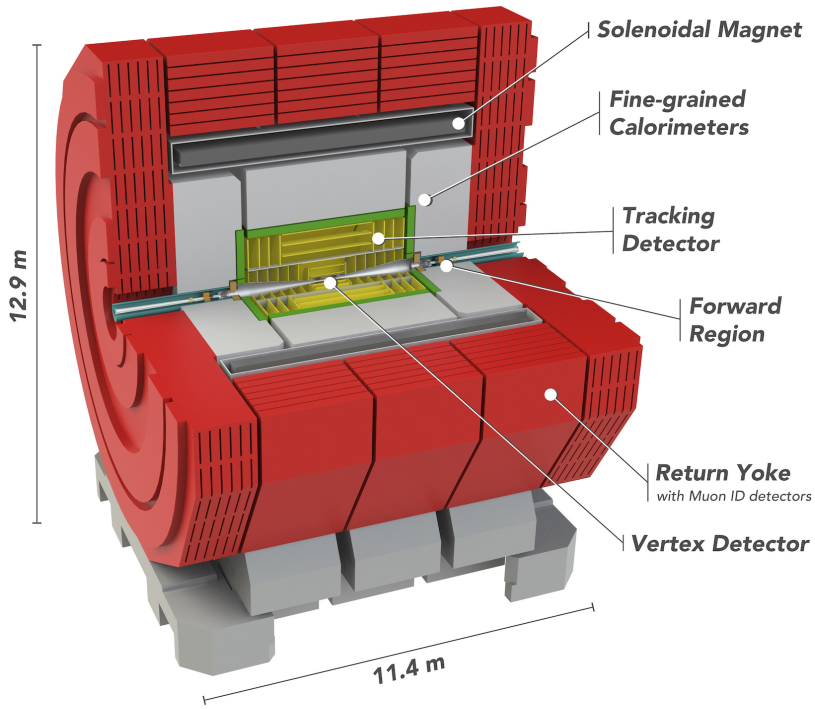

Figure 2.6: A 3D diagram of the CLIC detector design. It has pixelated low-mass inner detectors, fine-grained calorimeters optimised for particle flow analysis, 4 T superconducting solenoid magnet, and a muon identification system within the iron yoke. Image from [38].

layer closest to the interaction point. Approximately one physics event will occur per bunch train at CLIC, therefore the beam-induced backgrounds significantly affect the precision and accuracy of track reconstruction.

2.3 The CLIC detector

To precisely measure the particles produced when the CLIC e^+ e^- beams are collided, an advanced detector is required. The cylindrical CLIC detector design, named CLICdet, is shown in Figures 2.6, 2.7, and 2.8. Each detector layer performs particular measurements required to achieve the physics potential of CLIC. The CLICdet design, described in detail in [6] and [37], has been optimised using detailed simulation studies and results from technology R&D.

2.3.1 CLICdet outer detectors

The outermost layer of CLICdet is the return iron yoke, which stops the detector's magnetic field from permeating throughout the detector cavern. It also contains large area detectors for muon identification, as muons are the only detectable particles that can pass through all layers of the detector. A 4 T magnetic field is created using a superconducting solenoid magnet.

CLIC has two sampling calorimeters to measure the energy of particles, each using interleaved layers of dense absorbers and fine-grained sensors. This sampling design allows the optimal materials to be used to induce and detect particle showers respectively. The high-granularity of the CLIC

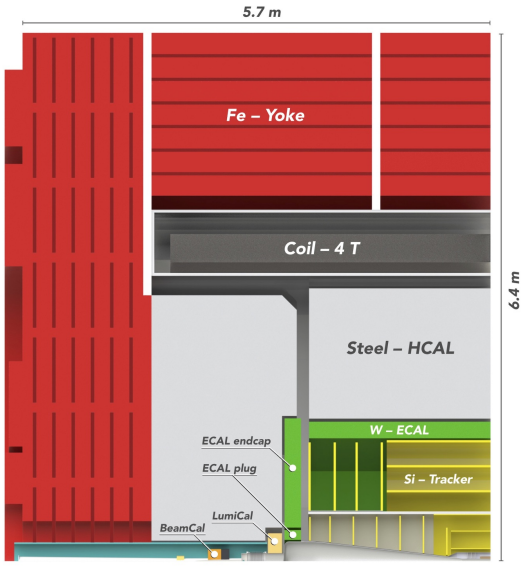

Figure 2.7: A 2D cross-sectional diagram of one quadrant of the CLIC detector design. Image from [38].

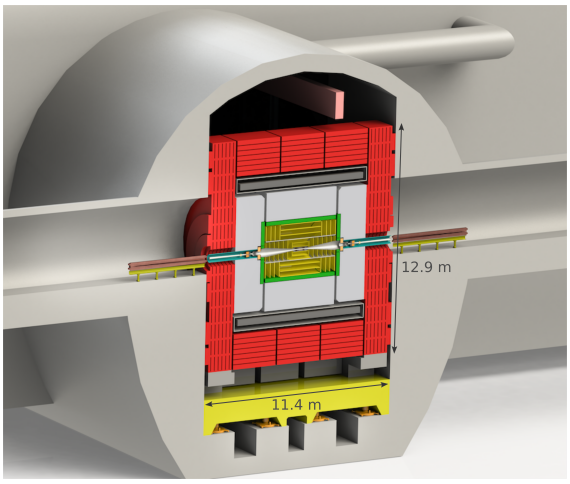

Figure 2.8: Diagram of the CLIC detector design, as would be placed in the detector cavern of CLIC. Image from [38].

calorimeters is optimised for particle flow analysis using reconstruction software, as discussed in [6]. Particle flow analysis combines information from each subdetector to determine the path and energy of each particle [39], enabling CLICdet to have excellent jet-energy resolution of $\sigma_E/E \leq 3.5\%$ in the range 100 GeV to 1 TeV.

The hadron calorimeter (HCAL) aims to measure the energy of hadronic particles. It consists of 60 alternating layers of 19 mm thick steel absorber plates and 3 mm thick scintillator tiles. Each scintillator tile is $30\times$ 30 mm^2 in size, with the total area of scintillating material covering 8700 m^2. The interaction between the dense steel layers and incoming particles causes a cascade of lower-energy particles. When hit by the induced particle shower, the scintillating material produces an amount of photons proportional to the energy of the original particle. The produced photons are then measured by silicon photomultlipiers.

The next layer of the CLIC detector is an electromagnetic calorimeter (ECAL) to measure the energy of charged particles. It is made of 40 alternating layers of 1.9 mm thick tungsten absorber plates and silicon pixel cells. Silicon sensors with a pad size of 5×5 mm^2 will cover a total area of 2500 m^2.

2.3.2 Inner detectors

The CLIC detector has two subsystems in the central detector region: the tracking detector and vertex detector. Each consists of barrel and end-cap regions made of silicon pixel detectors.

2.3.2.1 Inner detector requirements

The physics goals and beam structure of CLIC imposes strict requirements on the design of the inner detectors [37].

The main requirement of the tracking detector from the CLIC physics goals is to have a transverse momentum resolution of $\sigma_{p_T}/p_T^2 \leq 2\times10^{-5}\text{GeV}^{-1}$ for tracks with momenta $\geq$100 GeV. Assuming a 4 T magnetic field as designed, this corresponds to a single point resolution requirement of $\leq$7 µm and a material budget requirement of $\leq$1-2% X_0 per layer.

The transverse impact parameter resolution of the CLIC vertex detector is required to be σ_{d_0}=5$\oplus$15 /(p[GeV]$sin^{3/2}\theta$)µm to accurately reconstruct secondary vertices and thereby enable heavy flavour tagging. To achieve this, a single point resolution of $\leq$3 µm and material budget of $\leq$0.2% X_0 per layer is required.

Occupancies of more than a few percent in the detector layers of each subsystem would degrade the track reconstruction efficiency. The level of beam-induced backgrounds, discussed in Subsection 2.2.3, therefore sets the minimum radius of the vertex detector from the interaction point, and constrains the choice of detector technologies for the inner regions. The readout granularity of the tracking detector is constrained to 1–10 mm for the barrel region along the beam axis, where the size constraint depends on the radius. To maintain occupancies of a few % in the vertex detector and achieve the required spatial resolution of $\leq$3 µm, each pixel cell cannot exceed 25 µm$\times$25 µm at a radius of 31 mm. The impact of beam-induced backgrounds can be further minimised by requiring precise time-tagging with an accuracy of around 5 ns in the tracking and vertex systems, so background particles can be separated from the desired collision event. In addition, each pixel layer must have a hit detection efficiency of $\geq$99.7% to maintain the levels of intrinsic detector inefficiency and of noise occupancy below those caused by beam-induced backgrounds. A full discussion of the occupancy levels of each detector subsystem can be found in [6].

A low-mass, forced-flow air cooling system will be employed in the vertex detector to achieve a low level of material per layer. Each detector element must therefore have an average heat dissipation of $\leq$50 mW cm^{-2}. The tracking detector will use a liquid cooling system that can cope with an average heat dissipation of $\leq$150 mW cm^{-2}. These heat dissipation levels are accomplished through power-pulsing, a scheme which exploits the low duty cycle of CLIC. The pixel assemblies of the inner detectors are set to a low power state during the 20 ms between particle bunch trains.

A low level of radiation tolerance is required for the inner detectors of CLIC, compared to the radiation levels experienced at hadron colliders, due to the lack of large QCD backgrounds in lepton collisions. The inner layers of the vertex detector are expected to be exposed to $6\times10^{10} n_{eq}$cm^{-2}/year of radiation, with a maximum total ionising dose of approximately 300 Gy/year, including safety factors.

Currently, no pixelated detector technologies can fulfil all of the demanding inner detector requirements simultaneously. To this aim, the CLIC detector and physics collaboration (CLICdp) is carrying out an extensive R&D programme to develop novel pixel detector prototypes for both inner subsystems.

2.3.2.2 CLIC tracking detector layout and technologies

The CLIC tracking detector, pictured in Figure 2.9, is designed with six barrel layers, seven inner disks, and four outer disks of silicon pixel detectors. Inner and outer regions of the tracker are separated by a cylindrical support tube. Monolithic technologies are foreseen to be used in the CLIC tracker, as the detector has a large active area of 137 m^2, therefore hybrid technologies with complex interconnection process is not feasible.

The CLIC Tracking Detector (CLICTD) [40] is a demonstrator technology developed to achieve the tracking detector requirements. It is produced in a 180 nm modified Complementary Metal Oxide Semiconductor (CMOS) imaging process and has a small collection electrode. The CLICTD design aims to reduce the charge collection time within the sensor, while keeping the amount of digital circuitry within each pixel low. Each 300 µm$\times$30 µm detector channel of the 128$\times$16 matrix consists of eight sub-pixels. Every sub-pixel has an analogue front-end, but share a digital front-end across the channel. The 37.5 µm$\times$30 µm size of the sub-pixels was optimised using 3D transient TCAD simulations that modelled the complex, non-linear electric field within the sensor [41]. Analysis of laboratory and test-beam data shows that CLICTD prototype assemblies achieve the CLIC tracking

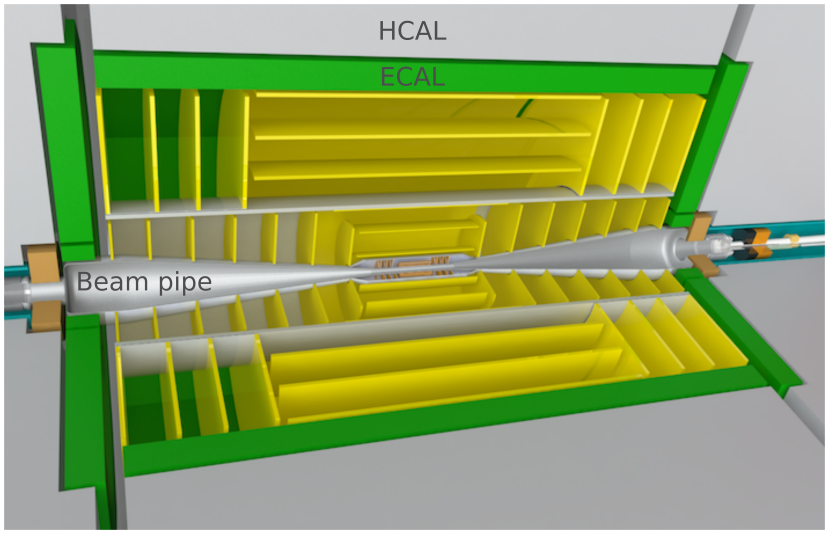

Figure 2.9: Schematic of the CLIC tracking detector, depicted in yellow. The cylindrical support tube of the tracker, shown in light grey, separates the inner and outer regions of the tracker. Image modified from [38].

detector requirements for spatial resolution, timing resolution, hit detection efficiency, and power consumption [42].

The ATLASpix_Simple has been developed for the inner tracker upgrade of the ATLAS experiment and also targets the CLIC tracker requirements. It is a High Voltage Monolithic Active Pixel Sensor (HV-MAPS) technology with elongated pixels. Each pixel is 130 µm×40 µm in size and arranged in a 25×400 matrix [43]. ATLASpix_Simple assemblies have been manufactured with P-type substrates of different resistivities and compared in laboratory and test-beam analysis. From these studies, it has been found that ATLASpix_Simple meets the material budget, efficiency, and timing resolution requirements of the CLIC tracker [44] [45].

2.3.2.3 CLIC vertex detector layout and technologies

The vertex subsystem is the most central region of the CLIC detector. It consists of end-cap disks and three double barrel layers as pictured in Figure 2.10. The end-caps have a spiralled pattern to enable air cooling, a design that was found to have no significant negative impact on the flavour-tagging performance of CLICdet through Geant4-based full detector simulations [46].

The requirements of the CLIC vertex detector are more stringent than those of the tracker, as discussed in Subsection 2.3.2.1. The requirements of small pixel pitch and thin sensor thickness are particularly challenging. The technologies under study for the vertex subsystem are hybrid pixel detectors, which can take advantage of advanced Application-Specific Integrated Circuit (ASIC) processes within small feature sizes and innovative sensor technologies.

The CLICpix2 chip is a fine-pitch, pixelated readout ASIC produced in a 65 nm CMOS process. They have been bump-bonded to thinned active-edge planar silicon sensors, as described in Chapter 3. As the main focus of this study, the laboratory characterisation and test-beam analysis of the CLICpix2 planar sensor assemblies are discussed in the following chapters.

Hybrid bump-bonding at a small pixel pitch is a complex and expensive process, as discussed in Section 1.4. The ASIC and sensor can instead be connected using a thin glue layer, where the charge signal can be capacitively coupled between the two layers. This process has been tested for CLICpix2 ASICs and active CLICpix Capacitively Coupled Pixel Detector (C3PD) sensors targeting the CLIC vertex requirements [47]. The active C3PD sensor is fabricated in an 180 nm HV-CMOS process, and

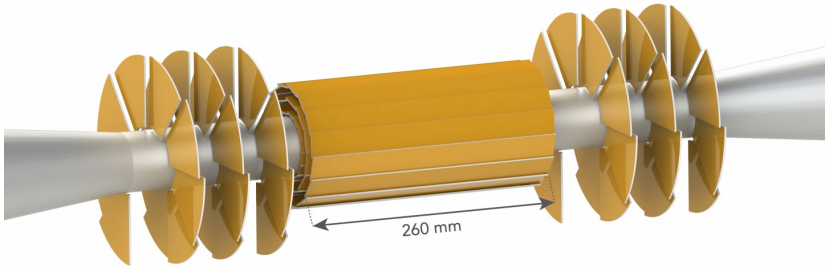

Figure 2.10: Schematic of the CLIC vertex detector and beam pipe. The barrel section of the vertex detector has three double layers, and the end-caps have a spiralled design. The first barrel layer of the detector is at a radius of 31 mm from the interaction point. Image from [38].

amplifies the signal to enable the capacitive charge transfer. Refined gluing techniques and improved characterisation of the signal transfer chain are needed to further improve this technology [6].

One challenge for hybrid devices with thin planar sensors is the limited positional resolution. The amount of charge sharing between pixels is restricted by the small sensor thickness, therefore the positional resolution is limited to the binary hit resolution of pitch/$\sqrt{12}$, as discussed in Section 1.1. By reducing the pixel pitch the resolution can be improved, however this is often not possible due to the space required for the in-pixel electronics. The Enhanced LAteral Drift (ELAD) sensor concept aims to increase the amount of pixel-to-pixel charge sharing while maintaining a fixed pixel pitch and thin sensor thickness [48]. Detailed 2D and 3D TCAD simulation studies of ELAD sensor designs have been carried out to optimise the implant design for pixel pitches of 25 µm and 55 µm, corresponding to the footprint of CLICpix2 and Timepix3 readout ASICs, introduced in Chapter 3 and Subsection 5.2.1.1 respectively.

A monolithic technology is under study for the CLIC vertex detector, fabricated using a Silicon On Insulator (SOI) 200 nm CMOS process. A SiO_2 planar insulator is sandwiched between a High Resistivity (HR) substrate and a Low Resistivity (LR) silicon layer. By using this structure, the separated HR sensor layer can be fully depleted and the readout electronics can be placed in the LR layer, mimicking a hybrid technology while avoiding the challenge of fine-pitch bump bonding. Demonstrator SOI assemblies with a pixel pitch of $30\times30\,\mu m^2$ have been produced, where different wafer compositions and different front-ends have been tested [49].

Part II

Characterisation of CLICpix2 planar sensor assemblies

Chapter 3

CLICpix2 hybrid assemblies with planar sensors

The beam conditions expected at Compact Linear Collider (CLIC) impose strict requirements on the design of the inner detectors in order to achieve the physics programme, as discussed in Section 2.3.2.1. Currently, no technology can fulfil the precise spatial and timing resolution, high hit efficiency, low material budget, and low average power dissipation required for the vertex detector simultaneously. Consequently, the CLIC detector and physics (CLICdp) collaboration develops and tests novel sensors and readout technologies for hybrid pixel detectors [6].

The CLICpix readout Application-Specific Integrated Circuit (ASIC) [50] [51] is produced in a commercial 65 nm Complementary Metal Oxide Semiconductor (CMOS) process as part of the Timepix/Medipix family [52]. Its small pixel pitch, simultaneous charge and time measurements, and the power-pulsing capabilities of the test chip are designed to fulfil the CLIC vertex requirements. The next iteration, the CLICpix2 readout ASIC, aims to improve on the original design [7]. To achieve the low material budget requirements, thin planar active-edge sensors are currently under study for the CLIC vertex detector.

For this study, CLICpix2 ASICs were bump-bonded to active-edge planar silicon sensors using a novel single-chip bonding process.

3.1 CLICpix2 readout ASIC

The CLICpix2 readout ASIC is described in detail within the CLICpix2 user manual [7].

The readout ASICs CLICpix and its successor CLICpix2 are produced in the same 65 nm CMOS imaging process and both have a pixel pitch of 25 µm. When compared to its predecessor, the CLICpix2 readout chip has an enlarged pixel matrix which is beneficial for testing CLICpix2 assemblies in a particle beam. CLICpix2 also has increased Time-over-Threshold (ToT) and Time-of-Arrival (ToA) counter sizes, and this increased dynamic range allows for efficient testing of the chip. A number of features are also added in this new iteration, such as improved noise isolation, the inclusion of a band-gap reference voltage, and on-chip test pulsing capabilities. The main design features of the CLICpix2 ASIC are presented and compared to the CLICpix readout chip in Table 3.1.

3.1.1 ASIC design

The CLICpix2 pixel matrix consists of 128 columns and 128 rows, with the pixel in the bottom-left corner as coordinate (0,0) for the ASIC orientation shown in Figure 3.1. Starting from this pixel, each set of 2×8 pixels is named a 'super-pixel' and each set of two columns is named a 'double column'. Odd and even numbered columns have a mirrored design, as can be seen from the top-layer design shown in Figure 3.2, causing a difference in routing lengths of the data lines between these sets of columns.

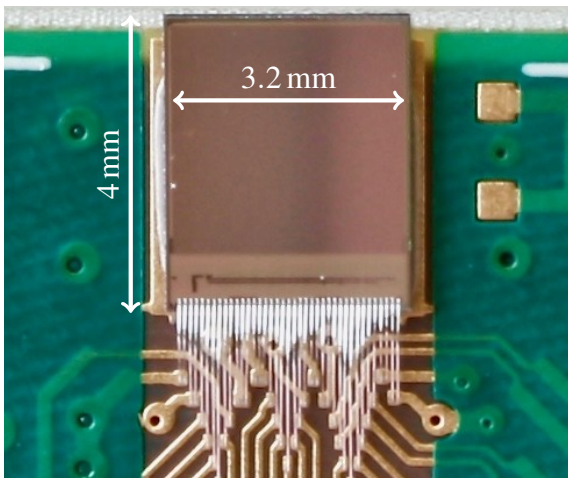

Figure 3.1: Image of a CLICpix2 ASIC glued and wire-bonded to to a readout PCB. Image credit CLICdp.

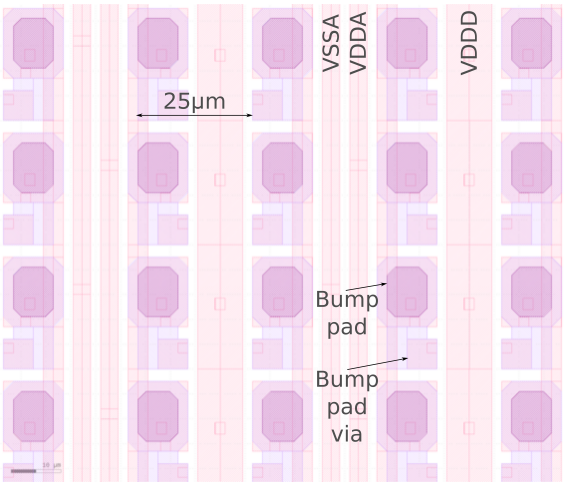

Figure 3.2: Layout design of the top-metal layers of the CLICpix2 ASIC in a grid of 5x4 pixels, showing the mirrored column design.

Table 3.1: Summary of the main design parameters of the CLICpix2 ASIC design [51] [7].

Parameter	**CLICpix**	**CLICpix2**
ASIC size	1.85 mm×3 mm	3.35 mm×4.06 mm
Active area	1.6 mm×1.6 mm	3.2 mm×3.2 mm
Matrix size	64 × 64 pixels	128 × 128 pixels
CMOS technology	65 nm	65 nm
Pixel pitch	25 µm×25 µm	25 µm×25 µm
ToT counter depth	4 bit	5 bit
ToA counter depth	4 bit	8 bit
ToA bin size	10 ns	10 ns
ENC without sensor	60 electrons	67 electrons
Minimum threshold (6σ margin)	388 electrons	440 electrons
Acquisition mode	Frame-based	Frame-based
Readout mode	Single column readout	1/2/4/8 parallel column readout
Data encoding	-	8 bit / 10 bit
Readout system	µASIC	Caribou
Voltage reference	External	Bandgap
Test pulse injection	External	Internal or External
Analogue power diss./pixel	7 µW	6.6 µW
Amplifier gain	44 mV/ke$^-$	33 mV/ke$^-$
Slow control	Custom	SPI
Clock speed	100 MHz (acquisition) and 320 MHz (readout)	
Data type	Zero compression (pixel, super-pixel and column skipping)	
Power saving	Clock gating (digital part), power gating (analogue part)	

Table 3.2: Summary of periphery DACs of the CLICpix2 ASIC important to the study [7].

Signal	Resolution	Description	Type
vfbk	4.5 mV	Provides the voltage bias for the baseline of the preamplifier output	V
threshold_LSB/MSB	0.5 mV	Configures the global hit detection threshold of the pixel matrix	V
test_cap_1_LSB/MSB	0.5 mV	Sets the voltage of the 1st plate of the capacitor used to generate test-pulses	V
test_cap_2	4.5 mV	Sets the voltage of the 2nd plate of the capacitor used to generate test-pulses	V
ikrum	0.1 nA	Determines the time in which the signal returns to the baseline	I

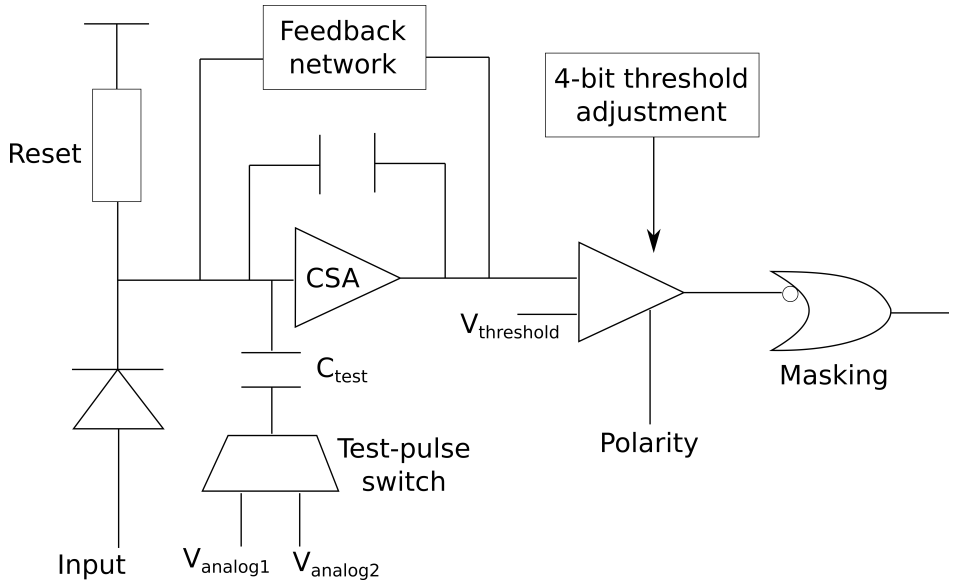

Figure 3.3: Schematic of the CLICpix2 analogue front-end.

Seventeen Digital to Analogue Converters (DACs) have been implemented on the periphery, providing reference or biasing voltages and currents for the pixel matrix. A summary of the CLICpix2 periphery DACs important to this study can be found in Table 3.2. These are separated into current DACs and voltage DACs, depending on their respective output. A summary of all the CLICpix2 periphery DACs can be found in [7].

A simplified schematic of the CLICpix2 ASIC analogue front-end circuit is presented in Figure 3.3. The test-pulse circuit, consisting of two input voltages, a switch, and a capacitor before the charge sensitive amplifier (CSA), is discussed in Subsection 3.1.2. Input charge originating from the sensor or the test-pulse circuit is integrated over by the CSA using preamplifier with a Krummenacher feedback network [53]. The resultant shaped voltage pulse is compared in a discriminator to the global threshold DAC voltage adjusted by a 4-bit threshold adjustment specific to each pixel. Analogue output from each pixel can be masked individually using the logic gate shown.

CLICpix2 employs a frame-based system to acquire data. To open the acquisition window, a shutter signal is asserted and when this signal is de-asserted the data taking window closes. Each frame would correspond to one CLIC bunch train in the final CLICdet design. The length of the data taking frame is configurable in units of 100 MHz clock cycles.

The in-pixel digital logic can record three different measurements during the data acquisition

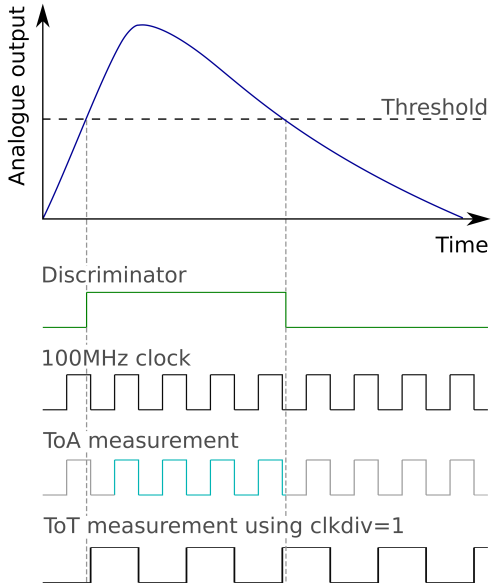

Figure 3.4: Diagram of the ToT and ToA pixel measurements of the CLICpix2 ASIC. Figure is not to scale and based on a similar image from [54].

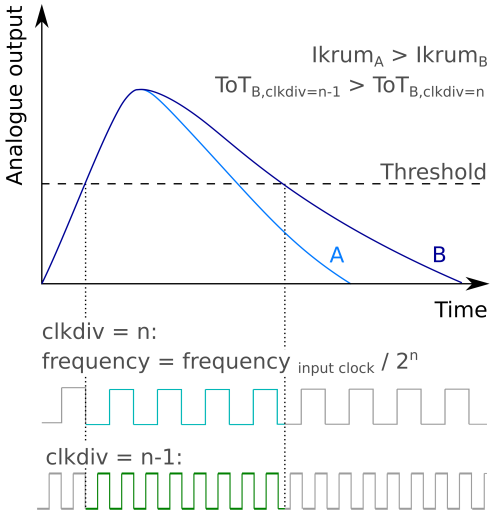

Figure 3.5: Illustration of the effect of ikrum and clock divider settings on the ToT measurement of CLICpix2. Diagram is not to scale.

window: ToT, ToA, and hit counts. Each of these measurements is explained in the following text and illustrated in Figure 3.4.

The ToT value indicates the magnitude of charge deposited in the sensor layer of a pixel. In the CLICpix2 ASIC, the ToT is measured as the number of positive clock edges that arrive at the pixel while the discriminator output is above the threshold. The default acquisition clock frequency is 100 MHz and the ToT units range from 0 to 30 clock cycles. The dynamic range of the ToT measurement to the charge generated in the sensor is adjusted using the ikrum and clock divider settings. The ikrum DAC changes the slope at which the signal returns to the baseline, and thus adjusts how many clock cycles a certain signal is above the threshold level. The clock divider DAC, `clk_div`, adapts the frequency used for the ToT measurement by specifying the number of times the default clock frequency should be halved. For a clock divider setting of 2, the 100 MHz clock would be divided by 4, leading to a 25 MHz clock being used for measuring the ToT. Lowering the frequency increases the magnitude of charge corresponding to one ToT unit. The effect of the ikrum and clock divider DACs are illustrated in Figure 3.5.

The ToA measurement corresponds to the arrival time of the pixel hit. The number of positive clock edges that arrive between the threshold crossing of the discriminator output and the falling edge of the shutter signal are counted. In combination with the time stamp of the shutter signal in the data acquisition (DAQ) system, the hit time can be calculated. Finally, event counting records the number of above-threshold signals that occur in the pixel during the data acquisition window. Any pixel hits before or after the data acquisition window are ignored in each of these three measurements.

These measurements are combined into four CLICpix2 operational modes: simultaneous 8-bit ToA and 5-bit ToT, simultaneous 8-bit hit-count and 5-bit ToT, 13-bit ToA, or 13-bit hit-count measurement.

All pixel hits recorded during the acquisition frame are read-out by DAQ system using a 320 MHz readout after the shutter signal is de-asserted and stored in a text file. The readout control register of

the ASIC determines how many double columns are read out simultaneously, up to eight parallel columns. While writing out data, the shutter cannot open and therefore no pixel hits can be recorded during this dead-time. An on-chip data compression method can be enabled, reducing the number of bits read out for pixels, super-pixels, or double-columns containing no hit pixels. The DAQ system used for CLICpix2 data taking is described in Section 4.1.

3.1.2 Notable features of the ASIC

A number of notable features have been implemented into the CLICpix2 ASIC to aid the testing of this technology. The first of these is a well-defined reference current, which can be generated as the ratio between the bandgap voltage and an internal resistor, allowing the proper operation of the periphery current DACs. An output pad is also present to facilitate off-chip probing, where the voltage of 22 different nodes can be recorded using an output multiplexer.

Another notable feature is on-chip temperature recording, which can be taken by extracting the voltage-temperature characteristics of the bandgap. The voltage of the temperature sensing buffer, V, is observed using the CLICpix2 output multiplexer and the temperature, T, is calculated using the equation:

$$V = -1.89T + 738.04, \tag{3.1}$$

where T is in °C and V is in mV. The measurement uncertainty is ± 2.7 °C from the uncertainty of the absolute temperature calibration. However, when calculating the difference between two temperature readings, the uncertainty decreases to that of the voltage measurement of ± 0.5 °C as any absolute calibration offset cancels out.

In addition, the analogue structures of the pixels can be put in a low power state column-by-column in a configurable manner. This so-called power pulsing is foreseen at the CLIC detector due to the low duty cycle of the accelerator, and these capabilities have been studied for CLICpix2 planar assemblies [55].

Finally, CLICpix2 has on-chip test pulsing capabilities where a test capacitor, denoted C_{test} in Figure 3.3, discharges directly into the front-end of one or more pixels. The voltage difference between the two capacitor plates determines the magnitude of the injected charge pulse. Shown in Figure 3.3 as $V_{analog1/2}$, these voltages are set using the `test_cap_1` and `test_cap_2` DACs. Test pulsing can be switched on or off per pixel, and the number and delay between the automatically generated pulses can be configured using the DAC described in [7]. Pulses are of both polarities, such that configuring five test pulses to be generated results in five positive polarity and five negative polarity pulses in alternating order. Measurements with test-pulse injection are useful to decouple the response of the ASIC and the sensor, and to calibrate the ToT response of each pixel.

3.2 Active-edge planar silicon sensors

Hybrid pixel detectors are currently considered for the CLIC vertex detector, with thin planar sensors due to the strict $0.2\%X_0$ per layer requirement on the material budget [6]. CLICpix2 ASICs were therefore combined with planar silicon sensors of different thicknesses during this study. These sensors are produced by two different foundries, FBK-CMM [56] and Advacam [57], and the ASIC-sensor bonding process is described in Section 3.3.

3.2.1 Advacam production

The N-in-P planar silicon sensors produced at Advacam for this study have different thicknesses: 50 µm, 100 µm, and 150 µm. A thin-film NiAu under bump metallisation (UBM) was used by Advacam on all sensors, excluding the 50 µm thick sensor where Pt was used.

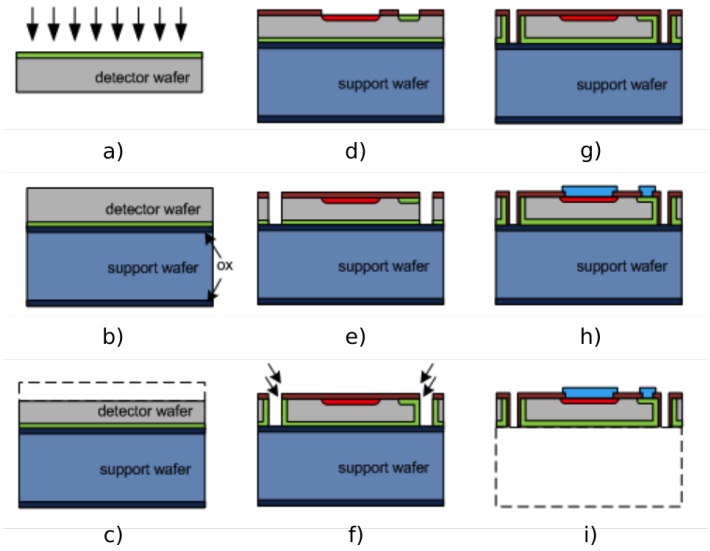

Figure 3.6: Illustration of the process flow of producing active-edge N-in-P sensors by the manufacturer. Image based on [59].

In most pixel technologies, inefficient regions occur at the matrix edges. Due to the effect, assembly-assembly overlaps are often introduced in a particle detector system so that it has hermetic coverage. However the CLIC vertex detector has a strict requirement of $0.2\%X_0$ per layer on the material budget, therefore overlaps and inactive areas need to be minimised. To this end, an active-edge design is employed for all planar sensors used for CLICpix2 assemblies. A Deep Reactive Ion Etching (DRIE) [58] process formed continuous implanted trenches around the Advacam sensor edge.

The process flow when producing N-in-P active-edge sensor at Advacam, illustrated in Figure 3.6, is as follows [57] [59]:

a) The backside implantation of the sensor wafer is performed by doping it with boron atoms.

b) The wafer is then bonded to a supporting wafer.

c) Grinding and chemical-mechanical planarisation polishes the sensor to the desired thickness.

d) The pixels, and guard rings where applicable, are implanted with phosphorus ions.

e) The DRIE etching is performed to uncover the edges of the detector.

f) The sidewalls are implanted with phosphorus ions to activate the sensor edges.

g) Annealing of the sensor in order the activate the dopants and oxidation of the edges.

h) Contacts to the aluminium patterning are opened and the UBM deposited for the pixels, and guard rings where applicable.

i) The support wafer is removed from the sensor.

This technology allows the sensor to collect charge efficiently up until the physical sensor edge, thus maximising the percentage of the assembly area that is active. When used in a particle detector system, active-edge devices can be seamlessly tiled with minimal inefficient areas.

When using an active-edge sensor, the potential gradient between the sensor edge and the outermost pixels of the matrix can be high, as explained in Section 1.4. The inclusion of a guard ring can prevent sensor breakdown, however it has been found to cause a decrease in edge efficiency as

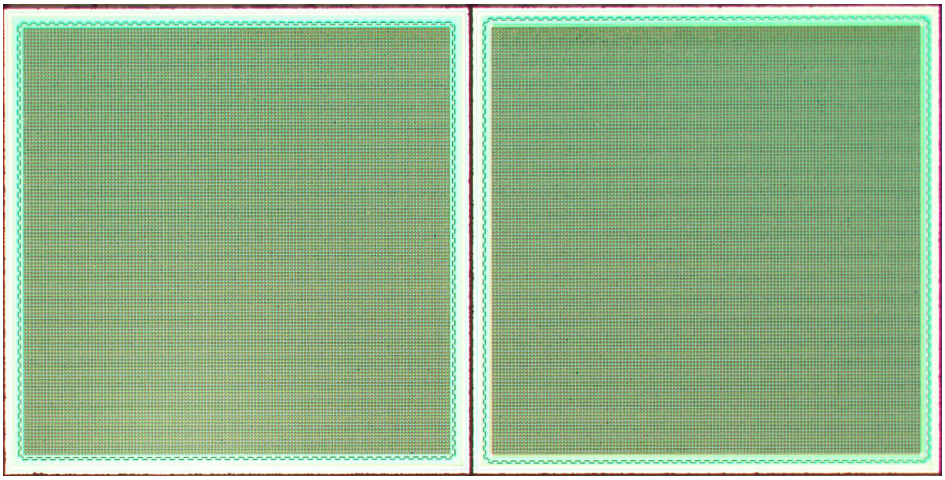

Figure 3.7: Image of two active-edge planar sensors from FBK-CMM, showing the design of the staggered active-edge implant trenches. The sensor on the left has no guard ring while it is present for the sensor on the right, as indicated by the larger distance between the implant trenches and the pixel matrix.

it reduces the active volume near the sensor surface [60]. Guard rings can either be kept floating or can be connected to the ground potential of the ASIC. To investigate this effect, guard rings with the designs described in [60] are included in four Advacam sensors, where two are floating and two are grounded.

3.2.2 FBK-CMM production

All planar silicon sensors provided by FBK-CMM have a thickness of 130 µm, are of type N-in-P, and come from a single wafer.

For these sensors, a UBM was deposited by Fraunhofer IZM (IZM) [6] [61]. The IZM UBM consists of a sputtered TiW/Cu plating base and an additional Cu pad that is deposited using an electro-plating process. The Cu layer of the plating base acts as a seed layer for the subsequent electro-plating process. The Cu pad is deposited due to metallurgical reasons: to provide material for the formation of the inter-metallic compounds between Cu and tin of the solder bumps, as discussed in Section 3.3.

The FBK-CMM active-edge sensors have also have a trench created using DRIE process, but with a staggered trench design, rather than a single trench, as this is a first test production of the technology. Figure 3.7 shows two FKB-CMM active-edge sensors with a staggered trench design. A number of these sensors also have guard rings. No guard ring is present on the left-hand sensor in Figure 3.7, while a floating guard ring design is used for the sensor on the right. When the guard ring is present, a larger distance is observed between the staggered trenches and the pixel matrix due to the trench design.

3.3 CLICpix2 bump-bonding at IZM

The bump-bonding process for small pitch, single-chip pixel devices presents many challenges, as discussed in Section 1.4. In particular, the deposition of approximately 12 µm diameter solder bumps onto pre-diced readout chips is a difficult task.

IZM [62] developed a single-chip bump-bonding process based on carrier-wafers for CLICpix2 assemblies. The carrier-wafer processing steps for the SnAg bump deposition include preparing the

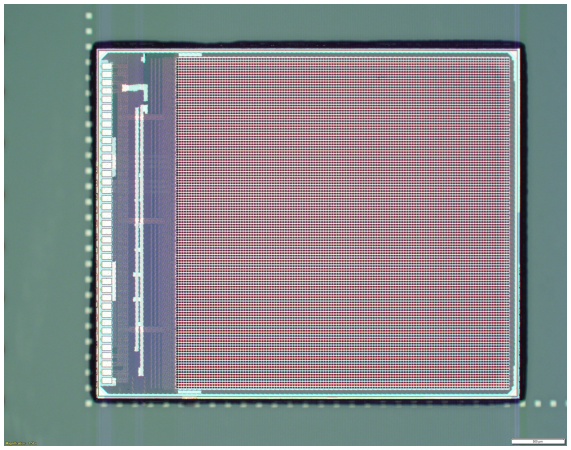

Figure 3.8: Image of a CLICpix2 ASIC with deposited solder bumps, showing the full pixel matrix. Image credit Fraunhofer IZM [62].

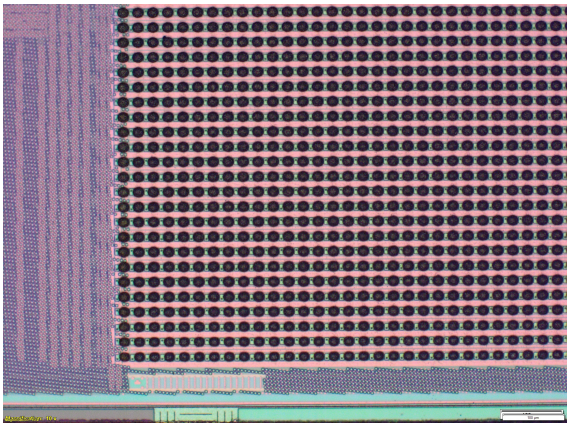

Figure 3.9: Image of a CLICpix2 ASIC with deposited solder bumps, showing a corner of the pixel matrix in more detail [6].

carrier wafers with mask alignment marks and a bonding layer. As the processing tools used at IZM are optimised for standard wafer size substrates, the single-chip dies are then bonded to the carrier wafer. To deposit the solder bumps onto each pixel pad, an electro-plating process using a thick photoresist layer is performed in the following steps [6]:

1. Deposition of a thick photoresist onto the matrix.
2. Lithography to create a mask layer of the required pattern, such that the solder bumps are the correct size for the pixel pitch and separated by 25 µm.
3. Galvanic deposition of the SnAg solder.
4. Removal of the photoresist and etching of any UBM outside bumps.
5. Reflow of solder bumps into a sphere-like shape at high temperature.
6. Removal of ASICs from carrier wafer.

Images of CLICpix2 ASICs with deposited solder bumps are shown in Figures 3.8 and 3.9. After the bump deposition, the ASIC is removed from the carrier wafer. A pick-and-place procedure is then performed by a flip-chip bonder tool to put the sensor on top of the ASIC. Finally, the solder bumps are re-flowed, forming a metallurgic connection to bond the CLICpix2 chip and planar sensor together [6].

In total, nine CLICpix2 planar assemblies have been produced using the bonding method described, an example of which is shown in Figure 3.10. Table 3.3 summaries the assembly numbers, sensor properties, and UBM materials of each device.

3.4 Material budget calculation of CLICpix2 planar assemblies

To properly model the scattering that occurs when particles interact with a pixel detector, precise knowledge of the detector material content is needed. For a uniform layer of material in the XY plane with particles incident along the Z axis, the material budget is the thickness of the layer in Z divided by the radiation length of the material.

To calculate the average material budget for CLICpix2 planar sensor assemblies glued to readout printed circuit boards (PCBs), the thickness and composition of each device layer must be estimated.

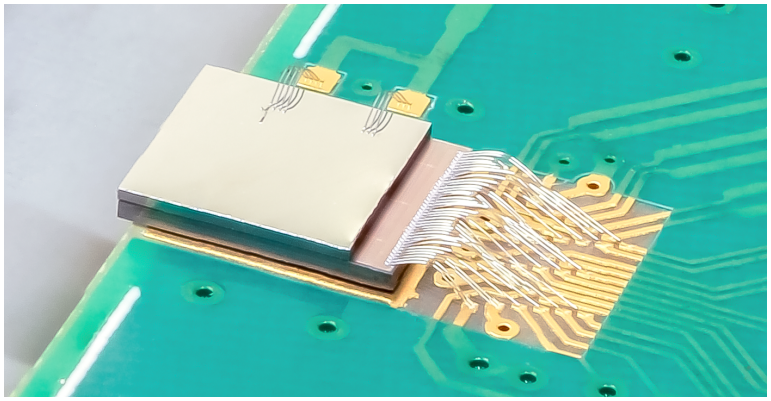

Figure 3.10: Image of a CLICpix2 assembly with a 130 µm thick active-edge sensor. The sensor (on-top) is bump-bonded to the ASIC (underneath), which is itself wire-bonded to a readout PCB [6].

Table 3.3: Summary of all CLICpix2 assemblies with N-in-P, active-edge planar sensors produced.

Assembly number	**Serial number**	**Sensor producer**	**Active edge**	**Guard ring (GR)**	**Sensor thickness**	**UBM**
9	ADV100-S4	Advacam	Continuous	Grounded GR	100 µm	NiAu
14	FBK-398-01	FBK-CMM	Staggered	Not confirmed[1]	130 µm	TiWCu
15	ADV150-S9	Advacam	Continuous	Grounded GR	150 µm	NiAu
16	FBK-398-02	FBK-CMM	Staggered	Not confirmed	130 µm	TiWCu
18	ADV100-S5	Advacam	Continuous	No	100 µm	NiAu
19	FBK-398-03	FBK-CMM	Staggered	Not confirmed	130 µm	TiWCu
20	FBK-398-04	FBK-CMM	Staggered	Not confirmed	130 µm	TiWCu
21	ADV100-S3	Advacam	Continuous	Floating GR	100 µm	NiAu
22	ADV050-S2	Advacam	Continuous	Floating GR	50 µm	Pt

Seven main layers were identified using the technical design of the CLICpix2 ASIC and PCB, and cross-sectional images of a bonded CLICpix2 planar assembly, shown in Figures 3.2, 3.12, and 3.13 respectively. These layers, shown schematically in Figure 3.11, are the sensor metallisation, planar silicon sensor, UBM, solder bump-bonds, top metal layer, CLICpix2 ASIC, and finally the PCB. All other components of the assembly are considered to be negligible to the material budget calculation, either due to their small thickness in Z or the low density of the layer material.

The overall material budget calculation for CLICpix2 assembly with a sensor from FBK-CMM is outlined in Table 3.4. For each of the seven layers, the material composition and thickness in Z are outlined. The radiation length of each material is taken from [20]. A fill factor is calculated to account for non-uniform area coverage in the XY plane. It is equal to the area covered by the material divided by the total area, and is therefore equal to 1 for a perfectly uniform layer in the XY plane. The fill factor of the solder bump-bonds was calculated using the cross-sectional image shown in Figure 3.13 and the assumption that each bump-bond is a perfect cylinder. Each solder bump is estimated to have a height of 10 µm and an average diameter of 15 µm. The top metal layer design in the XY plane, presented in Figure 3.2, was used to calculate the area of copper over the footprint of two pixels. Using the fill factor and the height of the material, an effective thickness along the Z axis can be calculated. This would be the thickness of the material if it were a uniform, flat layer covering the footprint of one pixel.

[1]The information on the GR layout of the FBK-CMM assemblies was not retained during the flip-chip process, and investigations using laboratory data, test-beam analysis, and microscope imaging have been inconclusive.

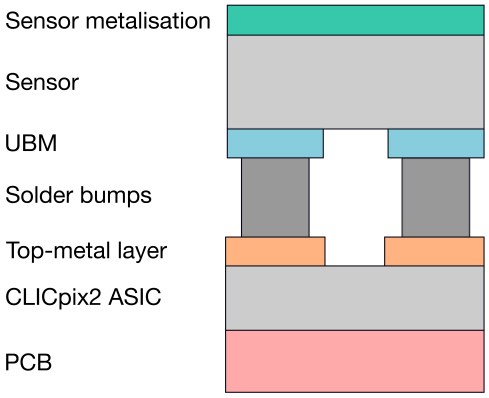

Figure 3.11: Pictorial representation of the vertical layers considered to calculate the material budget of CLICpix2+planar assemblies. This figure is not to scale and covers two pixel pads in the horizontal axis.

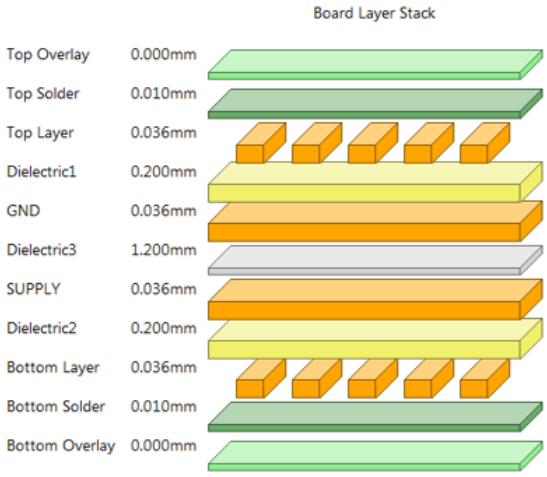

Figure 3.12: Diagram of the PCB layer stack used for CLICpix2+planar assemblies.

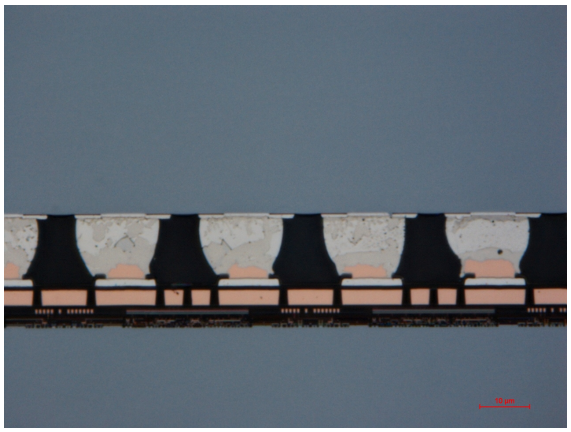

Figure 3.13: Cross-sectional image of a bonded CLICpix2+planar assembly. Image credit Fraunhofer IZM [62].

A total material budget of 2.40%X_0 is calculated, with the main contributions to this value coming from the assumed 130 µm thick planar sensor, the ASIC, and the PCB. In future iterations of the technology, the PCB can be easily thinned to reduce this value. For application to the vertex detector of CLIC, thinner sensors of approximately 50 µm thickness and thinned ASIC of 50 µm thickness would need to be used in conjunction with a low-mass support system to achieve the 0.2%X_0 per layer material budget requirement [6].

Table 3.4: Summary of the CLICpix2+planar assemblies material budget calculation.

Layer	**Material composition**	**X_0 of material (mm)**	**Z height of material (um)**	**Fill factor**	**Effective Z thickness (um)**	**X/X_0** (%)
Sensor metallisation	Al	88.97	0.5	1.0	0.5	0.0006
Planar sensor	Si	93.7	130	1.0	130	0.1387
UBM	Ti	35.6	0.2	1.0	0.2	0.0006
Solder bumps	Sn (95%)	12.06	9.5	0.28	2.66	0.0221
	Ag (5%)	8.54	0.5	0.28	0.14	0.0016
Top metal layer	Cu	14.36	3	0.66	1.98	0.0138
ASIC	Si	93.7	300	1.0	300	0.3202
PCB	Glass fibre (60% of FR-4)	97.66	960	1.0	960	0.9830
	Epoxy resin (40% of FR-4)	349.89	640	1.0	640	0.1829
	Cu	14.36	108	1.0	108	0.7521
					Total =	**2.4156**

Chapter 4

Laboratory characterisation of CLICpix2 planar sensor assemblies

Some results presented in this chapter have been published previously in [44].

Novel pixel detector assemblies often have challenging production processes or design parameters, and therefore must undergo detailed laboratory testing to determine their quality. These tests establish the basic functionality, manufacturing quality, and response characteristics of each assembly, and also test the design of the Application-Specific Integrated Circuit (ASIC).

With smaller and smaller pixel pitches, the hybrid bump bonding-process becomes very challenging due to handling difficulties, especially in a single-chip bonding process, as discussed in Section 1.4. This chapter presents the results of single-chip bump-bonding for a 25 µm pitch hybrid pixel detector. The bonding process has its own unique challenges, therefore assessing the interconnect quality and performance of each assembly in detail is very important. Insights from the laboratory testing were communicated to the manufacturer IZM, helping to optimise the bonding process.

To characterise the CLICpix2 planar sensor assemblies described in Chapter 3, an initial set of tests verified the basic functionality of the chip. Then in-depth categorisation studies could assess the response and interconnect quality of each pixel. During these studies, the usage of CLICpix2 assemblies identified any design issues of the ASIC. Finally the units of threshold and charge are calibrated into e^-, enabling the amount of energy deposited in the sensor to be compared to theory, simulations, and other pixel devices.

4.1 Caribou DAQ system and Peary DAQ software

4.1.1 Caribou DAQ system

The Caribou system was used for all data taking in the laboratory during this study. It is a data acquisition (DAQ) system developed for testing pixel detectors [63]. Due to its flexible design, Caribou allows various novel devices to be tested in different environments, such as laboratories and testbeams. The use of a versatile and well tested DAQ, rather than developing a device specific system each time, significantly reduces the time required to develop and characterise prototypes.

The Caribou DAQ system hardware consists of three parts: a chip board, a Control and Readout (CaR) board, and a ZC706 Field-Programmable Gate Array (FPGA) evaluation board using a System on Chip (SoC) architecture, as shown in Figure 4.1 [6]. Every custom chip board is specific to the type of device and directly connects to the universal periphery CaR board, providing the hardware environment for various target ASICs. This connects to the FPGA, either directly or via an Flexible Metallic Conduit (FMC) cable as shown in Figure 4.1. The FPGA contains both a CPU for data acquisition, which runs a full linux system, and a FPGA fabric for detector control and data handling. A power supply unit is needed to power the FPGA and CaR boards. It should be noted that this set-up requires no dedicated PC, as the user can access the SoC via a secure shell (SSH) using an ethernet link. During CLICpix2 laboratory measurements, a separate high-voltage power supply unit provided

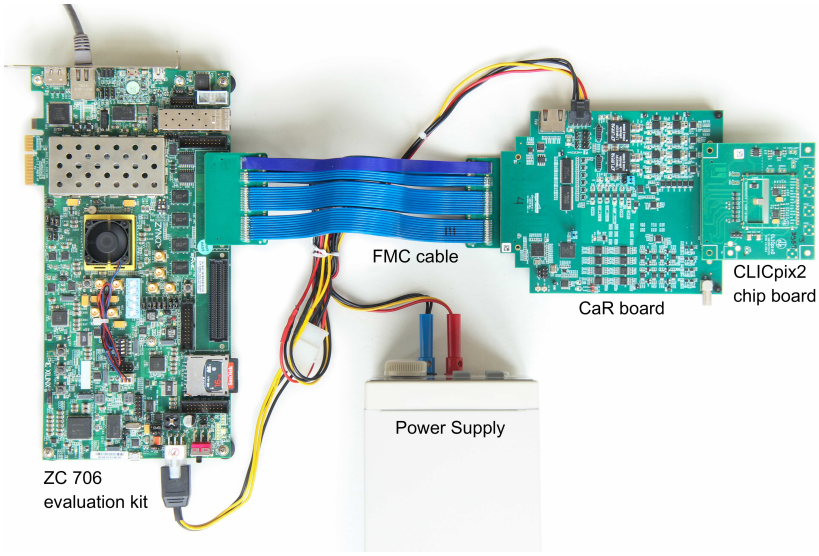

Figure 4.1: An example Caribou set-up for laboratory measurements. Image from [6].

the bias voltage applied across the sensor, which was the only additional piece of equipment used during assembly testing.

4.1.2 Peary DAQ software

The Peary DAQ software [64] has been developed concurrently to the Caribou project. It provides hardware abstraction for periphery components through a common interface. Pixel data is easily recorded due to the inclusion of device-specific functions, logging verbosity levels, and a command-line interface.

For CLICpix2 data taking, a matrix and pattern generator configuration files are read in using Peary to configure the assembly.

Each pixel in the CLICpix2 matrix has a range of individual settings, which are configured using the matrix configuration file. If the output of the pixel front-end is to be masked, for example due to high noise, a masking bit can be set to 'true' in this file. In addition, test-pulse injection can be enabled per-pixel and the desired data taking mode can also be specified in the matrix file. Finally, the user can set a 4-bit local threshold adjustment to mitigate pixel-to-pixel differences. The applied threshold per pixel is therefore a combination of the local adjustment and the global setting from the `threshold` Digital to Analogue Converter (DAC).

The timing in clock-cycles of the powering and shutter control of the device is defined using a pattern generator text file. It specifies the pattern in time that the chip is powered, the shutter signal is asserted, and the shutter is de-asserted in units of 100 MHz clock cycles.

The Peary software is also used to configure DACs and Analogue to Digital Converters (ADCs) on the chip. The majority of the CLICpix2 DACs are 8-bit in length while the `threshold` and `test_cap_1` DACs are 16-bits long, consisting of a least significant byte (LSB) and a most significant byte (MSB). It should be noted that these two DACs have a non-monotonic behaviour when changing the MSB, meaning the voltage of the DAC has a non-linear behaviour with increasing DAC codes. For example, Figure 4.2 presents the voltage output of the `threshold_LSB/MSB` DACs. A linear increase in voltage is observed when the `threshold_LSB` increases from 0 to its maximum value of 255. When increasing the MSB and resetting the LSB to zero, the voltage jumps to a lower value therefore multiple combinations of LSB and MSB will provide the same voltage output. To avoid non-monotonic behaviour, the DAC can be linearised such that the user inputs a single `threshold` or `test_cap_1` value and within the data taking software the appropriate LSB and

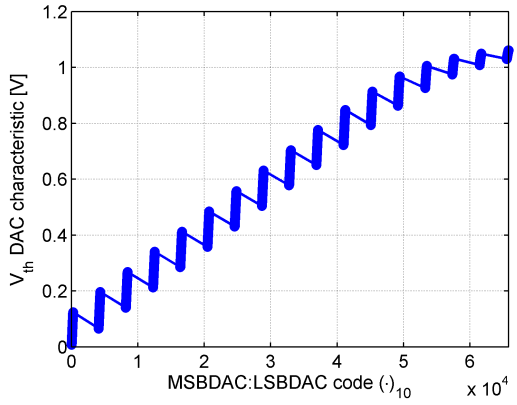

Figure 4.2: Voltage of the `threshold_LSB /MSB` measured by the CLICpix2 ASIC output multiplexer, showing the non-monotonic behaviour of the DAC between MSB values. Image from [7].

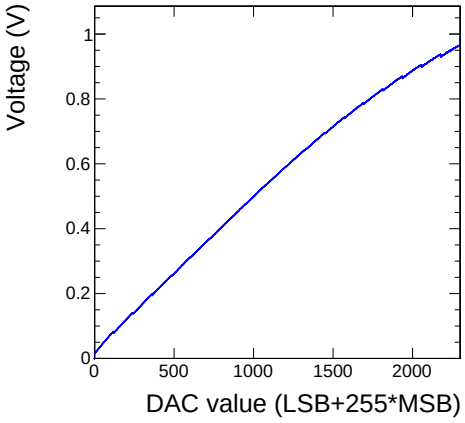

Figure 4.3: Graph of the measured linearised `threshold` voltage output of CLICpix2 planar sensor assembly 16.

MSB values are calculated to make the voltage output linear for all input values. The equation used for the `threshold` DAC in the Peary DAC software is presented below, where *input_threshold* is the input value from the user:

$$\begin{aligned} \texttt{threshold_LSB} &= (\text{input_threshold } \textit{mod } 121) + 64 \\ \texttt{threshold_MSB} &= \text{floor}(\text{input_threshold}/121) \times 14 \end{aligned} \tag{4.1}$$

For the `test_cap_1` DAC the equation below is used:

$$\begin{aligned} \texttt{test_cap_1_LSB} &= (\text{input_threshold } \textit{mod } 121) + 84 \\ \texttt{test_cap_1_MSB} &= \text{floor}(\text{input_threshold}/121) \times 14 \end{aligned} \tag{4.2}$$

An example graph showing the response of the linearised `threshold` DAC using Equation 4.1 is shown in Figure 4.3.

4.2 Initial testing

The first step when receiving a new CLICpix2 planar assembly from the manufacturer was to check the assembly responsiveness. This included testing that the device could be powered, responded to commands such as writing and reading DAC values, and that noise hits could be acquired given a low enough hit detection threshold. Once the functionality was verified, the following tests and measurements were carried out to determine the basic properties of the assembly: visual inspection of X-ray images, I-V response of the ASIC, and equalisation of the local threshold across the matrix. In this section, each of these tests are described in turn and the results summarised.

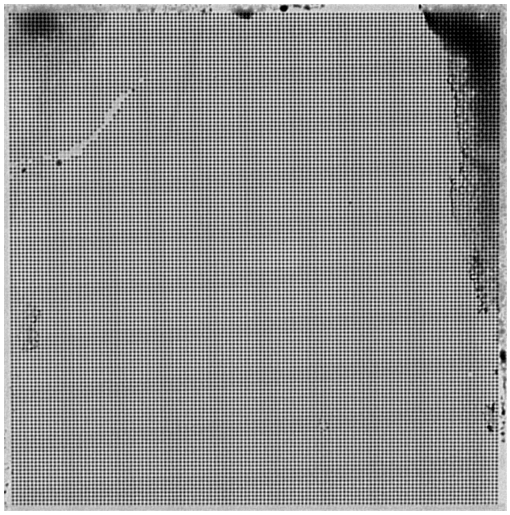

Figure 4.4: X-ray image of CLICpix2 assembly 16, provided by the manufacturer [62].

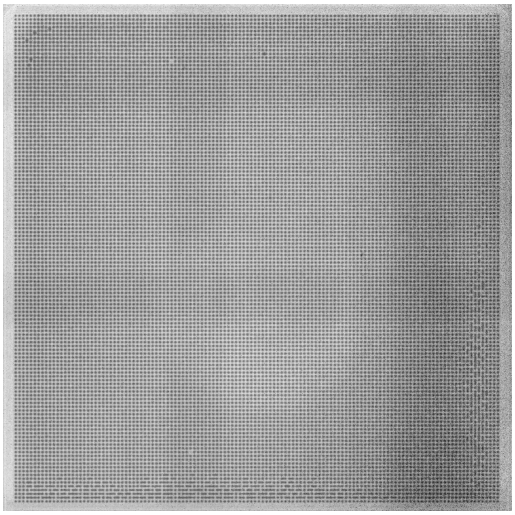

Figure 4.5: X-ray image of CLICpix2 assembly 19, provided by the manufacturer [62].

4.2.1 X-ray imaging

The manufacturer provided X-ray images of each assembly, made after the flip-chip bonding process described in Section 3.3. To create these images, the assemblies were exposed to a source of X-rays and the photon attenuation was measured after they passed through the sample. Individual solder bumps are visible in these pictures, therefore any irregular bumps can be identified and counted by eye, such as those with an abnormal radius, that have merged, or are missing [8].

An example X-ray image is shown in Figure 4.4 for assembly 16. The majority of the pixel matrix has visible solder bumps on the pixel pads, showing a high deposition yield. Identifiable features include a section of missing solder bumps in the top left-hand corner consisting of approximately 40 pixels, thought to have been peeled off during handling of the assembly due to low adhesion. The large dark areas around the edges of the image were probably caused by polymeric residues between the solder bumps and are not thought to effect the bonding quality of the assembly, however they obscure the visual analysis in the affected regions. A small number of missing or merged bumps can be identified, collectively less than 1% of the total number of pixels.

X-ray images for assemblies 19, 20, and 21 are presented in Figures 4.5, 4.6, and 4.7 respectively. Similar to assembly 16, high bump yields are observed across the matrices. The large grid pattern of the carrier gel pack can be seen in these images, which is not a feature of the devices themselves but the material underneath the ASIC. A small number of merged bumps are located on the bottom and right-hand sides of assembly 19, while missing bumps can be identified in the top-right corner of assembly 21. The X-ray images of the remaining assemblies are shown for reference in Figures A.1 to A.4.

The number of irregular bumps identified for all assemblies are a small percentage of the total number, indicating a high yield of deposited bumps despite the small pixel pitch.

4.2.2 I-V characteristics

Measuring the sensor leakage current of each assembly as a function of applied bias voltage (I-V) determines the voltage range over which it can be safely operated, as discussed in Section 1.3.1.1. During an I-V measurement, the negative voltage applied across the sensor of the CLICpix2 device was decreased from 0 V in steps of -1 V and the current recorded. Applying a high bias voltage can cause a breakdown of the silicon sensor to occur, therefore a limit was set such that the current could

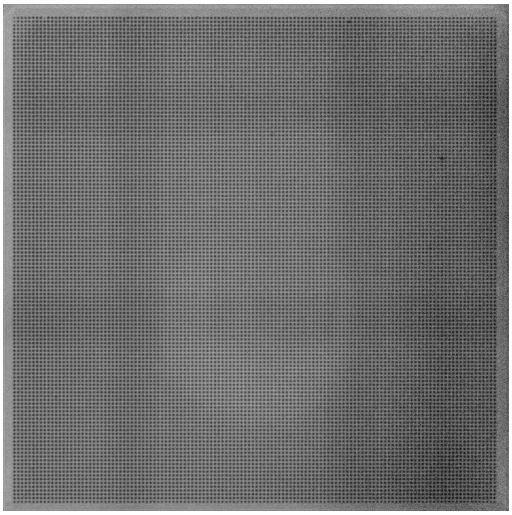

Figure 4.6: X-ray image of CLICpix2 assembly 20, provided by the manufacturer [62].

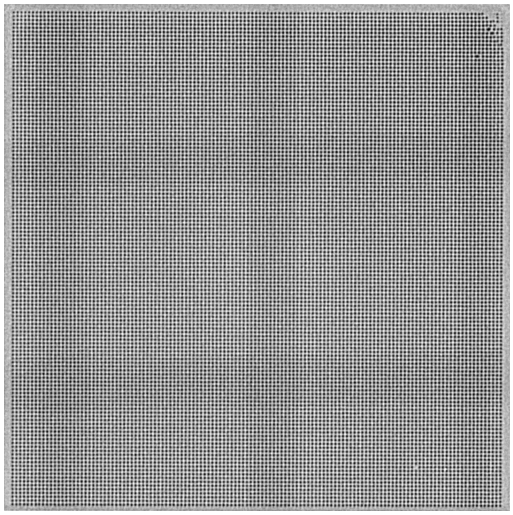

Figure 4.7: X-ray image of CLICpix2 assembly 21, provided by the manufacturer [62].

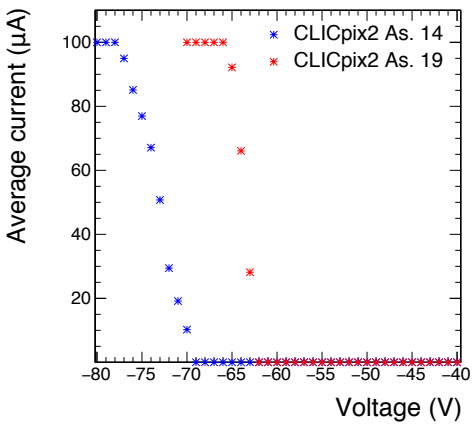

Figure 4.8: IV curve for CLICpix2 planar sensor assemblies 14 and 19, where the current limit of 100 µA was reached at a bias voltage of −78 V and −66 V respectively.

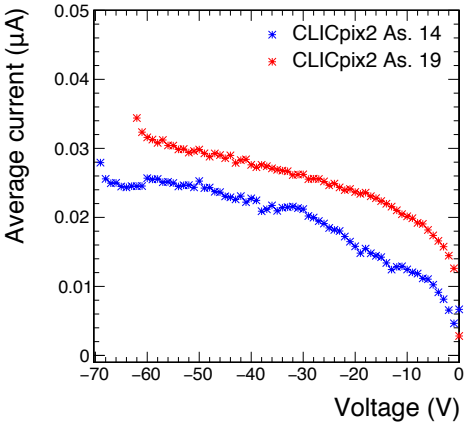

Figure 4.9: IV curve for CLICpix2 planar sensor assembly 14 and 19, zoomed into the low current range.

not exceed 100 µA. This measurement was repeated five times per assembly and an average current was calculated for each bias voltage. As the breakdown voltage can be affected by temperature, the laboratory was maintained at a temperature of approximately 22 °C using an air-conditioning unit.

Figure 4.8 shows the I-V curves obtained for assemblies 14 and 19. The measured current increases as the magnitude of the voltage increases, quickly at first and then with a smaller slope between the voltages of −10 V and −60 V. For assembly 19 the current rapidly increases at −62 V, reaching the current limit at a bias voltage of −66 V. Assembly 14 reached the current limit at a voltage of −78 V. The maximum operational bias is the maximum voltage at which the device can be operated, which includes a margin of safety. The majority of CLICpix2 planar sensor assemblies are determined to have a maximum operational bias voltage of −60 V.

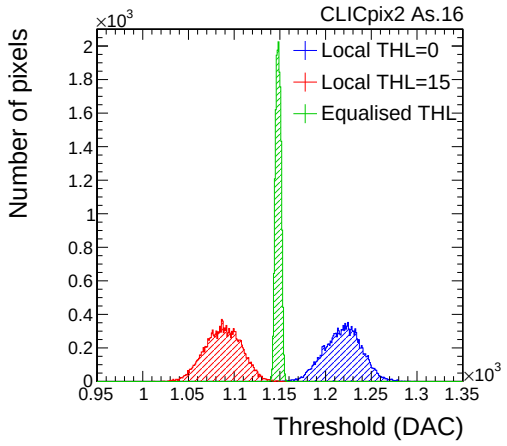

Figure 4.10: Equalisation measurement of CLICpix2 planar sensor assembly 16 with an applied bias voltage of −60 V.

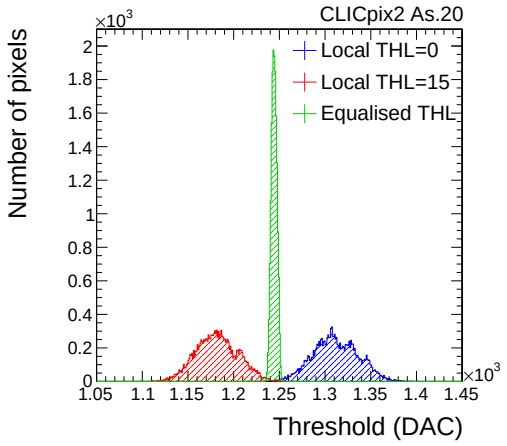

Figure 4.11: Equalisation measurement of CLICpix2 planar sensor assembly 20 with an applied bias voltage of −60 V.

4.2.3 Pixel equalisation

Variations of the electronics and manufacturing of each pixel can cause differences in their performance within the matrix [8], as discussed in Section 1.3.2.1. This can impact certain parameters, most importantly the threshold level of each in-pixel discriminator causing a wide difference in pixel response to incident particles. Equalisation minimises the dispersion of the effective threshold across the matrix so the chip has a more uniform behaviour. This is achieved by adjusting the local threshold per pixel, where the effective threshold of a pixel is a summation of the global and local thresholds.

The method described in [65] was employed to determine the equalised settings. The local threshold of each pixel in the matrix was first configured to its lowest setting (0) and data was acquired for a scan of the global `threshold` DAC. At a certain `threshold` in this scan, the baseline level of the pixel crosses the applied threshold and the pixel starts recording noise hits. This point is named the 'turn-on' threshold of this pixel, and as the threshold decreases an increasing number of pixels pass their respective turn-on points. Once all functional pixels in the matrix have reached their turn-on threshold, as the threshold decreases further it moves away from the baseline level causing the number of hit pixels in the matrix to decrease. The resultant distribution is expected to be Gaussian-like if no problems are present, as shown in blue in Figure 4.10 for assembly 16. The same process was then carried out for when the local threshold values were all set to their highest value (15), shown in red in Figure 4.10.

The mean value of a Gaussian fit to these distributions represents the most common turn-on threshold of the pixel matrix for these settings. Measuring the width of the Gaussian function represents the threshold dispersion of this device with these settings, caused by pixel-to-pixel variations between readout channels. The mid-point between the low and high local threshold distributions is the target baseline of the device, which is a threshold of 1148 DAC values for assembly 16.

Assuming a linear response between the lowest and highest local thresholds, the equalised local threshold is the setting that makes the turn-on point of the pixel closest to the baseline. If this linear interpolation failed for a pixel, due to it having a large noise or being unresponsive, it was masked in the matrix configuration file by the equalisation algorithm. Performing the threshold scan using the calculated local threshold settings resulted in an equalised distribution, shown for assembly 16 in green in Figure 4.10 and as a 2D map in Figure 4.12. The equalised distribution has a smaller

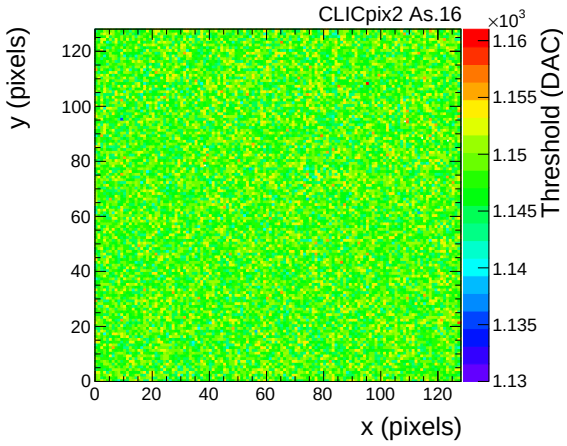

Figure 4.12: 2D map of turn-on threshold for CLICpix2 planar sensor assembly 16 with an applied bias voltage of −60 V, using equalised matrix settings.

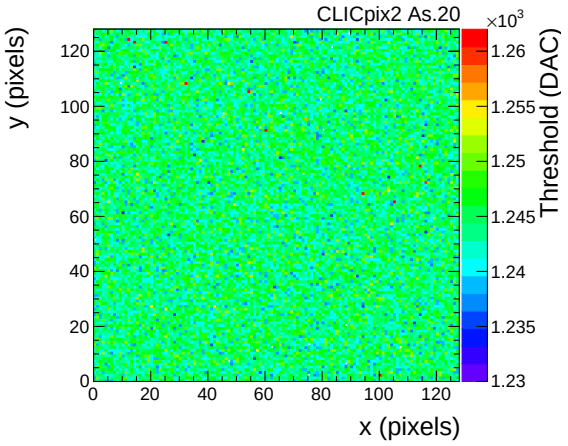

Figure 4.13: 2D map of turn-on threshold for CLICpix2 planar sensor assembly 20 with an applied bias voltage of −60 V, using equalised matrix settings.

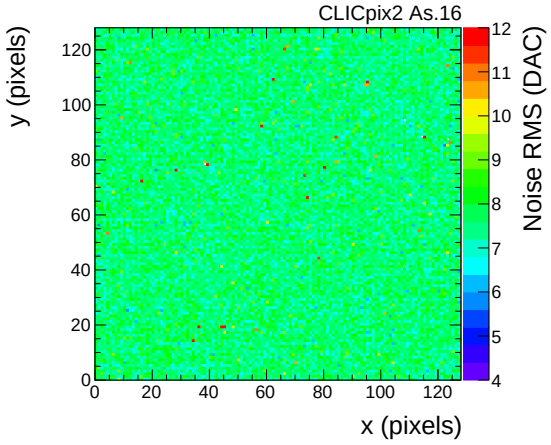

Figure 4.14: 2D map of the noise RMS width for CLICpix2 planar sensor assembly 16 with an applied bias voltage of −60 V, using equalised matrix settings.

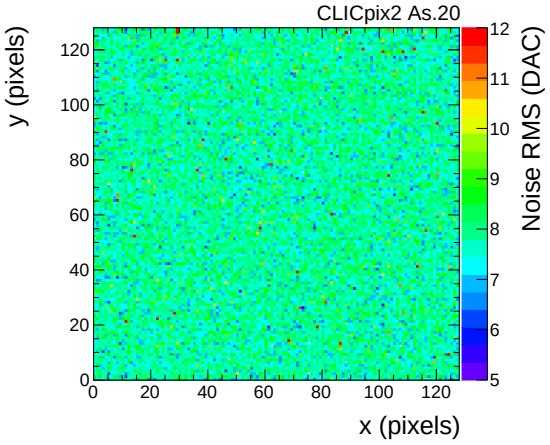

Figure 4.15: 2D map of the noise RMS width for CLICpix2 planar sensor assembly 20 with an applied bias voltage of −60 V, using equalised matrix settings.

width, therefore the threshold dispersion is reduced but not eliminated entirely. In general, threshold dispersion can not be reduced to zero due to contributions from the electronic noise of pixel circuits [8] and the limited accuracy of the local threshold adjustment. In the 2D map, the equalised turn-on threshold is approximately uniform and has no observed structure across the matrix, with only a small number of localised outliers. Figure 4.14 shows the RMS width of the noise distribution for assembly 16 as a 2D map. The noise is approximately uniform across the matrix with negligible outliers.

It should be noted that the threshold equalisation method described could be further optimised

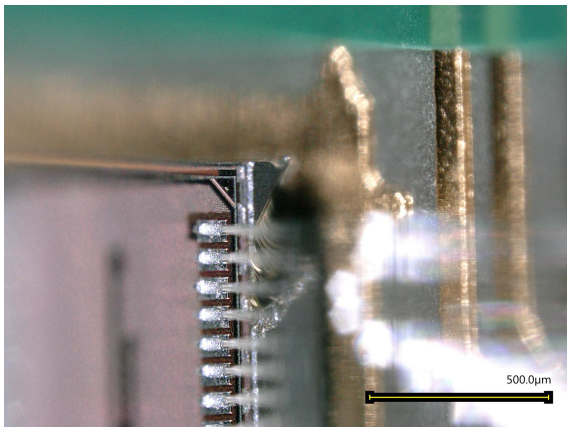

Figure 4.16: Microscope image of the damaged region of the ASIC of CLICpix2 planar sensor assembly 18.

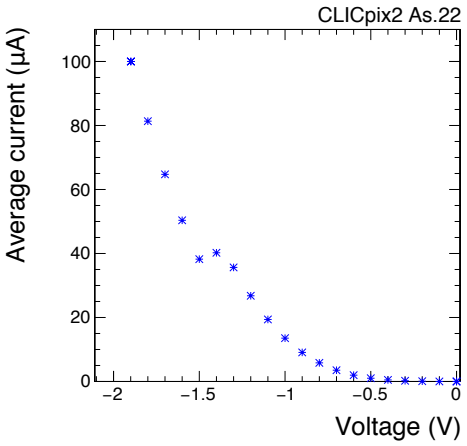

Figure 4.17: IV curve for CLICpix2 planar sensor assembly 22.

by repeating the threshold scan multiple times for both local settings and calculating an average turn-on threshold. By only measuring the turn-on threshold once per pixel, noise could effect the measurement and cause the baseline to be measured at a higher DAC value.

The operational threshold of the assembly can also be determined from the equalised peak. A global threshold value more than 5σ above the baseline is chosen, such that only a small number of noisy pixels were observed and any decrease of the global threshold causes a large increase in noise. These noisy pixels were masked by the user.

Figures 4.11, 4.13, and 4.15 show the equalisation results for assembly 20.

4.2.4 Summary of initial laboratory testing results

Nine CLICpix2 ASICs bump-bonded to planar, active-edge silicon sensors, as described in Subsection 3.1.1, were tested with the methods described. Seven assemblies function well in the initial testing by being responsive and having a high bump yield in X-ray images, a high magnitude breakdown voltage, and equalised local threshold settings. Table 4.1 summarises the initial testing results for each assembly.

All functional assemblies with Advacam sensors have a high average noise level and therefore higher threshold dispersion. Assembly 19 also displays a high noise occupancy by the large number of pixels masked by the equalisation algorithm, due to the linear interpolation failing. The cause of the noise in each assembly is unclear from these tests, therefore the behaviour needed to be investigated with further measurements.

Assembly 18 was found to be unresponsive as no pixel hits could be recorded with the device over a wide range of thresholds. Since the digital processes of the assembly are fully functional, namely the VDDA and GND, it is thought that a small piece of damage on the CLICpix2 ASIC had affected the analogue power and ground, as shown in Figure 4.16. No initial testing beyond this point could be performed, therefore this assembly is not included in Table 4.1.

Meanwhile, assembly 22 had a high leakage current level during I-V testing compared to other devices, as shown in Figure 4.17. The current limit of 100 µA was reached with a bias voltage of -1.8 V. Due to substantial areas of noisy pixels when powered, an operational voltage of -0.4 V was

determined. The assembly had to be equalised while the sensor was unbiased to obtain a Gaussian-like distribution. With this low maximum operational voltage, the depleted region of the silicon sensor is likely be too thin to detect incident particles. The number of noisy pixels and small depletion depth makes it difficult to identify the cause of the high current drawn by this assembly. This is undesirable as assembly 22 was the only CLICpix2 ASIC bump-bonded to a 50 µm sensor, an interesting thickness for this study.

Due to these factors, assemblies 18 and 22 were not subject to any further laboratory testing.

In the following sections, all data has been recorded using the maximum operational bias voltage, operational threshold, and an equalised matrix configuration unless otherwise stated.

4.3 Pixel categorisation

Seven assemblies passed the initial testing, therefore detailed information could be collected on how each pixel responds to input charge. To assess this, a data-driven categorisation system was devised to classify the response of each pixel. These categories combine the results of the previously described threshold equalisation and two other measurements: test pulse injection and radioactive source exposure. This combination allows the response of the pixels to charge deposited by an incident particle and injected into the ASIC frontend to be determined separately, isolating the cause of any observed issues.

4.3.1 Radioactive source exposure

The behaviour of the CLICpix2 assemblies to ionising particles entering the planar sensor was investigated by placing a Strontium-90 radioactive source above each device, obtaining pixel hits across the matrix. The source emits β^- particles of an energy of 0.546 MeV as it decays into Yttrium-90 [20]. Placing the source approximately 15 cm above the pixel matrix ensured that the pixel hits were evenly distributed across the matrix, as is required to properly determine the assembly characteristics. The readout system described in Section 4.1 was used for the measurements. Each exposure was 5-6 hours long to gain sufficient statistics, approximately 100 hits per pixel.

Using the acquired data, the response strength of each pixel is determined from the recorded number of hits. A 1D histogram of recorded above-threshold signals per pixel during the exposure is created, and an example is shown in Figure 4.18 for assembly 20. As a width of $\sqrt{N}$ is expected for a perfectly uniform source illumination, this distribution is fit with a Gaussian function. Most pixels are expected to be within 3σ of the fit mean, therefore any tails above and below the 3σ cut corresponds to pixels deemed to be 'high rate' or 'low rate' respectively. A Gaussian distribution contains 99.7% of the entries within a $\pm 3\sigma$ interval around the mean, therefore in a perfect assembly 25 pixels are expected to be high rate and 25 to be low rate. If the number of high rate pixels is higher than 25, this indicates that the pixels are either noisy and should be masked, electrical shorts between pixels cause additional hits in the pixel, or the charge sharing between pixels is non-uniform in the region. A larger number of low rate pixels could be due to non-linear charge sharing effects, an issue with the sensor in the region, or a problem with the interconnect quality for this pixel.

In Figure 4.18, the Gaussian function has a mean value of 105.1 pixel hits and a sigma of 13.5, and this figure shows the hit rate at which the 3σ cut-off lines occur for this assembly. Using the 3σ range, 255 pixels are classified as high rate and 371 are deemed to be low rate for assembly 20. A small peak at zero is observed in this histogram, corresponding to masked pixels, pixels with missing bumps, or pixels with a non-functioning front-end.

Figure 4.19 presents the hit rate recorded by assembly 15 during a similar Strontium-90 radioactive source exposure. For this assembly a large number of pixels are high rate due to a large tail to

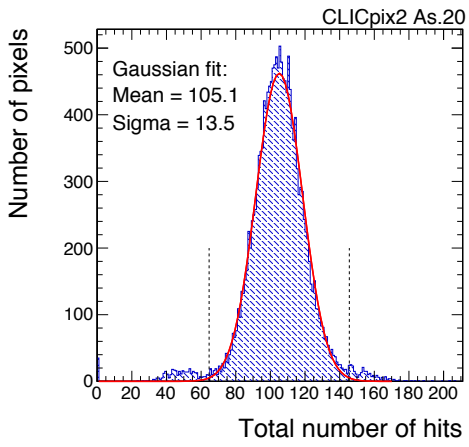

Figure 4.18: Histogram of the hit rate observed for a radioactive source measurement using CLICpix2 planar sensor assembly 20 with nominal operational threshold and bias voltage applied. The dashed lines indicate a region of $\pm 3\sigma$ around the mean of the Gaussian fit.

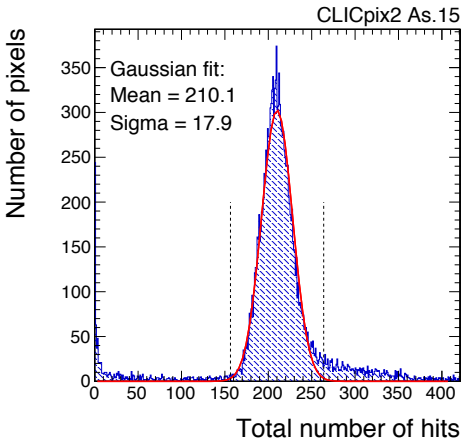

Figure 4.19: Histogram of the hit rate observed for a radioactive source measurement using CLICpix2 planar sensor assembly 15 with nominal operational threshold and bias voltage applied. The dashed lines indicate a region of $\pm 3\sigma$ around the mean of the Gaussian fit.

Table 4.1: Summary of initial testing results of CLICpix2 planar sensor assemblies. The threshold equalisation results of assemblies 16 and 20 can be found in units of e^- in Table 4.3.

Assembly number	**Sensor type**	**Sensor thickness** (μm)	**Maximum operational bias voltage** (V)	**Baseline (DAC)**	**Operational threshold (DAC)**	**Threshold dispersion (DAC)**	**Average noise (DAC)**	**Number of masked pixels**
9	Advacam	100	-60	1187	1295	4.5	16.0	1
14	FBK-CMM	130	-60	1200	1250	2.4	5.4	50
15	Advacam	150	-60	1166	1235	3.6	8.0	71
16	FBK-CMM	130	-60	1148	1190	2.9	7.6	19
19	FBK-CMM	130	-60	1113	1190	3.1	7.8	270
20	FBK-CMM	130	-60	1244	1290	3.0	7.8	32
21	Advacam	100	-50	1184	1285	3.6	12.6	23
22	Advacam	50	-0.4	1183	1335	3.7	16.9	135

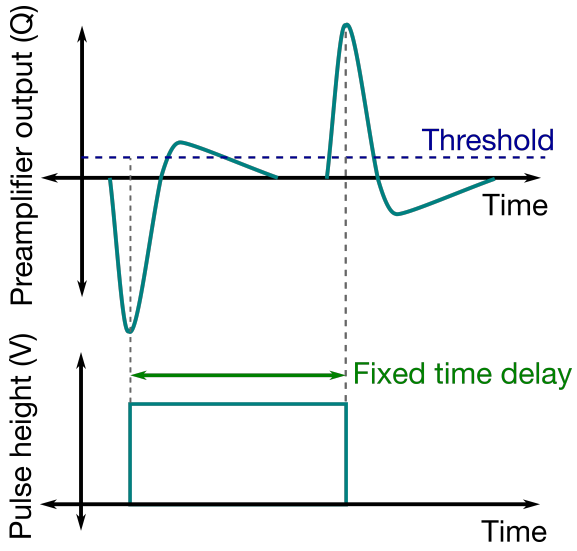

Figure 4.20: Diagram of test pulse generation using the test capacitor of CLICpix2, drawn not to scale. Charge pulses of equal magnitude are generated in both polarities. If the pulse height is large, significant secondary overshoot peaks are generated from charge conservation.

higher counts. In addition, a significant number of pixels recorded fewer than 5 hits and are therefore classified as low rate.

4.3.2 Test-pulse injection

Charge of a fixed magnitude was directly injected into the CLICpix2 ASIC frontends so that the ASIC response could be seen independently from sensor effects and the interconnect quality per pixel. This was achieved using the on-chip test-pulse generation mechanism, as described in the CLICpix2 user manual [7]. Charge collected over an internal test capacitor is directly injected into the pixel frontend. The voltage difference over the two plates of the test capacitor defines the magnitude of the generated pulse, configured using two DACs as described in Section 3.1.2.

Pulses are generated with both polarities by the capacitors discharge, such that one generated pulse consists of two peaks of opposite sign with a small delay period in between as illustrated in Figure 4.20. Due to charge conservation, an additional peak is created as an 'overshoot' after each initial pulse. This overshoot is of the opposite polarity and has a longer tail than the original injection, resulting in four separate peaks as seen in Figure 4.20. For large magnitude test pulses, the overshoot crosses the threshold level causing a count value of two to be recorded by the pixel.

During the test-pulse measurement, a series of 100 pulses were injected to each pixel in the CLICpix2 assembly. The pattern generator file was configured such that the capacitor was discharged once per acquisition window. Due to the large test-pulse height used, a hit count of 2 was expected per pixel from the positive polarity pulse and the overshoot peak from the negative polarity pulse. Only one pixel in each superpixel was pulsed at a time such that no adjacent pixels were pulsed simultaneously, so that any potential cross-talk between pixels could be observed.

By analysing the way different pixels responded to the injected charge, certain issues can be identified. Any pixels that do not record counts for over 90% of the test pulses injected are said to be 'unresponsive'. This can occur for many reasons, including the pixel readout being previously masked due to high noise or the pixel having a non-functional front-end. In addition to these ASIC specific considerations, the pixel could be electrically connected through solder bump-bonds or under bump metallisation (UBM) to a large number of pixels. The input signal is therefore shared between them, meaning that the charge within each pixel does not cross the detection threshold. During some

measurements pixels were found to record hit counts due to neighbouring pixels being pulsed. If this occurs ≥90% of the time that neighbouring pixels are pulsed then this indicates the presence of unwanted electrical connections between these pixels. The presence or absence of cross-talk can therefore be used to separate the ASIC response from the interconnect quality.

4.3.3 Categorisation of pixels

To better understand the performance of each assembly as a whole, the results from the described laboratory measurements are combined to classify pixels into six categories. These data-driven category definitions are detailed below. Each category used the taken measurements to separate the response of the ASIC from that of the bump-bonds and sensor. It should be noted that each pixel can only be in one category, with lower-numbered categories taking precedence.

1. Masked: Pixels of this category have been masked by the user due to observed large noise or during threshold equalisation as discussed in Subsection 4.2.3. No information is gathered from these pixels, therefore their response cannot be characterised further.

2. Unresponsive: Pixels in this category responded less than 10% of the time to direct charge injection.

3. Cross-talk: These pixels are measured to have hits due to cross-talk when one or more neighbouring pixels are pulsed ≥90% of the time, indicating an electrical connection between pixels caused by an interconnect issue.

4. Bonding or sensor issues: Pixels in this category were found to be low rate during source exposure but have the expected test pulse performance. These are said to have bonding or sensor issues, as these two causes could not be decoupled with the available information.

5. High rate: This set of pixels were found to have a high rate during a source measurement. This could be due to noise, electrical shorts, or a non-linear charge sharing region.

6. Expected response: The expected responses are seen in all tests for this pixel: normal test pulse response, normal rate from source measurement, no other issues identified.

The pixel categories are used to define the interconnect yield using the following formula:

$$Interconnect\ yield(\%) = \frac{N_6 + N_5}{128 \times 128 - N_1 - N_2} \tag{4.3}$$

where N_X is the number of pixels in category X. In this calculation, yield inefficiencies are only caused by pixels in categories three and four as these are related to bump-bonding issues. It should be noted that category two pixels can be caused by a large area of connected pixels as previously discussed, therefore formula 4.3 only applies to assemblies where this is not the case. This can be determined by ensuring the category two pixels are not in concentrated areas of the matrix and are not a significant percentage of the pixels total number of pixels (≤ 1%).

The results of the pixel classification for CLICpix2 planar sensor assemblies are summarised in Table 4.2 and shown in Figures 4.21, 4.22, 4.25 to 4.29. Assemblies 9 and 25 are not included in this table for the reasons discussed in Subsection 4.3.3.3.

4.3.3.1 Assemblies 16 and 20

The highest quality devices are assemblies 16 and 20, with the results seen in Figures 4.21 and 4.22 respectively. Pixels within category two are judged to be caused by unresponsive front-ends, and not interconnected large areas of pixels, by analysing the location and number of pixels. Therefore

Table 4.2: Summary of pixel categorisation results for CLICpix2 planar sensor assemblies. The CLICpix2 ASIC has a total of 16384 pixels.

CLICpix2 assembly:	**Assembly 14**	**Assembly 16**	**Assembly 19**	**Assembly 20**	**Assembly 21**
Sensor type and thickness:	FBK-CMM, 130 µm	FBK-CMM, 130 µm	FBK-CMM, 130 µm	FBK-CMM, 130 µm	Advacam, 100 µm
Category 1: Masked	50 (0.31%)	19 (0.12%)	270 (1.65%)	32 (0.20%)	23 (0.14%)
Category 2: Unresponsive	12 (0.07%)	157 (0.96%)	10 (0.06%)	2 (0.01%)	0 (0.00%)
Category 3: Cross-talk	23 (0.14%)	4 (0.02%)	359 (2.19%)	2 (0.01%)	8646 (52.77%)
Category 4: Bonding or sensor issues	11265 (68.76%)	57 (0.35%)	3 (0.02%)	344 (2.10%)	1306 (7.97%)
Category 5: High rate	200 (1.22%)	1212 (7.40%)	59 (0.36%)	247 (1.51%)	59 (0.36%)
Category 6: Expected response	4834 (29.50%)	14935 (91.16%)	15683 (95.72%)	15757 (96.17%)	6350 (38.76%)

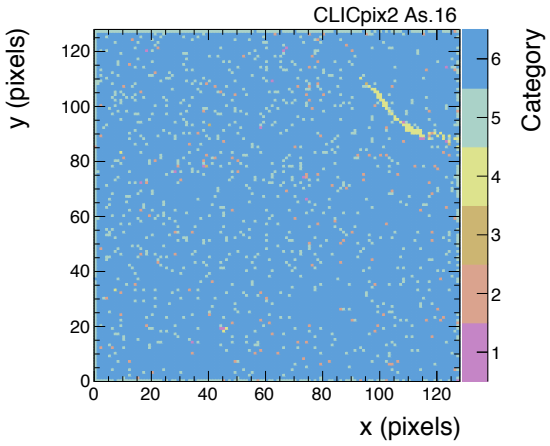

Figure 4.21: Pixel categorisation results for CLICpix2 planar sensor assembly 16 for nominal threshold and bias voltage.

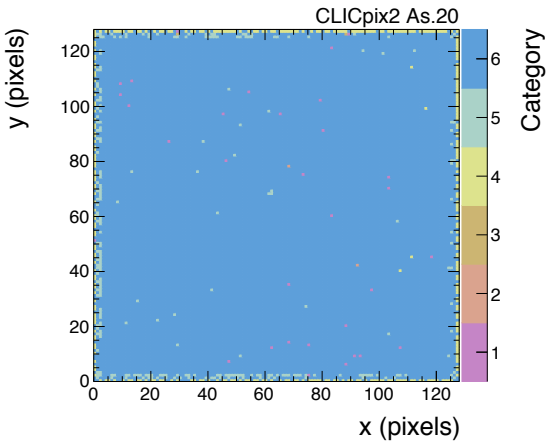

Figure 4.22: Pixel categorisation results for CLICpix2 planar sensor assembly 20 for nominal threshold and bias voltage.

formula 4.3 can be used to calculate interconnect yields of 99.6% and 97.9% for assemblies 16 and 20 respectively. The high interconnect yields verify the feasibility of single-chip bump-bonding using this method for small pixel pitches of 25 µm, despite the difficulty of depositing approximately 12 µm solder bumps onto pre-diced readout chips.

Although assembly 20 has approximately 300 pixels in category four, the lower signal received in these pixels and the number of category five pixels around the matrix edge are both thought to be caused by the active-edge of the sensor.

As presented in [60], the electric field lines of active-edge planar sensors extend directly from the sensor edge to the closest pixels and charge can be collected at full efficiency up until the physical sensor edge. For other pixels in the matrix, the electrical field lines are not distorted: a vertical line between the pixel implant and the bottom of the sensor, as expected for a planar sensor. The edge pixels collect charge efficiently over a larger volume of silicon than other pixels in the matrix and therefore could be expected to have a higher hit-rate during a uniform source exposure.

For a detector with a sensor and pixel pitch of similar size, the higher hit-rate would be expected to occur in the columns and rows at the immediate matrix edge. For a small pixel pitch of 25 µm and a larger sensor thickness of 130 µm, it could be expected by geometry that the charge collection from the active-edge would occur predominantly in the pixels 2nd or 3rd from the sensor edge. A pattern in the high-rate behaviour is expected between the 2nd and 3rd pixels from the matrix edge due to the staggered design of the active-edge, as shown in Figure 3.7. With the effect described, pixels at the immediate edge of the matrix would receive a lower amount of charge compared to the matrix average, while the columns or rows one to two pixels from the edge would receive higher amounts. The categorisation results of this assembly, Figure 4.22, show this exact effect.

To provide evidence for this hypothesis, assembly 20 was exposed to a source of X-rays from a copper target to create a uniform, high-statistics hit-map for the matrix. Figure 4.23 shows the result of the exposure as a 2D histogram of pixel counts. Around the matrix edge, a clear 'ring' of high-rate pixels can be seen in the 3rd row or column from the matrix edge. In the 2nd row or column from the edge, neighbouring pixels have higher and lower rates in a staggered pattern attributed to the staggered design of the active-edge. Finally, pixels directly at the matrix edge have the lowest hit-rate in the matrix. An additional observed effect are the groups of high-rate pixels at the matrix corners, thought to occur from a convolution of the edge effect from two side of the matrix. The lines

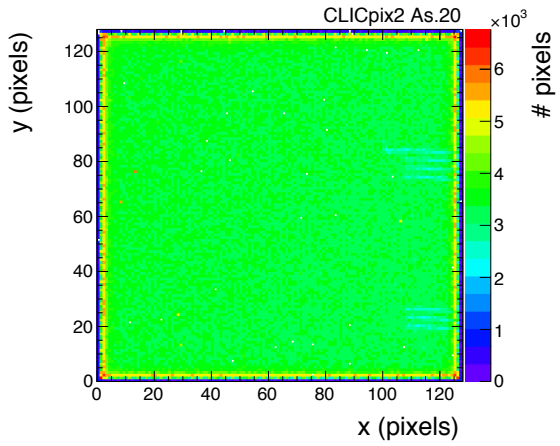

Figure 4.23: 2D histogram of pixel counts for CLICpix2 planar sensor assembly 20 when exposed to a source of fluorescence X-rays created using an electron beam incident on a copper target.

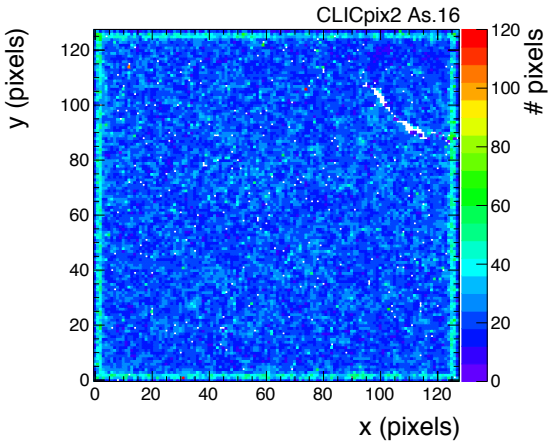

Figure 4.24: 2D histogram of pixel counts for CLICpix2 planar sensor assembly 16 when exposed to a particle beam from the CERN SPS facility [66].

seen on the right-hand side of the matrix are attributed to a reduced exposure of the sensor due to the wire-bonds to the readout Printed Circuit Board (PCB), as shown in Figure 3.1.

The results from the categorisation measurements and the X-ray exposure are in agreement, providing evidence that the edge effect comes from the active-edge of the sensor. This hypothesis can be further tested using reconstructed test-beam data, where a pattern in 2D efficiency or asymmetric tails in the residuals for pixel at the matrix edge would be corroborative evidence. Any effect from the active-edge is due to the sensor design, and therefore would not be considered a defect of the assembly.

The active-edge effect is not as apparent for assembly 16 in Figure 4.21 as it is for assembly 20. A number of category four pixels can be seen at the immediate edge of the matrix, with more present in column 128 than row 1. No ring of high-rate pixels are observed around the matrix edge, while this was present for assembly 20. The active-edge effect would not be seen clearly on the edges of any assemblies that have issues that effect the distribution of hit rates from the radioactive source exposure. A region of category four pixels is seen for assembly 16 in the top right-hand corner of the matrix, which corresponds to the region of missing solder bumps identified in Figure 4.4. These unresponsive pixels can affect the parameters of the Gaussian fit function to the hit rate histogram. To verify that the active-edge effect is observed for assembly 16, it was exposed to a particle beam provided by the CERN Super Proton Synchrotron (SPS) test-beam facility described in detail in Chapter 5. Using this high-rate particle beam with a uniform profile across the sensor, the active-edge effect is clearly observed in a 2D histogram of particle counts as seen in Figure 4.24.

The categorisation scheme employed correctly identified missing pixels, an effect from the staggered active edge of the planar sensor, and pixels that respond as expected.

4.3.3.2 Assemblies 19 and 14

Assembly 19 is also found to have a large percentage of pixels in category six, however a number pixels with cross-talk are also identified. As seen in Figure 4.25, the noisy regions of assembly 19 are located along the bottom and right edges of the matrix. This correlates with the X-ray image of this

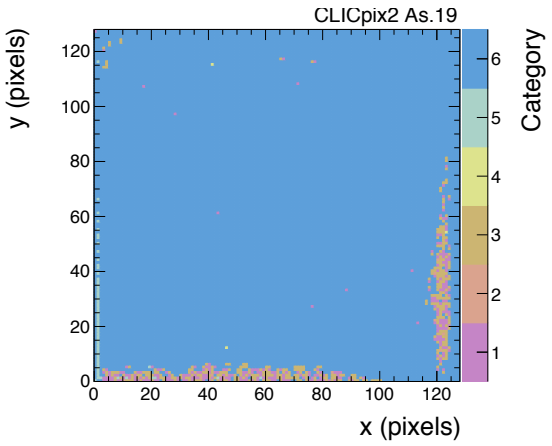

Figure 4.25: Pixel categorisation results for CLICpix2 planar sensor assembly 19 for nominal threshold and bias voltage.

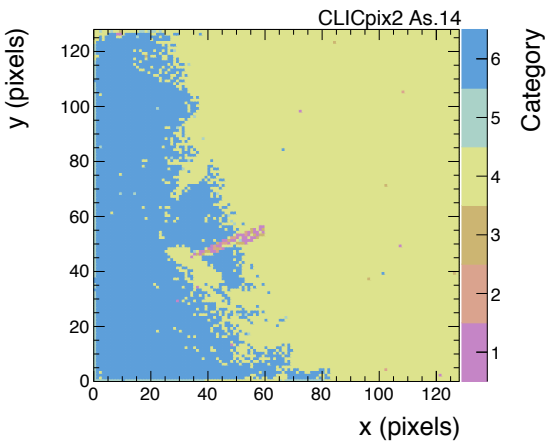

Figure 4.26: Pixel categorisation results for CLICpix2 planar sensor assembly 14 for nominal threshold and bias voltage.

device, Figure 4.5, as it shows connected solder bumps in these two areas. Due to the shorted areas, a non-Gaussian hit-rate distribution is obtained from radioactive source exposure, explaining why the number of pixels in category four is lower than the expected 25.

Figure 4.26 shows the 2D categorisation results of assembly 14, where the left-hand side responds as expected but the rest of the matrix is placed into category four with a distinct separation in between. These results suggested that assembly 14 has a gradient in height between the ASIC and sensor layers, where for a region of the matrix the gap between the sensor and ASIC is larger than the solder bump diameter. The effect is likely due to an uneven pressure being applied during bonding, causing the region of unconnected bumps. To improve the hybrid bonding procedure this information was communicated to the manufacturer and the process parameters adapted accordingly, though the handling difficulties of single-chip bump-bonding remained. The well-connected left-hand side of the matrix performs well and the active-edge effect identified for assembly 20 can also be seen on this side. In addition, a region of masked and unresponsive pixels is observed on the matrix and, by comparison with the X-ray images, a collection of merged solder bumps is identified as the cause.

It is unclear from the categorisation results of assemblies 14 and 19 if the active-edge effect around the matrix edge is present due to the noise and bonding issues discussed. To observe the effect, each assembly was exposed to a particle beam and a 2D histogram of counts was created. In Figure 4.27 the active-edge effect on the number of pixel counts can be seen on the left-hand side of the matrix, as well as the well-bonded regions of the matrix top and bottom. The effect is also seen for assembly 19 in Figure 4.28 along the matrix edges not affected by the two noisy regions.

4.3.3.3 Assemblies 9, 15 and 21

Considering the assemblies with Advacam sensors, a large percentage of pixels with cross-talk are present in assembly 21, while assemblies 9 and 15 are not included in Table 4.2 as the full categorisation testing was not performed on these devices. In consultations with the manufacturer, a concern was raised that the NiAu UBM material used on the planar silicon sensors from one of the sensor producers would be incompatible with the bump-bonding process foreseen to be used, as described in Section 3.3.

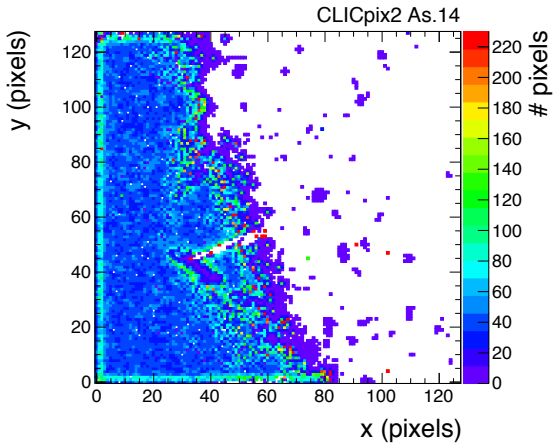

Figure 4.27: 2D histogram of pixel counts for CLICpix2 planar sensor assembly 14 when exposed to a particle beam from the CERN SPS facility [66].

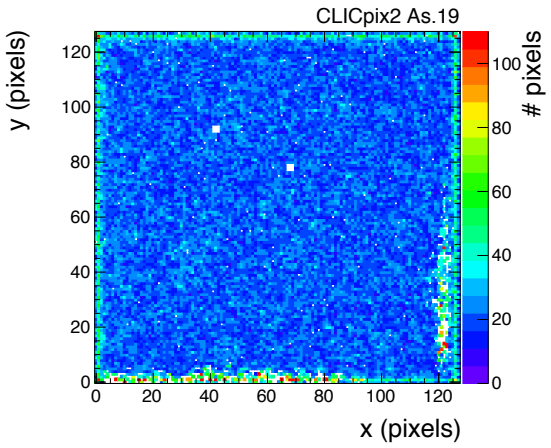

Figure 4.28: 2D histogram of pixel counts for CLICpix2 planar sensor assembly 19 when exposed to a particle beam from the DESY II facility [67].

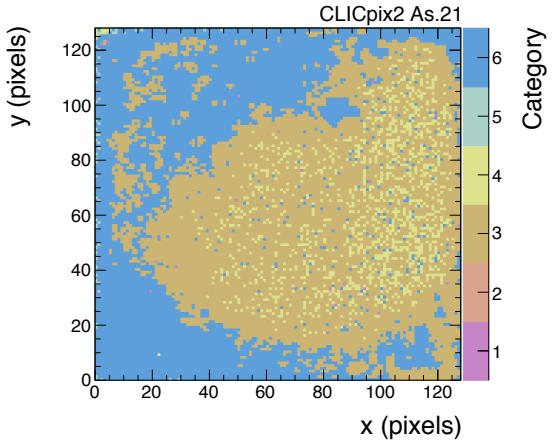

Figure 4.29: Pixel categorisation results for CLICpix2 planar sensor assembly 21 for nominal threshold and bias voltage.

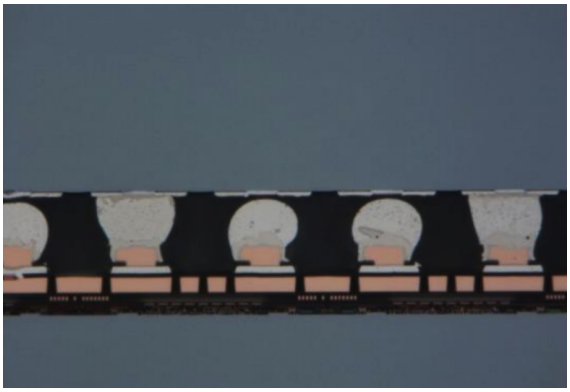

Figure 4.30: Solder bump cross-section of CLICpix2 planar sensor assembly 9 showing three unconnected bumps, provided by the manufacturer [62].

To verify these conclusions, both laboratory measurements and cross-sectional images were used to assess the outcome of the bump-bonding for these assemblies. The cross-sectional image of assembly 9 shown in Figure 4.30 displays solder bumps over five pixels near the centre of the matrix. Three of these solder bumps have an approximately spherical shape, compared to the column-like profile expected for well connected bumps, as discussed in Section 1.4.

By studying the metallurgy of the sample, the combination of SnAg solder and NiAu UBM materials used for these samples is likely to have caused the misshapen bump bonds. Due to the formation of an unwettable surface during the bonding process, no soldering has occurred for these bumps and,

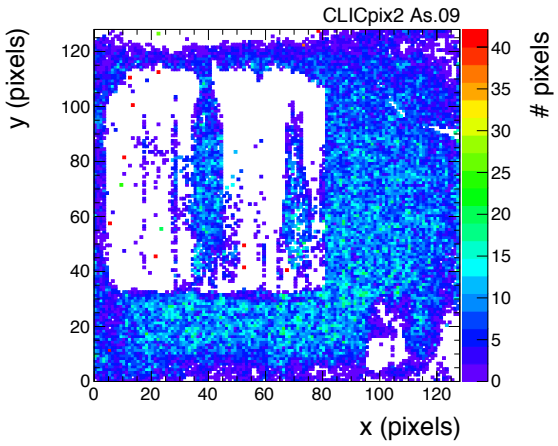

Figure 4.31: 2D hit map of pixel counts from a Sr-90 source exposure measurement of CLICpix2 planar sensor assembly 9 for nominal threshold and bias voltage.

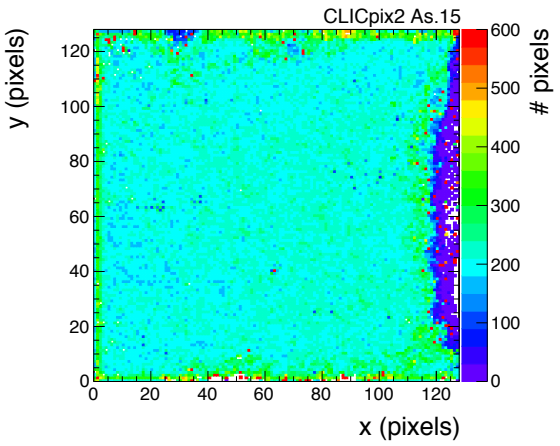

Figure 4.32: 2D hit map of pixel counts from a Sr-90 source exposure measurement of CLICpix2 planar sensor assembly 15 for nominal threshold and bias voltage.

despite any physical contact to the opposing pixel pad, no metallic contact has been made.

These findings are corroborated by the radioactive source measurements of assemblies 9 and 15 shown in Figures 4.31 and 4.32 respectively. Regions with imperfect bump bonds do not record pixel hits from incident particles. Test-pulse measurements of assembly 21 identify an area of noisy pixels covering the centre and right-hand side of the matrix, seen in the categorisation results of this assembly in Figure 4.29. Given a large charge injection into one of these pixels, the entire affected area can record pixel hits simultaneously thus indicating that these pixels are all electrically shorted. These conclusions are consistent with the incompatible UBM hypothesis and therefore no further testing was carried out on these three assemblies.

By combining different laboratory measurement results, the categorisation method successfully describes and identifies unexpected behaviour of the devices. The large number of category six pixels for assemblies 16 and 20 verify the viability of single-chip bump-bonding at a pixel pitch of 25 µm. All identified issues related to bump-bonding were used as feedback to the manufacturer to improve the hybrid bonding process used.

4.4 Temperature stability studies

The measurements described in Section 4.3 aimed to characterise the response of individual pixels. By recording this data, the functionality of the CLICpix2 ASIC was also tested and any ASIC design issues could be identified. Such an issue was identified during these measurements by observing the variation of the voltage DACs with temperature. In this section the cause, implications, and mitigation of the dependence are discussed in detail.

4.4.1 Voltage DAC temperature dependence

During the previously discussed laboratory measurements, an inconsistent behaviour of the CLICpix2 ASIC was discovered. This concerns the output of the voltage DACs over time, and the effect was studied in detail for assembly 16. To investigate the issue, the voltage of every CLICpix2 voltage DAC was measured six times in quick succession each minute for nearly 2 hours, using the output pad

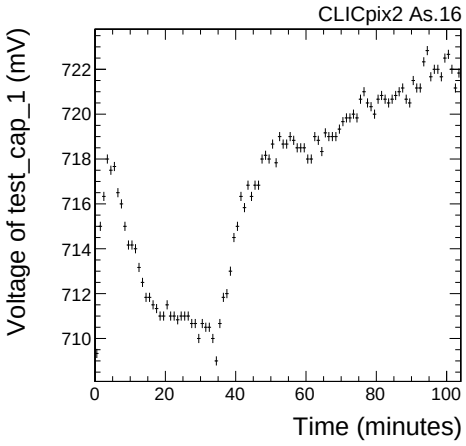

Figure 4.33: Graph showing the voltage of `test_cap_1` vs. time for CLICpix2 assembly 16 with nominal threshold and bias voltage applied.

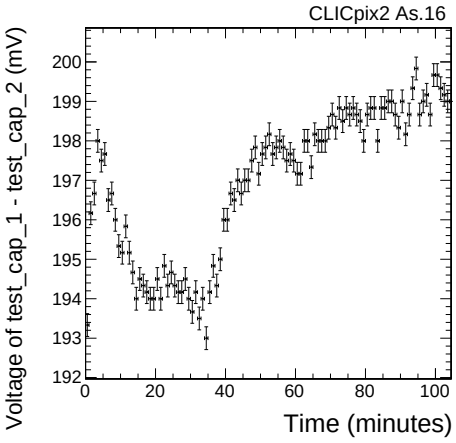

Figure 4.34: Graph showing the voltage of (`test_cap_1-test_cap_2`) vs. time for CLICpix2 assembly 16 with nominal threshold and bias voltage applied.

described in Subsection 3.1.2. All DACs were at their default settings as described in the CLICpix2 manual [7] apart from the following: `threshold` is 1190, and `test_cap_1` is 1400.

Figure 4.33 is a profile plot of the linearised `test_cap_1` DAC showing the recorded voltage measurement fluctuating over time. The uncertainties of the profile plots take into account the spread in Y of the data and the uncertainty of each measurement. As this DAC was set to a fixed value of 1400, the expectation is that it would be at a constant value within the uncertainty of the voltage measurement. A decrease is observed in the measured voltage approximately 5 minutes after an initial steep increase. The voltage then increases again after approximately 35 minutes, initially sharply and then with a smaller slope from 50 minutes onwards.

Voltage variations of the same shape and phase are observed for all other voltage DACs during the same data taking period, but with different magnitudes of fluctuation. In Figure 4.34 the difference between the linearised `test_cap_1` and `test_cap_2` DACs is shown over time. Although both DACs were set to fixed values, the voltage difference between them changes over time and the distribution mimics the shape seen in Figure 4.33.

All current DACs are stable during the same time period by measuring the voltage induced over a resistor with the CLICpix2 output pad.

The cause of the unexpected behaviour is deemed to be fluctuations in temperature. Figure 4.35 shows that the on-chip temperature measurement, described in Subsection 3.1.2, also follows the same fluctuation pattern and phase during the data taking. It should be noted that the temperature values shown have a granularity of $\pm 0.5\,^{\circ}\mathrm{C}$ and all temperatures are measured relative to the first recorded temperature of the measurement period. The profile plot shown includes uncertainties in Y that took into account both the spread and individual uncertainty of each temperature measurement, however the resultant uncertainty was very small for most points. During the approximately 2 hour measurement period, a window was opened in the measurement room after 5 minutes and closed 30 minutes later. The temperature decrease and increase in the room corresponds exactly in time to the decrease and increase respectively of the fluctuating DACs. The observed increase in temperature and voltage between 0 and 5 minutes is due to the chip heating up after being powered.

The reason for the temperature dependence was isolated using a transistor-level simulation of the CLICpix2 ASIC front-end [68]. The voltage DAC circuit in the CLICpix2 ASIC contains two

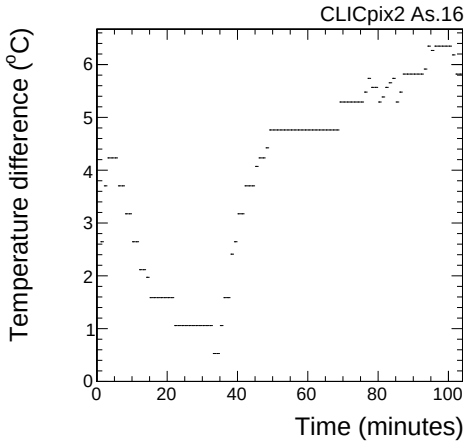

Figure 4.35: Graph showing the on-chip measured temperature vs. time for CLICpix2 assembly 16 with nominal threshold and bias voltage applied.

resistors, named R_{DAC} and R_{BIAS} for reference, such that the total resistance is proportional to $\frac{R_{DAC}}{R_{BIAS}}$. R_{DAC} is found to have a high temperature coefficient, meaning the resistance changes significantly with temperature change, and this coefficient is not the same value as for R_{BIAS}. Since the total resistance is proportional to their ratio, the mismatch in temperature coefficient causes an overall change in the resistance, and hence the voltage output, of the DAC with variations in chip temperature. From this conclusion, the current DACs of the chip are expected to be unaffected, as is observed in the data analysed. In this simulation a variation of approximately $1.5\,\mathrm{mV\,^{\circ}C^{-1}}$ is expected for the threshold DAC at its nominal setting, which is approximately ten times larger than if the discussed resistors had the same low temperature coefficient.

To better understand the CLICpix2 temperature dependence and verify its cause, the data described was used to calculate the temperature coefficient of each voltage DAC. Figure 4.36 shows the average measured `test_cap_1` voltage as a function of temperature, and Figure 4.37 shows the same for the `threshold`. By performing a linear fit to the data, a temperature variance of $(1.56 \pm 0.01)\mathrm{mV\,^{\circ}C^{-1}}$ is calculated for the threshold DAC, which is close to the simulated value. Using the same method, the `test_cap_1` voltage is calculated to change by $(2.24 \pm 0.01)\mathrm{mV\,^{\circ}C^{-1}}$. The value of these coefficients are dependent on the DAC setting and the assembly used.

4.4.2 Mitigation measures during CLICpix2 data taking

These findings have implications on data taken using a CLICpix2 device, whether in a test-beam or laboratory environment.

The global threshold applied to the pixel matrix is the voltage difference between the `threshold` and `vfbk` DACs. As the assemblies are mostly operated at the lowest threshold possible without entering the baseline noise, this voltage difference is very small and therefore has minimal temperature dependencies. For data where the threshold is scanned from low to high values, there would be a larger temperature coefficient for larger applied thresholds. If no external temperature changes occur, such as an open window or door, the laboratory has a stable temperature to within 1-5 °C due to an installed air-conditioning unit. When an additional fan is focussed towards the CLICpix2 assembly, the temperature variation of the device is found to reduce further.

Additional complications occur when performing test-pulse measurements. The magnitude of injected charge corresponded to the voltage difference between the `test_cap_1` and `test_cap_2`

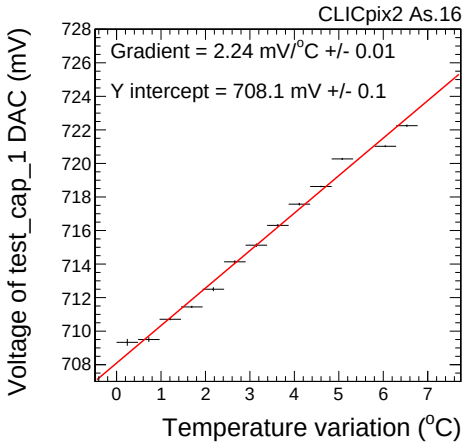

Figure 4.36: Graph showing the voltage of `test_cap_1` vs. temperature for CLICpix2 assembly 16 with a linear fit with nominal threshold and bias voltage applied.

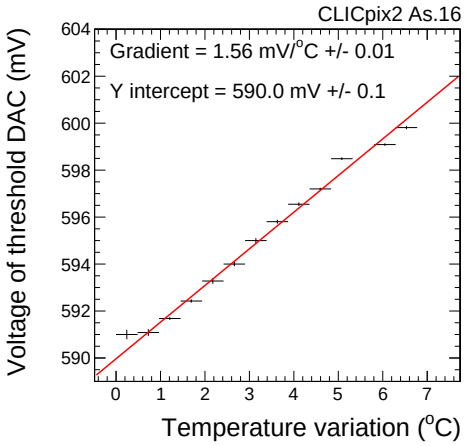

Figure 4.37: Graph showing the voltage of `threshold` vs. temperature for CLICpix2 assembly 16 with a linear fit with nominal threshold and bias voltage applied.

DACs. As seen in Figure 4.34, this voltage difference fluctuates with temperature. For the pixel categorisation tests, described in Subsection 4.3.2, the charge injection would always be large enough to pass the level of the threshold, even with the magnitude of fluctuations observed. Test pulse injection is used to measure if a pixel is unresponsive or recorded cross-talk, and this is minimally affected by a change in the charge injection magnitude above the threshold.

With all of these factors considered, the conclusions of the pixel categorisation scheme shown in Section 4.3 are deemed to be unaffected. For data taking where the temperature change of the environment is significant, the charge measurement is crucial, or the threshold is far from the baseline, precautions must be taken to ensure an approximately stable chip temperature.

4.5 Charge and threshold calibration

Comparisons of the amount of energy deposited in the sensor to theoretical expectations, simulations, or other pixel devices, requires the units of Time-over-Threshold (ToT) and threshold to be calibrated into physical units. In the following text, the methods used to calibrate the `threshold` DAC units using sources of X-rays, and to calibrate the units of ToT using test-pulse injection are described. Calibration was performed on the two best performing CLICpix2 planar sensor assemblies, numbered 16 and 20.

4.5.1 Threshold calibration

To determine the applied threshold in e^-, the assemblies were calibrated using photons of a well-defined energy from X-ray fluorescence, as shown in Figure 4.38 [69]. Inside of the X-ray machine, the incidence of an electron beam onto a primary target material produces X-rays. A secondary target material is exposed to these X-rays, creating fluorescence X-rays at the characteristic emission peaks of the target material. By measuring the fluorescence spectra of the secondary target material at different thresholds, the `threshold` DAC value corresponding to the spectral peak can be identified. This was then related to the expected emission energy in e^- from literature and a calibration factor of e^- per `threshold` was extracted for the CLICpix2 assembly used.

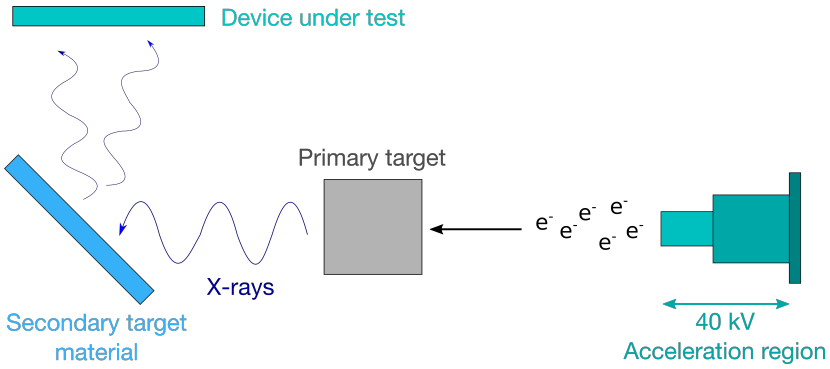

Figure 4.38: Schematic of the set-up used for X-ray fluorescence measurements, where the DUT is a CLICpix2 planar sensor assembly. Image from [70].

A Caribou data taking set-up and CLICpix2 planar sensor assemblies 16 and 20 were placed into the X-ray machine. The set-up was sealed inside the container of the machine and a fan was directed onto the CLICpix2 assembly to ensure minimal temperature variations during the performed measurements.

Using two secondary targets of iron (Fe) and copper (Cu), the fluorescence spectra of each material was measured by each CLICpix2 planar sensor assembly. For iron, the characteristic spectral K_α peak is expected to be at an emission energy of 6.4 keV. The characteristic peak for copper is expected at an energy of 8.04 keV [71]. Assuming that 3.65 eV would be needed to create an $e^- h^+$ pair in silicon [72], the K_α peaks of iron and copper correspond to 1753 and 2203 e^- respectively. During data taking, the `threshold` DAC was scanned from the baseline to higher thresholds and the number of counts recorded for each pixel. This scan was repeated ten times per target, and twice when no X-ray beam was incident.

For each target material, multi-pixel clusters are excluded to minimise the effects of charge sharing on the calculated calibration. Differences in the routing length between neighbouring columns of the pixel matrix, as discussed in Subsection 3.1.2, are expected to cause differences in the parasitic capacitance of odd and even columns. Analysing single-pixel clusters from odd and evenly numbered columns separately takes these differences into account. For odd and even columns, the data from each target material are combined into profile plots of single-pixel normalised counts as a function of the `threshold` DAC value. The resultant distributions for assembly 20 can be seen in Figures 4.39 and 4.40 for even and odd columns respectively. The green data points correspond to the pixel noise of the baseline when no X-rays were incident on the pixel matrix, while the Fe and Cu target data are shown in black and red respectively.

As the threshold increases, three effects occur: the total number of events decreases, the fraction of single-pixel clusters increases, the high change of hit-rate in the region of the spectral peak. From the baseline threshold, a linear increase in counts from the target materials is observed along the X axis which corresponds to the higher likelihood of single pixel clusters occurring at these higher thresholds. The maximum of each distribution is the location of the K_α peak for the target material. As the threshold increases to values higher than the peak, the number of pixels with deposited charge over the threshold level decreases causing a Gaussian-like curve over this region. These two effects caused the distribution seen in Figures 4.39 and 4.40, where the data at thresholds lower than the fluorescence peak was linear, and a Gaussian function describes the data at higher thresholds than the peak. This cause difficulties when determining the peak position using a fit function.

To isolate the Gaussian-like region of each dataset, a Gaussian function is fit over the high threshold range of each maximum. By adapting the fit range in X to minimise the χ^2 per number of degrees of freedom (NDOF) of each Gaussian function, a good fit to the peak and decreasing region was ensured. For the even columns of assembly 20, these maxima are located at `threshold` values of

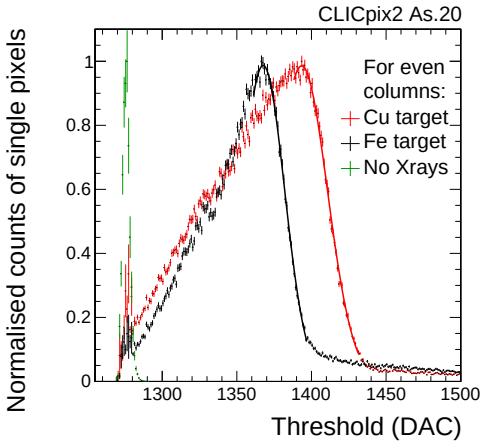

Figure 4.39: Histogram of the normalised average number of counts in even columns as a function of `threshold` value for CLICpix2 planar sensor assembly 20 at a bias voltage of -60 V. Three data sets are shown: X-ray fluorescence spectrum of a Cu target, X-ray fluorescence spectrum of a Fe target, and when no X-ray source present.

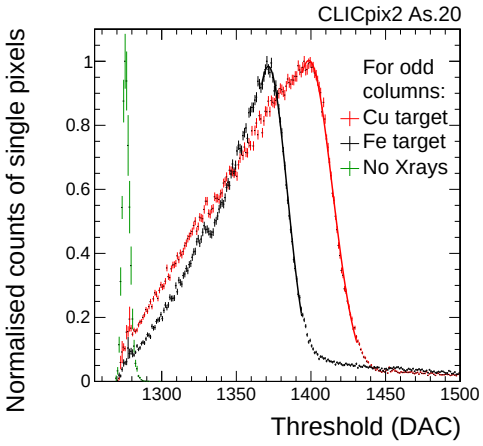

Figure 4.40: Histogram of the normalised average number of counts in odd columns as a function of `threshold` value for CLICpix2 planar sensor assembly 20 at a bias voltage of -60 V. Three data sets are shown: X-ray fluorescence spectrum of a Cu target, X-ray fluorescence spectrum of a Fe target, and when no X-ray source present.

(1367.6 ± 0.2) DAC and (1393.4 ± 0.2) DAC for the K_α peak of Fe and Cu respectively, where the quoted uncertainty is the error of the mean from the Gaussian fit function. When considering data from odd columns, the fluorescence peaks of the Fe and Cu targets are calculated to be at `threshold` values of (1371.4 ± 0.2) DAC and (1398.6 ± 0.2) DAC respectively. It should be noted that adapting the fit range of the Gaussian function changes the mean value, and the quoted uncertainties does not account for these fluctuations that are on the order of ± 1 DAC.

Similar data was taken for assembly 16 and these results are presented in Figures 4.41 and 4.42. The maxima are located at `threshold` values of (1266.9 ± 0.3) DAC and (1293.2 ± 0.3) DAC for the iron and copper target materials respectively for even columns of the matrix. For odd columns the maxima are located at (1269.3 ± 0.2) DAC and (1296.4 ± 0.2) DAC for copper and iron targets respectively.

A small maximum in the normalised counts is observed between `threshold` 1330-1335 DAC in Figures 4.39 to 4.42. As the 'bump' occurs at the same `threshold` for each assembly when using both target materials, this effect cannot occur from the X-ray photons themselves. No non-linearity of the `threshold` DAC voltage output is observed in the region of 1331 DAC. As the peak is assembly and target independent and does not occur near the K_α peak of any distribution, the impact of the maximum on the threshold calibration is small. The cause of the maximum was not investigated further.

Assuming that the baseline threshold of each device corresponds to an energy of 0 e^- with an uncertainty equal to the threshold dispersion, these three data points were plotted on a graph of energy in e^- against `threshold` DAC. The resulting plots for the two CLICpix2 assemblies tested are shown in Figures 4.43 to 4.46 for each column type. An uncertainty of ± 1 DAC is used for the mean values of the Gaussian functions to account for uncertainties arising from the fit range. Other sources of uncertainty, such as row variations in the threshold calibration, are unquantified and therefore not

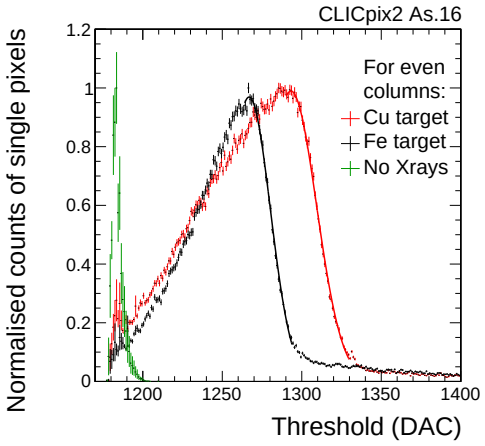

Figure 4.41: Histogram of the normalised average number of counts in even columns as a function of `threshold` value for CLICpix2 planar sensor assembly 16 at a bias voltage of −60 V. Three data sets are shown: X-ray fluorescence spectrum of a Cu target, X-ray fluorescence spectrum of a Fe target, and when no X-ray source present.

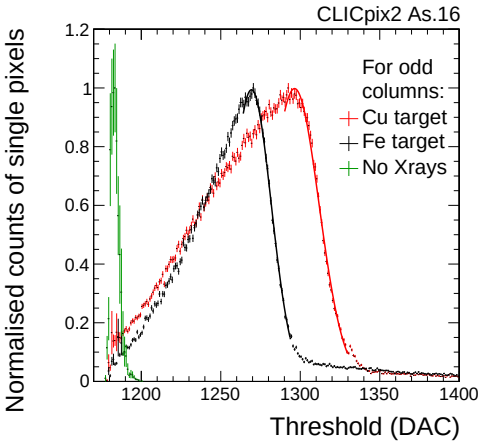

Figure 4.42: Histogram of the normalised average number of counts in odd columns as a function of `threshold` value for CLICpix2 planar sensor assembly 16 at a bias voltage of −60 V. Three data sets are shown: X-ray fluorescence spectrum of a Cu target, X-ray fluorescence spectrum of a Fe target, and when no X-ray source present.

Table 4.3: Threshold equalisation of CLICpix2 planar sensor assemblies 16 and 20 in units of e^-.

Assembly number	**Sensor type**	**Sensor thickness** (µm)	**Maximum operational bias voltage** (V)	**Operational threshold** (e^-)	**Threshold dispersion** (e^-)	**Average noise** (e^-)
16	FBK-CMM	130	-60	626 ± 8	43 ± 1	113 ± 2
20	FBK-CMM	130	-60	665 ± 9	43 ± 1	113 ± 2

included in this ±1 DAC range. Fitting a linear function to the data provides the desired calibration factor. However the uncertainty is unable to account for the non-linear offset of the data points, leading to χ^2 per NDOF values larger than 1. For assembly 16, calibration factors of (15.1 ± 0.2) e^-/threshold DAC and (14.7 ± 0.2) e^-/threshold DAC are calculated for even and odd columns respectively. For assembly 20, factors of (14.7 ± 0.2) e^-/threshold DAC and (14.2 ± 0.2) e^-/threshold DAC are obtained.

The operational threshold of the two calibrated assemblies can be converted into units of e^-. This calculation uses an average e^-/threshold DAC value, as well as the values in DAC from Table 4.1. Table 4.3 summaries the threshold equalisation results of CLICpix2 planar sensor assemblies 16 and 20 in units of e^-. It should be noted that the uncertainty values quoted take into account the average uncertainty in linear dependence between threshold and e^-.

4.5.2 Time-over-threshold calibration

The magnitude of charge deposited in a pixel is measured as the Time-over-Threshold in units of clock cycles using a frequency of 25 MHz, set using a clock divider setting of '2' and a 100 MHz

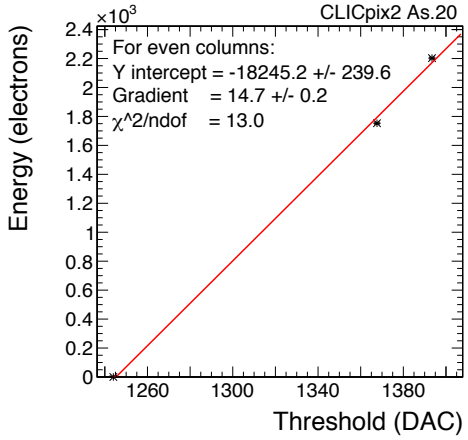

Figure 4.43: Graph of `threshold` value as a function of energy for the even columns of CLICpix2 planar sensor assembly 20 at a bias voltage of −60 V.

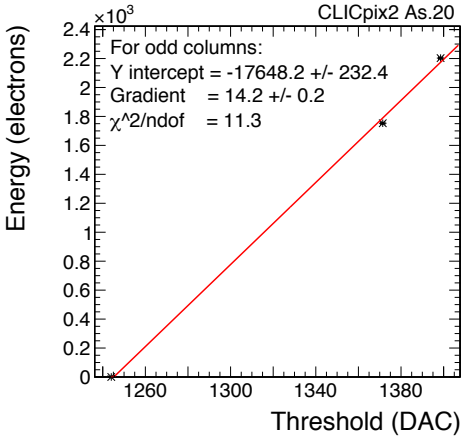

Figure 4.44: Graph of `threshold` value as a function of energy for the odd columns of CLICpix2 planar sensor assembly 20 at a bias voltage of −60 V.

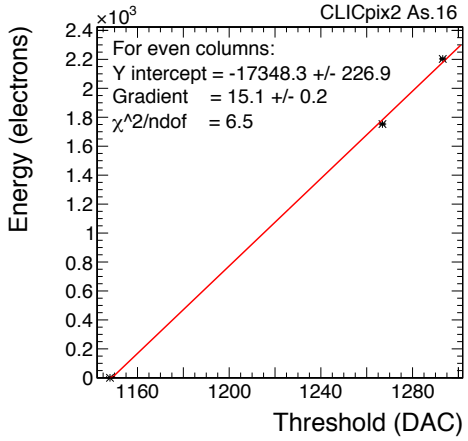

Figure 4.45: Graph of `threshold` value as a function of energy for the even columns of CLICpix2 planar sensor assembly 16 at a bias voltage of −60 V.

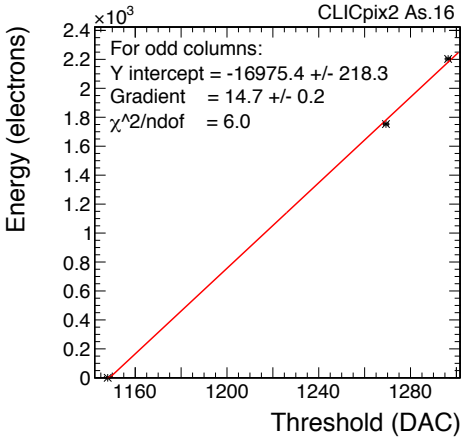

Figure 4.46: Graph of `threshold` value as a function of energy for the odd columns of CLICpix2 planar sensor assembly 16 at a bias voltage of −60 V.

clock frequency. These units ranged from 0 to 30 in the case of CLICpix2 [7], and are equal to an unknown number of e^- that differs pixel-to-pixel in the matrix.

To calibrate the charge per-pixel, a combination of test-pulse injection measurements and the previously calibrated threshold is used [69]. Firstly, the threshold value equal to a certain test pulse height is identified and used to determine an e^- per mV conversion factor for odd and even columns. Secondly, the ToT values recorded by each pixel for different injected pulse heights is measured for a fixed threshold value. This provided a ToT distribution for each pixel as a function of threshold voltage, which can then be converted into a calibration curve of ToT as a function of e^-.

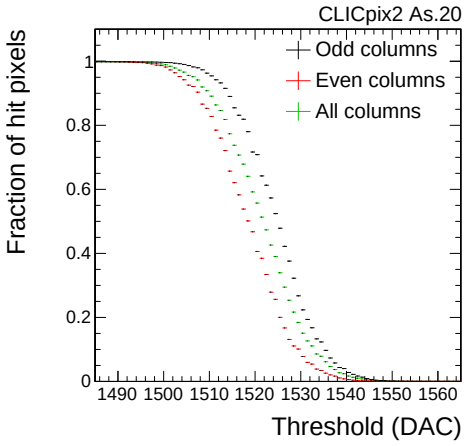

Figure 4.47: Profile histograms of the fraction of hit pixels recorded in the matrix during test pulse injection as a function of `threshold` for CLICpix2 planar sensor assembly 20 at a bias voltage of -60 V. Distributions are shown for when all pixels are analysed, and when odd or even columns are considered separately.

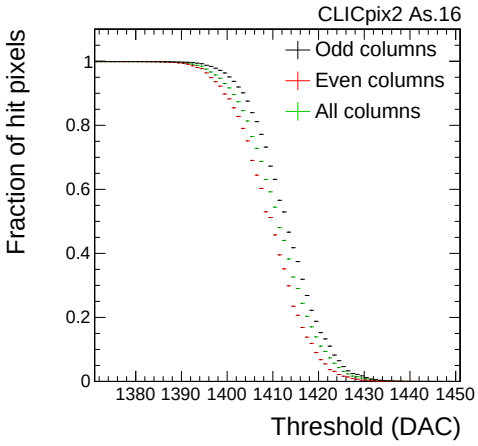

Figure 4.48: Profile histograms of the fraction of hit pixels recorded in the matrix during test pulse injection as a function of `threshold` for CLICpix2 planar sensor assembly 16 at a bias voltage of -60 V. Distributions are shown for when all pixels are analysed, and when odd or even columns are considered separately.

To reduce temperature effects during the measurements, a fan was applied to the assembly and temperature fluctuations inside the laboratory were minimised. The calibration data was taken at a room temperature of (21.1 ± 0.5)°C. It is important to match the calibration conditions to those used during data taking, especially for the `ikrum` and `clk_div` settings. The settings should be optimised using test-beam data, balancing dynamic range and signal precision. For the calibration of these two CLICpix2 assemblies, the settings of `clk_div` '2' and `ikrum` '8' were used.

4.5.2.1 Calibration of test-pulse injection

Creation of the ToT calibration curves first required the calculation of an e^- per mV conversion factor. This was achieved by identifying the threshold that corresponds to a certain test-pulse magnitude for odd and even columns, which could then be converted into e^- using the calibration from Subsection 4.5.1. DACs `test_cap_1` and `test_cap_2` were fixed to provide a pulse height of (81.00 ± 0.05)mV and the `threshold` was scanned from the operational to higher values. For each `threshold`, the number of hit pixels was recorded for ten acquisition frames, where one pulse was injected per frame.

A profile plot showing the fraction of hit pixels in the matrix as a function of `threshold` was created, an example of which is shown in Figure 4.47 for assembly 20. The green curve shows the distribution if all pixels in the matrix are taken into account, while the red and black curves are for even and odd columns respectively. A ± 0.5 DAC uncertainty in X is used for each point to account for the `threshold` DAC step size of 1, while the Y axis uncertainty reflects the spread of the ten measurements.

To identify the threshold at which the mean of each S-shaped distribution is situated, a Gauss error function:

$$Erf(x) = \frac{2}{\sqrt{\pi}} \int_0^x e^{-t^2} dt \tag{4.4}$$

was fit to the data curves of the form:

$$F(x) = AErf(Bx+C)+D \tag{4.5}$$

Extracting the mean from the fit provids a value of 1518 DAC for the even columns of assembly 20 with an uncertainty of ± 0.0077 DAC from the fit function. For the odd columns of assembly 20 the mean is calculated to be (1525.00 ± 0.75) DAC. As the uncertainty for both fit functions is less than 1% of the threshold, the uncertainty on each fit mean is assumed to be negligible.

For CLICpix2 planar sensor assembly 16, the same process was carried out and the results can be seen in Figure 4.48. The mean of the surrogate function fit to the odd column data was calculated to be (1413.00 ± 0.72) DAC, and for even columns is (1409.00 ± 0.72) DAC.

To calculate the e^- per mV conversion factor, denoted F, the following equation was used:

$$F\ (\text{e/mV}) = \frac{C \times 10^{-3}}{Q_e} = \frac{n_e \times Q_e}{V_{TP}} \times \frac{10^{-3}}{Q_e} = \frac{n_e \times 10^{-3}}{V_{TP}} \tag{4.6}$$

where C is the capacitance of the test capacitor on the CLICpix2 ASIC, Q_e is the charge of an electron in Coulombs, n_e is the number of e^- corresponding to the mean threshold of the error function fit, and V_{TP} is the height of the injected pulse in volts. The number of e^- injected by the pulse is calculated using the mean `threshold` of the fit function, the `threshold` of the baseline, and the threshold calibration factors calculated in Subsection 4.5.1. For the even columns of assembly 20:

$$\begin{aligned} F_{even,20}(\text{e/mV}) &= \frac{n_{e_{even,20}} \times 10^{-3}}{V_{TP}} \\ &= (49.7 \pm 0.7)\ \text{e}^-/\text{mV} \end{aligned} \tag{4.7}$$

For the odd columns of assembly 20:

$$\begin{aligned} F_{odd,20}(\text{e/mV}) &= \frac{n_{e_{odd,20}} \times 10^{-3}}{V_{TP}} \\ &= (49.3 \pm 0.7)\ \text{e}^-/\text{mV} \end{aligned} \tag{4.8}$$

Uncertainties on these values are propagated from the e^- per threshold uncertainty calculated in Subsection 4.5.1. The fractional uncertainty of the measured test pulse voltage is an order of magnitude lower than that of the e^- per threshold, and therefore is deemed to be negligible.

The same calculation was used on the data from assembly 16, calculating the following factors: $F_{even,16} = (48.7 \pm 0.6)\ \text{e}^-/\text{mV}$; $F_{odd,16} = (48.1 \pm 0.6)\ \text{e}^-/\text{mV}$.

As seen from Equation 4.6, the capacitance C of the CLICpix2 test capacitor can be calculated using the measurement results. This calculated value could then be compared to the design value of 10 fF to verify their compatibility. The capacitance for assembly 20 is calculated as follows for even columns:

$$\begin{aligned} C_{even,20} &= \frac{n_{e_{even}} \times Q_e}{V_{TP}} \\ &= (7.97 \pm 0.11)\ \text{fF} \end{aligned} \tag{4.9}$$

The capacitance for odd columns of assembly 20 is found to be:

$$\begin{aligned} C_{odd,20} &= \frac{n_{e_{odd}} \times Q_e}{V_{TP}} \\ &= (7.89 \pm 0.11)\ \text{fF} \end{aligned} \tag{4.10}$$

Similarly for assembly 16, values of $C_{even,16} = (7.80 \pm 0.10)$ fF and $C_{odd,16} = (7.70 \pm 0.10)$ fF are

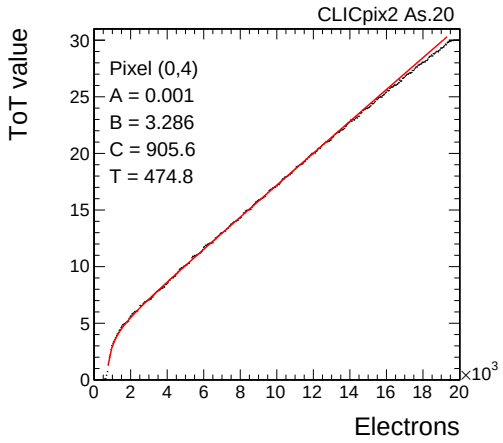

Figure 4.49: ToT calibration curve for pixel (0,4) of CLICpix2 planar sensor assembly 20 with nominal threshold and bias voltage applied.

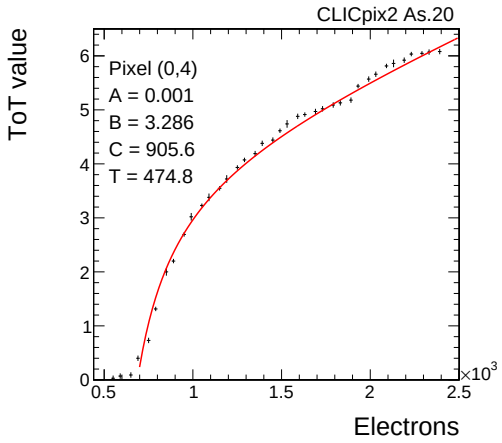

Figure 4.50: ToT calibration curve for pixel (0,4) of CLICpix2 planar sensor assembly 20 with nominal threshold and bias voltage applied, zoomed into the low ToT region.

calculated. The 10 fF design value of the capacitance has a quoted uncertainty of 20%. The calculated values are within 23% of the design value, and therefore are close to this uncertainty range.

4.5.2.2 Surrogate function calibration curves

The ToT response of each pixel in the matrix can be parameterised by fitting a function to a histogram of ToT versus injected e^-. Creating a calibration curve per pixel, rather than per column, accounts for differences in the readout channels of the chip.

To obtain the calibration curves, data was taken for both CLICpix2 planar sensor assemblies for different magnitudes of charge injection. The `test_cap_2` DAC was fixed at a value of 128 DAC and `test_cap_1` was scanned over a range of values, such that the ToT response of most pixels covered the range of 0 to 30. Test pulses were injected once per frame for 50 acquisitions, and the ToT response of each pixel was recorded. Using the calculations from the previous subsection, the magnitude of the test-pulse injections were converted into units of e^- using the appropriate factor. Due to the CLICpix2 readout method, only pixels that recorded a hit are contained within the output data file. Less than 50 entries per pixel were contained within the data file, where the missing entries correspond to below threshold test-pulse injections with a ToT of 0. To account for this in the average ToT values, the appropriate number of zeros were filled into each histogram bin to ensure 50 entries per test-pulse height.

An example distribution can be seen in Figures 4.49 and 4.50 for pixel (0,4) of assembly 20. The uncertainties of the profile plot accounts for the spread of the recorded ToT over the 50 measurements, as well as the ± 0.5 ToT uncertainty on each measurement due to the granularity of the ToT counter.

To parameterise the shape of this curve, the data is fit with a surrogate function of the formula:

$$y = Ax + B - \frac{C}{x - T} \tag{4.11}$$

where the A and B parameters describe the linear region of the data set, C describes the curvature of the low ToT region, and T is the value of the X intercept of the function [73]. The CLICpix2 ToT counter saturates at a value of 30 and this flat region is not described by the surrogate function,

therefore only the first data point with a ToT of 30 was included in the fit range. Any pixel that did not have data spanning the region of 0.5 to 25 ToT were excluded from the calibration as the curved and linear regions of the dataset could not be fully described. For both assemblies, less than 0.5% of pixels were excluded and the majority of these pixels exhibited a noisy behaviour.

The parameters of the surrogate function are observed to be highly dependent on the fit range over the X axis. This was partially caused by the fluctuation of the data points due to the integer nature of the ToT values, which created a step-like behaviour as observed in Figure 4.49. Another factor affecting the surrogate function fit comes from the large number of data points in the linear region compared to the curved section, which for some pixels resulted in a surrogate function fit with no curved section at low ToT. The inverse curvature of the data at ToT values below 0.3 due to the truncation of the ToT at 0 also affected how well the surrogate function fit to the data set. To mitigate these effects, the range of the fit function was carefully adapted as required on any curve with a χ^2 per NDOF above three. First the fit range over the X axis was adapted to cover the range to 0.3 to 20 ToT. Then the resultant A, B, C, T parameters were used as starting values for a surrogate function fit over the original X axis range. If this resulted in a χ^2 per NDOF above three, then the process was repeated twice more using different X axis ranges to obtain a χ^2 per NDOF closer to one.

The resultant A, B, C, T parameter and χ^2 per NDOF values are shown in Figures 4.51 to 4.60 for assembly 20. In the surrogate function, parameter A describes the gradient of the linear region and is inversely proportional to the gain of the pixel. When plotted as a 2D map, shown in Figure 4.51, a difference in the A parameter is observed between odd and even columns, as are a small number of randomly distributed outliers. The width of the 1D distribution for all pixels is large compared to its mean value as observed in Figure 4.52. As is shown by the red and black curves, this width is attributed to the difference in the A parameter of odd and even columns where two distinct peaks are observed. The use of differing e/mV conversion factors increases the difference in the linear gradient between odd and even columns, causing the peak separation.

For the B parameter, the 2D distribution is observed in Figure 4.53. An odd-even column pattern similar to that obtained for the A parameter is seen, but in addition a small gradient can be seen between the top and bottom of the matrix not present for A. The 1D B distribution has a small width for all pixels and a small offset between odd and even columns observed in Figure 4.54,. This is expected, as any difference in the linear region between column types is expected to be small at low ToT and larger at higher ToT, therefore minimally affecting the Y intercept.

C describes the surrogate function curvature at low ToT, and both row and column effects are observed for this parameter in Figure 4.55. Odd and even columns differ and the overall effect is shown in Figure 4.56. Both distributions have a similar shape with a small offset between, comparable to the previous parameters.

Finally, the T parameter describes the X-axis intercept of the function. This parameter is poorly constrained due to the low number of data points at ToT values lower than 1, as shown in Figure 4.50. Any fluctuation in the data due to the integer nature of the ToT or statistical fluctuations causes large differences in the T parameter extracted from the fit function. Corresponding to a ToT value of zero, T is particularly interesting to study as it provides the threshold of the sample in e^-. In Figure 4.57, no distinct even-odd column pattern is observed. In the 1D histogram of T values for all pixels, shown in Figure 4.58, a convolution of two peaks of different widths and heights is observed. The T parameter of odd columns has two peaks at approximately 530 e^- and 630 e^- with large overlapping tails. For even columns, the main peak at approximately 560 e^- is distinct from the much smaller secondary peak at 670 e^-, and both peaks are thinner than in the odd column distributions. The cause of the distribution shape for different columns was not investigated further. The large width of the overall T distribution could be expected from the uncertainty of the threshold calibration, discussed in Section 4.5.1, and the T parameter uncertainty.

Figures 4.59 to 4.60 show the surrogate function χ^2 per NDOF, the results of which show that each

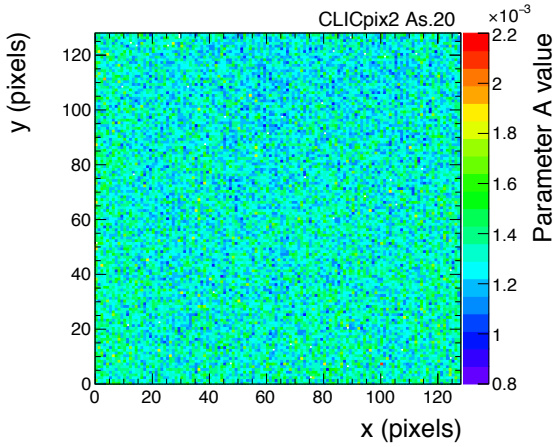

Figure 4.51: 2D map of the A parameters obtained from the surrogate function fit to the ToT calibration curve of the pixel. For CLICpix2 planar sensor assembly 20 with nominal threshold and bias voltage applied.

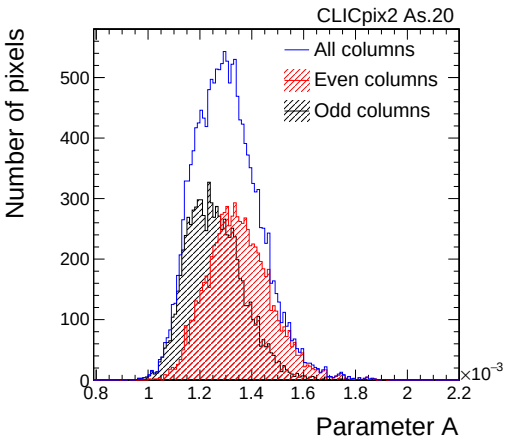

Figure 4.52: 1D histograms of the A parameters obtained from the surrogate function fit to the ToT calibration curve of the pixel, showing the difference between odd and even columns. For CLICpix2 planar sensor assembly 20 with nominal threshold and bias voltage applied.

surrogate function fit describes the dataset well, despite the fitting difficulties described previously. A small gradient between the rows at the top and bottom of the pixel matrix is observed in Figure 4.59, following the same trend as seen for parameters B and C in Figure 4.55. The 1D distribution shown in Figure 4.60 peaks at a value of 1.7. For odd columns the χ^2 per NDOF is found to be higher than for even columns, with peak values of 2.1 and 1.5 respectively. The discrepancy between these values and the ideal value of 1 reflects the fact that the surrogate function fits are not expected to describe the data points over the whole range, as previously discussed.

The ToT calibration procedure was also carried out for CLICpix2 planar sensor assembly 16, where similar results are obtained. Histograms in 1D and 2D for each surrogate function parameter can be found in Appendix A for this assembly.

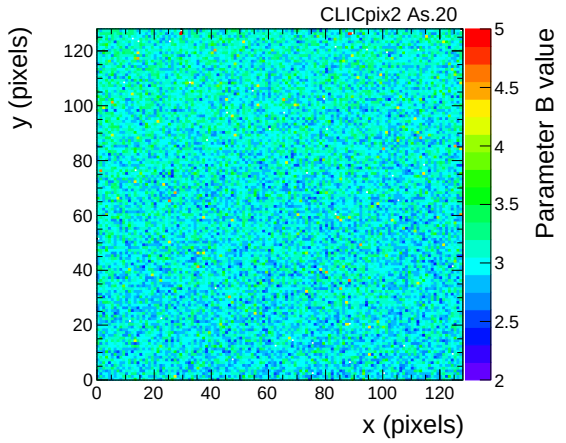

Figure 4.53: 2D map of the B parameters obtained from the surrogate function fit to the ToT calibration curve of the pixel. For CLICpix2 planar sensor assembly 20 with nominal threshold and bias voltage applied.

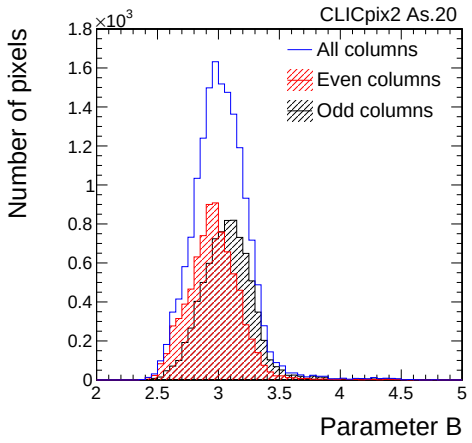

Figure 4.54: 1D histograms of the B parameters obtained from the surrogate function fit to the ToT calibration curve of the pixel, showing the difference between odd and even columns. For CLICpix2 planar sensor assembly 20 with nominal threshold and bias voltage applied.

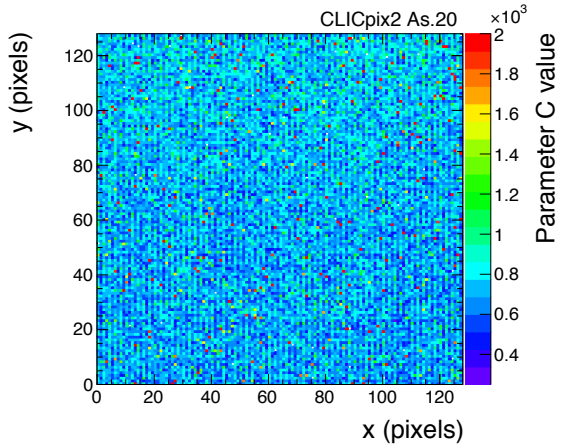

Figure 4.55: 2D map of the C parameters obtained from the surrogate function fit to the ToT calibration curve of the pixel. For CLICpix2 planar sensor assembly 20 with nominal threshold and bias voltage applied.

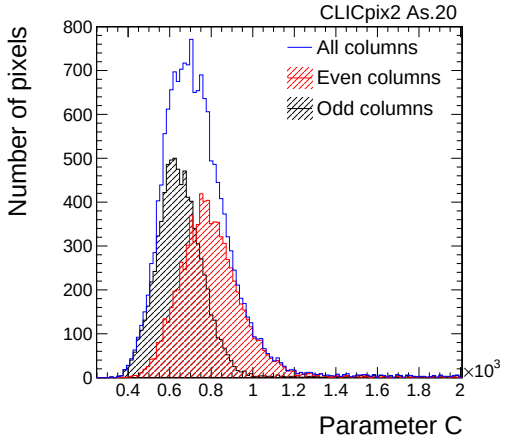

Figure 4.56: 1D histograms of the C parameters obtained from the surrogate function fit to the ToT calibration curve of the pixel, showing the difference between odd and even columns. For CLICpix2 planar sensor assembly 20 with nominal threshold and bias voltage applied.

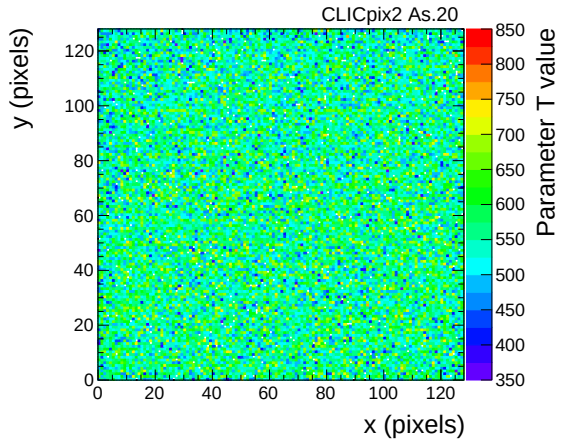

Figure 4.57: 2D map of the T parameters obtained from the surrogate function fit to the ToT calibration curve of the pixel. For CLICpix2 planar sensor assembly 20 with nominal threshold and bias voltage applied.

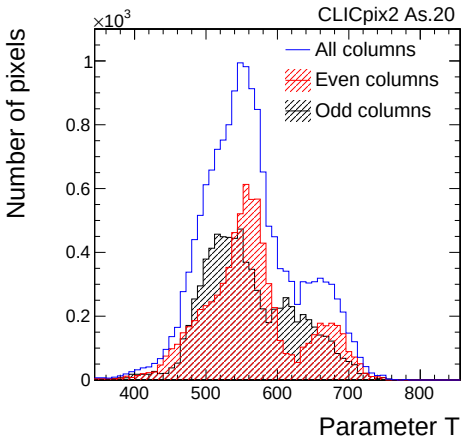

Figure 4.58: 1D histograms of the T parameters obtained from the surrogate function fit to the ToT calibration curve of the pixel, showing the difference between odd and even columns. For CLICpix2 planar sensor assembly 20 with nominal threshold and bias voltage applied.

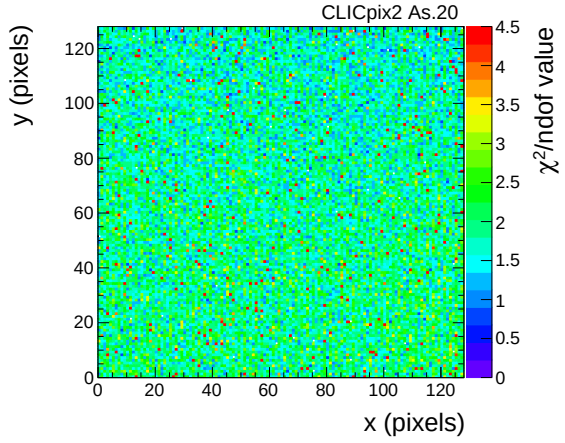

Figure 4.59: 2D map of the χ^2 per NDOF values obtained from the surrogate function fit to the ToT calibration curve of the pixel. For CLICpix2 planar sensor assembly 20 with nominal threshold and bias voltage applied.

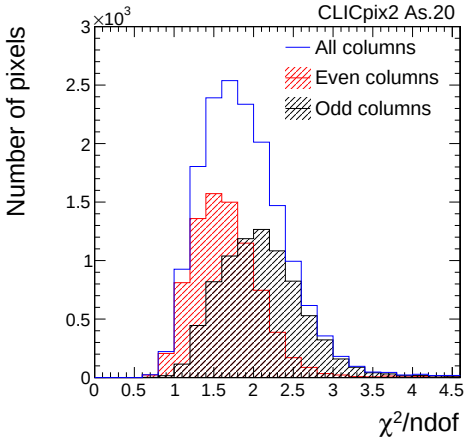

Figure 4.60: 1D histograms of the χ^2 per NDOF values obtained from the surrogate function fit to the ToT calibration curve of the pixel, showing the difference between odd and even columns. For CLICpix2 planar sensor assembly 20 with nominal threshold and bias voltage applied.

4.6 Summary of laboratory testing of CLICpix2 planar sensor assemblies

CLICpix2 assemblies bump-bonded to planar sensors have been extensively tested to assess their performance, an important process when receiving a novel device. This chapter has summarised the aims, method, and results for each stage of the laboratory testing.

Almost all assemblies behaved as expected during an initial round of measurements, which included I-V curves and threshold equalisation. Detailed information was obtained on the bonding quality of each pixel using a data-driven categorisation scheme. By combining the results of different tests, such as radioactive source exposure and test-pulse injection, a number of features of the assemblies were correctly identified. These included an effect of the active-edge sensor design on the pixel hit rates, UBM incompatibility, bump-bonding issues, and regions of pixels with cross-talk. All of these results and insights were communicated to the manufacturer to improve the challenging single-chip bonding process utilised. Two assemblies out of nine were found to have a high bump yield, up to 99.6%, verifying the feasibility of single-chip bump-bonding at a pixel pitch of 25 µm.

During these periods of data taking, a temperature dependence of the voltage of certain DACs was identified, assessed, and mitigated. The output of CLICpix2 voltage DACs increased with increasing temperature due to a resistor mismatch in these DAC circuits. This dependence can be mitigated by minimising environmental temperature fluctuations, operating the assemblies at a threshold close to the baseline, and the application of a fan to the chip.

Finally, calibration of the `threshold` and ToT into physical units used X-ray fluorescence and test-pulse injection measurements respectively. The K_α spectral peaks of two target materials were used to calculate the threshold calibration factor for odd and even columns. Then the ToT response of each pixel was measured for varying amounts of injected charge. By applying the threshold calibration results, these ToT units were plotted as a function of e^- and parameterised using a surrogate function fit. The fit parameters describing the linear region and curvature of the function behaved as expected, while the T parameter has an unexplained distribution in 1D. From the χ^2 per NDOF distributions of the surrogate functions it is observed that each describes the dataset well, considering the multiple fitting difficulties encountered.

Characterising and assessing the interconnect quality of the CLICpix2 assemblies was vitally important to understand and improve the challenging single-chip bump-bonding process utilised by the manufacturer. Calibrating the highest quality assemblies allows their performance to be compared to other technologies or theoretical predictions, both in laboratory measurements and test-beam analysis.

Part III

Performance evaluation of CLICpix2 planar sensor assemblies

Chapter 5

Test-beam facilities and telescopes

It is essential to make use of well defined and understood reference detectors to evaluate prototype detector performance. During a test-beam, a beam of minimally ionising particles (MIPs) passes through a reference telescope of pixel detectors and one or more devices under test (DUTs). Using dedicated software, as discussed in Chapter 6, the particle trajectories are reconstructed into tracks and used to determine the device performance through track-DUT comparison. Compared to laboratory radioactive source exposure, test-beam measurements can achieve higher rates and energies of incident particles, determine the resolution and hit detection efficiency of the DUT, and noise hits can be removed through track-DUT matching.

In this chapter, the general concepts of test-beam measurements will be discussed. For these studies, data was taken for CLICpix2 planar sensor assemblies at two facilities: the CERN Super Proton Synchrotron (SPS) North Area and the test-beam facility of the DESY-II synchrotron. Both of these facilities are described, as well as the reference telescopes used in each beam-line. Information is given on the mechanical set-up, DUT integration, and data acquisition (DAQ) systems used in each case.

5.1 Test-beam and telescope concepts

The particle beams used at test-beam facilities usually operate under well known conditions and are often configurable in terms of particle composition, energy range, rate, and spill pattern. Depending on the measurement aims and the detectors used, different beam conditions could be preferable.

A conventional test-beam telescope consists of several well-characterised pixel detectors along the particle beam axis, as illustrated in Figure 5.1. The global coordinate system used for test-beam telescopes in this study is also shown: a right-hand cartesian system with the particle beam travelling along the positive Z axis. Each telescope reference plane measures the incidence time and position of particles with high accuracy. Using the combined information, the true trajectory of each particle can be reconstructed.

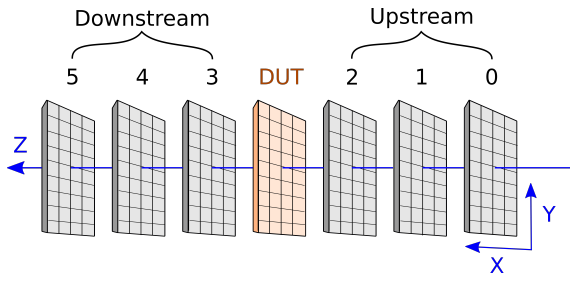

Figure 5.1: Illustration of a typical test-beam telescope set-up, consisting six reference planes and a central DUT. The coordinate system used in this study is indicated.

The performance of a test-beam telescope system is measured as its track resolution in space and time, with contributions originating from the individual reference plane performance, multiple coulomb scattering of the beam particles, and the telescope geometry. To improve the telescope performance, pixel detectors with high spatial resolution, timing resolution, and hit detection efficiency should be chosen. Within the telescope, the amount of multiple scattering that occurs is described by Equation 1.4. It is therefore dependent on the beam momentum, beam composition, material budget of the reference planes, and the volume of air that the particles traverse. For this reason, the assemblies used for telescope planes and their mechanical set-up should have a low material budget.

Other telescope design considerations include cooling systems to stabilise the operating conditions of the pixel detectors. However, cooling systems can introduce more material into the particle beam and increase scattering. A sturdy mechanical system for mounting each plane is also required to ensure the devices do not move significantly over time, as these misalignments would deteriorate the spatial resolution of the system.

The DUT is typically placed in the centre of the reference system, where the telescope pointing resolution is best. All telescope planes placed before and after the DUT are referred to as the 'upstream' and 'downstream' arms of the telescope respectively, as indicated in Figure 5.1. Particle tracks, reconstructed from the telescope data, are interpolated to find the predicted incidence point of the track and the DUT plane. By comparing the DUT clusters to the predicted track-DUT incidence point in time and space, the response of the novel detector to incident, high-energy particles can be assessed.

Test-beam data is recorded in time periods called runs and data from each run is stored separately. In this study, the telescope planes received a synchronising signal at the start of each run. The synchronisation of readout and data storage requires a dedicated DAQ system. Each pixel detector within the test-beam set-up can employ a different readout scheme, as discussed in Section 1.2, therefore synchronising these data streams can be a difficult task. Pixel data from each plane is recorded and stored on disk by the DAQ system for offline analysis.

5.2 CERN, SPS test-beam facilities

A portion of the test-beam measurements carried out on CLICpix2 planar sensor assemblies used the Compact Linear Collider detector and physics (CLICdp) Timepix3 telescope at the CERN SPS North Area test-beam facility [65].

The North Area hall, pictured in Figure 5.2, receives a particle beam from the SPS [66] accelerator of CERN, which is then split into six beam-lines [74]. It contains multiple experiments, such as COMPASS and SHINE, as well as test areas for detector and accelerator R&D.

The CLICdp telescope is located in the H6B beam area [75] and typically receives a 120 GeV π^+-proton beam with a narrow beam profile. Particles in the beam are configured to arrive at a typical rate of 1-3$\times 10^5$ particles per second, tuned using beam collimators. The beam intensity was limited by the allowed integrated level of ionising radiation caused by parasitic muon flux, measured behind the beam stopper downstream of the H6B area. Particles are delivered in a bunched structure, typically with 6 second spills every 30-60 seconds. The spill pattern is related to the duty-cycle of the various experiments that receive protons from the SPS.

5.2.1 CLICdp Timepix3 telescope

The high-performance, reference tracking system of the CLICdp telescope has a design based on the LHCb Timepix3 telescope [76]. It consists of seven angled reference planes housed inside an enclosing box, with three planes upstream of the DUT and four downstream as pictured in Figures 5.3

Figure 5.2: Image of the North Area experimental hall of CERN, showing the H6B beam-line area when facing downstream.

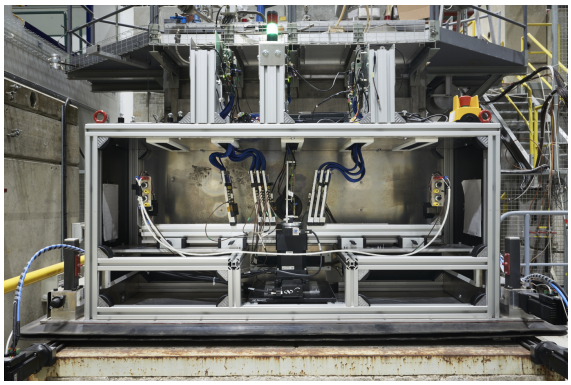

Figure 5.3: Image of the CLICdp Timepix3 telescope in the H6B beam-line of the CERN SPS North Area hall, showing its light-tight enclosure and mechanical systems. The particle beam from the SPS propagates along the positive Z axis from the right of the image to the left [77].

Figure 5.4: Image of the CLICdp Timepix3 telescope in the H6B beam-line of the CERN SPS North Area hall, showing seven reference planes and a CLICpix2 planar sensor assembly as a DUT [77].

and 5.4. The telescope planes are hybrid pixel detectors consisting of a Timepix3 readout chip bump-bonded to 300 µm thick N-in-P planar sensors [65].

5.2.1.1 The Timepix3 readout ASIC

The Timepix3 hybrid readout Application-Specific Integrated Circuit (ASIC) was designed in a 130 nm Complementary Metal Oxide Semiconductor (CMOS) process as a general purpose chip for semiconductor or gaseous pixel detectors [54] [78]. It has a 256×256 pixel readout matrix grouped into 128 double-columns, with each double-column being divided into 64 4×2 super pixels. The pixels themselves are 55 × 55 µm and a schematic diagram of the Timepix3 pixel logic can be seen in Figure 5.5. Each pixel is capable of recording 18-bit time-of-arrival (ToA) timing and 10-bit time-over-threshold (ToT) charge measurements simultaneously.

Efficient hit identification is achieved via a high gain of approximately 50 mV/1000 e and a low noise of approximately σ=75 e. The ToT counter can measure deposited charge up to 150 ke, by measuring the number of 40 MHz clock cycles while the discriminator output is asserted.

Timepix3 gains its timing measurement accuracy by having a high resolution time-to-digital converter (TDC) for each superpixel, based on the layout of a start-stop ring oscillator as described in [54]. The time of a pixel hit is known to within one 640 MHz clock period, corresponding to a fine

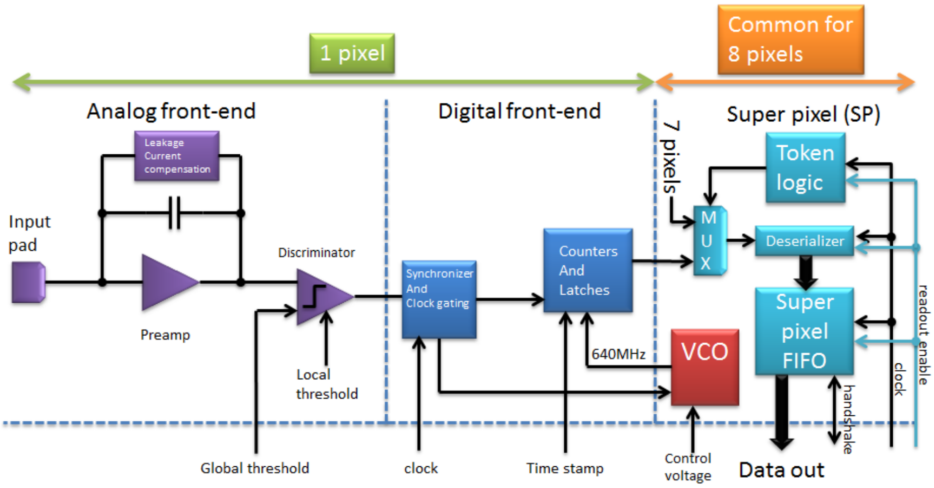

Figure 5.5: A schematic of the front-end logic of single pixels and superpixels. Diagram from [54].

timestamp binning of 1.56 ns. A coarse time stamp binning of 25 ns is also recorded and combined with the fine timestamp to form the ToA measurement.

5.2.1.2 Telescope set-up

The high spatial resolution and precise hit-time measurement of the Timepix3 ASIC makes it a desirable technology for a test-beam reference telescope. In the CLICdp telescope, each Timepix3 plane has an applied voltage of 50 V and threshold of approximately 1 ke^- [65]. A light-tight metal box houses the telescope system to minimise the number of noise hits on the pixel detectors within. Two fans circulate air within the box, ensuring the assemblies maintain a stable temperature.

For stability and alignment purposes, the aluminium holders of the Timepix3 assemblies are mounted onto two metal beams that extend along the Z axis. The Z position of these upstream and downstream arms can both be adjusted by hand, as can the position of the Timepix3 holders. The arms of the telescope are often moved in Z during a test-beam when installing the DUT device and DAQ.

To measure the relative Z alignment of each assembly, a ruler with spacings of 1mm is used. By using holders on the static metal support beams, the relative Z rotation and X/Y translation of each telescope plane is near zero. In addition, the X/Y rotations of the telescope planes are known to be approximately 9° from the Timepix3 holder design. These X/Y rotations increase the average cluster sizes created by incident particle tracks, therefore improving the spatial resolution of each telescope plane. An angle of 9° was found to be optimal during a Timepix telescope study [79].

In addition to the plane-by-plane alignment, the telescope-beam alignment is also important to ensure a high rate of particles through each Timepix3 plane. The light-tight box housing the telescope system is placed on a motor system that can accurately move the telescope box translationally in X/Y. By observing 2D histograms of the recorded pixel hits, the telescope system can be centred on the beam by moving the box accordingly. The angle of the telescope system to the incident beam is non adjustable and was aligned during the initial telescope construction using a laser system.

By utilising the precise measurements of the Timepix3 technology, the CLICdp test-beam telescope has a track-incidence time resolution in the order of 1 ns and a $\leq$2 µm spatial track resolution on the DUT plane [6].

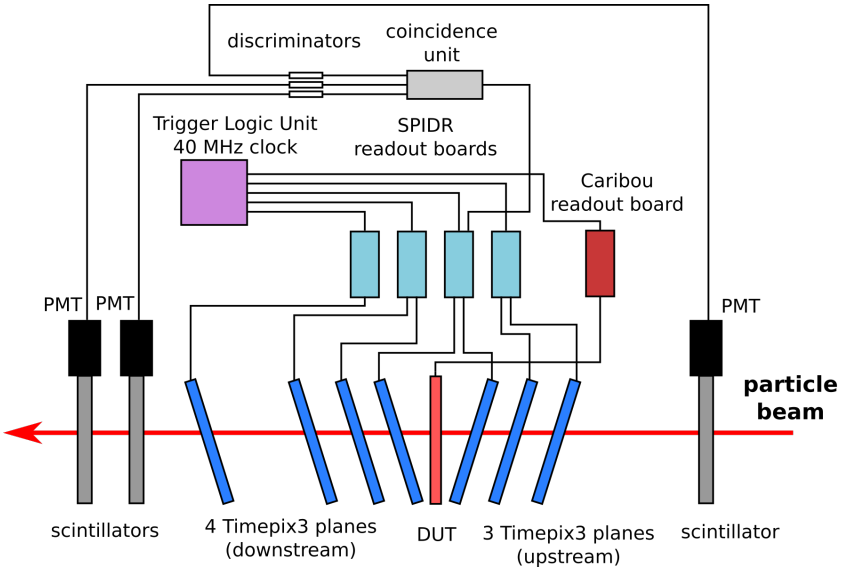

Figure 5.6: Schematic of the DAQ system for the CLIC Timepix3 telescope at the SPS test-beam facility.

5.2.1.3 CLICpix2 device integration

The DUT is placed between telescope planes 2 and 3 on a movement stage that can perform X/Y translations and Y axis rotations. The automatic movement capabilities are useful to align the DUT plane to the particle beam and other telescope planes, as well as for angular studies. Figure 5.4 shows a CLICpix2 planar sensor assembly in this position. The CLICpix2 device is attached to a Caribou Control and Readout (CaR) board, as described in Section 4.1, and mounted with screws onto a plastic holder for support. As the metal enclosure of the telescope system is equipped with fans, no additional cooling system is applied to the CLICpix2 DUT. A bias voltage is applied across the planar sensor using a Keithly 2450 source meter.

5.2.1.4 Test-beam DAQ system

A run control system initiates and ends each data run, and can be configured to scan parameters such as DUT rotation or applied bias voltage. To record the data taking parameters and any error messages, a logging system is included in the run control system.

A schematic of the telescope DAQ hardware is shown in Figure 5.6. The Speedy PIxel Detector Readout (SPIDR) readout system [80] is used for the high-rate Timepix3 data stream [6]. Each Timepix3 ASIC operates in a data-driven, zero-suppressed readout mode to minimise the dead-time during readout. Each set of two telescope planes is read out by one commercial field-programmable gate array (FPGA) development board (Xilinx VC707) hosting a Virtex 7 FPGA SPIDR board. Timepix3 data packets are then encapsulated in user datagram protocol (UDP) frames and sent to a PC via an optical 10 Gigabit link.

The frame-based pixel data from the CLICpix2 planar sensor DUT is acquired using the Caribou DAQ system detailed in Section 4.1. An additional flexible metallic conduit (FMC) cable has been introduced between the system on chip (SoC) placed outside of the metal telescope box and the control and readout (CaR) board of the CLICpix2 mounted on the DUT rotation stage. Every CLICpix2 data frame is written out and sent to a PC via the network hub.

Three scintillators are included in the set-up as an external timing reference and as a trigger source for DUTs requiring an external trigger. They are read out by photomultiplier tubes (PMTs), and the

Figure 5.7: Image of the DATURA telescope in beam-line 21 of the DESY Test-Beam Facility. The telescope set-up, TLU unit, voltage sources, and DAQ system can all be seen. The particle beam propagates parallel to the telescope system, from right to left in the image.

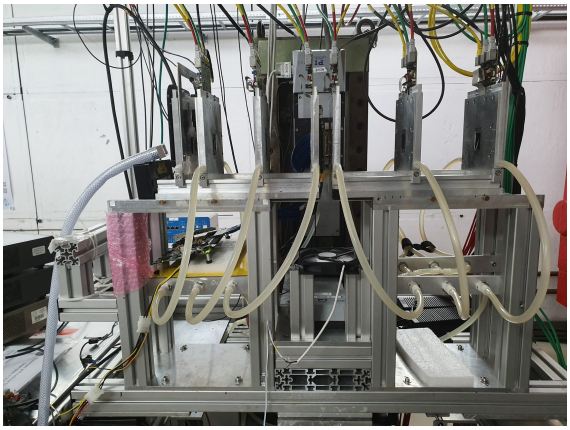

Figure 5.8: Image of the DATURA telescope at the DESY Test-Beam Facility, with the Z axis from right to left. Six Mimosa26 telescope planes are seen. The additional Timepix3 time-reference plane is the last plane of the telescope in Z. A CLICpix2 planar sensor DUT is present between telescope planes 2 and 3.

discriminated PMT pulses are sent to a configurable coincidence logic unit. The coincidence signal is then sampled by the TDC input of the downstream SPIDR board.

Each telescope plane and the DUT receive a common 40 MHz clock and a synchronous clock reset signal at the start of each run from a trigger logic unit (TLU). By matching the hit time stamps of the telescope planes and the time stamp of the CLICpix2 shutter signals, the recorded test-beam data can be reconstructed and analysed offline using a software such as Corryvreckan, see Chapter 6.

5.3 DESY II test-beam facilities

Located in Hamburg, the DESY Test-Beam Facility is a user of the DESY-II e^-/e^+ synchrotron [67]. The primary beam runs through the hall, where thin carbon fibres and conversion targets create three secondary e^- beams. Each independent beam-line provides an e^- or e^+ beam with a maximum momentum of 6.3 GeV and a particle momentum spread of less than 5%. Particular ranges of particle momentum can be selected using a magnet and collimator, which also changes the particle rate between a few Hz to 100 kHz. A beam momentum of 5.4 GeV is used in this study. Particles circulate within the DESY-II ring at a frequency of 1.024 MHz with a bunch length of 3 ps. The beam spill pattern includes regular periods of time where a lower rate of particles are provided, corresponding to when DESY-II is used to fill the PETRA-III storage-ring based X-ray radiation source.

5.3.1 EUDET Mimosa26 telescope

The Mimosa26 telescope utilised in beam-line 21 was built within the EUDET, AIDA, and AIDA-2020 programmes [81] [82] [83]. The telescope set-up and mechanical infrastructure are pictured in Figures 5.7 and 5.8, and detailed in [81]. It consists of six perpendicular planes of Mimosa26 pixel detectors [84], to which an additional Timepix3 plane is added as a timing reference for the CLICpix2 test-beam measurements.

5.3.1.1 The Mimosa26 monolithic detector

The Mimosa26 pixel detector is produced using a 350 nm CMOS process and is based on the Monolithic Active Pixel Sensor (MAPS) technology [81] [84]. It has a 1152×576 matrix of 18.4 µm pitch square pixels. Each assembly has a thinned silicon sensing layer of 50 µm to reduce the overall material budget of the telescope. Charge carriers are collected by diffusion from a 10 µm thick epitaxial layer. The hit detection threshold of the Mimosa26 planes is configured as multiples of the Root Mean Square (RMS) noise, such that a setting of '6' corresponds to a hit detection threshold six times higher than the noise level.

5.3.1.2 Telescope set-up

The EUDET telescope is configured to use 50 µm thick Mimosa26 planes with three evenly-spaced devices on each upstream and downstream arm, as shown in Figure 5.8 [81]. Each Mimosa26 assembly has an applied bias voltage of 8 V and a threshold of 6. The central telescope planes are placed as close as mechanically possible to the DUT to better constrain the particle track in this region. Four coincident scintillators are also present, with two situated at each end of the telescope. To gain a more precise track-time measurement in these studies, an additional Timepix3 planar assembly was placed directly after the last scintillator in Z. The Timepix3 assembly had an applied bias voltage of −20 V and a silicon sensor thickness of 100 µm.

Each Mimosa26 telescope plane is mounted such that the column direction is aligned with the telescope X axis. They are housed within a light-tight aluminium and Kapton foil holder with a water-cooling system that maintains a stable temperature of 18 °C. The Timepix3 assembly is placed in a rigid plastic holder and has a dedicated fan cooling system through the tube shown in Figure 5.8.

Each holder attaches using metal clamps to a mechanical frame aligned with the Z axis, where the Z position of the planes can be adjusted by hand. By using a support frame to mount the assemblies, the translational X/Y difference between the telescope planes is minimised and the Z rotation of each plane is approximately zero.

To ensure the particle beam is incident on the centre of each plane, the telescope is placed on a moveable support stage. Using this automated movement stage, the mechanical support for the telescope and DUT can be moved translationally along the X/Y axes

The spatial track resolution of the telescope system at the DUT position is approximately 1.8 µm for the settings and geometry used in the study [81].

5.3.1.3 CLICpix2 device integration

A specialised aluminium and plastic holder for a CLICpix2 assembly and the Caribou CaR board, as introduced in Section 4.1, has been manufactured for use in the EUDET telescope system. An additional FMC cable is introduced between the SoC and the CaR board of the DUT for mechanical reasons, as can be observed in Figure 5.9. The DUT holder pictured in Figure 5.9 is mounted in-between telescope planes 2 and 3 along the X axis, as shown in Figures 5.8 and 5.10, using a combined X/Y high-precision linear stage translation system for support. The automated movement of this system was used to align the DUT with the centre of the telescope planes via X/Y translation.

As shown in Figure 5.8, a fan placed underneath the DUT cooled the CLICpix2 assembly to minimise temperature fluctuations. A bias voltage is applied across the planar sensor using a Keithly 2450 source meter.

5.3.1.4 Test-beam DAQ system

The EUDAQ2 modular framework is used for the DAQ of this telescope system [85]. The central run control of the framework is used to send commands to all other modules and to receive their

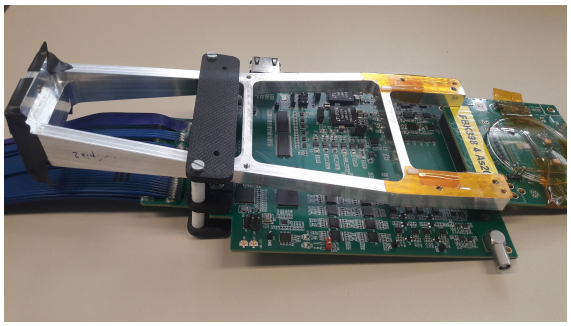

Figure 5.9: Image of the CLICpix2 aluminium holder made for the EUDET telescope at DESY. A CLICpix2 planar assembly, Caribou CaR board, and FMC cable are attached to the holder using screws and plastic sections.

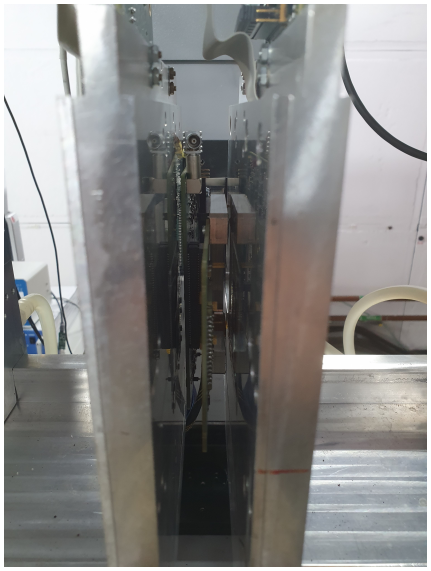

Figure 5.10: Image of a CLICpix2 planar sensor mounted between telescope planes 2 and 3 of the DATURA EUDET telescope at DESY. The Z axis of the telescope system goes from right to left in this picture. The DUT holder is mounted along the X axis using a supporting translation stage.

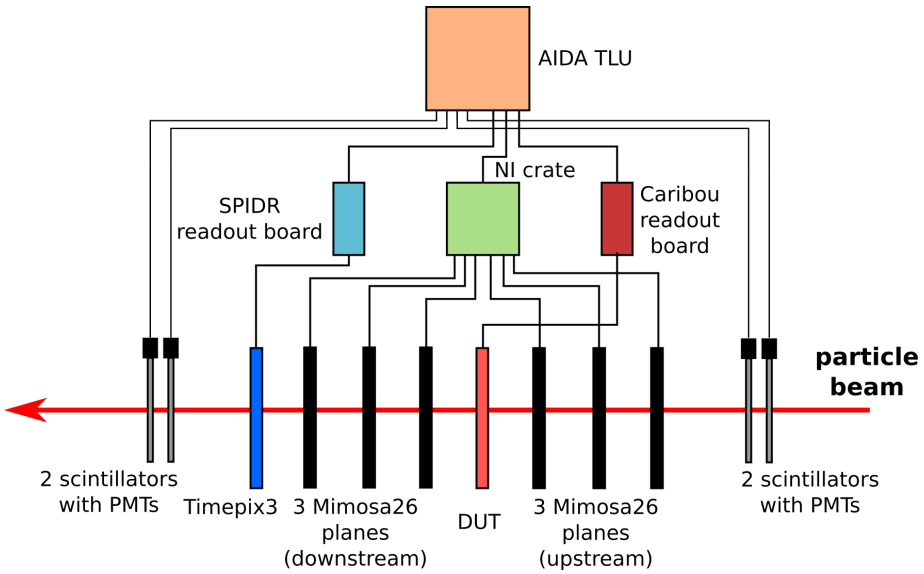

Figure 5.11: Schematic of the DAQ system for the DATURA Mimosa26 telescope at the DESY II test-beam facility.

status. Each type of detector has a producer module that controls and communicates with the attached devices. Data collector modules receive the incoming data streams from the producers and assign them to particular trigger signals where applicable. The raw data is then modified into a EUDAQ2 event structure and stored to disk in a binary format with a single data stream per device type.

A schematic of the DAQ hardware used for the EUDET Mimosa26 telescope is shown in Figure 5.11. Trigger signals are provided and recorded using a TLU developed within the AIDA-2020

project [86]. The TLU generates and provides a common trigger signal to all connected detectors, where the trigger is generated by the coincidence of the telescope scintillators. Each set of coincident scintillators are readout using PMTs. Every trigger signal has a recorded timestamp in units of a 40 MHz clock frequency and are numbered for reference. During test-beam data taking, the coincidence of the two upstream scintillators was used for triggering and their overlap covers approximately the area of the Mimosa26 sensors.

The Mimosa26 planes operate in a triggered rolling-shutter readout scheme. When a trigger is received by a Mimosa26 device, it generates a 'busy' signal during the rolling shutter period of 115 µs. More information on the DAQ system of the EUDET telescope can be found in [81].

The Timepix3 telescope plane is operated in data-driven, zero-suppressed readout mode and therefore supplies a near-continuous data stream. A SPIDR readout board is used for the Timepix3 plane. Data frames from the CLICpix2 planar sensor DUT are acquired using the Caribou DAQ system, as described in Section 4.1 . As the front-end of the CLICpix2 employs a frame-based readout scheme with a fixed acquisition pattern, the frames are not synchronised with the triggered telescope readout and dead-time occurs during the readout of each frame.

By matching the trigger signals to the corresponding Mimosa26, CLICpix2, and Timepix3 data, the recorded test-beam data can be reconstructed and analysed offline.

Chapter 6

The Corryvreckan reconstruction framework

Development and maintenance of Corryvreckan, as one of the main developers of the software, was an integral part of the work of this thesis.

Pixel detector prototypes are commonly characterised by testing the novel device in a high-precision reference telescope, as discussed in the previous chapter. To analyse the performance of the device under test (DUT), the particle tracks need to be reconstructed from the raw test-beam data files using a software framework.

In a typical reconstruction chain, the software first parses the raw data files to determine the position and time of every pixel hit on each detector plane. Neighbouring hit pixels are then grouped into clusters, as they are likely to correspond to the same incident particle due to charge sharing. Incident particle trajectories are reconstructed from clusters on each plane of the reference telescope. By predicting the track incidence point on the DUT, clusters from the DUT can be associated with the particle that produced those pixel hits. Associated cluster-track comparison allows the performance parameters of the DUT to be determined, such as efficiency and resolution in time and space. Some examples of test-beam data reconstruction software are the currently available frameworks EUTelescope [87], Judith [88], and Proteus [89].

Recent developments in telescope design and pixel detector technologies require additional functionality in a reconstruction software. Reference telescope designs are becoming more complex, for example with timing data from every telescope plane or multiple detectors utilising different readout schemes. The diversity of new pixel assemblies used as DUTs requires a highly configurable software that has the flexibility to describe a range of device characteristics and to adapt the reconstruction chain to different analysis needs.

Corryvreckan is a software written in modern C++ designed to reconstruct and analyse test-beam or laboratory data that balances adaptability and ease of use. It employs a flexible, modular design: the core component deals with the parsing of configuration files, central event loop, and coordinate transformations; the modules each implement an individual step of the reconstruction process. The configurability of the modular framework allows a range of test-beam telescope designs and novel assembly capabilities to be described. Some notable features of Corryvreckan are its tracking and clustering algorithms using 4D information, and its ability to synchronise data from devices with a variety of readout schemes. The software is well documented, and the Corryvreckan code repository is maintained by the authors through detailed Continuous Integration (CI) testing, code review, and issue tracking. Development and maintenance of this software was an integral part of the work of this thesis.

In the following text, Corryvreckan version 2.0 is described. This chapter will introduce the main concepts of Corryvreckan and highlight points important to this project, and is therefore not intended to be a complete description of the software. A comprehensive overview can be found in the Corryvreckan user manual found on the online code repository [90], and a description of version 2.0 is presented in [91].

6.1 Architecture of the software

The flexibility of Corryvreckan arises from its modular structure, where functionally independent modules are separated from the framework core. Modules are algorithms for specific reconstruction or analysis tasks. Meanwhile, the core component contains utilities required by each module, such as the event loop and configuration parsing. It is designed to be light-weight, easily configurable, and to have fast processing time.

6.1.1 Object data storage

The clipboard is the core frameworks infrastructure for temporarily storing information during data processing.

A key element of the clipboard is the event object, which is a time-slice of the input raw data streams. The Corryvreckan event loop processes each event in turn, either until the end of the input data files or a configured end point. Events store vital information about the data currently being processed on the clipboard, such as the time-window of the data and any associated trigger numbers. The data contained in each event is defined as discussed in Section 6.2.1.

The clipboard is available for every module to read and temporarily store Corryvreckan objects. Objects are classes of information that need to be transferred between modules, such as pixel, cluster, or track objects. After an event is processed, the clipboard is cleared of this information. In addition, a persistent storage is available to store information used in multiple events.

6.1.2 Configuration files

Configuring the reconstruction and analysis work-flow requires two files: one describing the modules to be executed; the other describing the detector set-up. For ease of use, these files utilise the Tom's Obvious Minimal Language (TOML) format [92] and specify configurable parameters as key/value pairs. Corryvreckan can interpret the readable unit types of configuration parameters for convenience.

The main configuration file is passed directly to the Corryvreckan executable, an example of which is shown in Figure 6.1. It contains the global framework configuration, a list of all modules to be instantiated, and the individual configuration of the modules. Global framework parameters, which are placed underneath the `[Corryvreckan]` header, are inherited by all modules during the reconstruction. These include the path of the output ROOT file [93], the number of events to be processed, and the global verbosity level of logging information printed to the terminal. Modules are then listed in the order in which they should be processed. Every module contains its own set of configurable values, ranging in scope from adapting the algorithm method itself to smaller changes to the output histograms.

An example of the detector configuration file can be seen in Figure 6.2. This describes the position, orientation, and properties of each detector plane in the data taking set-up. It is in this configuration file that the roles of each detector are defined, such as being a 'DUT'. The detector given the role of 'reference' functions as an anchor for relative alignments. In addition, all correlations histograms are made with respect to this plane, which measure the relative difference in position between two planes. Devices that provide additional information to the reconstruction other than pixel data, such as trigger signals from a Trigger Logic Unit (TLU), should have the role of an 'auxiliary' device. Devices with this assignment do not participate in the reconstruction algorithms, only in the event building process.

```
[Corryvreckan]
run_time = 700s
log_level = "WARNING"
detectors_file = "Alignment_file.geo"
histogram_file = "histogram_file.root"

[EventLoaderEUDAQ2]
file_name = "tbdata/my_data_file.raw"
```

Figure 6.1: An example section of a Corryvreckan main configuration file, showing configuration parameters of the framework and of a module.

```
[MyDetector]
mask_file = "pixels_to_mask.txt"
material_budget = 0.001
number_of_pixels = 200, 200
orientation = 0.4deg, -0.1deg, 1.2deg
orientation_mode = "xyz"
pixel_pitch = 50um, 50um
position = 150um, 30um, 1.1mm
spatial_resolution = 14.4um, 14.4um
time_resolution = 20us
type = "my_prototype"
role = "dut"
```

Figure 6.2: An example section of a Corryvreckan detector configuration file, specifying the properties of one device.

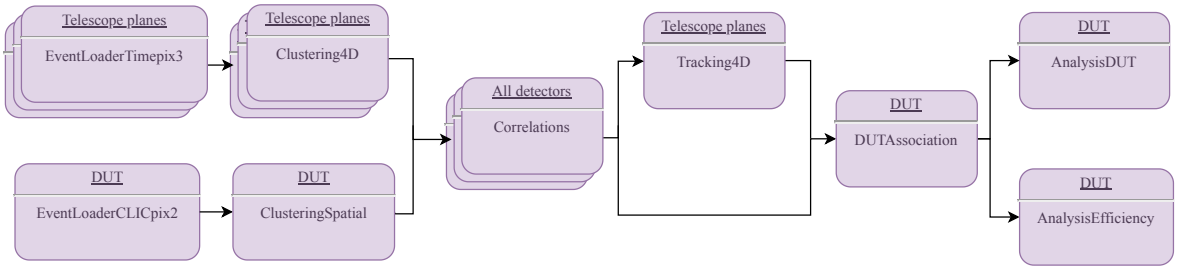

Figure 6.3: Diagram of a typical Corryvreckan module chain for reconstruction of a telescope set-up containing a DUT, using an aligned geometry set-up.

6.2 The modular reconstruction chain

Data reconstruction in Corryvreckan requires an input of raw data and a set of selected modules to perform the desired reconstruction and analysis tasks. A typical module chain for test-beam data requires the following types of modules: an event loader to convert the input data into pixel objects; a clustering module to combine neighbouring pixels into clusters; a tracking algorithm to combine clusters from telescope planes into track objects; a DUT-track association module; and finally modules to determine the desired DUT performance parameters. The choice of modules and their configuration is highly dependent on the data being analysed. Additional modules can be flexibly inserted or removed as required to create the desired chain of processes for the particular use case. The modular algorithm design allows reconstruction chains for different data sets to be quickly set-up.

In the example reconstruction chain shown in Figure 6.3, raw data from Timepix3-type telescope planes are converted into pixel objects. Clustered pixels are reconstructed into tracks, which are then associated with clustered pixel data from a CLICpix2-type DUT. Analysis plots are produced using this information to determine different performance parameters of the DUT. Correlation plots of the clustered data from all detectors are produced at an intermediate stage, so that the user can verify that the planes are well aligned in space and time. It should be noted that this reconstruction chain assumes an aligned geometry set-up, where alignment is discussed in Section 6.2.3.

6.2.1 Data input

Data can be loaded into Corryvreckan either as raw data or data objects. Event loader modules are used for raw data files and are specific to a data structure, so the correct event loader should be chosen

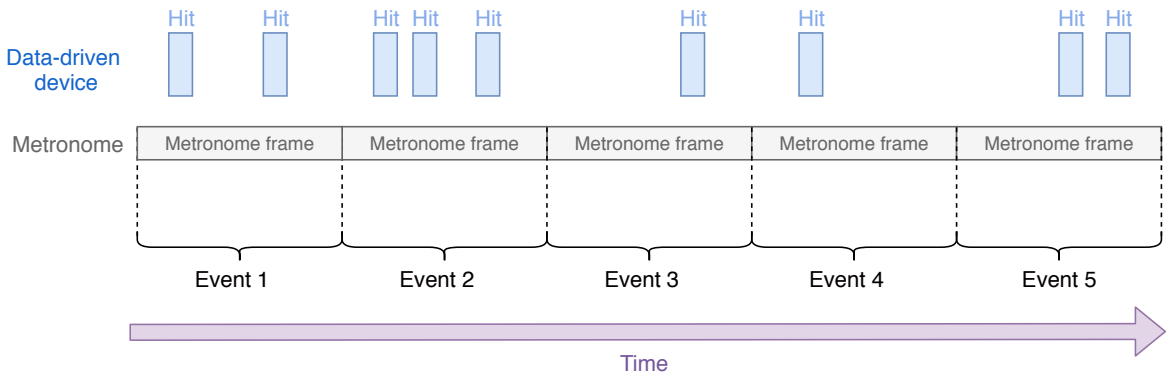

Figure 6.4: Schematic of the Corryvreckan event definition by the `[Metronome]` module.

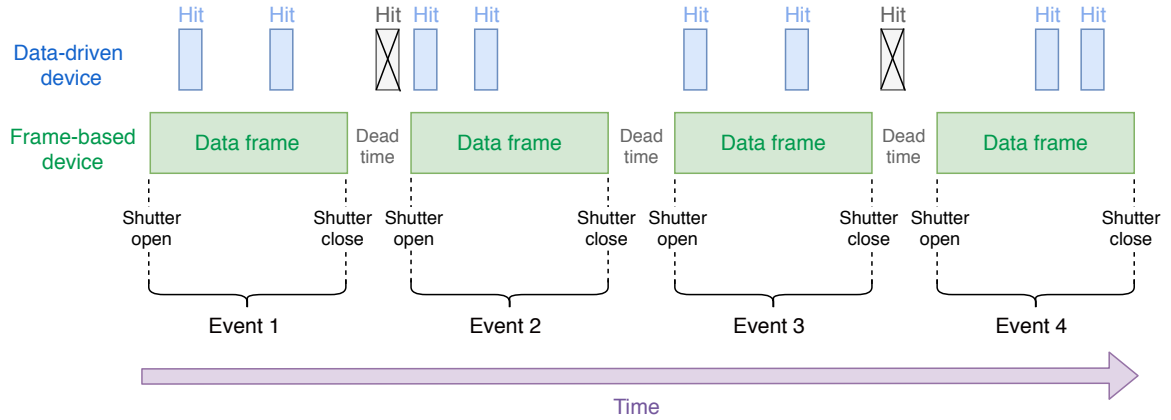

Figure 6.5: Schematic of the Corryvreckan event definition by a detector using a frame-based readout. The event building is configured to only add data from the data-driven detector if it is fully contained within the event time-window.

for each detector. These modules process the input file, storing the pixel hit parameters as pixel data objects for each event on the clipboard. Certain event loaders can read in calibration files for charge or timing measurements, applying this calibration to the pixel data before storing it on the clipboard. Corryvreckan data objects output using the `[FileWriter]` module can be read back into the framework for further analysis using the `[FileReader]` module.

Time-slices of data are defined to help process the input files in smaller data packets. In the reconstruction event loop, an event is fully processed on the clipboard before moving on to the next time slice. The detector whose data is processed first defines the event, where the order is given in the main configuration file. The defined event length depends on the combination of readout schemes used in the set-up. Data from devices with data-driven, frame-based, and triggered readout schemes can be easily combined in the same reconstruction chain.

A data-driven readout scheme has no innate time partitions. In the case where a data-driven device is first detector processed, the event length is user defined using the `[Metronome]` module. This partitions the data into events of a fixed, configured length starting from 0 seconds, as shown in Figure 6.4.

When a frame-based device defines the Corryvreckan event, the start and end signals of the frame designate the time window as shown in Figure 6.5. Data recorded by another device in the set-up is added to the event if it is within the defined time window, as illustrated. This exclusion allows the efficiency of frame-based devices to be accurately measured despite the dead-time outside of an acquisition frame.

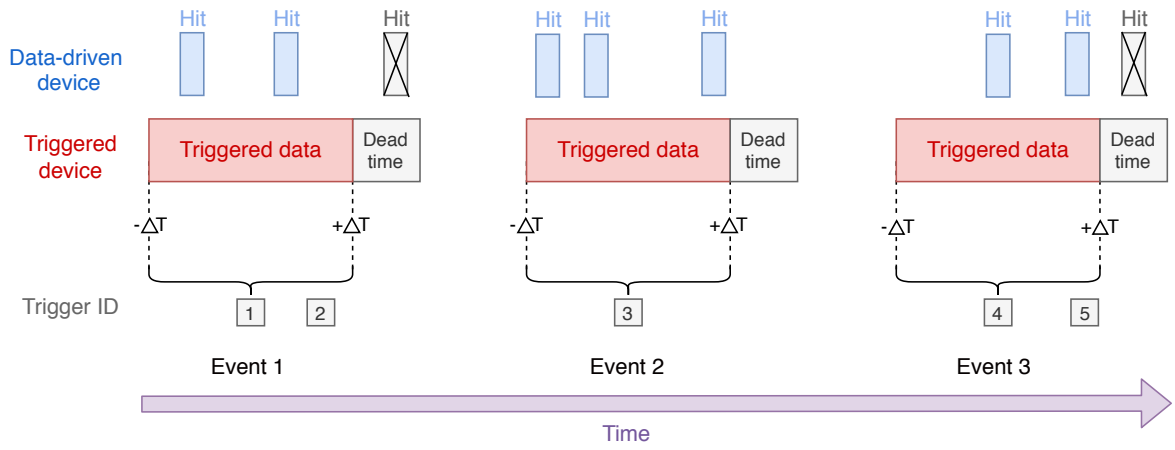

Figure 6.6: Schematic of the Corryvreckan event definition by a TLU, combining trigger ID and timing information. The event is defined in time by the trigger timestamp and an optional time window indicated by $\pm\Delta$T.

Finally, triggered devices can define the Corryvreckan event object. If only triggered devices are included in the reconstruction, no timing information is necessary. Each event is defined by a single trigger ID from the first reconstructed device, and all subsequent data streams are matched to the appropriate trigger ID. However, if a mixture of readout schemes are combined, then the determination of the event is more complex. In such a case, a device that records both trigger ID and timing information can be used to combine the data streams. Alternatively, a time-window around the trigger signals can be defined that accounts for the integration time of the triggered detectors. Figure 6.6 shows the situation where a configured time-window of $\pm\Delta T$ is set around the trigger signals. Data from the triggered detector is added to the correct event by matching the trigger ID numbers stored in the data stream, and pixel data from the data-driven device is stored in the event if it is within the configured window.

It should be noted that the examples given assume a common clock frequency or trigger signals can be used to synchronise the data streams in time.

6.2.2 Usage of timing information in reconstruction

Using timing information during clustering, track formation, and DUT cluster-track association improves the accuracy of these algorithms by reducing the combinatorics, minimising association errors, and reducing the impact of noise hits. The magnitude of each timing cut can either be defined as an absolute value or as a multiple of the timing resolution of the device.

Clustering algorithms combine neighbouring pixels likely to have originated due to charge sharing from the same incident particle. If per-pixel charge information is available, the centre of each cluster is calculated using a charge-weighted centre-of-gravity algorithm. The `[Clustering4D]` module uses both spatial cuts along the X and Y axes, and a time frame cut to associate pixels to clusters. Timing cuts in this module allow individual clusters to be recovered accurately in very high-rate environments.

Tracking algorithms add clusters from successive telescope planes along the Z axis to a track model. Currently two track models are available: a straight line model which does not account for multiple scattering; a General Broken Lines (GBL) track model [94] that models scattering by having kink angles for each scattering material with a linear propagation in between. The `[Tracking4D]`

modules applies both timing and spatial cuts for particle track reconstruction, reducing the combinatorics of the algorithm and allowing tracks to be accurately reconstructed in high-rate or noisy environments.

Similarly, clusters from a DUT plane are associated with tracks by the `[DUTAssociation]` module, where employing timing information minimises the chance of misassociation and therefore inaccurate DUT performance evaluation.

6.2.3 Telescope and DUT alignment

The physical position and orientation of the detector planes may not be known to a high precision. Algorithms utilising the reconstructed tracks can adapt the initial detector geometries until accurately aligned.

Aligning the geometry of a multi-plane system is a common problem for reconstruction software packages. Corryvreckan offers multiple modules dedicated to alignment that perform different algorithms and affect detectors of different roles. It is intended that the user will run a selection of these modules in iterative succession, until a stable and accurate alignment is produced. The choice of alignment modules to use should be based on the accuracy of the initial alignment of the detector planes. A dedicated guide to alignment is available in the Corryvreckan users manual.

The pre-alignment module performs a positional alignment by centering the correlation residuals between the detector and the designated reference plane.

The telescope planes can be simultaneously aligned using two separate modules, where both are based on reconstructed tracks and perform translational and rotational alignments. The first telescope alignment module uses a track χ^2 minimisation algorithm. The second is based on the Millepede algorithm [95], which allows local and global alignment parameters to be fit simultaneously. It should be noted that the track model used for track formation is configurable, and the choice of model may affect the outcome of the alignment.

Finally, the DUT is aligned by minimising the unbiased residuals calculated from the track intercepts with the plane. This process therefore requires the telescope alignment to be performed before the DUT alignment.

6.2.4 η correction

The position of a cluster is defined as the cluster centre, calculated using a charge-weighted centre-of-gravity algorithm where a linear sharing of charge between pixels is assumed. An η distribution can be used to correct the calculated cluster centre for non-linear charge sharing within the sensor using a tracking-based method.

To apply an η correction for a device in Corryvreckan, two modules are required. Firstly, the η correction is calculated along the X and Y axes separately using the `[EtaCalculation]` module, where only clusters with a width of two along the considered axis are included in the calculation. The DUT-track intercept position and the associated DUT cluster centre are compared within a 2-pixel unit cell and the resulting profile distribution is fit with a user-defined function.

The second η correction module should replace the first in a new reconstruction. By using the calculated fit function parameters as input, the `[EtaCorrection]` module corrects the cluster centre position of DUT clusters to that of the corresponding track intercept position.

6.2.5 Data and analysis output

Most modules create histograms to help identify possible problems within the reconstruction process or analysis plots for detector evaluation. Histograms are stored in an output ROOT file for the user, but can also be viewed using the `[OnlineMonitor]` module. This module creates a pop-up

window during the event loop, providing an interactive Graphical User Interface (GUI) displaying a configurable set of histograms from instantiated modules. Each histogram is continually updated as events are processed. Monitoring GUIs are not only useful for identifying and solving issues in the reconstruction, but also can be used to quickly assess the quality of the data being taking in a test-beam environment due to the high processing speed.

To analyse the performance of a DUT, multiple dedicated modules are available that produce histograms to investigate key performance parameters such as efficiency or timing resolution.

Corryvreckan data objects, such as pixels or tracks, can be output as a ROOT TTree at any point during the reconstruction chain for further independent analysis.

6.3 Documentation and code repository

Documentation and maintenance of the software code repository was an integral part of the work of this thesis.

The Corryvreckan user manual is a continuously updated document available on the Corryvreckan code repository [90]. It contains descriptions of the core framework and module architecture, syntax of configuration files and the Corryvreckan executable, and a guide to alignment procedures. In addition, the functionality of each module is described in detail. The user manual of Corryvreckan version 1.0 is also available as a published document [96].

Corryvreckan code quality is maintained through CI testing, code contribution guidelines, and code review.

Updates to the Corryvreckan code are checked on the code repository using an automatic series of CI tests. First, the updated code is compiled on all supported platforms to identify any compilation warnings or errors. A number of selected data sets are then reconstructed using differing sets of modules. By comparing these results to those gained previously, the code modification is ensured to reproduce the same results. The formatting of the source code then is checked, helping to maintain a consistent code style across the software. Finally, the documentation is compiled to ensure no compilation errors occur.

Any issues can be reported or questions discussed with the Corryvreckan maintainers on the repository issue tracker. When a merge request to add code to the main repository is created, the maintainers check the functionality and quality of the code, as well as the level of documentation provided.

Chapter 7

Test-beam data reconstruction

The reconstruction of test-beam data in Corryvreckan generally uses the same algorithmic steps, as discussed in Section 6.2. However, careful consideration should be paid to the choice and configuration of each Corryvreckan module to account for differences between test-beam telescopes. Depending on the set-up, the event building scheme, track model, and acceptance criteria employed can vary significantly. In addition, the type of Device Under Test (DUT) can influence the choice and configuration of modules for event construction, DUT-track association, and DUT performance evaluation.

The test-beam telescopes used in this study are introduced in Chapter 5. Each telescope plane of the Compact Linear Collider detector and physics (CLICdp) Timepix3 telescope records per-pixel timing information, therefore the event building and 4D track reconstruction process is relatively simple. The combination of readout schemes employed in the EUDET Mimosa26 test-beam telescope leads to a more complex Corryvreckan configuration. In both measurement campaigns, a CLICpix2 planar sensor assembly was used as the DUT. The two assemblies with the highest interconnect quality, assessed in Section 4.3, were chosen.

The Corryvreckan configurations used in this study for test-beam reconstruction and DUT performance analysis are presented in this chapter. For each facility, the test-beam data sets recorded, the Corryvreckan modules and configuration chosen for reconstruction, and the calculated telescope resolution are discussed. In addition, an analysis of the temperature recorded during each test-beam data taking period is performed to assess the temperature change of the CLICpix2 planar sensor assemblies.

7.1 Reconstruction of CLICdp Timepix3 telescope test-beam data

Test-beam data was taken in November 2018 using the CLICdp Timepix3 telescope, described in Section 5.2. It should be noted that during this study the data from the last Timepix3 plane in Z is excluded, therefore six telescope planes are used in the reconstruction process. CLICpix2 planar sensor assembly 16 is used as the DUT. It has a 130 µm thick silicon sensor produced by FBK-CMM, a nominal operational threshold of $(626 \pm 8)e^-$, and an interconnect quality of 99.6%.

The data runs recorded can be separated into two data sets based on how the CLICpix2 detector was operated. The first set used an applied bias voltage of -60 V, a nominal threshold of 626 e^-, and a simultaneous 8-bit Time of Arrival (ToA) and 5-bit Time over Threshold (ToT) data taking mode. In the second data set, the applied bias voltage was varied from -5 V to -65 V in steps of 5 V, while the device was operated at nominal threshold in a simultaneous 8-bit hit count and 5-bit ToT data taking mode. Due to the difference in per-pixel information between the timing data and bias voltage scan, the reconstruction for each data set will differ in terms of the selection range used.

Table 7.1: Temperature measurements of four Timepix3 planes within the CLICdp Timepix3 telescope at the SPS test-beam facility. The data spans the period 6.30pm 09/11/2018 to 8.04am 12/11/2018.

Timepix3 plane	**Lowest temperature** (°C)	**Highest temperature** (°C)	**Average temperature** (°C)	**Maximum temperature change** (°C)
A	57.0	58.9	58.1	1.9
B	63.4	65.5	64.8	2.1
C	59.3	61.1	60.4	1.8
D	59.9	61.7	60.9	1.8

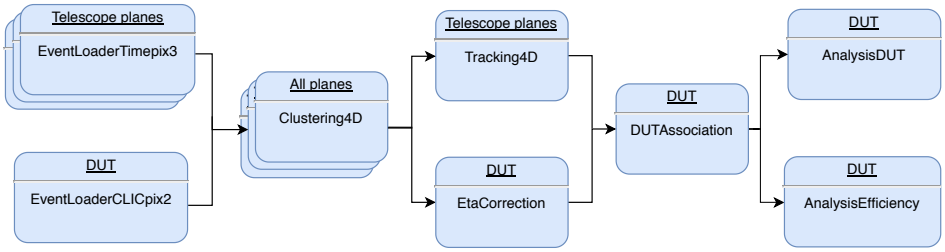

Figure 7.1: Diagram of the Corryvreckan modules used to reconstruct test-beam data taken using the CLICdp Timepix3 test-beam telescope with a CLICpix2 planar sensor assembly DUT.

7.1.1 Temperature analysis of test-beam data

The voltage Digital to Analogue Converters (DACs) of the CLICpix2 readout chip have a temperature dependent output, as discussed in Section 4.4. This could significantly impact the CLICpix2 planar sensor performance, since the applied threshold is affected by this dependence. The temperature change of the CLICpix2 assemblies during the test-beam period is therefore analysed using the on-chip temperature measurement described in Section 3.1.2.

The on-chip temperature of the CLICpix2 DUT was not recorded during the November 2018 test-beam period at the CERN Super Proton Synchrotron (SPS) facility, therefore the direct chip temperature cannot be investigated. The recorded temperature of the Timepix3 telescope planes can be used to investigate the environmental temperature variations within the enclosing metal box of the set-up, since both the telescope planes and the DUT were cooled by the same fan system. Table 7.1 presents the temperature readings recorded by four of the six used telescope planes over the entire data taking period. Although the absolute lowest, highest, and average temperatures fluctuate between the devices, the maximum change in temperature is approximately 2 °C.

The telescope planes use a different readout chip, data readout mode, and have a different position with respect to the fan compared to the DUT. A direct extrapolation therefore cannot be made from the effect environmental temperature has on the Timepix3 planes to the CLICpix2 detector. To have a conclusive measurement of how temperature affects the performance of CLICpix2 planar sensor assemblies during test-beam data taking, on-chip temperature readings are required, as discussed in Section 7.2.1.

7.1.2 Corryvreckan configuration

The Corryvreckan configuration files used to reconstruct the data taken can be found in Appendix B, and a diagram showing the Corryvreckan modules used can be seen in Figure 7.1.

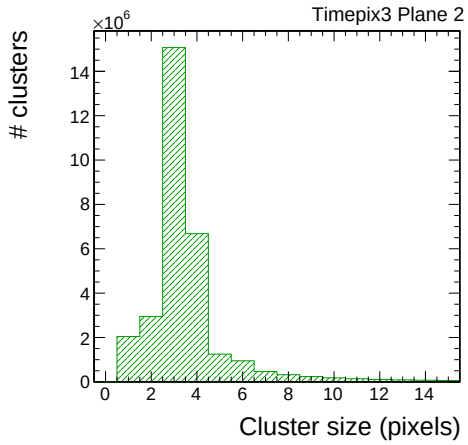

Figure 7.2: Cluster size distribution of telescope plane 2 of the CLICdp Timepix3 test-beam telescope.

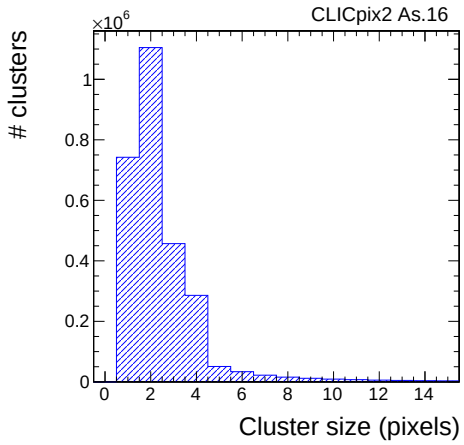

Figure 7.3: Cluster size distribution of CLICpix2 planar sensor assembly 16, before DUT-track association.

Event loaders: The `[EventLoaderCLICpix2]` module is placed first in the main Corryvreckan configuration file. The timestamps of the shutter open and close signals of the CLICpix2 readout frames are used to define events on the clipboard, in the method described in Section 6.2.1. For CLICpix2 data in ToT and hit-count data readout mode each frame is of length 600 µs, while when timing information was recorded the frame length is 2.5 µs. In addition, the ToT calibration calculated in Section 4.5.2 is applied to the DUT pixels within this module. The appropriate Timepix3 pixel data is added to the clipboard event using the per-pixel timestamps.

A time offset exists between the Timepix3 and CLICpix2 data streams due to the time it takes for the reset signals from the Trigger Logic Unit (TLU) to reach each set of detectors. Using the CLICpix2 data where ToA information is available for each pixel, this offset is calculated to be 93 ns from the measured timing correlations. This correction is declared in the geometry configuration file, and the shutter open and close timestamps are adjusted accordingly before defining the clipboard event.

Clustering: Pixels from each detector are clustered using a nearest-neighbour method with additional timing selection criterion, as discussed in Section 6.2.2. For the CLICpix2 data taken in ToT and ToA mode, an acceptance range of ± 20 ns is used. A timing selection criterion of 60 ns is used for the telescope planes. Per-pixel timing information is not available for the other CLICpix2 data set, therefore a timing selection range that encompasses the entire 600 µs frame is used.

Each cluster is assigned a position, charge, and timestamp. A charge-weighted centre-of-gravity algorithm calculates the cluster centre, while the cluster charge is the sum of all associated pixel charge. The cluster timestamp is that of the pixel with the highest charge, known as the seed pixel. Figure 7.2 presents the cluster size of the first telescope plane in Z. The detector has a most probable value (MPV) of cluster size of three pixels, which is expected due to the 9° rotation of the telescope planes around the X and Y axes. Figure 7.3 shows the size of all clusters on the DUT. The mean DUT cluster size is larger than one pixel, as expected due to the 25 µm pixel pitch and sensor sensor thickness of 130 µm.

η ***correction***: The in-pixel DUT cluster position is corrected for non-linear charge sharing using the tracking-based method outlined in Section 6.2.4. A correction function was calculated for each data run separately as each run has a separate geometry alignment. An example η distribution for a run is shown in Figure 7.4 for the X axis of CLICpix2 planar assembly 16 when operated at the

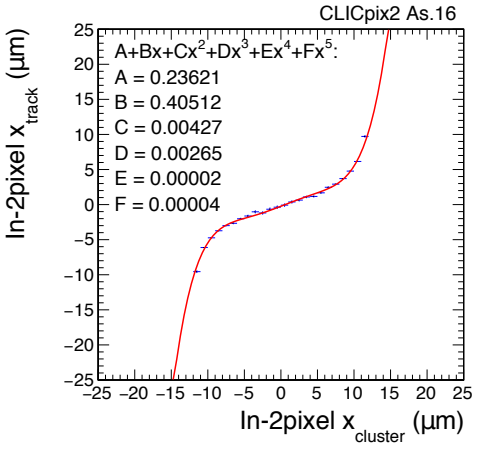

Figure 7.4: η distribution for in-pixel cluster position correction for CLICpix2 planar sensor assembly 16 operated at a threshold of 626 e^- and an applied bias voltage of -25 V within the CLICdp Timepix3 test-beam telescope.

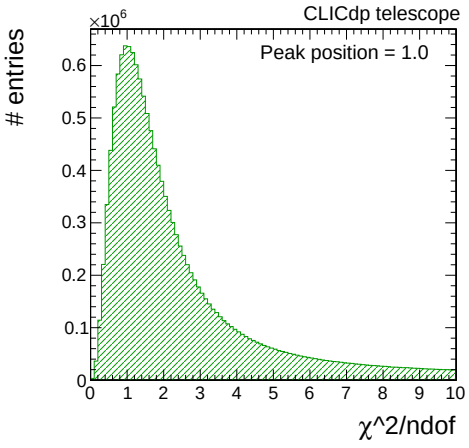

Figure 7.5: χ^2 per NDOF of reconstructed tracks using a GBL track model for data taken with the CLICdp Timepix3 test-beam telescope.

nominal threshold and a bias voltage of -25 V. Due to the statistical limitations of some data runs, the entire run time was used to calculate the correction function. This could bias the DUT position however, using a number of high statistics runs, any effect on the residual width outcome is found to be below the level of uncertainty. The distribution is non-linear near the interface between the two pixel cells, and therefore the η function can correct the in-pixel cluster position to account for this effect. The X and Y η distributions of each run are parameterised using a fifth order polynomial fit function, and used to correct the in-pixel cluster position before track-DUT cluster association.

Tracking: The 120 GeV particle momentum of the SPS beam means that a minimal amount of multiple scattering occurs within the set-up. A General Broken Lines (GBL) track model is used to account for these small deviations. Both timing and spatial acceptance criteria are used to associate clusters from each telescope plane to the track model, with values of 50 µm and 60 ns respectively. One associated cluster from every Timepix3 detector is required for track formation, and the track time is taken as the average time over the six clusters. The χ^2 per number of degrees of freedom (NDOF) is shown in Figure 7.5, a measure of how well the reconstructed tracks fitted the track model. The distribution peaks at a value of 1.0 and decreases to higher χ^2 per NDOF values. The spatial acceptance range was tuned to reduce the number of tracks with high χ^2 per NDOF values, while maintaining a high total number of reconstructed tracks. From this distribution, a value of 3 χ^2 per NDOF is deemed appropriate to exclude high χ^2 per NDOF tracks from the DUT analysis.

Track-DUT cluster association: Clusters from the CLICpix2 detector are associated to reconstructed telescope tracks using spatial and timing acceptance criteria. For the DUT data taken in ToT and ToA mode, an acceptance range of 20 ns is used between the DUT cluster time and the track time. The data set taken in ToT and counting mode uses a timing selection criterion of ± 300 µs to cover the entire CLICpix2 readout frame length. For all data, a spatial selection criterion of 20 µm is used between the track incidence point and the nearest pixel in a cluster. Using the nearest pixel prevents efficiency loss from δ-electrons, where the cluster centre is further from the track incidence point due to the secondary charge deposition.

The spatial association criterion can significantly change the hit detection efficiency obtained for

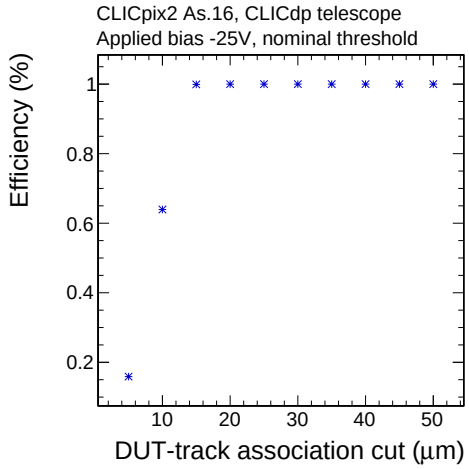

Figure 7.6: Hit detection efficiency as a function of spatial association criterion between DUT clusters and track incidence position, for CLICpix2 planar sensor assembly 16.

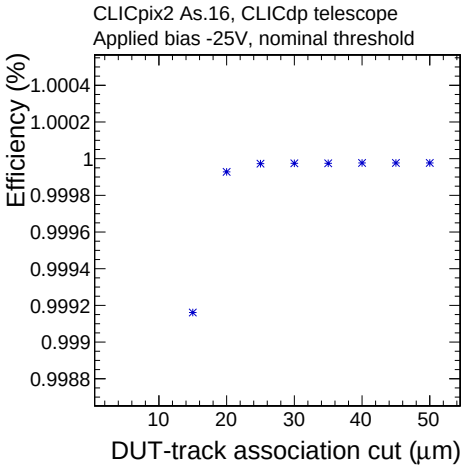

Figure 7.7: Hit detection efficiency as a function of spatial association criterion between DUT clusters and track incidence position for CLICpix2 planar sensor assembly 16, zoomed into the high efficiency region.

the DUT. Any track outside spatial acceptance range due to a mismatch between predicted track position and real track position caused by, for example, the multiple-scattering tails of track residuals will significantly effect the measured efficiency. A value of 20 µm is determined using Figures 7.6 and 7.7. Runs with the same DUT operating conditions were reconstructed using spatial selection ranges from 5 µm to 50 µm, and the efficiency was measured using the `[AnalysisEfficiency]` module. It should be noted that all telescope tracks with a χ^2 per NDOF > 3 are excluded. The histogram trend shows efficiencies higher than 99.95% are obtained for acceptance criteria $\geq$20 µm, and the efficiency steeply decreases for values $<$20 µm. A spatial acceptance range of 20 µm is therefore chosen for track-DUT cluster association.

DUT performance: The remaining two modules are used to assess different DUT performance figures of merit. Within each of these modules, only tracks with a χ^2 per NDOF $\leq$3 are used. Additionally, all tracks incident in the three columns or rows closest to the matrix edge are excluded to mitigate the edge hit-rate effect discovered in Section 4.3.3. The effect is thought to be caused by the staggered active-edge design and the large ratio between pixel pitch and sensor thickness. A smaller sensor to pitch ratio and continuous active-edge design would be used in the CLIC vertex detector, therefore these edge pixels are excluded from the analysis using a region of interest (ROI) cut in the Corryvreckan geometry configuration file.

In addition to those shown in Figure 7.1, Corryvreckan modules were used to align the telescope and DUT planes as explained in Section 6.2.3. The `[MaskCreator]` module recorded the position of pixels with a rate significantly (5σ) higher than the local average for each detector. These noisy pixels are removed from the analysis. For CLICpix2 planar sensor assembly 16, all pixels found to be within categories 1 to 4 inclusive in Section 4.3 are also masked due to their interconnect issues, allowing the efficiency and resolution of the well-bonded regions of the matrix to be assessed. In addition, all pixels neighbouring unresponsive pixels are also masked. In total, 466 pixels are masked.

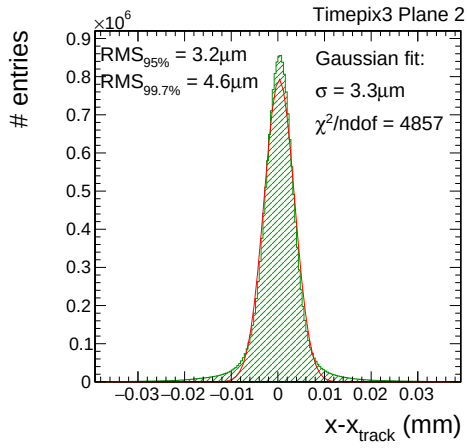

Figure 7.8: Biased track residual along the X axis of telescope plane 2 from the CLICdp Timepix3 test-beam telescope.

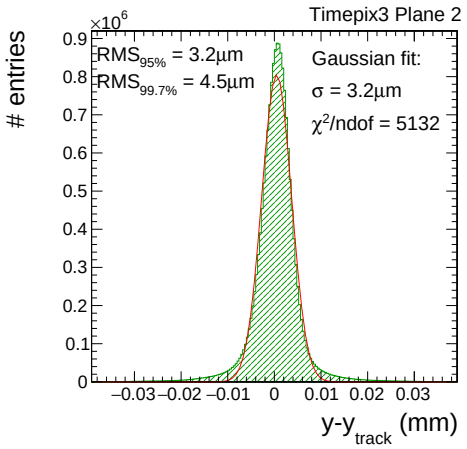

Figure 7.9: Biased track residual along the Y axis of telescope plane 2 from the CLICdp Timepix3 test-beam telescope.

7.1.3 Telescope performance

The biased spatial residuals in X and Y obtained for Timepix3 telescope plane 2, placed directly before the DUT in Z, are shown in Figures 7.8 and 7.9 respectively. The χ^2 of the Gaussian fit functions to these residuals are much larger than the ideal value of 1, caused by the observed non-Gaussian tails. These are thought to occur from tracks with a large χ^2, which are included in these distributions. Each distribution is centred around 0 with a narrow width, showing that the detector is well aligned within the telescope.

The spatial resolution of the reference telescope at the Z position of the DUT was calculated using [97], which models the scattering that occurs within the telescope. Table 7.2 presents the parameters input to the simulation, along with a beam momentum of 120 GeV. The material budget of the Timepix3 assemblies is taken from [65], as is the intrinsic spatial resolution of these rotated planes. Using these values, the telescope resolution at the DUT position is calculated to be 1.85 µm for the November 2018 test-beam data taken. The uncertainty of this value was determined by varying each of the input parameters and recording the resulting resolution change. Each Z position of the planes was independently moved by ±1 mm. The intrinsic spatial resolution of all detectors was simultaneously adapted by ±200 nm, and the material budget of all planes were changed by ±0.5% X_0. These values are motivated by the intrinsic resolution measured in [65] and the observed stability of the telescope set-up. An uncertainty range of (1.85 ± 0.07) µm was calculated. In addition to this uncertainty, the spatial resolution of the CLICdp Timepix3 telescope at the DUT Z position has been shown to differ along the X and Y axes in Monte Carlo simulation studies [65]. The asymmetry is calculated to be 0.1-0.2 µm for the particular plane geometry modelled.

The timing resolution of the CLIC Timepix3 telescope is taken as (1.11 ± 0.03) ns [98].

7.2 Reconstruction of EUDET Mimosa26 telescope test-beam data

Test-beam data was taken in July 2019 using the EUDET Mimosa26 telescope, described in Section 5.3, with CLICpix2 planar sensor assembly 20 as the DUT. Assembly 20 has a 130 µm thick

Table 7.2: Input parameters for spatial resolution simulation of the CLICdp Timepix3 telescope at SPS North Area, CERN. The Z positions were measured for the data taking period of November 2018.

Detector plane	**Z position** (mm)	**Material budget** (% X_0)	**Intrinsic spatial resolution** (µm)
Timepix3, plane 0	0.0	4.0	4.0
Timepix3, plane 1	21.5	4.0	4.0
Timepix3, plane 2	43.5	4.0	4.0
CLICpix2 DUT	105.0	2.4	-
Timepix3, plane 3	186.5	4.0	4.0
Timepix3, plane 4	208.0	4.0	4.0
Timepix3, plane 5	231.5	4.0	4.0

silicon sensor produced by FBK-CMM, a nominal operational threshold of $(665 \pm 9)e^-$, and an interconnect quality of 97.9%, as discussed in Chapter 4. Test-beam data was also taken using CLICpix2 planar sensor assembly 19, used only to assess the on-chip temperature in Section 7.2.1.

Multiple data runs were recorded, which can be separated into six data sets. The first data set is a small number of runs in the simultaneous 8-bit ToA and 5-bit ToT data taking mode using a frame length of 2.5 µs. All other data sets used the simultaneous 8-bit hit count and 5-bit ToT data taking mode with a 2 ms frame length. In the second data set, the nominal threshold is applied to the DUT but the applied bias voltage was varied from 0 V to −60 V in steps of 5 V, with additional runs at a bias of −75 V. To increase the statistics at interesting bias voltages, supplementary runs were taken at applied bias voltages of −25 V and −60 V. Data sets five and six consist of runs at a bias voltages of −25 V and −60 V where the threshold was varied. The threshold was scanned from the nominal value to approximately (16.6 ± 0.2) ke$^-$ with varying step sizes.

7.2.1 Temperature analysis of test-beam data

The temperature of the CLICpix2 assemblies was measured to investigate the effect temperature change may have on test-beam data. An on-chip temperature reading, as described in Section 3.1.2, was inserted into the data streams of CLICpix2 planar sensor assemblies 19 and 20 every 1000 readout frames during each run. Any temperature variations within each run can be observed, as well as between runs.

7.2.1.1 Temperature variation within single runs

Figure 7.10 presents the on-chip temperature change recorded by assembly 19 during two runs: one where a fan was directed at the DUT as pictured in Figure 5.8, and one where the fan was turned off. The time is indicated as the Corryvreckan event number, where events are defined by the CLICpix2 readout frame of length 2 ms, as described in Section 6.2.1 and Section 7.2.2. The on-chip temperature measurement has an uncertainty of ±2.7 °C from the absolute temperature calibration uncertainty. To reduce the error of the measurement to ±0.5 °C, the change in temperature is calculated with respect to the value recorded during the initial frame.

A distinct shape can be seen for both runs in Figure 7.10: an initial increase in temperature followed by a steady plateau. The initial increase in temperature occurs at the same rate for both

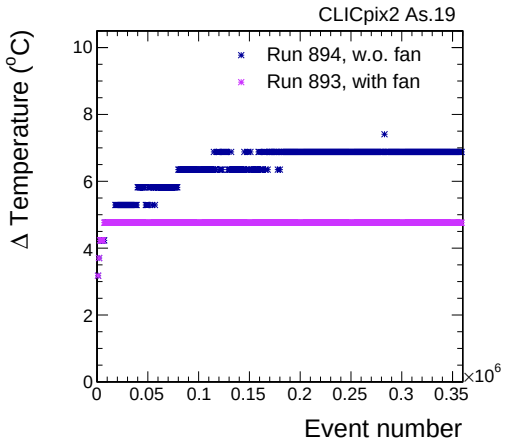

Figure 7.10: Histogram of recorded temperature CLICpix2 assembly 19. Each temperature is measured with respect to the initially recorded value.

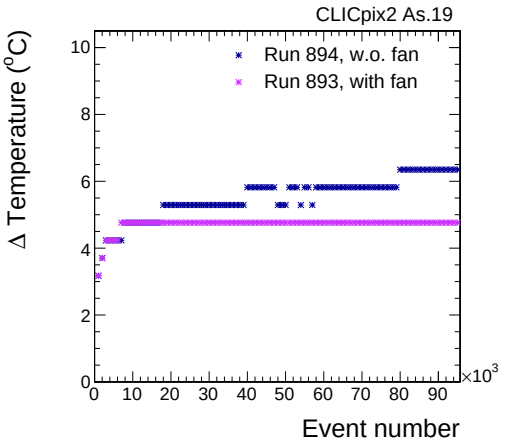

Figure 7.11: Histogram of recorded temperature CLICpix2 assembly 19, zoomed in to show the initial temperature increase. Each temperature is measured with respect to the initially recorded value.

runs, as shown in Figure 7.11. This fan independent temperature increase is attributed to the heat dissipated as the readout chip is powered on at the start of each run. When a fan is applied to the DUT, the temperature increase spans a time period of 14 s. The plateau temperature is dependent on the surrounding air temperature and flow, as a steady value is reached at a lower temperature when a fan is applied to the CLICpix2 device. Over a period of hours, both plateaus maintain a stable temperature within the $\pm 0.5\,^{\circ}\mathrm{C}$ error.

Any change in CLICpix2 chip temperature will change the output of the voltage DACs, including the hit detection threshold of each pixel. By relating the recorded temperatures to the reconstructed test-beam data, the effect of chip temperature change on the measured ToT can be evaluated.

For the same two data runs, a histogram of the cluster ToT was created every 1000 Corryvreckan events. It should be noted that all CLICpix2 clusters are used in this analysis, the ToT is not calibrated into units of e^{-}, and each bin only contained data from 1000 events. By comparing the Corryvreckan event number to Figure 7.10, a value of temperature can be related to each ToT distribution. Every histogram corresponding to the same temperature measurement was summed together to obtain one ToT distribution per recorded temperature difference. The MPV of ToT was extracted using a Landau-Gaussian fit function, motivated by the discussion in Section 1.1.2. The resulting distributions of MPV as a function of temperature change are shown in Figures 7.12 and 7.13 with and without a fan applied to the DUT respectively. It should be noted that the temperature difference used on the X axis is the difference with respect to the initially recorded value in the run, not the temperature change over each 1000 data frames. The errors on the MPV are those obtained from the Landau-Gaussian fit functions.

Figure 7.12 uses a data run where a fan was applied to the CLICpix2 assembly, and the maximum difference in temperature from the initial value is approximately 4.8 °C. The maximum difference in MPV is 0.28 ToT, or less than 0.05 ToT when accounting for the uncertainty of the data points. As only four data points are present in this graph, no conclusive statement can be made on the dependence of cluster charge on temperature.

Figure 7.13 uses the data run where no fan was applied to the CLICpix2 assembly, and hence the range of recorded temperatures is larger. The maximum difference in temperature from the initially

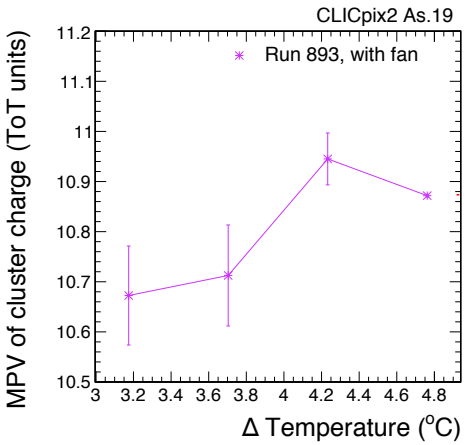

Figure 7.12: Variation of cluster charge MPV as a function of temperature difference with respect to the initial temperature value of the data run, where a fan was applied to the CLICpix2 DUT.

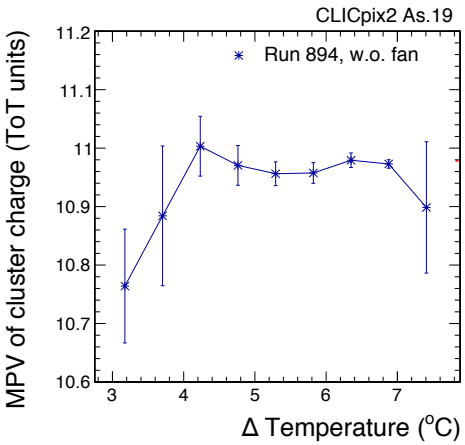

Figure 7.13: Variation of cluster charge MPV as a function of temperature difference with respect to the initial temperature value of the data run, where no fan was applied to the CLICpix2 DUT.

recorded value is approximately 7.4 °C. The maximum difference in MPV is 0.24 ToT over a temperature range of approximately 4 °C, or less than 0.04 ToT when accounting for the uncertainties. The effect of temperature on the cluster charge is deemed to be negligible.

The on-chip temperature when a fan is applied to the CLICpix2 device is stable to within ±0.5 °C after approximately 14 s, and the measured MPV of cluster charge is independent of the chip temperature change. With these results, the effect of temperature within a single run is determined to be negligible.

7.2.1.2 Temperature variation over multiple runs

Although the temperature change within a single run is negligible, the difference over the full data taking period of 30 h could be significant. This is especially relevant for the plateau temperature, which is dependent on the surrounding air temperature and flow.

Test-beam data spanning the 30 h period was analysed using the method described in Section 7.2.1.1. Figure 7.14 shows the results, where the X axis is the time change in hours from the start of the CLICpix2 data taking period. Each bar represents one run, where all temperatures are measured with respect to a single arbitrary temperature reading. The lower edge of the black bar is the initially recorded temperature in the run, and the upper edge of the black bar is the plateau temperature, measured as the average value of the last 20 temperature readings in the run. Each black bar is extended by a grey bar of ±0.5 °C to indicate the uncertainty of each temperature measurement. The red star indicates the mean temperature of the run.

The mean temperature is close to the measured plateau value for all runs, as expected. However, variations are seen in all observables over the 30 h period. Four distinct regions can be seen in Figure 7.14: 0 to 5 h, 8 to 24.5 h, 24.5 to 29 h, and 29 to 30 h.

Runs taken between hours 0 and 5 used CLICpix2 planar sensor assembly 19, while all others had assembly 20 as the DUT. A difference in the temperature calibration between CLICpix2 assemblies is to be expected, explaining the offset in temperature of these runs. All runs using assembly 19 are consistent: measured initial, plateau, and mean temperature values are within ±0.5 °C when comparing each run.

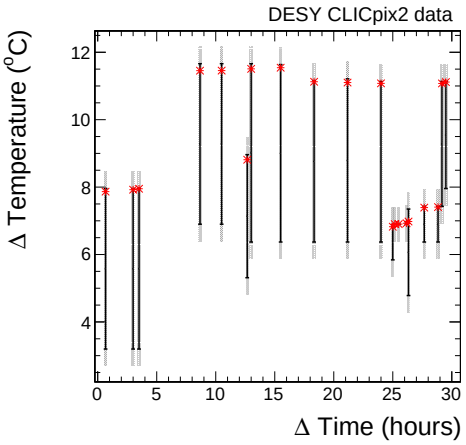

Figure 7.14: Graph of the on-chip temperature change of CLICpix2 planar sensor assemblies over a 30 h period, where each bar represents temperature data from one run. The black bar is the temperature change from the initial value to the plateau temperature, the red star indicates the mean temperature of the run, and the grey bars show the $\pm 0.5\,^{\circ}\mathrm{C}$ measurement uncertainty.

Two data taking modes were used when assembly 20 was the DUT. Periods 8 to 24.5 h and 29 to 30 h employed a simultaneous 8-bit hit count and 5-bit ToT data taking mode. Within each of these runs, the measured mean value is close to the plateau temperature. This shows that the temperature rise time of the detector is small compared to the total length of the run, as observed in Section 7.2.1.1. The plateau and mean temperatures recorded in these runs are within $\pm 0.5\,^{\circ}\mathrm{C}$ of each other, with one outlier at approximately 12.5 h. The CLICpix2 detector had been powered off for a period of approximately 2 h directly before this outlying run, therefore the temperatures recorded were lower. No other runs had a significant time directly before data taking where the DUT was turned off, and the data run directly after records the expected values.

A simultaneous 8-bit ToA and 5-bit ToT data taking mode was used during the timeframe 24.5 to 29 h. The shutter length was shortened from 2 ms to 2.5 µs in this mode due to the increased noise level observed and the ToA counter length. However, the dead-time between CLICpix2 frames is similar for both modes, measured to be approximately 1 ms on average. In addition, the power consumption of the CLICpix2 assemblies is dominated by the analogue circuitry. When in ToT and ToA data taking mode, the assembly spends more time in a low power consumption state compared to shutter length, therefore a smaller overall temperature fluctuation during a run is expected. This is the effect observed in Figure 7.14, where the plateau and mean temperatures are significantly lower than those recorded in ToT and counting mode. One run is seen to have an initial temperature reading lower than all others, however the mean temperature of the run is still within the uncertainty range.

The plateau temperature is dominant for all runs taken within the 30 h period, and the variation of the plateau temperature is within the measurement uncertainty of $\pm 0.5\,^{\circ}\mathrm{C}$ for the same CLICpix2 assembly operated in the same data taking mode. Coupled with the negligible effect of temperature change on the cluster charge MPV within a run, it can be concluded that the effect of temperature on CLICpix2 test-beam data taken with the EUDET Mimosa26 telescope is negligible.

No dependence was observed from environmental temperature changes larger than $2\,^{\circ}\mathrm{C}$, such as the day-night cycle, hence it is also concluded that the affect of temperature on CLICpix2 test-beam data taken with the CLICdp Timepix3 telescope, discussed in Section 7.1.1, is also negligible.

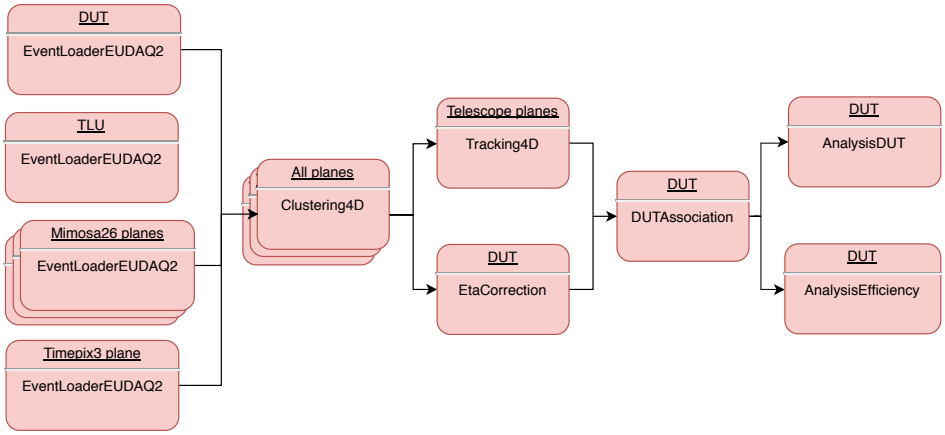

Figure 7.15: Diagram of the Corryvreckan modules used to reconstruct test-beam data taken using the EUDET Mimosa26 test-beam telescope with a CLICpix2 planar sensor assembly DUT.

7.2.2 Corryvreckan configuration

The Corryvreckan configuration files used to reconstruct the data taken using the EUDET Mimosa26 test-beam telescope can be found in Appendix B, and a diagram showing the chosen reconstruction chain can be seen in Figure 7.15. The modules are similar to those described in Section 7.1.2, however significant differences are present in the event building scheme and acceptance criteria used.

Event loaders: Figure 7.16 illustrates the event building scheme employed using the four inputs. The `[EventLoaderEUDAQ2]` module is used for all devices, and is first instantiated for the CLICpix2 DUT. The Corryvreckan clipboard event is therefore defined by the shutter open and close signals of the CLICpix2 readout frames of length 2 ms, with the method described in Section 6.2.1.

The next device considered in the event building is the TLU, which provides trigger signals with an associated ID. A time-window is applied around each trigger signal, ranging from $t-115\,\mu s$ to $t+230\,\mu s$, using the method discussed in Section 6.2.1. This accounts for the maximum integration time of the triggered Mimosa26 detectors [99]. Each trigger is then associated with the clipboard event only if the full time-window is contained within the clipboard event. This method ensures that the efficiency of the CLICpix2 DUT can be calculated accurately, as no telescope tracks outside of the CLICpix2 active time-window are considered.

Pixel data from the Mimosa26 detectors are added to the clipboard by matching the trigger IDs in the data stream to those associated to the Corryvreckan event.

Pixel hits from the Timepix3 device have individual timestamps, which are then matched to the clipboard event window. All Timepix3 data with a timestamp of 2 s or less are excluded from the event building process to remove data taken before the synchronising time signal from the TLU. Sections of Timepix3 pixel data can be stored out of time order, therefore a buffer window can be used to time-sort a selected number of hits before comparing them to the clipboard event. A buffer depth of 100 pixel hits is selected for this analysis, which was found to account for all Timepix3 stored out of time.

In addition to event building, the `[EventLoaderEUDAQ2]` module applies the ToT calibration of CLICpix2 planar sensor assembly 20, calculated in Section 4.5.2, to the pixel data.

Timing correlations between the Timepix3 detector and assembly 20 are determined using the CLICpix2 data set taken in ToT and ToA mode. In this case, the DUT frames of 2.5 µs define the Corryvreckan event. Trigger signals are added to the clipboard without the condition for the full time frame to be fully included in the event, as the CLICpix2 frames are significantly shorter in this case. Mimosa26 and Timepix3 data is then associated as previously described. The offset in time between the data streams is calculated to be 100 ns, and this correction is declared in the geometry

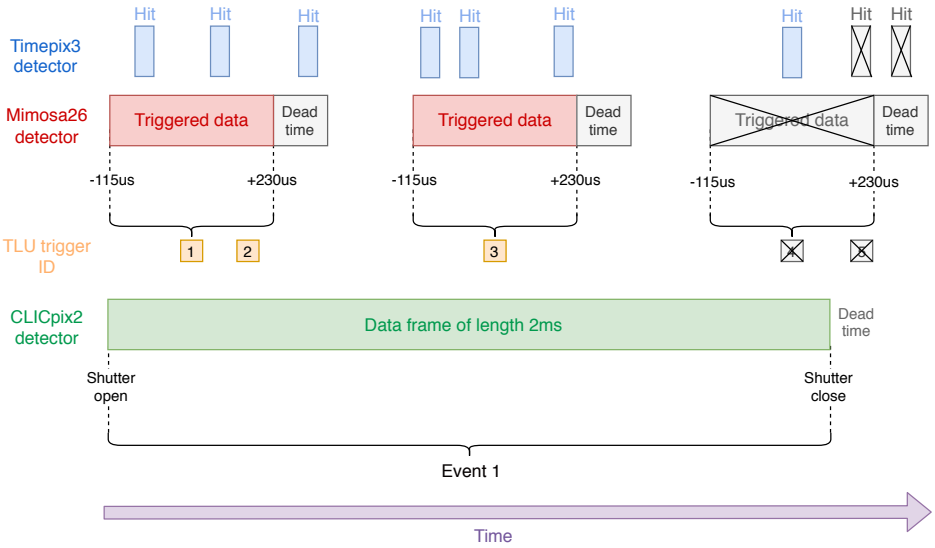

Figure 7.16: Diagram illustrating the event building scheme used in Corryvreckan to reconstruct the test-beam data taken using an EUDET Mimosa26 telescope with a CLICpix2 planar sensor DUT.

configuration file such that the recorded shutter open and close timestamps are adjusted accordingly before defining the clipboard event. As the data set recorded in the simultaneous 8-bit ToA and 5-bit ToT data taking mode is exclusively used to determine the time offset, the reconstruction of this data set was not continued past event building.

Clustering: Pixels from each detector are clustered using a nearest-neighbour method with an additional timing criterion, as discussed in Section 6.2.2. A charge-weighted centre-of-gravity algorithm calculates the cluster centre, while the cluster charge is the sum of all associated pixel charge. The timestamp assigned to each cluster is dependent on the detector type. For the Mimosa26 telescope planes, a timing selection criterion of $\pm 230\,\mu s$ is used and the cluster is assigned the timestamp of the associated trigger signal. As the CLICpix2 data used does not have per-pixel timing information, the timing acceptance range encompasses the full 2 ms frame length and each cluster is assigned the timestamp of the frame centre. An acceptance range of three times the time resolution of the detector was used for the Timepix3 plane, corresponding to 4.7 ns. Figures 7.17, 7.18, and 7.19 present the cluster size distributions of telescope plane 3, the CLICpix2 DUT, and the Timepix3 telescope plane respectively. The Mimosa26 plane has the expected two-peaked cluster size distribution, characteristic of the detector. The two CLICpix2 devices are expected to have similar cluster size distributions, as is observed when comparing Figure 7.3 to Figure 7.18. Compared to Figure 7.2, the cluster size of the Timepix3 detector added to the EUDET telescope has a much smaller mean cluster size. In the CLICdp telescope, the Timepix3 detectors are rotated by 9° around the X and Y axes to increase charge sharing and have a 200 µm thicker sensor layer. A significantly lower cluster size is therefore expected for this Timepix3 assembly, as observed in Figure 7.19.

η correction: The in-pixel DUT cluster position is corrected for non-linear charge sharing using the tracking-based method outlined in Section 6.2.4. An example η distribution is shown in Figure 7.20 for CLICpix2 planar assembly 20 for a particular data run, operated at nominal threshold and a bias voltage of $-25\,V$. The η distribution of each run is parameterised using a fifth order polynomial fit function, and used to correct the in-pixel cluster position before track-DUT cluster association. Due to the statistical limitations of each data run, the entire run time was used to calculate the correction function. This could bias the DUT cluster position, however any effect is found to be lower than the residual width uncertainty using high-statistics runs taken at the SPS facility. As no high-statistics runs are available for CLICpix2 assembly 20, this measurement could not be repeated

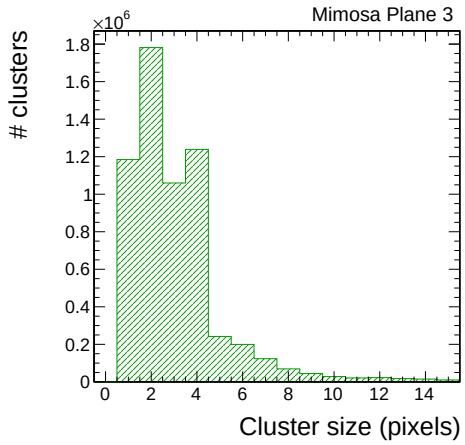

Figure 7.17: Cluster size distribution of telescope plane 3, a Mimosa26 detector, of the EUDET Mimosa26 test-beam telescope.

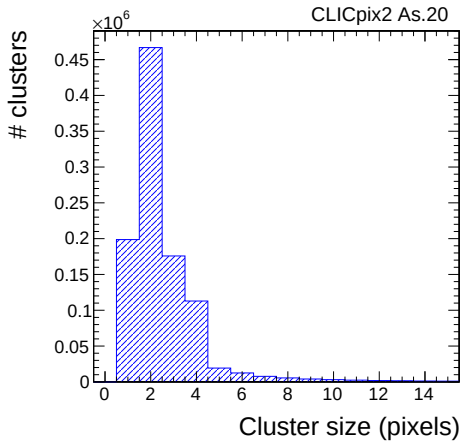

Figure 7.18: Cluster size distribution of CLICpix2 planar sensor assembly 20, before DUT-track association.

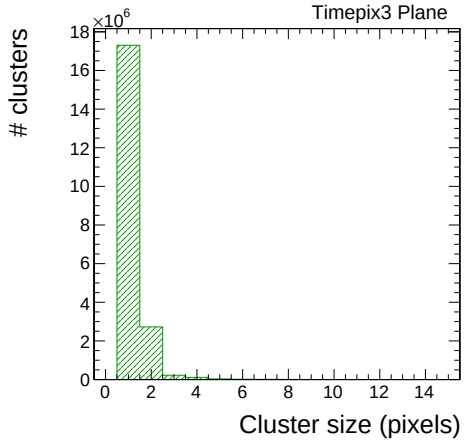

Figure 7.19: Cluster size distribution of telescope plane 6, a Timepix3 detector, of the EUDET Mimosa26 test-beam telescope.

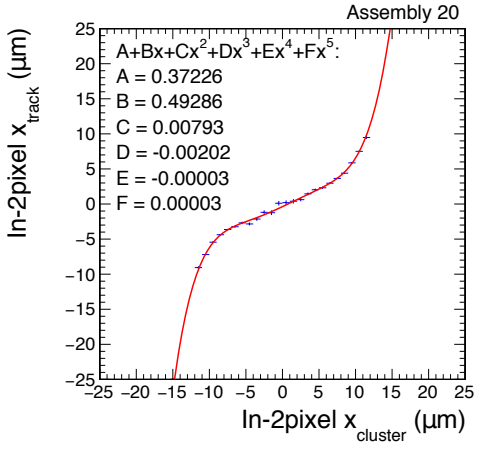

Figure 7.20: η distribution for in-pixel cluster position correction for CLICpix2 planar sensor assembly 20 operated at a threshold of 665 e^- and an applied bias voltage of -25 V within the EUDET Mimosa26 test-beam telescope.

for reconstruction of test-beam data from the DESY facility.

Tracking: Significant multiple scattering occurs when the beam particles traverse the EUDET Mimosa26 telescope, due to the material budget of the set-up combined with the 5.4 GeV beam momentum. To account for the angular deviations the particles make at each detector plane, a GBL track model is used in the test-beam data reconstruction. Clusters from at least six of the seven telescope planes are used for track formation, but a cluster from the Timepix3 detector is required as this defines the timestamp of the reconstructed track. A selection criterion of $\pm 230\,\mu s$ ensures that all Mimosa26 clusters within the readout time are included. To account for scattering and the 55 µm pixel pitch

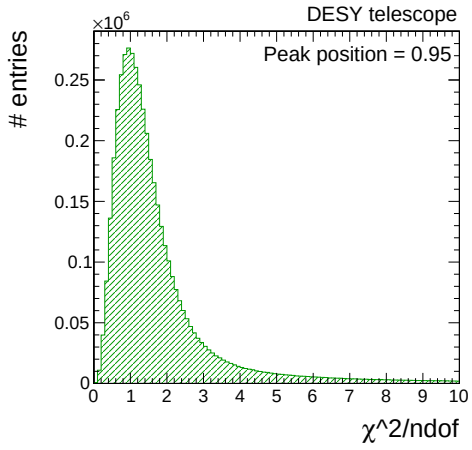

Figure 7.21: χ^2 per NDOF of reconstructed tracks using a GBL track model for data taken with the EUDET Mimosa26 test-beam telescope.

of the Timepix3 detector, a larger spatial acceptance criterion is required for the Timepix3 telescope plane. Appropriate spatial acceptance ranges were estimated using the measured track kink angles, alignment uncertainties, and biased residual of each each telescope plane. These values were found to be approximately equivalent to using a relative spatial range of 27 times the spatial resolution for all planes. This corresponds to an acceptance range of 86.4 µm for the Mimosa26 detectors and 345.6 µm for the Timepix3 detector. Figure 7.21 shows the χ^2 per NDOF distribution obtained for the reconstructed tracks. The distribution peaks at a value of 0.95, which is close to the ideal value of 1, and has a steep decrease to higher χ^2 per NDOF values. A lower proportion of high χ^2 per NDOF valued tracks is seen compared to Figure 7.5. From this distribution, a value of 3 χ^2 per NDOF is deemed appropriate to exclude high χ^2 per NDOF tracks from the DUT analysis.

Track-DUT cluster association: Clusters from the CLICpix2 DUT were associated to reconstructed telescope tracks using 4D selection criteria. To encompass the full CLICpix2 readout frame, a selection range in time of ± 1 ms is used.

The hit detection efficiency of the CLICpix2 detector is expected to decrease and the residual width to increase significantly at high thresholds and high bias voltages. For this reason the spatial acceptance range was determined separately for two scenarios: the nominal threshold of 665 e^- and an applied bias voltage of -25 V, and a threshold of approximately 16.6 ke^- and an applied bias voltage of -60 V. In both cases only telescope tracks with a χ^2 per NDOF of ≤ 3 are used. The resultant histogram of efficiency as a function of spatial association criteria is shown for the first scenario in Figures 7.22 and 7.23. The trend of the histogram shows a high efficiency $>99.95\%$ for acceptance ranges ≥ 25 µm, and that efficiency decreases for acceptance cuts <25 µm. A spatial cut value of 25 µm was therefore chosen, equal to one pixel pitch. Figures 7.24 and 7.25 show the resultant distributions for the second scenario, where the threshold and applied bias voltage are higher in magnitude. A second order polynomial function was fitted to the higher efficiency region of 20 µm to 100 µm. The quadratic profile in this region implies that the efficiency increase is caused by the association combinatorics. Clusters from other tracks within the same time frame are associated, as the acceptance range increases proportional to the radius squared. A spatial criterion of 25 µm was also deemed to be appropriate for this scenario.

DUT performance: The remaining two modules are used to assess different performance figures of merit for the DUT. All tracks incident in the three columns or rows closest to the matrix edge or with a χ^2 per degree of freedom >3 are excluded from the analysis.

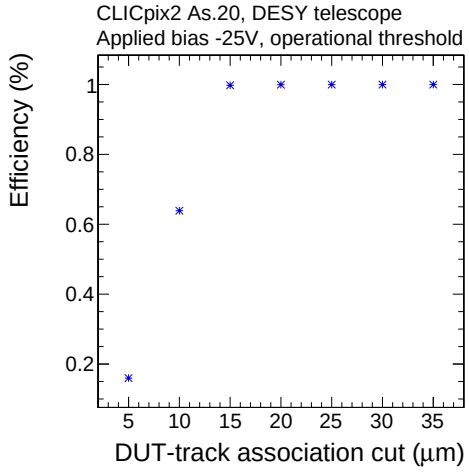

Figure 7.22: Hit detection efficiency as a function of DUT-track spatial association criterion, for CLICpix2 planar sensor assembly 20.

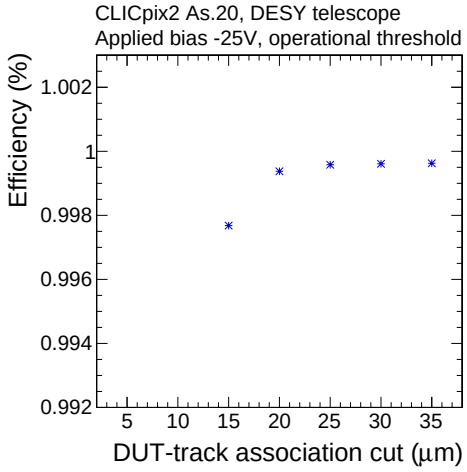

Figure 7.23: Hit detection efficiency as a function of DUT-track spatial association criterion for CLICpix2 planar sensor assembly 20, focussing on the high efficiency region.

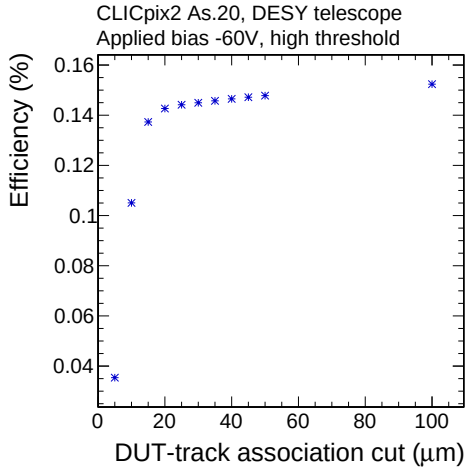

Figure 7.24: Hit detection efficiency as a function of DUT-track spatial association criterion, for CLICpix2 planar sensor assembly 20 operated at a 16.6 ke$^-$ threshold.

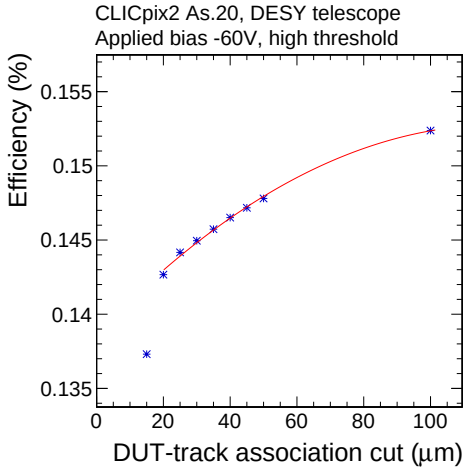

Figure 7.25: Hit detection efficiency as a function of DUT-track spatial association criterion for CLICpix2 planar sensor assembly 20 operated at a 16.6 ke$^-$ threshold, with a 2^{nd} order polynomial function fitted to the high efficiency region.

In addition to those shown in Figure 7.15, modules were used to align the telescope and DUT planes as explained in Section 6.2.3. Due to the increased NDOF in the GBL track model, the alignment of the telescope and DUT plane is more challenging to perform to a high precision. The `[MaskCreator]` module was also used for each detector to detect noisy pixels with a rate significantly higher than the local average, which were subsequently removed from the analysis. For

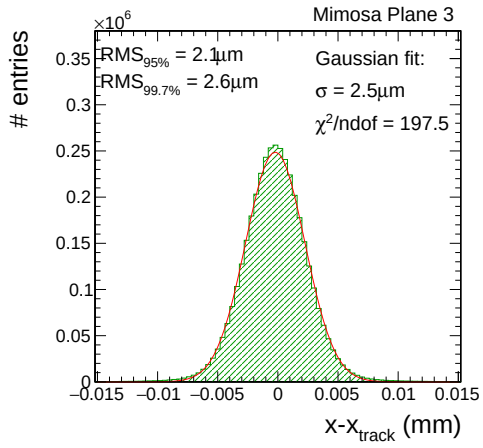

Figure 7.26: Biased spatial residual along the X axis of telescope plane 2, a Mimosa26 detector, from the EUDET Mimosa26 test-beam telescope.

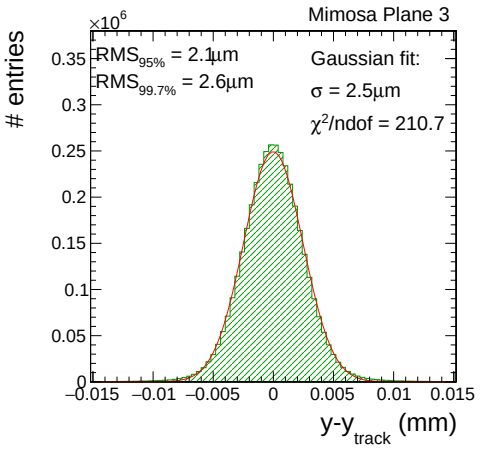

Figure 7.27: Biased spatial residual along the Y axis of telescope plane 2, a Mimosa26 detector, from the EUDET Mimosa26 test-beam telescope.

CLICpix2 planar sensor assembly 20, all pixels found to be within categories 1 to 4 inclusive in Section 4.3 were also masked due to their interconnection issues, allowing the efficiency and resolution of the well-bonded regions of the matrix to be assessed. All pixels neighbouring unresponsive pixels are also masked. In total, 192 pixels are masked.

7.2.3 Telescope performance

The biased spatial residuals along the X and Y axes obtained for the Mimosa26 telescope plane 3, directly after the DUT in Z, are shown in Figures 7.26 and 7.27. Each distribution is centred around 0 with a narrow width, showing that the detector is well aligned within the telescope. Figures 7.28 and 7.29 show the same distributions for the Timepix3 telescope plane. The width of the Timepix3 biased spatial residuals is much larger than that of the Mimosa26 detector due to the larger pixel pitch of the device and the increased amount of scattering that occurs before the Timepix3 plane.

The spatial resolution of the reference telescope at the DUT Z position is calculated using [97], which models the scattering that occurs within the telescope. The parameters in Table 7.3 were used as an input to the simulation, along with a beam momentum of 5.4 GeV. The material budget and intrinsic resolution of the Timepix3 plane are taken from [65], while these values for the Mimosa26 detectors are taken from [81]. It should be noted that the 12.8 µm spatial resolution used is larger than the 4.0 µm value quoted in Table 7.2. The Timepix3 planes of the CLICdp telescope are rotated by 9° around the X and Y axes and have a 200 µm thicker silicon sensor, therefore the spatial resolution is smaller due to the increased charge sharing. Using these values, the EUDET Mimosa26 telescope resolution at the DUT position is calculated to be 2.64 µm for the July 2019 test-beam data taken. The uncertainty of this value was determined by varying each of the input parameters and recording the resulting resolution change. Each Z position of the planes was independently moved by ±1 mm. The intrinsic spatial resolution of all detectors was simultaneously adapted by ±200 nm, and the material budget of all planes were changed by 10% of the original value. An asymmetric uncertainty range of (2.64+0.12-0.14)µm was calculated.

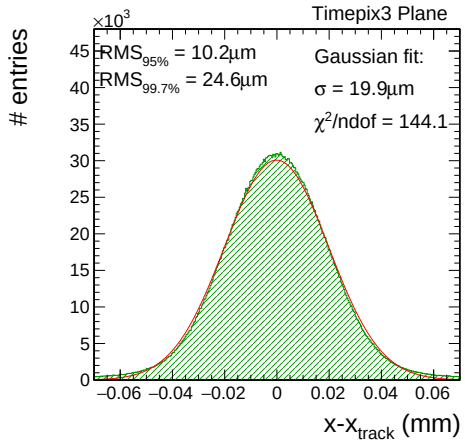

Figure 7.28: Biased spatial residual along the X axis of telescope plane 6, a Timepix3 detector, from the EUDET Mimosa26 test-beam telescope.

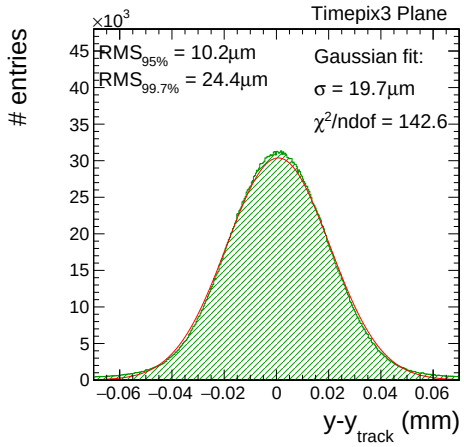

Figure 7.29: Biased spatial residual along the Y axis of telescope plane 6, a Timepix3 detector, from the EUDET Mimosa26 test-beam telescope.

Table 7.3: Input parameters for spatial resolution simulation of the EUDET Mimosa26 telescope at the DESY II test-beam facility. The Z positions were measured for the data taking period of July 2019.

Detector plane	**Z position** (mm)	**Material budget** (**% X_0**)	**Intrinsic spatial resolution** (µm)
Mimosa26, plane 0	0.0	0.076	3.2
Mimosa26, plane 1	153.0	0.076	3.2
Mimosa26, plane 2	305.0	0.076	3.2
CLICpix2 DUT	329.0	2.4	-
Mimosa26, plane 3	346.0	0.076	3.2
Mimosa26, plane 4	455.0	0.076	3.2
Mimosa26, plane 5	565.0	0.076	3.2
Timepix3, plane 6	629.0	4.0	12.8

Chapter 8

CLICpix2 performance

To determine if a prototype detector achieves a specific set of requirement criteria, certain performance figures of merit are measured, as discussed in Section 1.3.3. The prototype detector performance can be measured and compared for different operating conditions, such as hit detection threshold and applied bias voltage, to find the optimal operating values.

This chapter presents the analysis of test-beam data from the two best performing prototype CLICpix2 planar sensor assemblies, determined in Chapter 4 to be assemblies number 16 and 20. The test-beam reconstruction was performed using the Corryvreckan software framework, introduced in Chapter 6, with the configuration described in Chapter 7. First, the amount of charge sharing between pixels is investigated by observing the cluster size and charge under different operating conditions. Then the three main performance figures of merit are presented: hit detection efficiency, spatial resolution, and timing resolution. Each values is compared to the CLIC vertex detector requirements, described in Section 2.3.2.1.

Both assemblies evaluated in this Chapter have a 130 µm thick active-edge silicon sensor produced by the FBK-CMM foundry, high interconnect qualities, and both have threshold and Time-over-Threshold (ToT) calibrations performed. Despite these similarities, a number of differences remain in the data sets recorded for each device. Test-beam data for assembly 16 was recorded using the CLIC detector and physics (CLICdp) Timepix3 telescope in the 120 GeV π^+-proton beam of the SPS facility, while the EUDET Mimosa26 telescope was used for assembly 20 with a 5.4 GeV e^- beam from the DESY-II facility, as described in Chapter 7. The telescopes differ significantly in their design, resolution, and the data reconstruction process used. Assembly 16 also has a lower nominal operational threshold of (626 ± 8) e^- compared to assembly 20, whose nominal threshold is (665 ± 9) e^-.

8.1 Analysis of track-associated clusters

It should be noted that all of the results in this chapter concern clusters from the device under test (DUT) that are associated to tracks, where the association used both spatial and timing acceptance criteria. The choice of acceptance criteria is discussed in Chapter 7.

8.1.1 Cluster size

8.1.1.1 Cluster size as a function of bias voltage

The size of track-associated DUT clusters provides information on the amount and direction of charge sharing within the detector.

Figure 8.1 shows the distribution of cluster sizes for assemblies 16 and 20, when the nominal thresholds and a bias voltage of -25 V is applied. The entries have been normalised to account for the difference in statistics between the data sets. In both cases the most probable value (MPV) is a size of two pixels, which is expected from the large ratio between the 25 µm pixel pitch and sensor

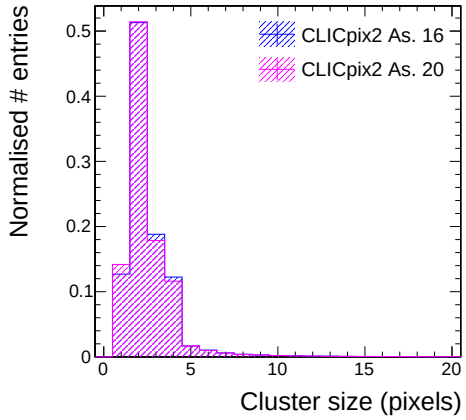

Figure 8.1: Cluster size distribution of assemblies 16 and 20, for the nominal threshold values and an applied bias voltage of −25 V.

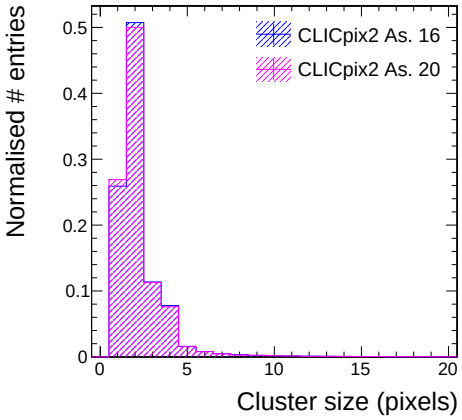

Figure 8.2: Cluster size distribution of assemblies 16 and 20, for the nominal threshold values and an applied bias voltage of −60 V.

thickness of 130 µm. The mean cluster size is larger for assembly 16: fewer one-pixels clusters occur, and more three and four pixel clusters are seen than for assembly 20. This could be attributed to the approximately 0.1 ke^- lower threshold applied for assembly 16 compared to assembly 20, leading to larger amounts of above-threshold charge sharing.

The same trend of higher average cluster size for assembly 16 is also observed at a bias voltage of −60 V. Figure 8.2 is a histogram of normalised cluster size for assemblies 16 and 20, when the nominal thresholds and a bias voltage of −60 V is applied. A higher proportion of two-pixel clusters and a lower proportion of one-pixel clusters occur for assembly 16 compared to assembly 20, although the difference in mean value is not as pronounced as in Figure 8.1. The lower average cluster size at a bias voltage of −60 V observed for both detectors compared to −25 V is expected, as an increase in bias voltage past the depletion voltage causes a reduction in charge carrier diffusion, as discussed in Section 1.1.3. With a lower amount of diffusion, the sharing of deposited charge between pixels is reduced and the measured cluster sizes are smaller. A bias voltage of −60 V is known to be significantly larger than the depletion voltage for the sensor thickness, using Equation 1.15. These cluster size distributions are shown in Figures C.1 and C.2 using a logarithmic scale for reference.

Cluster size is shown to be dependent on the bias voltage applied, therefore a bias voltage exists where maximal amount of charge sharing occurs. Using test-beam data sets where the applied bias voltage was varied, the mean cluster size for different voltages was measured for both detectors as shown in Figure 8.3. The uncertainty of the mean value is shown by bars along the Y axis. Any uncertainty in the applied bias voltage is assumed to be negligible. A clear peak in mean cluster size occurs at a bias voltage of −25 V for both CLICpix2 planar sensor assemblies. For reverse bias voltages larger than −25 V, the decreased diffusion reduced the mean cluster size. When a bias voltage lower than −25 V is applied, the reduced cluster size suggests that the sensor is not fully depleted. A reduced depletion depth causes fewer electron-hole pairs to be measured, reducing the mean cluster size. Using Figure 8.3, the depletion voltage is estimated to occur between −25 V and −20 V for these detectors. In this figure, the systematically higher total cluster size for assembly 16 compared to assembly 20 can be observed at every bias voltage.

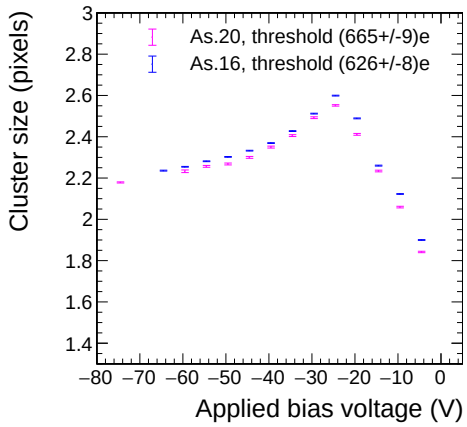

Figure 8.3: Mean cluster size of assemblies 16 and 20 as a function of the applied bias voltage, where the threshold of each detector is set to the nominal value.

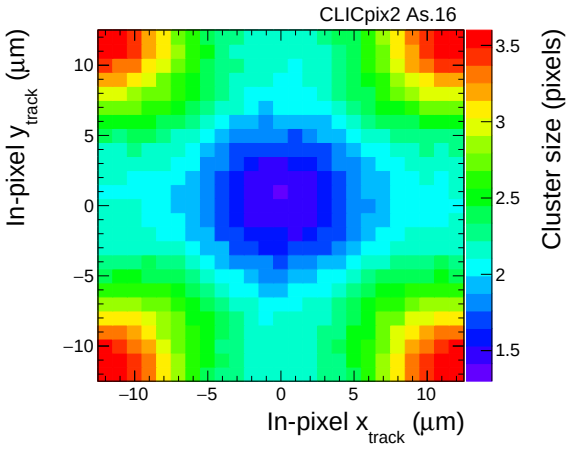

Figure 8.4: In-pixel cluster size distribution of assembly 16 operated at a bias voltage of −25 V and nominal threshold.

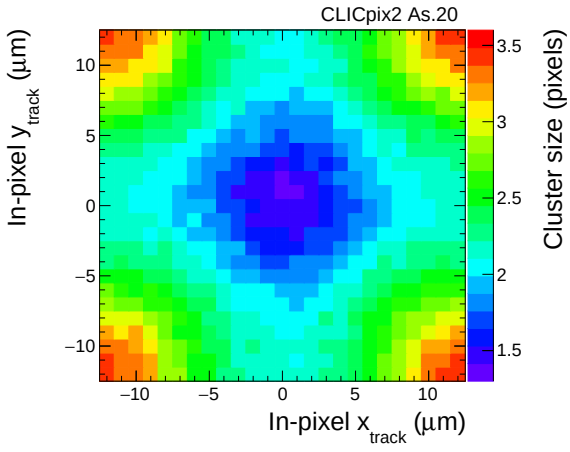

Figure 8.5: In-pixel cluster size distribution of assembly 20 operated at a bias voltage of −25 V and nominal threshold.

8.1.1.2 In-pixel cluster size

To further investigate the systematic difference in cluster size between the assemblies, in-pixel 2D histograms are produced of the cluster size. In Figures 8.4 and 8.5, each DUT cluster size is filled at the in-pixel incidence position of the associated track for assemblies 16 and 20 respectively. Both detectors are operated at an applied bias voltage of −25 V and the nominal operating thresholds. The expected symmetric in-pixel pattern is observed: when a track is incident in the centre of a pixel, it is unlikely that diffusion causes above-threshold charge sharing in neighbouring pixels, therefore the average cluster size is smaller in this region. When tracks are incident closer to the pixel edges, especially at the corners, the average cluster size increases as the diffusion range of the charge carriers encompasses a larger area of neighbouring pixels. The larger cluster size of assembly 16 is also evident in these histograms, especially in the corner regions as expected.

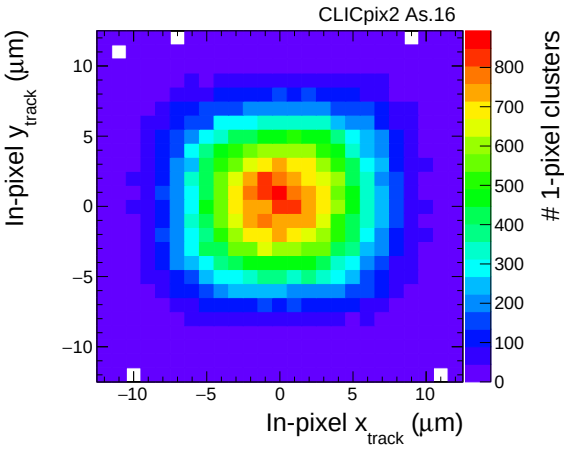

Figure 8.6: In-pixel distribution of one-pixel sized clusters for assembly 16, operated at a bias voltage of −25 V and nominal threshold.

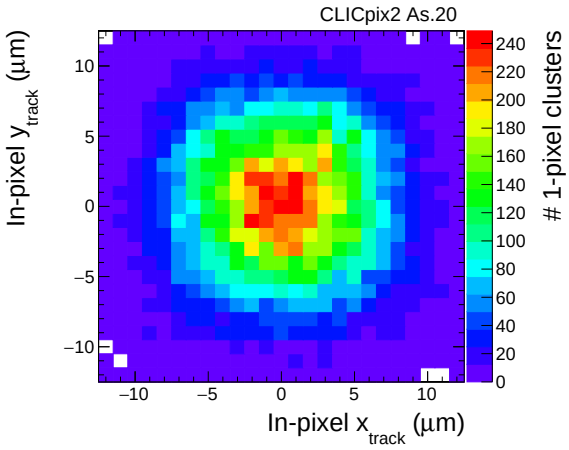

Figure 8.7: In-pixel distribution of one-pixel sized clusters for assembly 20, operated at a bias voltage of −25 V and nominal threshold.

The in-pixel areas in Figures 8.4 and 8.5, where one-pixel sized clusters occur are significantly smaller than the pixel pitch. Figures 8.6 and 8.7 show the in-pixel track position of associated one-pixel clusters for assemblies 16 and 20 respectively. A bias of −25 V and the nominal thresholds values have been applied to both detectors. A central region contains the majority of one-pixel sized clusters, while almost no one-pixel sized clusters occur at the border and corner regions of the pixel as expected. For one-pixel sized clusters, the effective pixel pitch is therefore much lower than 25 µm.

8.1.1.3 Cluster size as a function of threshold

Test-beam data was recorded for CLICpix2 planar sensor assembly 20 over a range of threshold values. The effect of increasing threshold on the mean cluster size is shown in Figure 8.8 for applied bias voltages of −25 V and −60 V. An increase in hit detection threshold is predicted to decrease the average cluster size, as diffused charge carriers shared to neighbouring pixels are more likely to be under threshold. As previously shown, the average cluster size at nominal threshold is higher at a bias voltage of −25 V compared to −60 V. This trend is observed for thresholds lower than approximately 2 ke^-, after which the average cluster size is similar for both voltages due to the larger fraction of one-pixel clusters. After a threshold of approximately 9.5 ke^-, the cluster size saturates close to a value of one.

The decreased cluster size due to increased threshold can be observed in Figure 8.9, an in-pixel cluster size histogram for assembly 20 test-beam data with an applied bias voltage of −25 V and a threshold of (9.2 ± 0.1) ke^-. The increase in threshold of approximately 8.5 ke^- from the nominal operational threshold causes the average cluster size to significantly decrease across the pixel. The majority of clusters have a size of one, with a small amount of above-threshold charge sharing occurring adjacent to the corners and edges of the pixel.

8.1.2 Pixel and cluster charge

Charge deposition within a semiconductor sensor is discussed in Subsection 1.1.2.

The distribution of pixel charge within associated clusters shows distinct individual peaks, as shown in Figures 8.10 and 8.11 for assemblies 16 and 20 respectively. Each peak corresponds to

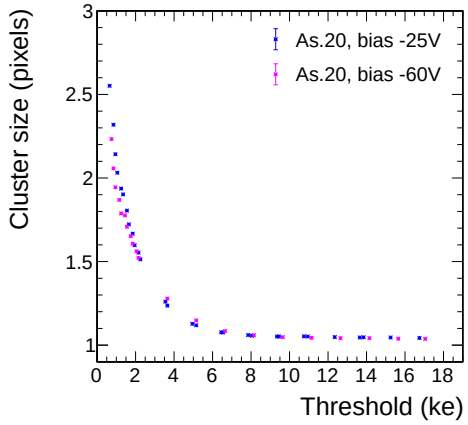

Figure 8.8: Mean cluster size of assembly 20 as a function of threshold, for applied bias voltages of −25 V and −60 V.

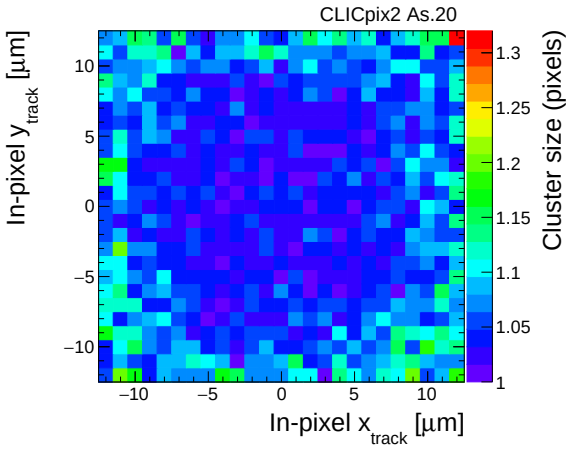

Figure 8.9: In-pixel cluster size distribution of assembly 20 operated at a bias voltage of −25 V and a threshold of 9.2 ke⁻.

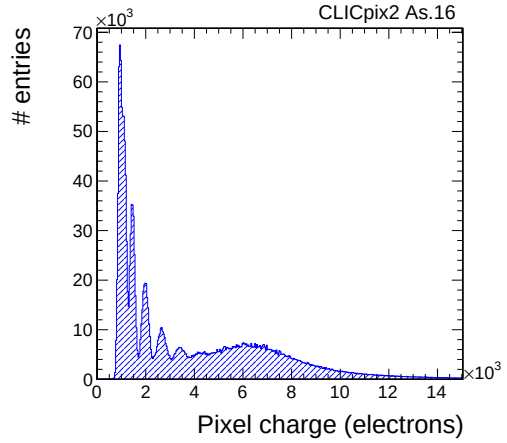

Figure 8.10: Pixel charge distribution of assembly 16 for the nominal threshold value and an applied bias voltage of −25 V.

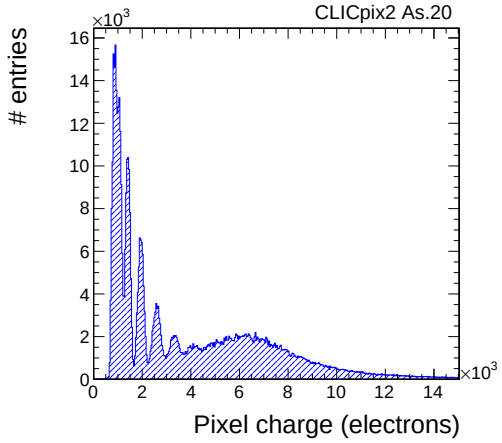

Figure 8.11: Pixel charge distribution of assembly 20 for the nominal threshold value and an applied bias voltage of −25 V.

a certain ToT value range, since the pixel charge is measured in integer units of clock cycles and calibrated into e^- units in the data reconstruction. For high ToT values, the corresponding number of e^- increases significantly with increasing ToT due to the straight profile of the surrogate function fit in this region, as discussed in Subsubsection 4.5.2.2. For lower ToT values, the increase in e^- per ToT unit is smaller as the distribution is highly curved. The peaks overlap for higher charge values due to the difference in gain between pixels, as shown in Section 4.5.2.2, causing the peaks to widen with increasing charge.

The pixel with the highest charge within a cluster is called the seed pixel. The in-pixel distributions of cluster size and seed pixel charge should have similar but inverse distribution patterns, since smaller cluster size implies less charge sharing. Figures 8.12 and 8.13 present the in-pixel seed

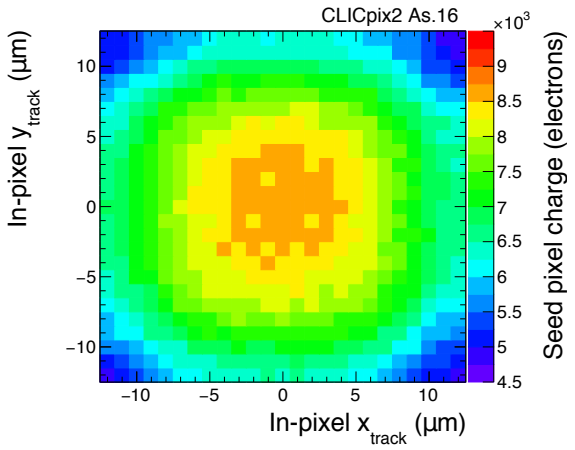

Figure 8.12: In-pixel seed pixel charge distribution of assembly 16, operated at a bias voltage of −25 V and nominal threshold.

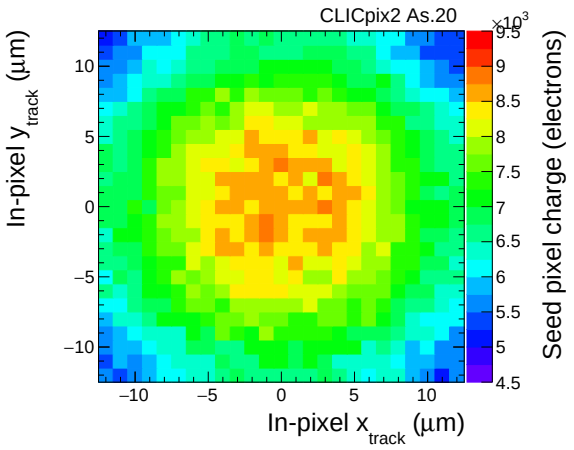

Figure 8.13: In-pixel seed pixel charge distribution of assembly 20, operated at a bias voltage of −25 V and nominal threshold.

pixel charge for assemblies 16 and 20 respectively. Both assemblies exhibit an inverse distribution pattern to the in-pixel cluster sizes shown in Figures 8.4 and 8.5 as expected. In areas where predominantly one-pixel clusters occur, the charge deposited by the incident MIP is not significantly shared therefore the seed pixel charge is highest in the pixel centre. In areas of the pixel where multi-pixel clusters occur, a significant proportion of the MIP charge is shared to neighbouring pixels therefore the measured seed pixel charge is smaller.

The total amount of charge deposited by a MIP has a Landau-Gaussian distribution, and the MPV of cluster charge can be predicted theoretically. For a silicon planar sensor, 3.65 eV are theoretically required to create an electron-hole pair [72]. A MIP charge MPV of approximately 9.6 ke$^-$ is calculated, assuming a perpendicular particle incidence and full sensor depletion [100]. This provides an upper limit on the cluster charge peak value since below-threshold charge sharing will degrade the charge measurement efficiency. The theoretical value is assumed to be accurate to within 0.1% for $\beta\gamma > 500$ [101], which includes both the 5.4 GeV e$^-$ from DESY-II and the 120 GeV π^+-proton from the SPS.

The cluster charge distribution for assemblies 16 and 20 are shown in Figures 8.14 and 8.15 for an applied bias voltage of −25 V and nominal threshold. A convolved Landau-Gaussian function is applied to both distributions to identify the MPV, where the uncertainty is taken from the fit function parameter. Each distribution has the expected shape and the fit matches the distribution well, apart from the discrepancy in the peak height which could account for the χ^2 per number of degrees of freedom (NDOF) values obtained. A 7.4 ke$^-$ MPV is measured for both assembly 16 and 20, which is 23% smaller than the theoretical value. A difference in measured cluster charge between the assemblies of approximately 30-40 e$^-$ is observed.

The measurement accuracy of the cluster charge MPV is affected by several systematic effects. As discussed in Section 4.5.2.2, small adaptations to the X axis fit range of the surrogate function to the per-pixel ToT distributions significantly alters the calibration fit parameters. The fit range determination method used aimed to minimise the χ^2 of the surrogate function, however the effect of the distribution saturation at low and high ToT values and the ToT quantisation are not fully mitigated. The χ^2 values obtained also have a systematic pattern between the high and low matrix rows, seen in Figure 4.59. The discrete nature of the ToT measurement, shown in Figures 8.10 and 8.11, is expected

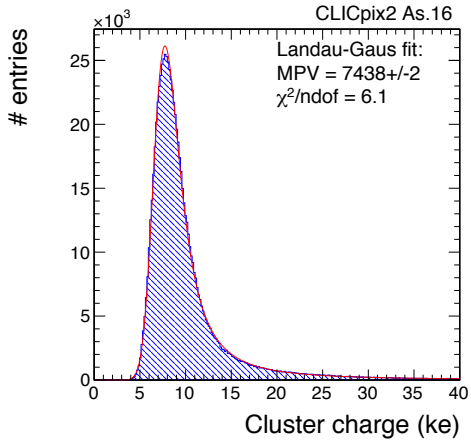

Figure 8.14: Cluster charge distribution of assembly 16 for the nominal threshold value and an applied bias voltage of −25 V, fit with a Landau-Gaussian function.

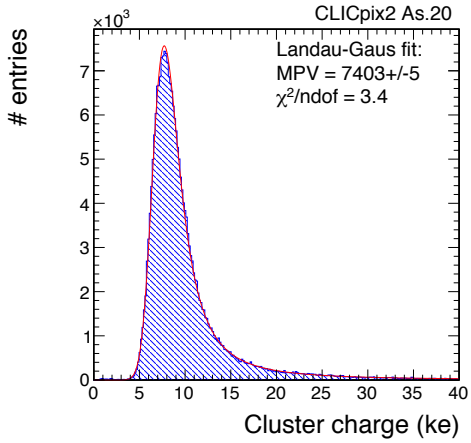

Figure 8.15: Cluster charge distribution of assembly 20 for the nominal threshold value and an applied bias voltage of −25 V, fit with a Landau-Gaussian function.

to cause an assembly-dependent systematic uncertainty on the cluster charge measurement. In addition, multi-pixel clusters may include pixels from odd and even columns, which are shown to have a significantly different conversion between ToT units and e^- units. Any cluster charge uncertainty value would need to account for these effects, depending on the pixel positions within the cluster. The uncertainty of the threshold calibration also directly affects the ToT calibration. The X axis fit ranges used in Section 4.5.1 were chosen to minimise the χ^2 per NDOF of each Gaussian function, however small adaptations to these ranges cause the mean value of each distribution to change. The quoted uncertainties on the threshold calibration do not fully account for these fluctuations, therefore this could be an important contribution to the MPV uncertainty. In addition, the assemblies are operated at a bias voltage close to the depletion voltage therefore an uncertainty in the applied bias of ±1 V could cause a change in cluster charge MPV in the order of 0.1 ke^-, as shown in Figures 8.16 and 8.17.

Sub-threshold charge losses may also play a significant role in the discrepancy between the measured and theoretical MIP charge MPV. Single pixel clusters suffer less from below-threshold charge losses, compared to multi-pixel clusters where the per-pixel signal is lower and is therefore closer to the threshold level. The average seed-pixel charge observed in Figures 8.12 and 8.13 near the pixel centre, where the majority of single pixel clusters occur, is >8.5 ke^-. For single pixel clusters the average seed-pixel charge is equivalent to the cluster charge, therefore the cluster charge for 1-pixel clusters is significantly closer to the theoretical maximum MIP charge MPV, compared to the measured MPV for all cluster sizes. This indicates that below-threshold charge sharing contributes to the 23% smaller measured MPV peak, in combination with the systematic effects previously outlined. Monte Carlo simulation studies and an increased number of CLICpix2 assemblies could determine the combination of causal factors and result in a quantitative estimate of the discussed uncertainties.

Section 8.1.1 predicts from the distribution of mean cluster size as a function of bias voltage that the depletion voltage of assemblies 16 and 20 occurs between −25 V and −20 V. The depletion voltage can be calculated by measuring the change in the MPV of cluster charge with bias voltage. Figure 8.16 shows this distribution for assembly 16, where two distinct regions are expected. At bias voltages below depletion, the measured charge increases linearly with increasing bias voltage, since the active silicon depth becomes larger following Equation 1.3. Once the silicon thickness is fully

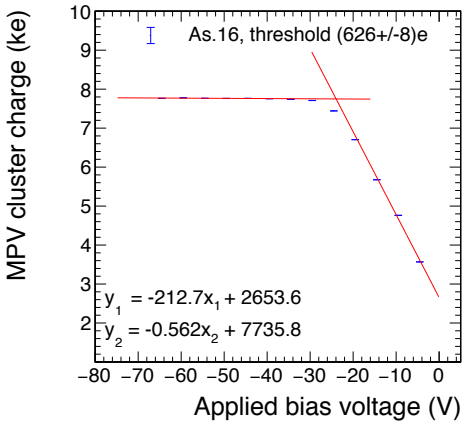

Figure 8.16: MPV of cluster charge as a function of applied bias voltage, for assembly 16 operated at the nominal threshold. Two linear fit functions are applied to the data in the ranges indicated.

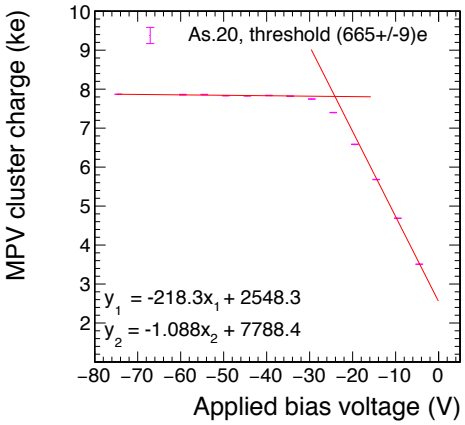

Figure 8.17: MPV of cluster charge as a function of applied bias voltage, for assembly 20 operated at the nominal threshold. Two linear fit functions are applied to the data in the ranges indicated.

depleted, increasing the bias voltage further will not increase the amount of collected charge significantly, therefore an approximately horizontal trend is predicted for these voltages. The bias voltage at which the transition occurs from one linear trend to the other is when full sensor depletion occurs. To measure this point, linear fit functions are applied to the low voltage and high voltage regions of the MPV distribution, using the fit ranges shown in Figure 8.16. Extrapolating the linear functions to thier intersection point defines the depletion voltage, calculated to be at -24.0 V for assembly 16. The same calculation is applied for assembly 20 using the distribution shown in Figure 8.17, where a depletion voltage of -24.1 V is calculated. The calculated voltages are within 0.1 V of each other and within the range predicted in Section 8.1.1.

8.2 Efficiency

8.2.1 Total efficiency

The hit detection efficiency of the prototype assemblies is measured as the percentage of tracks that are associated to pixel clusters out of the total number of tracks incident on the DUT. The total efficiency value is calculated using track associated DUT data, which in this analysis excludes all pixels masked due to high noise or issues identified during pixel categorisation in Section 4.3.3. The total efficiency value calculated for the entire matrix, including all pixels, would be lower than the values quoted.

For assembly 16 at the nominal threshold of (626 ± 8) e^-, an efficiency of (99.980±0.002)% is calculated for an applied bias voltage of -25 V. When the voltage is raised to -60 V, the calculated efficiency is (99.973±0.002)%. Assembly 20 has a total efficiency of (99.962±0.004)% at the nominal threshold of (665 ± 9) e^- and a bias voltage of -25 V. When the applied bias is -60 V, this value is (99.938+0.009 -0.011)%. Both assemblies achieve a total efficiency value $\geq$99.7%, a requirement for the CLIC vertex detector design, with the ROI applied and 466 and 192 pixels masked for assemblies 16 and 20 respectively.

Figure 8.18 shows the calculated efficiency of each detector as a function of applied bias voltage. Bias voltage has a minimal effect on the efficiency of both assemblies, remaining above 99.9% for all voltage values. Fluctuations are observed in the efficiency values measured, with less than 0.1%, with

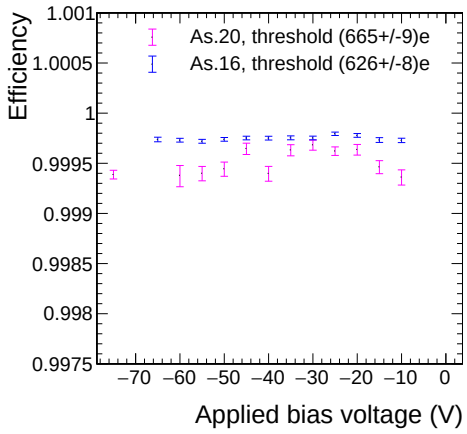

Figure 8.18: Hit detection efficiency as a function of applied bias voltage for assemblies 16 and 20, both operated at the nominal threshold values.

a trend towards slightly lower numbers for assembly 20. The trend of lower values for assembly 20 could arise from the lower spatial resolution of the test-beam telescope used for this detector, which can introduce artificial efficiency losses from the track reconstruction precision. In addition, tracks within a 25 µm radius of a masked pixel are excluded from the efficiency calculation to minimise the ambiguity of the efficiency value in these regions, but do not completely mitigate the effect. Both of these effects could be enhanced by low statistics, and there is a large difference in statistics between assemblies 16 and 20, as observed by the larger statistical uncertainty bars for the latter assembly. As both assemblies achieve efficiency values above 99.9% for all voltages, the variations are deemed to be of a negligible magnitude.

Figure 8.19 presents the efficiency of assembly 20 as a function of threshold for two bias voltages. An increase in threshold causes a reduction in cluster size and charge due to the increased number of below-threshold signals, as previously discussed. Detectors with high thresholds applied are predicted to have lower hit detection efficiencies from charge detection loss. For both voltages in Figure 8.19, a high efficiency plateau is observed until thresholds of approximately 3 ke^-, after which the efficiency decreases. The efficiency at a bias voltage of -25 V decreases at a faster rate than for a bias voltage of -60 V, as expected. A larger amount of charge sharing occurs at the lower bias voltage, therefore the rate of pixel charges falling below the increasing threshold level is higher. Figure 8.20 focuses on the high efficiency plateau of the same data set. In this region, the efficiency values obtained for each bias voltage agree within their uncertainties. The efficiency of assembly 20 decreases as the threshold increases from the nominal value, dropping below 99.90% at a threshold of approximately 1.5 ke^-.

8.2.2 Efficiency over the matrix and in-pixel efficiency

The total efficiency calculated for each detector takes into account associated clusters from across the pixel matrix. Figures 8.21 and 8.22 show the efficiency calculated for each pixel in the matrix of assemblies 16 and 20 respectively, where masked pixels are shown in white. For assembly 16 446 pixels are masked, while 192 pixels are masked for assembly 20. Tracks incident within the edge pixels, excluded in the DUT analysis as discussed in Section 7.1.2, are exclusively included in these plots to observe any inefficiencies in these regions. However, all tracks incident within 12.5 µm of the matrix edge are excluded to minimise inefficiencies caused by the track reconstruction accuracy. No pixels are seen in assembly 16 with an efficiency lower than 90%, while for assembly 20 a number

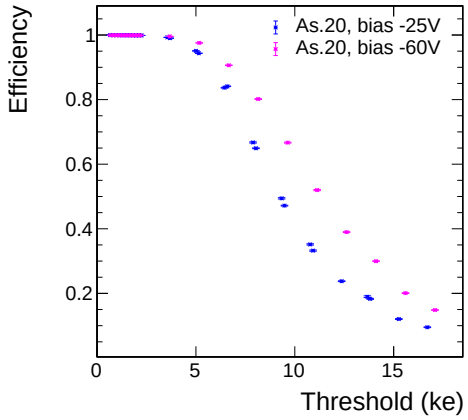

Figure 8.19: Hit detection efficiency as a function of threshold for assembly 20 operated at an applied bias voltage of −25 V and −60 V.

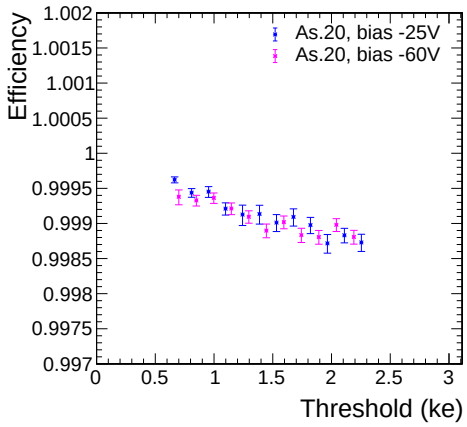

Figure 8.20: Hit detection efficiency as a function of threshold for assembly 20 operated at an applied bias voltage of −25 Vand −60 V, focused in on the high efficiency plateau.

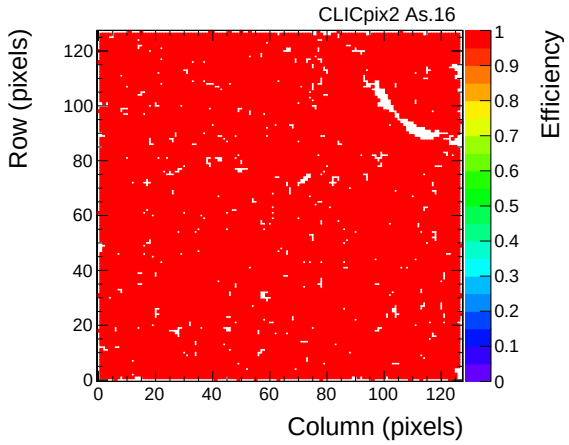

Figure 8.21: 2D map of hit detection efficiency across the matrix of assembly 16, operated at applied bias voltage of −25 V and nominal threshold, where the efficiency value is filled at the position of the associated DUT cluster.

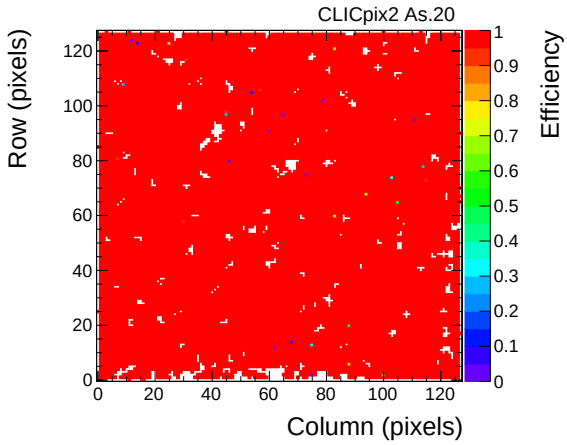

Figure 8.22: 2D map of hit detection efficiency across the matrix of assembly 20, operated at applied bias voltage of −25 V and nominal threshold, where the efficiency value is filled at the position of the associated DUT cluster.

of low efficiency pixels can be observed randomly across the matrix, accounting for the lower total efficiency of the detector. The cause of the low efficiency in these pixels is thought to be the track reconstruction precision, amplified by low statistics for this run, and further investigations using a higher statistics test-beam data set would be required to verify this hypothesis.

The in-pixel efficiency of assembly 20 at nominal threshold and a bias voltage of −25 V is as presented in Figure 8.23: a broadly flat distribution with random outliers across the pixel area. For a threshold value of (9.2 ± 0.1) ke$^-$ and a bias voltage of −25 V, the in-pixel distribution of efficiency

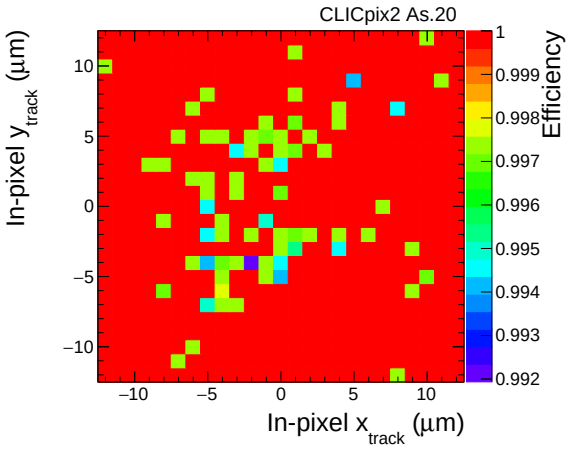

Figure 8.23: In-pixel efficiency distribution of assembly 20, operated at a bias voltage of −25 V and nominal threshold.

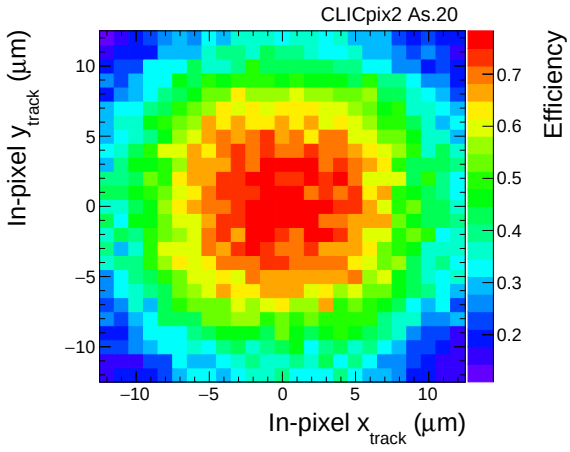

Figure 8.24: In-pixel efficiency distribution of assembly 20, operated at a bias voltage of −25 V and a threshold of 9.2 ke$^-$.

is shown in Figure 8.24. At this high threshold, efficiency losses occur at the pixel corners and edges. A higher amount of charge sharing occurs when a particle is incident in these regions, which at high threshold levels causes charge detection losses. The efficiency in-pixel distribution follows the same pattern as the in-pixel cluster size at this threshold value, presented in Figure 8.9.

8.3 Spatial resolution

The intrinsic spatial resolution of the prototype assemblies is measured with the method discussed in Section 1.3.3. A spatial residual is the difference between the charge-weighted DUT cluster position and the associated track incidence position along the given axis. Spatial residual distributions are unbiased if the data from the detector has not been included in the track reconstruction process. The distribution width can be measured as the width of a Gaussian fit function or as the Root Mean Square (RMS) of the central region of the distribution. The measured residual width is a quadratic sum of the telescope spatial resolution, calculated in Chapter 7, and the intrinsic resolution of the device, following Equation 1.17. Charge sharing should improve spatial resolution as more information is used to define the DUT cluster position.

8.3.1 Spatial residual and positional resolution along the X axis

Figure 8.25 shows the unbiased spatial residual along the X axis for assembly 16 at nominal threshold and a bias voltage of −25 V, and Figure 8.26 shows the same for assembly 20. For each distribution the width of a Gaussian fit function, the RMS of the central 95%, and the RMS of the central 99.7% are quoted.

The χ^2 per NDOF is quoted to quantise how well the Gaussian function describes the distribution, however it is anticipated that these values will be significantly higher than the ideal case of 1 due to the non-gaussian tails caused, for example, by δ-electrons. The statistical uncertainty on the width is taken from the fit uncertainty, which is measured to be less than ± 0.02 µm for all calculated values.

By measuring the RMS of the central 95% or 99.7% of the distribution, denoted as $\text{RMS}_{95\%}$ and $\text{RMS}_{99.7\%}$ respectively, the effect of the non-Gaussian tails or single outliers can be minimised,

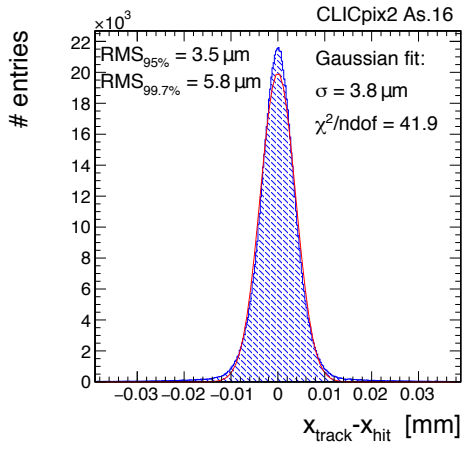

Figure 8.25: Spatial residual along the X axis of assembly 16, operated at nominal threshold and an applied bias voltage of −25 V.

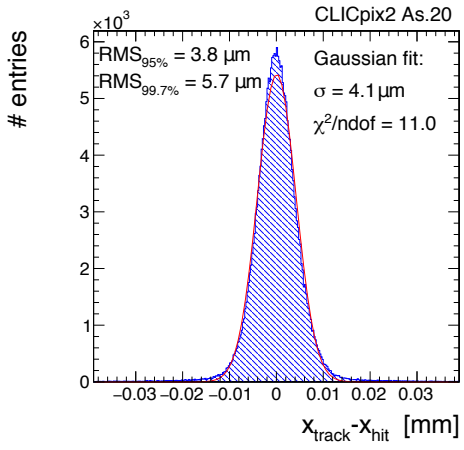

Figure 8.26: Spatial residual along the X axis of assembly 20, operated at nominal threshold and an applied bias voltage of −25 V.

as discussed in Section 1.3.3. The statistical uncertainty of the RMS is calculated using pseudo-experiments following the method described in [102]. Each bin of the spatial residual is smeared using a Poisson distribution centred on the bin, and the RMS width is calculated for the smeared residual. This process is repeated 10,000 times, and the resulting residual widths are filled into a histogram. The width distribution has a Gaussian profile, as expected from the central limit theorem. The σ of a Gaussian function fitted to the width distribution is used as the statistical uncertainty of the RMS value calculated for the original spatial residual distribution. For all RMS values, the statistical uncertainty is measured to be less than ± 0.02µm.

The spatial residual width in X of assembly 16 is measured as 3.5 µm using the $\text{RMS}_{95\%}$ method, 5.8 µm using the $\text{RMS}_{99.7\%}$ method, and as 3.8 µm from the Gaussian width. It is expected that the $\text{RMS}_{99.7\%}$ is larger than the $\text{RMS}_{95\%}$ value as the former includes a larger proportion of any non-Gaussian tails. Using the CLICdp Timepix3 telescope resolution of (1.85 ± 0.07)µm, the $\text{RMS}_{95\%}$ value corresponds to an approximate intrinsic spatial resolution of (2.9 +0.0 -0.1)µm in X of assembly 16.

For assembly 20, values of 3.8 µm, 5.7 µm, and 4.1 µm are obtained as the $\text{RMS}_{95\%}$, $\text{RMS}_{99.7\%}$, and σ respectively. Using the EUDET Mimosa26 telescope resolution of (2.64 +0.12 -0.14) µm, this $\text{RMS}_{95\%}$ value corresponds to a (2.7 +0.2 -0.1) µm intrinsic spatial resolution in X of assembly 20.

Comparing the Gaussian distributions of both detectors, the χ^2 per NDOF values for assembly 20 are significantly lower than those calculated for assembly 16. This implies the residual distribution for assembly 16 has more significant non-Gaussian tails, which could be due to the larger number of tracks with high χ^2 per NDOF values, as seen when comparing Figures 7.5 and 7.21.

Despite the large differences in test-beam set-up and reconstruction processes used on each data set, the measured intrinsic resolutions of the assemblies are in agreement. The intrinsic resolution along the X axis of CLICpix2 planar sensor assemblies with a 130 µm thick sensor is therefore calculated to be <3 µm.

8.3.2 Spatial residual and positional resolution along the Y axis

In Figure 8.27, the unbiased spatial residual along the Y axis of assembly 16 is shown. The $\text{RMS}_{95\%}$ of the distribution is measured as 3.2 µm, the $\text{RMS}_{99.7\%}$ as 5.5 µm, while the width of the Gaussian fit

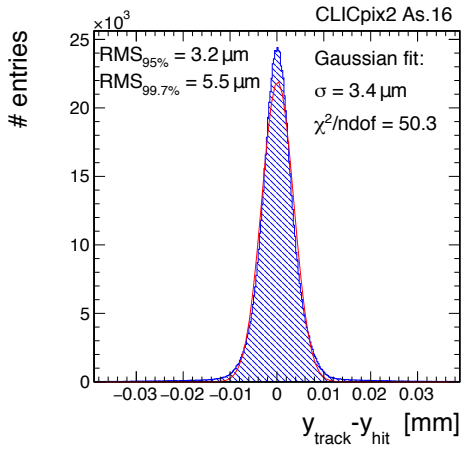

Figure 8.27: Spatial residual along the Y axis of assembly 16, operated at nominal threshold and an applied bias voltage of −25 V.

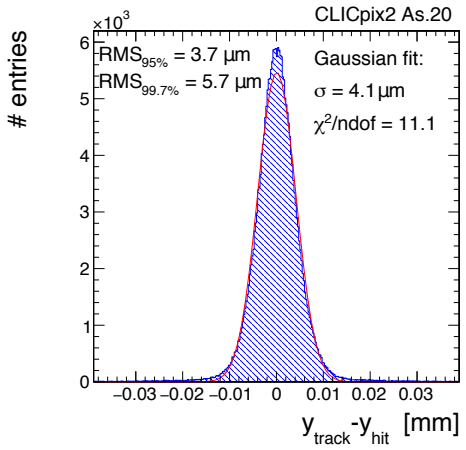

Figure 8.28: Spatial residual along the Y axis of assembly 20, operated at nominal threshold and an applied bias voltage of −25 V.

function to the residual is measured as 3.4 µm. An intrinsic spatial resolution of (2.6 +0.1 -0.0)µm is calculated using the $RMS_{95\%}$ value.

Figure 8.28 presents the spatial residual for assembly 20 along the Y axis for the nominal threshold and a bias of −25 V. Using the $RMS_{95\%}$ method the width is measured as 3.7 µm, while the $RMS_{99.7\%}$ is measured to be 5.7 µm. The σ method calculates the width as 4.1 µm. An intrinsic resolution is obtained for the Y axis of (2.6 ± 0.1)µm using the $RMS_{95\%}$.

The residual width values calculated along the Y axis are smaller than those calculated for the X axis, in the order of 0.1-0.3 µm. It is thought that this discrepancy is partially caused by the mirrored column pattern of the CLICpix2 ASIC design, as presented in Figure 3.2, shown to affect the threshold and ToT calibration parameters in Chapter 4. Using the methods described in the chapter, the calibration of these two values aimed to account for the effect, however the even-odd column differences are not fully mitigated. These differences in the design and calibration between columns could degrade the spatial resolution along the X axis. In addition, the spatial resolution of the CLICdp Timepix3 telescope has been shown to differ along the X and Y axes in simulation studies on the order of 0.1-0.2 µm [65]. A larger difference between X and Y residual widths is observed for assembly 16, therefore the asymmetric telescope spatial resolution could partially account for the differences seen. Small misalignments of the telescope or DUT plane would also contribute to the effect. A combination of the mirrored ASIC design, even-odd column calibration differences, and asymmetric telescope resolution is thought to cause the 0.1-0.3 µm XY residual width asymmetry of the CLICpix2 assemblies.

Similar to the X axis, the measured intrinsic resolutions of the assemblies are in agreement along the Y axis despite the differences in test-beam set-up and reconstruction processes used. The intrinsic resolution along the Y axis of CLICpix2 planar sensor assemblies with a 130 µm thick sensor is calculated to be <3 µm.

The spatial resolution of a CLICpix hybrid assembly solder bump-bonded to a 200 µm thick active-edge planar silicon sensor was measured to be approximately 4 µm [6]. The CLICpix2 planar sensor assemblies improve on this value along both axes with a 70 µm thinner sensor.

Pixel detectors for the CLIC vertex detector are required to have a pointing resolution of approximately 3 µm along the X and Y axes. Both CLICpix2 planar sensor assemblies meet this goal when operated at the optimal bias voltage for charge sharing and the lowest operational threshold outside

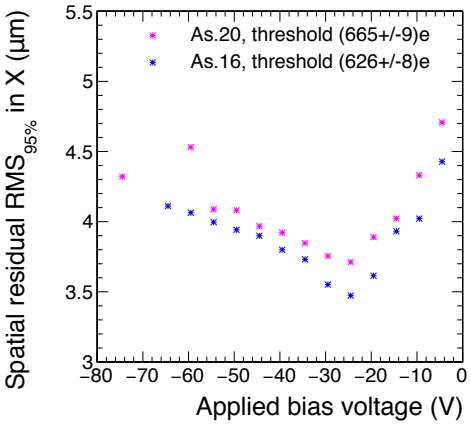

Figure 8.29: Spatial residual along the X axis of assemblies 16 and 20 as a function of applied bias voltage, both operated at nominal threshold.

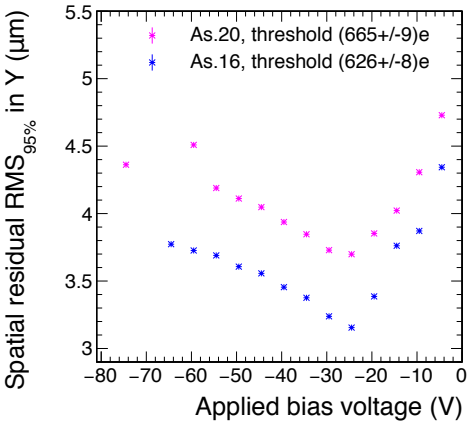

Figure 8.30: Spatial residual along the Y axis of assemblies 16 and 20 as a function of applied bias voltage, both operated at nominal threshold.

of the noise level. However, the 130 µm silicon sensor used for these assemblies has a larger material budget than the 50 µm sensors foreseen to be used for the vertex detector, required due to the limit of $\leq 0.2\% X_0$ per layer. With a thinner silicon sensor, the amount of charge sharing between pixels will be smaller and therefore the spatial resolution will be >3 µm. To reach the positional resolution requirement within the material budget limit using a CLICpix2 readout chip, a silicon sensor with enhanced charge sharing or a smaller pixel pitch will be required. An improved ASIC design with a lower noise level and threshold could improve the spatial resolution through increased charge sharing information.

8.3.3 Spatial residual as a function of bias voltage and threshold

An applied bias of −25 V is the optimal voltage for charge sharing between pixels, as discussed in Section 8.1.1. Higher bias voltages than this are expected to be detrimental to spatial resolution, as the amount of charge diffusion within the sensor is reduced. For bias voltages lower than −24 V, the sensor is not fully depleted and the smaller depletion depth has a negative effect on the spatial resolution. These two trends are observed in Figure 8.29, where the spatial residual width in X is shown for both assemblies as a function of applied bias voltage, where the width is measured as the $\text{RMS}_{95\%}$. The best resolution is predicted to occur at −25 V as the cluster size is largest at this bias voltage, which is the case for both detectors.

Figure 8.30 shows the spatial residual $\text{RMS}_{95\%}$ calculated along the Y axis, measured for both assemblies as a function of applied bias voltage. The predicted two trends of spatial residual width decrease and increase around the bias voltage of −25 V are observed for both assemblies.

Spatial resolution is expected to degrade with increasing threshold, corresponding to an increase in the spatial residual width measured. The reduction of charge sharing as threshold increases causes the cluster size to decrease and the spatial information of the track position to degrade. The effect of increasing threshold on the spatial residual $\text{RMS}_{95\%}$ value of assembly 20 is presented in Figures 8.31 and 8.32 for the X and Y axes, respectively. Data is shown for applied bias voltages of −25 V and −60 V. For both axes and voltages, the residual width increases with increasing threshold until a peak at approximately 5 ke^-. After this point, the spatial residual width slowly decreases. This effect is caused by efficiency losses at the pixel edges at high thresholds, as shown in Figure 8.24.

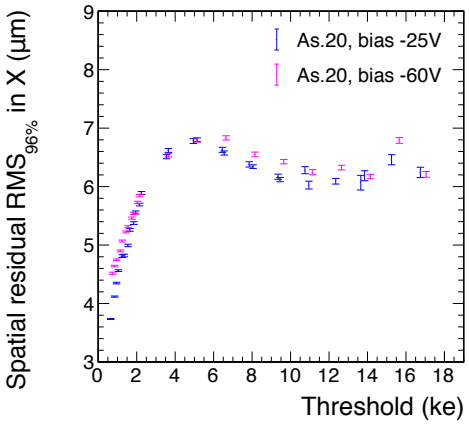

Figure 8.31: Spatial residual along the X axis of assembly 20 as a function of threshold, operated at applied bias voltages of −25 V and −60 V.

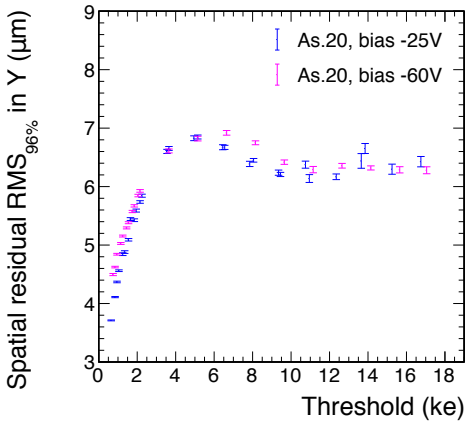

Figure 8.32: Spatial residual along the Y axis of assembly 20 as a function of threshold, operated at applied bias voltages of −25 V and −60 V.

The effective pixel pitch for one-pixel sized clusters is reduced by this, improving the spatial residual width measured. A decrease in statistics from the efficiency losses is also identified at higher threshold values by the statistical variations observed. The threshold point of 5 ke^- approximately corresponds to the region at which the hit detection efficiency falls below 98%, using the efficiency distribution shown in Figure 8.19.

8.3.4 Spatial residual for different cluster widths

The spatial residuals for clusters of different X axis widths are shown in Figures 8.33 and 8.34 for assemblies 16 and 20 respectively. Each distribution has been normalised by dividing by the total number of clusters along the axis. It should be noted that clusters of width N pixels have a total cluster size ≥N, since only the width along the X axis is restricted to be N pixels.

One-pixel wide clusters of assembly 16 have a spatial residual width of approximately 4.5 µm, measured as $RMS_{99.7\%}$. Using Equation 1.18, the expected residual width for one-pixel wide clusters would be 7.2 µm for a 25 µm pixel pitch. A smaller width is measured, as can be expected from Figures 8.6 and 8.7 where the effective pitch for one pixel sized clusters is shown to be significantly smaller than 25 µm. Multi-pixel clusters use a charge-weighted cluster position and occur across the entire pixel pitch of 25 µm. For two-pixel wide clusters the $RMS_{99.7\%}$ is measured to be 3.2 µm, and 10.8 µm for three-pixel wide clusters. The number of two-pixel wide clusters is significantly larger than of three-pixel wide, as can be expected from Figure 8.1, and an η correction is applied along the X axis to two-pixel wide clusters to correct for non-linear charge sharing. This accounts for the large residual width difference between the two multi-pixel cluster residuals.

The mean cluster size of assembly 20 is smaller than measured for assembly 16, as shown in Section 8.1.1, therefore the ratio of one-pixel and two-pixel wide clusters is smaller. Considering this, the similarity of the residual width for one and two-pixel wide clusters is to be expected, measured as 3.8 µm and 4.5 µm respectively. For three-pixel sized clusters, a larger $RMS_{99.7\%}$ value of 14.4 µm is measured due to the low proportion of this cluster width size and the absence of an η correction process.

The spatial residuals for different cluster widths along the Y axes of assemblies 16 and 20 are shown in Figures 8.35 and 8.36 respectively. For assembly 16, the residual width of one-pixel wide

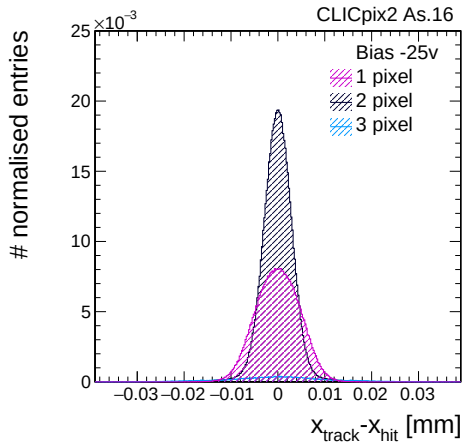

Figure 8.33: Spatial residual along the X axis of assembly 16 for different projected cluster widths, operated at nominal threshold and an applied bias voltage of −25 V.

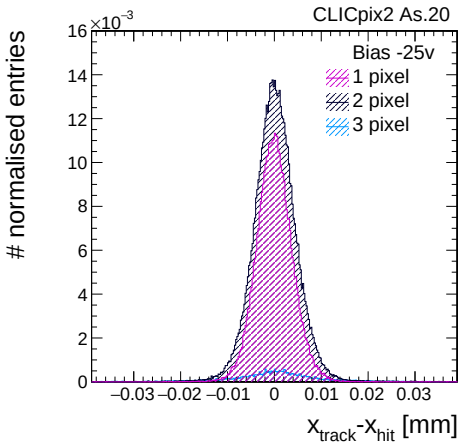

Figure 8.34: Spatial residual along the X axis of assembly 20 for different projected cluster widths, operated at nominal threshold and an applied bias voltage of −25 V.

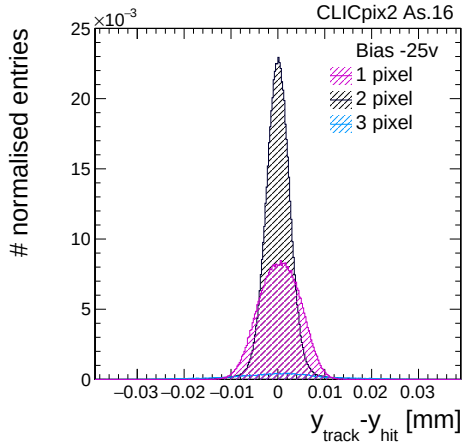

Figure 8.35: Spatial residual along the Y axis of assembly 16 for different cluster widths, operated at nominal threshold and an applied bias voltage of −25 V.

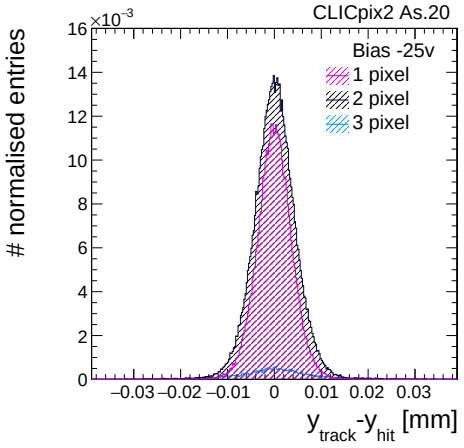

Figure 8.36: Spatial residual along the Y axis of assembly 20 for different cluster widths, operated at nominal threshold and an applied bias voltage of −25 V.

clusters is 4.5 µm. Two-pixel wide clusters have a residual width of 2.8 µm, and a value of 10.4 µm is measured for three-pixel wide clusters. These widths exhibit the same trend when compared to the corresponding X values, but the numerical difference in X and Y residual widths measured and discussed in Section 8.3.2 is observed. Near identical residual widths are measured for the X and Y axes of assembly 20: 3.7 µm, 4.5 µm, and 14.4 µm for one, two, three-pixel wide clusters respectively.

8.4 Timing resolution

Per-pixel timing information was recorded for CLICpix2 planar sensor assembly 16, allowing the timing resolution of the detector to be measured. This data set used the nominal threshold for the detector of (626 ± 8) e^- and an applied bias voltage of -60 V. The timing resolution will be better at higher bias voltages as the rising edge of the signal is faster, therefore the particle arrival time is better defined. Similar to the spatial resolution, the measured difference between the cluster timestamp and the associated track time is a quadratic sum of the intrinsic detector timing resolution and the timing resolution of the reference telescope, as shown in Equation 1.19. The timing resolution of the CLICdp Timepix3 test-beam telescope is assumed to be 1.1 ns [98].

Signals where the charge deposited is just above the threshold cause a slow discriminator response compared to larger signals, as discussed in Section 1.3.3. A non-linear dependence of the measured arrival time on the signal amplitude is caused by this effect, known as time-walk. The time-walk curve for assembly 16 is shown in Figure 8.37. For associated pixel charges above approximately 3 ke^-, the timing residual is close to 0 ns. The distribution for pixels with a lower charge curves towards negative time residuals. This is the expected behaviour, as the slower discriminator response causes later pixel timestamps to be recorded. Time-walk will cause the timing residual distribution of the detector to be wider, negatively affecting the intrinsic time resolution.

To correct for the time-walk effect, the distribution can be parametrised using a fit function of the equation:

$$F(x) = \frac{c}{x-t} + d \tag{8.1}$$

where c, t, and d are free parameters, and x is the pixel charge. The time-walk correction function is derived from geometrical considerations, as shown in [98]. $F(x)$ is the time offset required to centre the distribution to 0 for each value of pixel charge. Figure 8.38 shows a fit to the distribution of average time residuals as a function of pixel charge. Each data point is the average timing residual measured for each value of pixel charge, where the error bars account for the measurement spread. The fit function is seen to parameterise the distribution well for pixel charge below approximately 10 ke^-, above which statistical fluctuations cause a large deviation from the trend. Due to this, the fit function has a χ^2 per NDOF of 2.4.

The parameters c, t, and d are used to correct the timestamps of the input pixel data within the `[EventLoaderCLICpix2]` module of Corryvreckan. Figures 8.39 and 8.40 present the corrected time-walk curves for assembly 16. The 2D histogram shows that the timing residual for pixel charge below 3 ke^- is closer to 0 than observed in Figure 8.37. A small tail remains at low pixel charges towards negative time residuals, as also observed in Figure 8.40. The applied function has corrected the majority of the time-walk effect, however a small deviation remains for pixel charges below approximately 1.5 ke^-. As this data set includes all pixels within associated clusters, this tail is thought to include low charge pixels within larger clusters and therefore should not significantly impact the time residual measurement, which is dominated by the seed pixel timing.

Time-walk correction is expected to affect the timing residual of the detector by centring the distribution around 0 ns and reducing the measured width. Figure 8.41 shows that the time-walk correction function has the desired effect on the timing residual of assembly 16.

The width of the assembly 16 time residual, measured using three different methods, is shown in Figure 8.42. The mean value of the Gaussian occurs at (0.31 ± 0.03)ns, and the uncertainty of the σ value is ± 0.02 ns. Each RMS value has a statistical uncertainty of ± 0.1 ns. Taking the $RMS_{95\%}$ value and the telescope timing resolution of (1.10 ± 0.03)ns [98], CLICpix2 planar sensor assembly 16 is measured to have an intrinsic timing resolution of (4.2+0.0-0.1)ns. The intrinsic timing resolution of assembly 16 for the given operating conditions is below the 5 ns requirement of the CLIC vertex detector. It should be noted that when using the -25 V bias voltage that is optimal for charge sharing, the timing resolution of the detector is expected to be larger than the resolution calculated at -60 V.

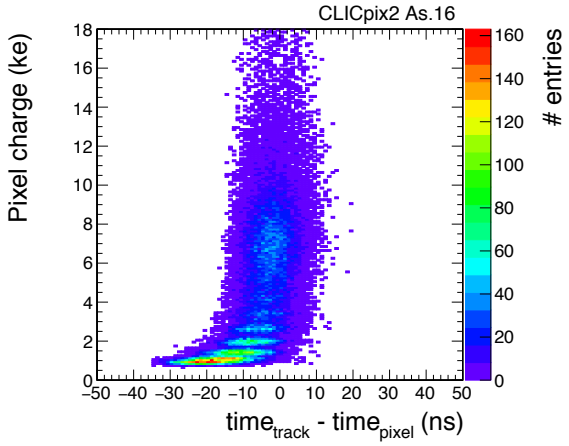

Figure 8.37: 2D distribution of pixel charge as a function of time residual for assembly 16, operated as an applied bias voltage of −60 V and nominal threshold.

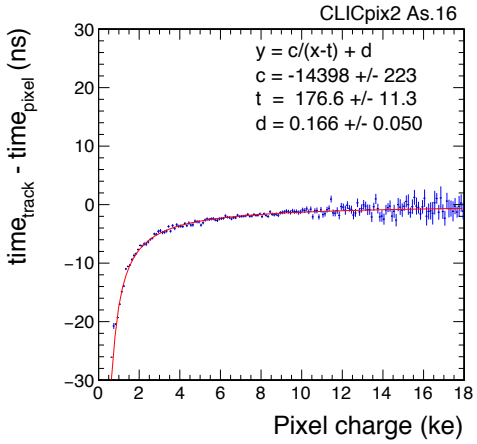

Figure 8.38: Profile distribution of average time residual as a function of pixel charge for assembly 16, operated as an applied bias voltage of −60 V and nominal threshold.

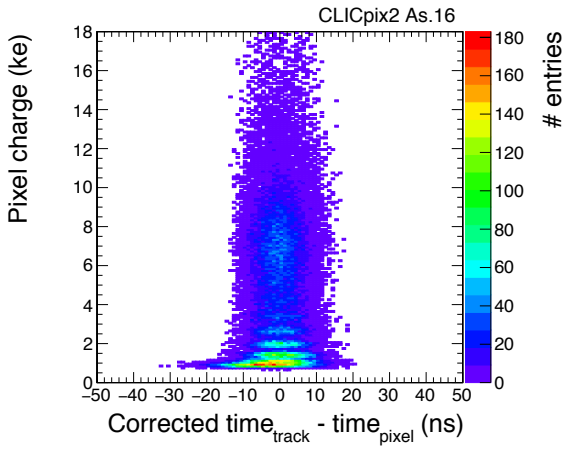

Figure 8.39: 2D distribution of pixel charge as a function of time residual for assembly 16 after time-walk correction, operated as an applied bias voltage of −60 V and nominal threshold.

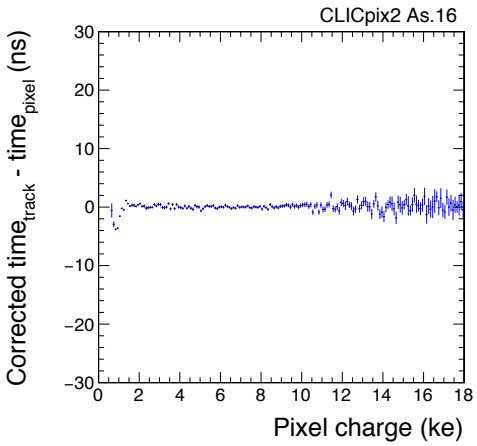

Figure 8.40: Profile distribution of average time residual as a function of pixel charge for assembly 16 after time-walk correction, operated as an applied bias voltage of −60 V and nominal threshold.

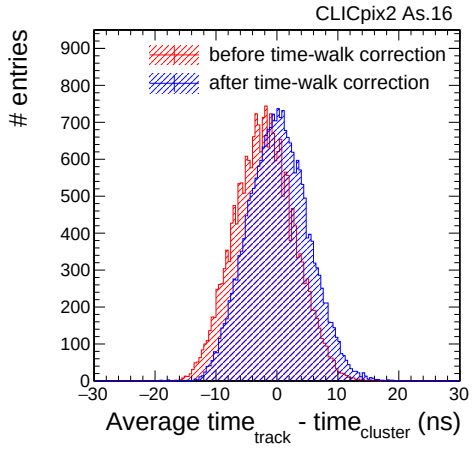

Figure 8.41: Timing residual of assembly 16 before and after time-walk correction, operated at nominal threshold and an applied bias voltage of −60 V.

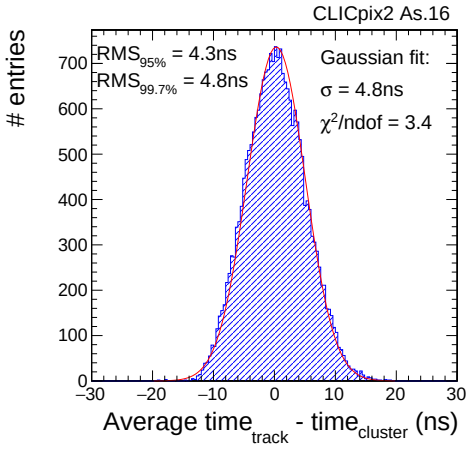

Figure 8.42: Timing residual of assembly 16 after time-walk correction, operated at nominal threshold and an applied bias voltage of −60 V.

Conclusion

This study has evaluated the performance of a semiconductor hybrid pixel detector aiming to fulfil the requirements of a future particle collider experiment. The Compact Linear Collider (CLIC) is a proposed future e^- e^+ collider for precision measurements of Standard Model processes and to search for new phenomena. The beam conditions expected at CLIC impose strict requirements on the design of the inner detector subsystems in order to achieve the foreseen physics programme. Pixel detectors to be used in the vertex detector subsystem are required to achieve a spatial resolution of approximately 3 µm, a hit detection efficiency $\geq$99.7%, a particle time resolution of $\leq$5 ns, and a material budget per layer of $0.2\%X_0$.

The CLICpix2 readout ASIC aims to fulfil these requirements. Designed in a 65 nm CMOS process, the ASIC has a matrix of 25×25 µm^2 sized pixels, each capable of simultaneous 8-bit ToA and 5-bit ToT measurements. Nine CLICpix2 ASICs were solder bump-bonded to active-edge planar silicon sensors from two different foundries. The bump-bonding process for small pitch, single-chip pixel detectors has many challenges, therefore it was important to assess the interconnect quality of each assembly in detail.

Laboratory characterisation measurements were performed on the CLICpix2 planar sensor assemblies to quantify the interconnect quality of each detector and characterise their response to deposited charge. The laboratory tests initially consisted of X-ray image inspection, leakage current measurements, and per-pixel threshold equalisation. Seven of the nine assemblies were found to operate as expected during these measurements.

To assess the solder bump-bond quality of each pixel, a data-driven categorisation scheme was developed. The pixel data recorded for each assembly during radioactive source exposure, direct test-pulse charge injection into the pixel front-end, and threshold equalisation were combined. Each of the six categories aimed to separate the response of the ASIC from that of the bump-bonds and silicon sensor using these data sets.

The categorisation method successfully identified unexpected behaviour of the devices. Assemblies 16 and 20 were measured to have high interconnect qualities with yields of 99.6% and 97.9% respectively, verifying the viability of the single-chip bump-bonding process at a pixel pitch of 25 µm. CLICpix2 planar sensor assembly 14 was found to have a large number of unconnected pixels, thought to be caused by a gradient in height between the ASIC and sensor. A region of interconnected solder bumps was observed for assembly 19, therefore a large number of noise hits were recorded for this detector. It was predicted that the NiAu UBM material used for assemblies 9, 15, 21 would be incompatible with the solder bump-bonding process. The pixel categorisation results confirm this, as large numbers of pixels of these assemblies were deemed to be unresponsive, have electrical shorts to neighbouring pixels, or to have a low hit-detection rate. In addition, the categorisation results identified a hit-rate pattern in the columns and rows close to the matrix edge. This was attributed to how charge carriers are collected from the active-edge of the sensors due to the large ratio between the sensor thickness and the pixel pitch.

Assemblies with high interconnect qualities were produced in low quantities. All identified issues related to the bump-bonding process were used as feedback to the manufacturer, allowing the interconnection process to be improved. The bonding process could be further optimised by testing a larger number of assemblies, and different small-pitch hybridisation techniques could be explored, such as Anisotropic Conductive Film (ACF) bonding [103].

Calibration measurements were performed on the two CLICpix2 planar sensor assemblies with the highest interconnect qualities, allowing their performance to be compared to other technologies or theoretical predictions. The conversion factor between the threshold units and electrons was calculated by exposing each detector to fluorescence X-rays from two target materials. Separate calibration factors were calculated for pixels within odd and even columns of the matrix to account for the difference in routing lengths of the data lines between these sets of columns. The operational threshold of assemblies 16 and 20 were determined to be (626 ± 8) e^- and (665 ± 9) e^- respectively, with an average threshold dispersion of (43 ± 1) e^- and noise (113 ± 2) e^-. The ToT units of 25 MHz clock-cycles were calibrated into physical units of electrons using the results of the threshold calibration and test-pulse injection measurements. A ToT calibration curve was created for each pixel, parameterised by a surrogate fit function.

A dependence of the CLICpix2 voltage Digital to Analogue Converter (DAC) output on temperature was discovered during the characterisation measurements. The output voltage increases linearly with increasing temperature due to a resistor mismatch in the voltage DAC circuits. The dependence of different voltage DACs was analysed, and mitigation methods were discussed.

The performance of two CLICpix2 planar sensor assemblies with the highest interconnect qualities were assessed using data recorded at the CERN and DESY test-beam facilities. The test-beam data was reconstructed and analysed using the Corryvreckan software framework, development of which was a part of this study.

An analysis was performed of the on-chip temperature readings of CLICpix2 assemblies during test-beam data taking, to quantify the effect the voltage DAC temperature dependence had on the measured cluster charge. With a fan applied to the detector, the on-chip temperature within a data run was stable within ± 0.5 °C approximately 14 s after the ASIC was powered. The change of cluster charge with temperature was deemed to be negligible. The mean on-chip temperature was found to be stable between multiple data runs within ± 0.5 °C for the same assembly operated in the same readout mode.

Despite the significant differences in the telescope set-up and reconstruction process used on each of the test-beam data sets, the DUT performance of the assemblies was similar. Both CLICpix2 planar sensor assemblies have a hit detection efficiency of above 99.95% when operated at the lowest noiseless threshold value and the optimal applied bias voltage for charge sharing. The intrinsic spatial resolution was determined to be <3 µm along both axes for an 130 µm thick planar sensor. A timing resolution of <5 ns was measured after a time-walk correction was applied to the pixel data.

The CLICpix2 assemblies meet the hit detection efficiency, spatial resolution, and timing resolution requirements of the CLIC vertex detector; this is very significant progress in the R&D for such a detector. However, this is achieved with planar silicon sensors of thickness 130 µm, whereas the material budget per layer of the vertex detector is $0.2\%X_0$, corresponding to sensors of approximately 50 µm thickness. A thinner silicon sensor yields lower charge sharing between pixels, and therefore the spatial resolution of a CLICpix2 planar sensor assembly using such as sensor would would exceed 3 µm. To reach the positional resolution requirement within the material budget limit using a CLICpix2 readout chip, a silicon sensor with enhanced charge sharing or a smaller pixel pitch would therefore be required, and this is the subject of ongoing work.

Appendix A

Additional figures from Chapter 4

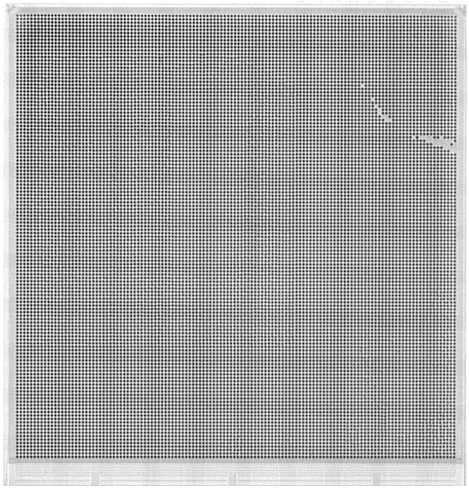

Figure A.1: X-ray image of CLICpix2 assembly 9, provided by IZM.

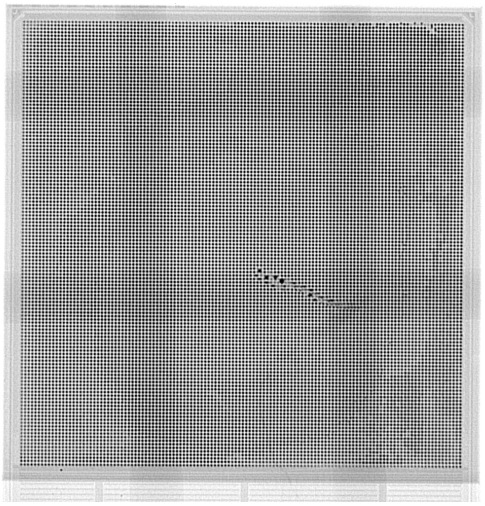

Figure A.2: X-ray image of CLICpix2 assembly 14, provided by IZM.

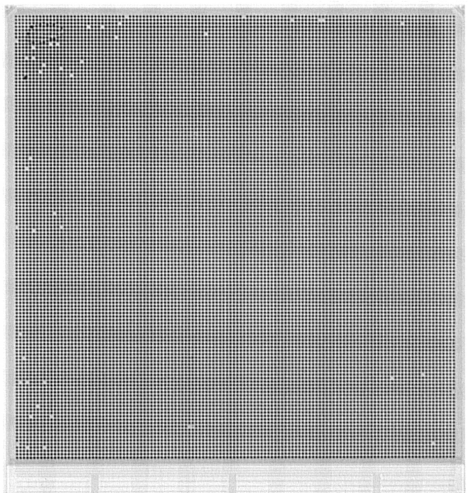

Figure A.3: X-ray image of CLICpix2 assembly 15, provided by IZM.

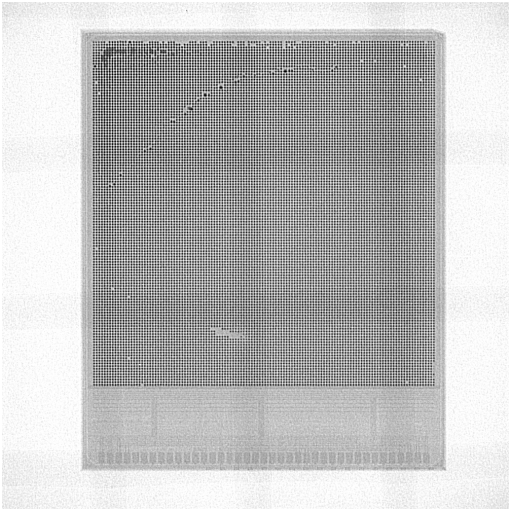

Figure A.4: X-ray image of CLICpix2 assembly 22, provided by IZM.

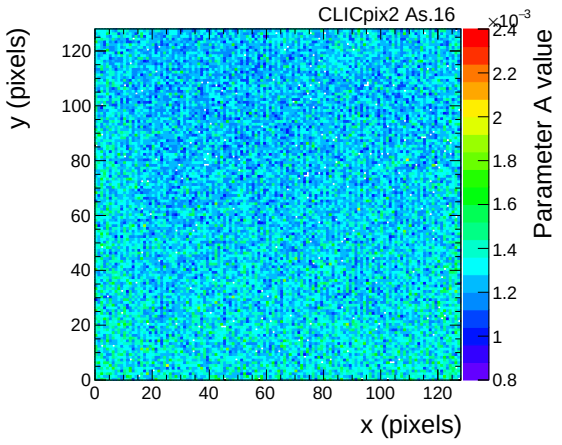

Figure A.5: 2D map of the A parameters obtained from the surrogate function fit to the ToT calibration curve of the pixel with nominal threshold and bias voltage applied for CLICpix2+planar assembly 16.

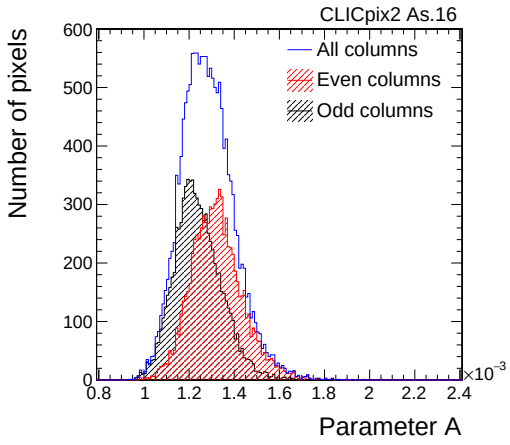

Figure A.6: 1D histograms of the A parameters obtained from the surrogate function fit to the ToT calibration curve of the pixel with nominal threshold and bias voltage applied for CLICpix2+planar assembly 16, showing the difference between odd and even columns.

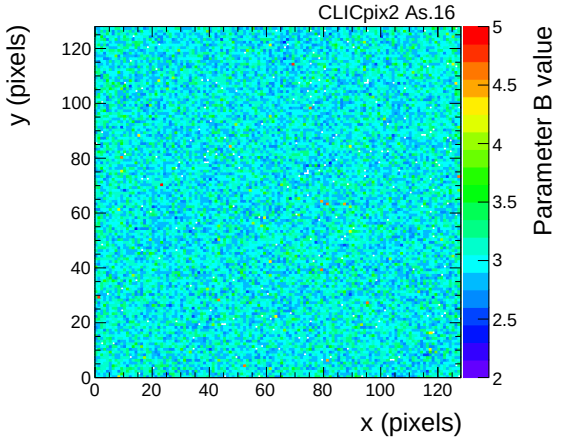

Figure A.7: 2D map of the B parameters obtained from the surrogate function fit to the ToT calibration curve of the pixel with nominal threshold and bias voltage applied for CLICpix2+planar assembly 16.

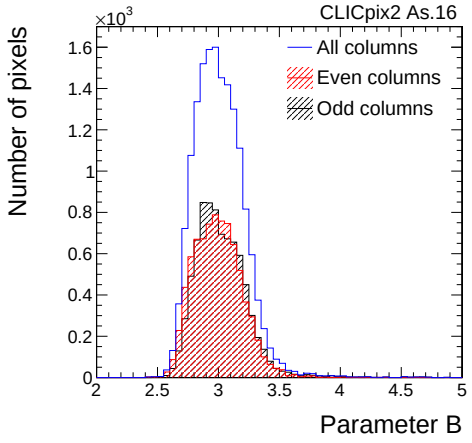

Figure A.8: 1D histograms of the B parameters obtained from the surrogate function fit to the ToT calibration curve of the pixel with nominal threshold and bias voltage applied for CLICpix2+planar assembly 16, showing the difference between odd and even columns.

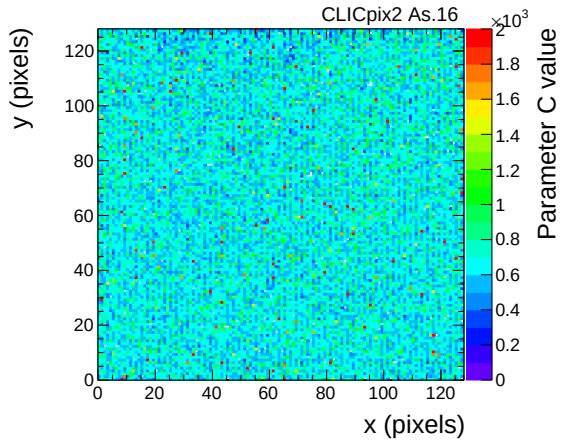

Figure A.9: 2D map of the C parameters obtained from the surrogate function fit to the ToT calibration curve of the pixel with nominal threshold and bias voltage applied for CLICpix2+planar assembly 16.

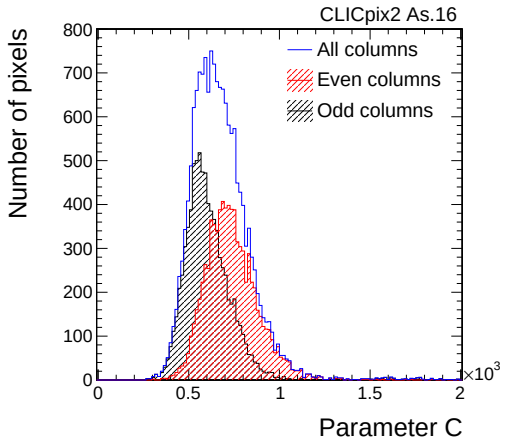

Figure A.10: 1D histograms of the C parameters obtained from the surrogate function fit to the ToT calibration curve of the pixel with nominal threshold and bias voltage applied for CLICpix2+planar assembly 16, showing the difference between odd and even columns.

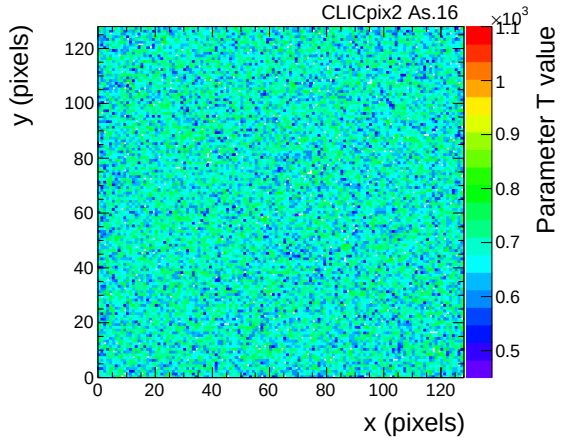

Figure A.11: 2D map of the T parameters obtained from the surrogate function fit to the ToT calibration curve of the pixel with nominal threshold and bias voltage applied for CLICpix2+planar assembly 16.

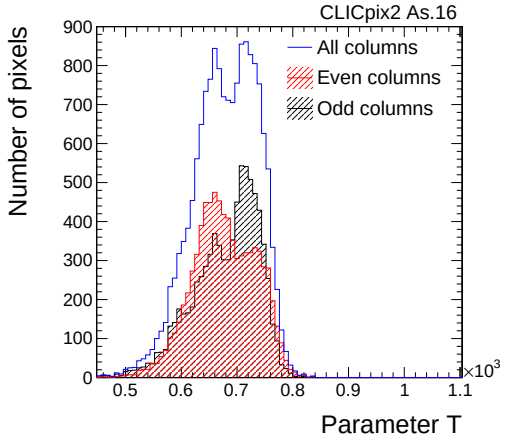

Figure A.12: 1D histograms of the T parameters obtained from the surrogate function fit to the ToT calibration curve of the pixel with nominal threshold and bias voltage applied for CLICpix2+planar assembly 16, showing the difference between odd and even columns.

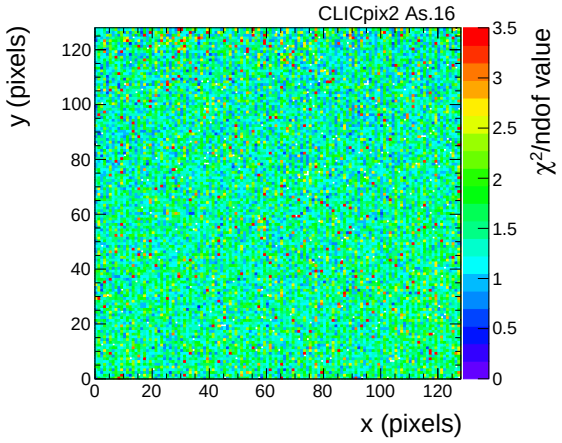

Figure A.13: 2D map of the χ^2/ndof values obtained from the surrogate function fit to the ToT calibration curve of the pixel with nominal threshold and bias voltage applied for CLICpix2+planar assembly 16.

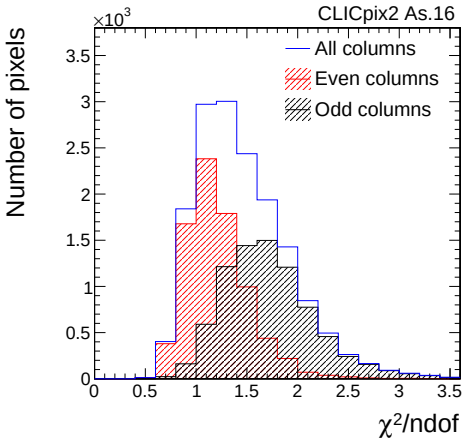

Figure A.14: 1D histograms of the χ^2/ndof values obtained from the surrogate function fit to the ToT calibration curve of the pixel with nominal threshold and bias voltage applied for CLICpix2+planar assembly 16, showing the difference between odd and even columns.

Appendix B

Corryvreckan test-beam reconstruction configuration files

```
log_level = "INFO"
log_format = "DEFAULT"
histogram_file = "histograms_@RunNumber@.root"
output_directory = "/eos/user/w/williamm/jobsub_output/CPX2_nov2018_voltagescan/"
detectors_file =  "/afs/cern.ch/user/w/williamm/local/jobsub_corryvreckan/@AlignmentFileName@"

[EventLoaderCLICpix2]
calibration_file="/afs/cern.ch/user/w/williamm/local/jobsub_corryvreckan/totcalib_binaryfile_as16.dat"
input_directory=@cpx2filename@

[EventLoaderTimepix3]
input_directory=@SpidrFileName@

[Clustering4D]
type="timepix3"
time_cut_abs=60ns

[Clustering4D]
name="016_CP_PS"
time_cut_abs=300us

[EtaCorrection]
name="016_CP_PS"
eta_constants_x_016_CP_PS = @p0_x@ @p1_x@ @p2_x@ @p3_x@ @p4_x@ @p5_x@
eta_constants_y_016_CP_PS = @p0_y@ @p1_y@ @p2_y@ @p3_y@ @p4_y@ @p5_y@

[Correlations]

[Tracking4D]
min_hits_on_track=6
spatial_cut_abs=50um 50um
track_model="gbl"
momentum=120GeV
time_cut_abs=60ns

[DUTAssociation]
spatial_cut_abs=20um 20um
time_cut_abs=300us
use_cluster_centre=false

[AnalysisDUT]
chi2ndof_cut=3

[AnalysisEfficiency]
chi2ndof_cut=3
```

Figure B.1: Corryvreckan main configuration file for reconstruction of test-beam data taken with the CLICdp Timepix3 telescope, SPS, CERN, using a ToT+Cnt data taking mode.

```
[W0013_D04]
material_budget = 0.01068
number_of_pixels = 256, 256
orientation = 11.1216deg,187.17deg,-1.3119deg
orientation_mode = "xyz"
pixel_pitch = 55um,55um
position = 1.24276mm,374.89um,0
spatial_resolution = 2.7um,2.7um
time_resolution = 1ns
type = "timepix3"

[W0013_E03]
material_budget = 0.01068
number_of_pixels = 256, 256
orientation = 11.3423deg,187.329deg,-1.03299deg
orientation_mode = "xyz"
pixel_pitch = 55um,55um
position = 53.242um,488.8um,21.5mm
spatial_resolution = 2.7um,2.7um
time_resolution = 1ns
type = "timepix3"

[W0013_G02]
material_budget = 0.01068
number_of_pixels = 256, 256
orientation = 10.649deg,187.693deg,-1.59924deg
orientation_mode = "xyz"
pixel_pitch = 55um,55um
position = 333.942um,463.112um,43.5mm
spatial_resolution = 2.7um,2.7um
time_resolution = 1ns
type = "timepix3"

[016_CP_PS]
mask_file = "maskfiles/mask_016_CP_PS.conf"
material_budget = 0.024
number_of_pixels = 128, 128
orientation = -1.07808deg,0.0912722deg,-1.65608deg
orientation_mode = "xyz"
pixel_pitch = 25um,25um
position = 711.097um,-315.035um,105mm
role = "dut"
spatial_resolution = 7.217um,7.217um
time_offset = -93ns
time_resolution = 300us
roi = [[3,3],[3,124],[124,124],[124,3]]
type = "clicpix2"

[W0013_G03]
material_budget = 0.01068
number_of_pixels = 256, 256
orientation = 8.99876deg,8.99412deg,-0.0178763deg
orientation_mode = "xyz"
pixel_pitch = 55um,55um
position = -10.202um,-11.943um,186.5mm
role = "reference"
spatial_resolution = 2.7um,2.7um
time_resolution = 1ns
type = "timepix3"

[W0013_J05]
material_budget = 0.01068
number_of_pixels = 256, 256
orientation = 7.8686deg,9.69141deg,1.28463deg
orientation_mode = "xyz"
pixel_pitch = 55um,55um
position = 420.062um,-585.771um,208mm
spatial_resolution = 2.7um,2.7um
time_resolution = 1ns
type = "timepix3"

[W0013_L09]
material_budget = 0.01068
number_of_pixels = 256, 256
orientation = 7.99712deg,9.96826deg,0.136421deg
orientation_mode = "xyz"
pixel_pitch = 55um,55um
position = -1.07073mm,-19.197um,231.5mm
spatial_resolution = 2.7um,2.7um
time_resolution = 1ns
type = "timepix3"
```

Figure B.2: Example geometry configuration file for Corryvreckan for reconstruction of test-beam data taken with the CLICdp Timepix3 telescope, SPS, CERN, using a ToT+Cnt data taking mode.

```
[Corryvreckan]
log_level = "WARNING"
log_format = "DEFAULT"
histogram_file = "histograms_@RunNumber@_aftertwcor2.root"
output_directory = "/eos/user/w/williamm/jobsub_output/CPX2_nov2018_tottoa/"
detectors_file =  "/afs/cern.ch/user/w/williamm/local/jobsub_corryvreckan/@AlignmentFileName@"

[EventLoaderCLICpix2]
calibration_file="/afs/cern.ch/user/w/williamm/local/jobsub_corryvreckan/totcalib_binaryfile_as16.dat"
input_directory=@cpx2filename@
timewalk_constants = -16575.1 261.154 -0.0152136

[EventLoaderTimepix3]
input_directory=@SpidrFileName@

[Clustering4D]
type="timepix3"

[Clustering4D]
name="016_CP_PS"
time_cut_abs=20ns

[EtaCorrection]
eta_constants_x_016_CP_PS = @p0_x@ @p1_x@ @p2_x@ @p3_x@ @p4_x@ @p5_x@
eta_constants_y_016_CP_PS = @p0_y@ @p1_y@ @p2_y@ @p3_y@ @p4_y@ @p5_y@
name="016_CP_PS"

[Correlations]

[Tracking4D]
min_hits_on_track=6
spatial_cut_abs=50um 50um
track_model="gbl"
momentum=120GeV
time_cut_abs=60ns

[DUTAssociation]
spatial_cut_abs=20um 20um
use_cluster_centre=false
time_cut_abs=20ns

[AnalysisDUT]
chi2ndof_cut=3

[AnalysisEfficiency]
chi2ndof_cut=3
```

Figure B.3: Corryvreckan main configuration file for reconstruction of test-beam data taken with the CLICdp Timepix3 telescope, SPS, CERN, using a ToT+ToA data taking mode.

```
[W0013_D04]
material_budget = 0.01068
number_of_pixels = 256, 256
orientation = 11.1216deg,187.17deg,-1.3119deg
orientation_mode = "xyz"
pixel_pitch = 55um,55um
position = 1.24276mm,374.89um,0
spatial_resolution = 2.7um,2.7um
time_resolution = 1ns
type = "timepix3"

[W0013_E03]
material_budget = 0.01068
number_of_pixels = 256, 256
orientation = 11.3423deg,187.329deg,-1.03299deg
orientation_mode = "xyz"
pixel_pitch = 55um,55um
position = 53.242um,488.8um,21.5mm
spatial_resolution = 2.7um,2.7um
time_resolution = 1ns
type = "timepix3"

[W0013_G02]
material_budget = 0.01068
number_of_pixels = 256, 256
orientation = 10.649deg,187.693deg,-1.59924deg
orientation_mode = "xyz"
pixel_pitch = 55um,55um
position = 333.942um,463.112um,43.5mm
spatial_resolution = 2.7um,2.7um
time_resolution = 1ns
type = "timepix3"

[016_CP_PS]
mask_file = "maskfiles/mask_016_CP_PS.conf"
material_budget = 0.024
number_of_pixels = 128, 128
orientation = -1.03923deg,0.0436021deg,-1.65424deg
orientation_mode = "xyz"
pixel_pitch = 25um,25um
position = 711.327um,-320.075um,105mm
role = "dut"
spatial_resolution = 7.217um,7.217um
time_offset = -93ns
time_resolution = 5ns
roi = [[3,3],[3,124],[124,124],[124,3]]
type = "clicpix2"

[W0013_G03]
material_budget = 0.01068
number_of_pixels = 256, 256
orientation = 8.99876deg,8.99412deg,-0.0178763deg
orientation_mode = "xyz"
pixel_pitch = 55um,55um
position = -10.202um,-11.943um,186.5mm
role = "reference"
spatial_resolution = 2.7um,2.7um
time_resolution = 1ns
type = "timepix3"

[W0013_J05]
material_budget = 0.01068
number_of_pixels = 256, 256
orientation = 7.8686deg,9.69141deg,1.28463deg
orientation_mode = "xyz"
pixel_pitch = 55um,55um
position = 420.062um,-585.771um,208mm
spatial_resolution = 2.7um,2.7um
time_resolution = 1ns
type = "timepix3"

[W0013_L09]
material_budget = 0.01068
number_of_pixels = 256, 256
orientation = 7.99712deg,9.96826deg,0.136421deg
orientation_mode = "xyz"
pixel_pitch = 55um,55um
position = -1.07073mm,-19.197um,231.5mm
spatial_resolution = 2.7um,2.7um
time_resolution = 1ns
type = "timepix3"
```

Figure B.4: Example geometry configuration file for Corryvreckan for reconstruction of test-beam data taken with the CLICdp Timepix3 telescope, SPS, CERN, using a ToT+ToA data taking mode.

```
[Corryvreckan]
log_level = "WARNING"
log_format = "DEFAULT"
output_directory = "/eos/user/w/williamm/jobsub_output/CPX2_july2019_voltagescan/"
detectors_file =  "/afs/cern.ch/user/w/williamm/local/jobsub_corryvreckan/@AlignmentFileName@"
histogram_file = "histograms_@RunNumber@_afteretacor.root"

[EventLoaderEUDAQ2]
name="CLICpix2_0"
file_name=@cpx2filename@
calibration_file="/afs/cern.ch/user/w/williamm/local/jobsub_corryvreckan/totcalib_binaryfile_as20.dat"

[EventLoaderEUDAQ2]
name="TLU_0"
inclusive=false
adjust_event_times=[["TluRawDataEvent", -115us, +230us]]
file_name=@nifilename@

[EventLoaderEUDAQ2]
type="MIMOSA26"
inclusive=false
file_name=@nifilename@

[EventLoaderEUDAQ2]
name="Timepix3_0"
skip_time=2s
inclusive=false
buffer_depth=100
file_name=@SpidrFileName@

[Clustering4D]
type="MIMOSA26"
time_cut_rel=2.0

[Clustering4D]
name="CLICpix2_0"
time_cut_abs=1ms

[EtaCorrection]
name="CLICpix2_0"
eta_constants_x_CLICpix2_0 = @p0_x@ @p1_x@ @p2_x@ @p3_x@ @p4_x@ @p5_x@
eta_constants_y_CLICpix2_0 = @p0_y@ @p1_y@ @p2_y@ @p3_y@ @p4_y@ @p5_y@

[Clustering4D]
name="Timepix3_0"

[Correlations]

[Tracking4D]
spatial_cut_rel=27
min_hits_on_track=6
exclude_dut=true
time_cut_abs=230us
require_detectors="Timepix3_0"
timestamp_from="Timepix3_0"
track_model="gbl"
momentum=5.4GeV

[DUTAssociation]
spatial_cut_abs=25um, 25um
time_cut_abs=1ms
use_cluster_centre=false

[AnalysisDUT]
chi2ndof_cut=3

[AnalysisEfficiency]
chi2ndof_cut=3
```

Figure B.5: Corryvreckan main configuration file for reconstruction of test-beam data taken with an EUDET Mimosa26 telescope, DESY-II, using a ToT+Cnt data taking mode.

```
[TLU_0]
material_budget = 4.99882e+217
orientation = 0,0,0
orientation_mode = "xyz"
position = 0,0,0
role = "auxiliary"
time_resolution = 1ms
type = "tlu"

[MIMOSA26_0]
mask_file = "maskfiles/mask_MIMOSA26_0.txt"
material_budget = 0.00075
number_of_pixels = 1152, 576
orientation = 0.459741deg,-0.175497deg,-0.315471deg
orientation_mode = "xyz"
pixel_pitch = 18.4um,18.4um
position = -286.294um,-208.649um,0
spatial_resolution = 3.2um,3.2um
time_resolution = 115us
type = "mimosa26"

[MIMOSA26_1]
mask_file = "maskfiles/mask_MIMOSA26_1.txt"
material_budget = 0.00075
number_of_pixels = 1152, 576
orientation = 0.749658deg,-0.315642deg,-0.192399deg
orientation_mode = "xyz"
pixel_pitch = 18.4um,18.4um
position = -157.198um,130.337um,153mm
spatial_resolution = 3.2um,3.2um
time_resolution = 115us
type = "mimosa26"

[MIMOSA26_2]
mask_file = "maskfiles/mask_MIMOSA26_2.txt"
material_budget = 0.00075
number_of_pixels = 1152, 576
orientation = 0,0,0
orientation_mode = "xyz"
pixel_pitch = 18.4um,18.4um
position = 0,0,305mm
role = "reference"
spatial_resolution = 3.2um,3.2um
time_resolution = 115us
type = "mimosa26"

[CLICpix2_0]
mask_file = "maskfiles/mask_CLICpix2_0_as20.txt"
material_budget = 0.024
number_of_pixels = 128, 128
orientation = 180.105deg,0.00767763deg,89.8148deg
orientation_mode = "xyz"
pixel_pitch = 25um,25um
position = -2.895um,-154.088um,329mm
role = "dut"
spatial_resolution = 7.217um,7.217um
time_offset = 100ns
time_resolution = 1ms
roi = [[3,3],[3,124],[124,124],[124,3]]
type = "clicpix2"

[MIMOSA26_3]
mask_file = "maskfiles/mask_MIMOSA26_3.txt"
material_budget = 0.00075
number_of_pixels = 1152, 576
orientation = 0.653344deg,-0.297537deg,-0.0121467deg
orientation_mode = "xyz"
pixel_pitch = 18.4um,18.4um
position = -988.307um,192.338um,346mm
spatial_resolution = 3.2um,3.2um
time_resolution = 115us
type = "mimosa26"

[MIMOSA26_4]
mask_file = "maskfiles/mask_MIMOSA26_4.txt"
material_budget = 0.00075
number_of_pixels = 1152, 576
orientation = -1.44403deg,0.786442deg,-0.403305deg
orientation_mode = "xyz"
pixel_pitch = 18.4um,18.4um
position = -896.493um,115.349um,455mm
spatial_resolution = 3.2um,3.2um
time_resolution = 115us
type = "mimosa26"

[MIMOSA26_5]
mask_file = "maskfiles/mask_MIMOSA26_5.txt"
material_budget = 0.00075
number_of_pixels = 1152, 576
orientation = -1.88354deg,0.912836deg,0.00784952deg
orientation_mode = "xyz"
pixel_pitch = 18.4um,18.4um
position = -820.843um,167.175um,565mm
spatial_resolution = 3.2um,3.2um
time_resolution = 115us
type = "mimosa26"

[Timepix3_0]
mask_file = "maskfiles/mask_Timepix3_0.txt"
material_budget = 0.01068
number_of_pixels = 256, 256
orientation = 177.864deg,0.753554deg,0.386575deg
orientation_mode = "xyz"
pixel_pitch = 55um,55um
position = -472.718um,-39.377um,629mm
spatial_resolution = 12.8um,12.8um
time_offset = 191ns
time_resolution = 1.56ns
type = "timepix3"
```

Figure B.6: Example geometry configuration file for Corryvreckan for reconstruction of test-beam data taken with an EUDET Mimosa26 telescope, DESY-II, using a ToT+Cnt data taking mode.

Appendix C

Additional figures from Chapter 8

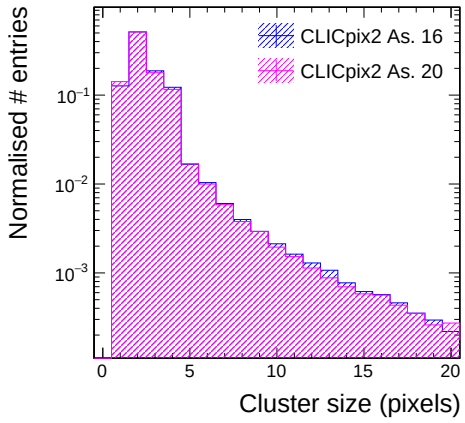

Figure C.1: Cluster size distribution of assemblies 16 and 20, for the nominal threshold values and an applied bias voltage of -25 V, with a logarithmic scale.

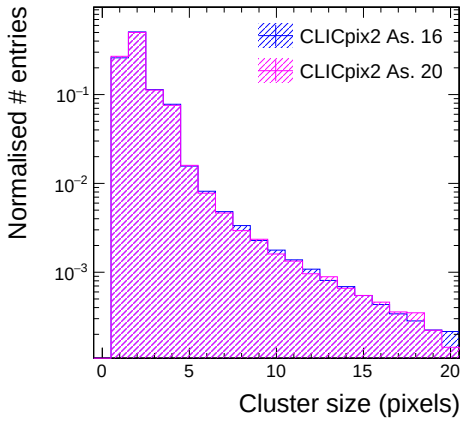

Figure C.2: Cluster size distribution of assemblies 16 and 20, for the nominal threshold values and an applied bias voltage of -60 V, with a logarithmic scale.

List of Acronymns

ASIC - Application-Specific Integrated Circuit
ADC - Analogue to Digital Converter
BSM - Beyond Standard Model
C3PD - CLICpix Capacitively Coupled Pixel Detector
CaR - Control and Readout
CERN - Organization Européen pour la Recherche Nucléaire (European Organization for Nuclear Research)
CI - Continuous Integration
CLIC - Compact LInear Collider
CLICdp - Compact LInear Collider detector and physics
CLICTD - Compact LInear Collider Tracking Detector
CM - Centre of Mass
CMOS - Complementary Metal Oxide Semiconductor
CSA - Charge Sensitive Amplifier
DAC - Digital to Analogue Converter
DAQ - Data AcQuisition
DESY - Deutsches Elektronen-Synchrotron (German Electron Synchrotron)
DRIE - Deep Reactive Ion Etching
DUT - Device Under Test
ECAL - Electronic CALorimeter
ELAD - Enhanced LAteral Drift
ENC - Equivalent Noise Charge
ENIG - Electroless Ni-Immersion Gold
ESPP - European Strategy for Particle Physics
EWT - ElectroWeak Theory
FMC - Flexible Metallic Conduit
FPGA - Field-Programmable Gate Array
GBL - General Broken Lines
GUI - Graphical User Interface
HCAL - Hadronic CALorimeter
HEP - High Energy Physics
HL-LHC - High Luminosity Large Hadron Collider
HV - High-Voltage
LHC - Large Hadron Collider
LSB - Least Significant Bit/Byte
MAPS - Monolithic Active Pixel Sensor
MIP - Minimally Ionising Particle
MPV - Most Probable Value
MSB - Most Significant Bit/Byte
NDOF - Number of Degrees Of Freedom
PCB - Printed Circuit Board
PMT - PhotoMultiplier Tube

PUC - Pixel Unit Cell
PVD - Physical Vapour Deposition
QCD - Quantum ChromoDynamics
QED - Quantum ElectroDynamics
QFD - Quantum FlavourDynamics
R&D - Research and Development
RMS - Root Mean Square
ROI - Region Of Interest
SM - Standard Model
SNR - Signal to Noise Ratio
SoC - System on Chip
SOI - Silicon On Insulator
SPIDR - Speedy PIxel Detector Readout
SPS - Super Proton Synchrotron
SSH - Secure SHell
TDC - Time-to-Digital Converter
TLU - Trigger Logic Unit
ToA - Time of Arrival
TOML - Tom's Obvious Minimal Language
ToT - Time over Threshold
UBM - Under Bump Metalisation
UDP - User Datagram Protocol

References

[1] CERN, *The Large Hadron Collider*, https://home.cern/science/accelerators/large-hadron-collider (last accessed 08/2020).

[2] *High-Luminosity Large Hadron Collider (HL-LHC): Technical Design Report V. 0.1*, **4/2017** (2017), ed. by G. Apollinari et al., DOI: 10.23731/CYRM-2017-004.

[3] CLIC and CLICdp collaborations, *Physics and Detectors at CLIC: CLIC Conceptual Design Report* (2012), DOI: 10.5170/CERN-2012-003.

[4] CLIC and CLICdp collaborations, *Updated baseline for a staged Compact Linear Collider* (2016), DOI: 10.5170/CERN-2016-004.

[5] R. Franceschini et al., *The CLIC Potential for New Physics* (2018), DOI: 10.23731/CYRM-2018-003.

[6] CLIC and CLICdp collaboration, *Detector Technologies for CLIC* (2019), DOI: 10.23731/CYRM-2019-001.

[7] E. Santin, P. Valerio, A. Fiergolski, *CLICpix2 User's Manual*, 2017, URL: https://edms.cern.ch/document/1800546/1.

[8] L. Rossi et al., *Pixel detectors: from fundamentals to applications*, Springer, 2006, DOI: 10.1007/3-540-28333-1.

[9] M. Grundmann, *The Physics of Semiconductors: An Introduction Including Nanophysics and Applications*, Springer, 2010, DOI: 10.1007/978-3-642-13884-3.

[10] W. Shockley, *Currents to Conductors Induced by a Moving Point Charge*, Journal of Applied Physics **9** (1938) 635, DOI: 10.1063/1.1710367.

[11] S. Ramo, *Currents induced by electron motion*, Proceedings of the IRE. **27** (1939) 584, DOI: 10.1109/JRPROC.1939.228757.

[12] G. R. Lynch, O. I. Dahl, *Approximations to multiple Coulomb scattering*, NIM B **58** (1991) 6, DOI: 10.1016/0168-583X(91)95671-Y.

[13] E. Segrè et al., *Experimental Nuclear Physics*, John Wiley and sons., 1953.

[14] J. Beringer et al., *Review of Particle Physics*, Phys. Rev. D **86** (1 2012) 010001, DOI: 10.1103/PhysRevD.86.010001.

[15] L. D. Landau, *On the energy loss of fast particles by ionisation*, Pergamon, 1965, DOI: 10.1016/B978-0-08-010586-4.50061-4.

[16] D. Dannheim et al., *Combining TCAD and Monte Carlo methods to simulate CMOS pixel sensors with a small collection electrode using the Allpix2 framework*, NIM A **964** (2020) 163784, DOI: 10.1016/j.nima.2020.163784.

[17] G. Blanchot, D. Dannheim, C. Fuentes, *Power-pulsing schemes for vertex detectors at CLIC*, JINST **9** (2014) C01005, DOI: 10.1088/1748-0221/9/01/C01005.

[18] S. Vahanen, *Solutions for flip chip bonding of future pixel detectors*, The 26th International Workshop on Vertex Detectors, 2017.

[19] B. Povh et al., *Particles and nuclei: An Introduction to the physical concepts*, Springer, 1995, DOI: 10.1007/3-540-36684-9.

[20] M. Tanabashi et al., *Review of Particle Physics*, Phys. Rev. D **98** (2018) 030001, DOI: 10.1103/PhysRevD.98.030001.

[21] G. Aad et al., *Observation of a new particle in the search for the Standard Model Higgs boson with the ATLAS detector at the LHC*, Physics Letters B **716** (2012) 1, DOI: 10.1016/j.physletb.2012.08.020.

[22] S. Chatrchyan et al., *Observation of a new boson at a mass of 125 GeV with the CMS experiment at the LHC*, Physics Letters B **716** (2012) 30, DOI: 10.1016/j.physletb.2012.08.021.

[23] *Standard Model*, URL: https://commons.wikimedia.org/wiki/File:Standard_Model_of_Elementary_Particles.svg.

[24] M. E. Peskin, *Concepts of elementary particle physics*, Oxford University Press, 2019, DOI: 10.1093/oso/9780198812180.001.0001.

[25] LIGO Scientific Collaboration and Virgo Collaboration, *GW170817: Observation of Gravitational Waves from a Binary Neutron Star Inspiral*, Phys. Rev. Lett. **119** (16 2017) 161101, DOI: 10.1103/PhysRevLett.119.161101.

[26] Super-Kamiokande Collaboration, *Evidence for Oscillation of Atmospheric Neutrinos*, Phys. Rev. Lett. **81** (8 1998) 1562, DOI: 10.1103/PhysRevLett.81.1562.

[27] SNO Collaboration, *Direct Evidence for Neutrino Flavor Transformation from Neutral-Current Interactions in the Sudbury Neutrino Observatory*, Phys. Rev. Lett. **89** (1 2002) 11301, DOI: 10.1103/PhysRevLett.89.011301.

[28] S. Myers, H. F. Schopper, *Particle physics reference library: Accelerators and colliders*, Springer Open, 2020, DOI: 10.1007/978-3-030-34245-6.

[29] CLICdp collaboration, *CLIC input to the European Strategy for Particle Physics Update 2018-2020*, https://clic.cern/european-strategy (last accessed 06/2020).

[30] CLIC project, *The Compact Linear Collider (CLIC) - Project Implementation Plan* (2018), DOI: 10.23731/CYRM-2018-004.

[31] CLIC Project, *CLIC accelerator schematic diagrams* (2019), URL: https://cds.cern.ch/record/2655160.

[32] CLIC, CLIC Project, *CLIC accelerator footprint* (2017), URL: https://cds.cern.ch/record/2297076.

[33] *CAS - CERN Accelerator School : 5th Advanced Accelerator Physics Course: Rhodes, Greece 20 Sep - 1 Oct 1993*, vol. 1, 1995, DOI: 10.5170/CERN-1995-006.

[34] Chen, Pisin, *Beamstrahlung and the QED, QCD backgrounds in linear colliders*, 9th International Workshop on Photon-Photon Collisions, 1992, p. 418.

[35] CLICdp Collaboration, *A detector for CLIC: main parameters and performance*, CLICdp-Note-2018-005 (2018), URL: https://cds.cern.ch/record/2649437.

[36] D. Arominski, A. Latina, A. Sailer, *Beam-induced backgrounds in CLICdet*, CLICdp-Note-2019-002 (2019), URL: http://cds.cern.ch/record/2668425.

[37] N. Alipour Tehrani et al., *CLICdet: The post-CDR CLIC detector model*, CLICdp-Note-2017-001 (2017), URL: https://cds.cern.ch/record/2254048.

[38] CLIC, CLIC Project, *CLIC detector model* (2019), URL: https://cds.cern.ch/record/2297387.

[39] M. Livan, R. Wigmans, *Calorimetry for Collider Physics, an Introduction*, Springer, 2019, DOI: 10.1007/978-3-030-23653-3_12.

[40] *CLICTD: A monolithic HR-CMOS sensor chip for the CLIC silicon tracker*, vol. TWEPP2019, 2020, p. 39, DOI: 10.22323/1.370.0039.

[41] M. Munker et al., *Simulations of CMOS pixel sensors with a small collection electrode, improved for a faster charge collection and increased radiation tolerance*, Journal of Instrumentation **14** (2019) C05013, DOI: 10.1088/1748-0221/14/05/c05013.

[42] K. Dort, *Silicon vertex and tracking detector R&D for CLIC* (2020), URL: https://cds.cern.ch/record/2740978.

[43] I. Perić et al., *A high-voltage pixel sensor for the ATLAS upgrade*, NIM A **924** (2019) 99, DOI: 10.1016/j.nima.2018.06.060.

[44] M. Williams, *R&D for the CLIC vertex and tracking detectors*, JINST **15** (2020) C03045, DOI: 10.1088/1748-0221/15/03/c03045.

[45] J. Kroeger, *Silicon pixel sensor R&D for the CLIC tracking detector*, Journal of Instrumentation **15** (2020) C08005, ISSN: 1748-0221, DOI: 10.1088/1748-0221/15/08/c08005.

[46] N. Alipour Tehrani, *Performance-Optimization Studies for the CLIC Vertex Detector*, MA thesis, EPFL, Lausanne, 2013.

[47] N. Alipour Tehrani et al., *Capacitively coupled hybrid pixel assemblies for the CLIC vertex detector*, NIM A **823** (2016) 1, DOI: 10.1016/j.nima.2016.03.072.

[48] A. Velyka, H. Jansen, *Enhanced Lateral Drift Sensors: Concept and Development*, vol. TIPP 2017: 213, 2018, p. 380, DOI: 10.1007/978-981-13-1316-5_71.

[49] R. Bugiel et al., *High spatial resolution monolithic pixel detector in SOI technology*, CLICdp-Pub-2020-004 (2020), URL: http://cds.cern.ch/record/2727594.

[50] P. Valerio, R. Ballabriga, M. Campbell, *Design of the 65 nm CLICpix demonstrator chip*, LCD-Note-2012-018 (2012), URL: https://cds.cern.ch/record/1507691.

[51] P. Valerio et al., *A prototype hybrid pixel detector ASIC for the CLIC experiment*, JINST **9** (2014) C01012, DOI: 10.1088/1748-0221/9/01/c01012.

[52] Medipix collaboration, *Medipix collaboration website*, https://medipix.web.cern.ch/ (last accessed 05/2020).

[53] F. Krummenacher, *Pixel detectors with local intelligence: an IC designer point of view*, NIM A **305** (1991) 527, DOI: 10.1016/0168-9002(91)90152-G.

[54] Poikela et al., *Timepix3: a 65k channel hybrid pixel readout chip with simultaneous ToA/ToT sparse readout.* JINST **9** (2014).

[55] S. Ruiz Daza, *Power pulsing with CLICpix2*, 2019, URL: https://cds.cern.ch/record/2690112.

[56] Fondazione Bruno Kessler, Center for Materials and Microsystems, FBK-CMM, *FBK-CMM website*, https://cmm.fbk.eu/en/ (last accessed 02/2020).

[57] ADVACAM Oy, *ADVACAM website*, http://www.advacam.com (last accessed 11/2019).

[58] T. Ryhänen, H. Pohjonen, *Overview - Impact of Silicon MEMS—40 Years After*, Handbook of Silicon Based MEMS Materials and Technologies, Second Edition, William Andrew Publishing, 2015, p. xix, DOI: 10.1016/B978-0-323-29965-7.00047-6.

[59] X. Wu et al., *Recent advances in processing and characterization of edgeless detectors*, JINST **7** (2012) C02001, DOI: 10.1088/1748-0221/7/02/c02001.

[60] N. Alipour Tehrani et al., *Performance evaluation of thin active-edge planar sensors for the CLIC vertex detector*, NIM A **953** (2020) 162850, DOI: 10.1016/j.nima.2019.162850.

[61] T. Fritzsch et al., *Flip chip assembly of thinned chips for hybrid pixel detector applications*, JINST **9** (2014) C05039, DOI: 10.1088/1748-0221/9/05/C05039.

[62] Fraunhofer Institute for Reliability and Microintegration IZM, *IZM website*, https://www.izm.fraunhofer.de/en.html (last accessed 12/2019).

[63] *Caribou – A versatile data acquisition system*, vol. TWEPP2019, 2020, p. 100, DOI: 10.22323/1.370.0100.

[64] The Peary Authors, *Peary Caribou DAQ software webpage*, http://peary-caribou.web.cern.ch/peary-caribou (last accessed 03/2020).

[65] N. Alipour Tehrani, *Test-beam measurements and simulation studies of thin pixel sensors for the CLIC vertex detector*, PhD thesis, 2016.

[66] CERN, *CERN North Area H6 beamline*, http://sba.web.cern.ch/sba/ (last accessed 01/2020).

[67] R. Diener et al., *The DESY II test beam facility*, NIM A **922** (2010) 265, DOI: 10.1016/j.nima.2018.11.133.

[68] X. Llopart Cudie, private communication, 2019.

[69] X. Llopart Cudie, *Design and Characterization of 64K Pixels Chips Working in Single Photon Processing Mode*, PhD thesis, 2007.

[70] F. Pitters et al., *Time resolution studies of Timepix3 assemblies with thin silicon pixel sensors*, JINST **14** (2019) P05022, DOI: 10.1088/1748-0221/14/05/P05022.

[71] E. P. Berton, *Principles and Practice of X-Ray Spectrometric Analysis*, Springer, 1975, DOI: 10.1007/978-1-4613-4416-2.

[72] F. Scholze et al., *Determination of the electron–hole pair creation energy for semiconductors from the spectral responsivity of photodiodes*, NIM A **439** (2000) 208, DOI: 10.1016/S0168-9002(99)00937-7.

[73] J. Jakubek et al., *Pixel detectors for imaging with heavy charged particles*, NIM A **591** (2008) 155, DOI: 10.1016/j.nima.2008.03.091.

[74] CERN, *Experimental Areas: North Area*, https://en-ea-le.web.cern.ch/experimental_areas/north-area (last accessed 06/2020).

[75] CERN, *CERN North Area H6 beamline*, http://sba.web.cern.ch/sba/BeamsAndAreas/resultbeam.asp?beamline=H6 (last accessed 01/2020).

[76] K. Akiba et al., *LHCb VELO Timepix3 telescope*, JINST **14** (2019) 5026, DOI: 10.1088/1748-0221/14/05/P05026.

[77] M. Brice, *The test beam telescope for silicon pixel detector R&D* (2018), URL: https://cds.cern.ch/record/2646928.

[78] *Development and applications of the Timepix3 readout chip*, vol. VERTEX2011, 2011, p. 046, DOI: 10.22323/1.137.0046.

[79] K. Akiba et al., *Charged Particle Tracking with the Timepix ASIC*, NIM A **661** (2012) 31, DOI: 10.1016/j.nima.2011.09.021.

[80] J. Visser et al., *SPIDR: a read-out system for Medipix3 and Timepix3*, vol. 10, 12, 2015, p. C12028, DOI: 10.1088/1748-0221/10/12/C12028.

[81] H. Jansen et al., *Performance of the EUDET-type beam telescopes*, EPJ Techniques and Instrumentation **3** (2016) 7, DOI: 10.1140/epjti/s40485-016-0033-2.

[82] J. Aguilar et al., *Infrastructure for Detector Research and Development towards the International Collider* (2012), eprint: 1201.4657.

[83] H. Jansen, *Resolution studies with the DATURA beam telescope*, JINST **11** (2016) C12031, DOI: 10.1088/1748-0221/11/12/c12031.

[84] *First reticule size MAPS with digital output and integrated zero suppression for the EUDET-JRA1 beam telescope*, vol. A623, 2010, p. 480, DOI: 10.1016/j.nima.2010.03.043.

[85] Y. Liu et al., *EUDAQ2—A flexible data acquisition software framework for common test beams*, JINST **14** (2019) P10033, DOI: 10.1088/1748-0221/14/10/p10033.

[86] P. Baesso, D. Cussans, J. Goldstein, *The AIDA-2020 TLU: a Flexible Trigger Logic Unit for Test Beam Facilities*, JINST **14** (2019), URL: http://cds.cern.ch/record/2690858.

[87] T. Bisanz et al., *EUTelescope: A modular reconstruction framework for beam telescope data*, JINST **15** (2020) P09020, DOI: 10.1088/1748-0221/15/09/p09020.

[88] G. McGoldrick et al., *Judith - Pixel particle detector testbeam analysis*, https://gitlab.cern.ch/gmcgoldr/juidth (last accessed 02/2020).

[89] M. Kiehn, M. et al., *Proteus beam telescope reconstruction software*, https://gitlab.cern.ch/proteus/proteus (last accessed 02/2020).

[90] The Corryvreckan Authors, *Corryvreckan software repository*, https://gitlab.cern.ch/corryvreckan/corryvreckan (last accessed 10/2020).

[91] D. Dannheim et al., *Corryvreckan: A Modular 4D Track Reconstruction and Analysis Software for Test Beam Data*, CLICdp-Pub-2020-005 (2020), URL: https://arxiv.org/abs/2011.12730.

[92] T. Preston-Werner, *Tom's Obvious Minimal Language website*, https://toml.io/en/ (last accessed 09/2020).

[93] R. Brun, F. Rademakers, *ROOT — An object oriented data analysis framework*, NIM A **389** (1997) 81, DOI: 10.1016/S0168-9002(97)00048-X.

[94] C. Kleinwort, *General broken lines as advanced track fitting method*, NIM A **673** (2012) 107, DOI: 10.1016/j.nima.2012.01.024.

[95] V. Blobel, *Software alignment for tracking detectors*, NIM A **566** (2006) 5, DOI: 10.1016/j.nima.2006.05.157.

[96] J. Kroeger, S. Spannagel, M. Williams, *User Manual for the Corryvreckan Test Beam Data Reconstruction Framework, Version 1.0*, 2019, URL: https://cds.cern.ch/record/2703012?ln=en.

[97] S. Spannagel, H. Jansen, *GBL Track Resolution Calculator v2.0*, 2016, DOI: 10.5281/zenodo.48795.

[98] F. M. Pitters, *Silicon Detector Technologies for Future Particle Collider Experiments*, Presented 2020, PhD thesis, 2019.

[99] G. Claus, *IPHC & NI Flex RIO DAQ for EUDET Mimosa 26 Beam Telescope*, http://www.eudet.org/e26/e28/e86887/e106215/EUDET-Memo-2010-25.pdf (last accessed 10/2020), 2010.

[100] H. Bichsel, *Straggling in Thin Silicon Detectors*, Rev. Mod. Phys. **60** (1988) 663, DOI: 10.1103/RevModPhys.60.663.

[101] J. Schwandt, D. Dannheim, S. Spannagel, private communication, 2020.

[102] S. Spannagel, *Test Beam Measurements for the Upgrade of the CMS Pixel Detector and Measurement of the Top Quark Mass from Differential Cross Sections*, PhD thesis, 2016.

[103] K. W. P. Myung Jin Yim, *Recent advances on anisotropic conductive adhesives (ACAs) for flat panel displays and semiconductor packaging applications*, Int. Journal of Adhesion and Adhesives **26** (5 2006) 304, DOI: 10.1016/j.ijadhadh.2005.04.004.